The observational phenomenology of a pulsating ultraluminous X-ray source

RAJATH SATHYAPRAKASH

The observational phenomenology of a pulsating ultraluminous X-ray source

by Rajath Sathyaprakash

A thesis submitted to the University of Durham in accordance with the regulations for admittance to the Degree of Doctor of Philosophy.

Department of Physics

University of Durham

United Kingdom

September 2020

Dedicated to

My parents and my sister.

The observational phenomenology of a pulsating ultraluminous X-ray source

Rajath Sathyaprakash

Submitted for the degree of Doctor of Philosophy
September 2020

Abstract

The extreme apparent luminosities of ultraluminous X-ray sources suggests that they are powered either by sub-Eddington accretion onto intermediate mass black holes, or a population of super-critically accreting stellar mass compact objects. The latter hypothesis is thought to apply for the majority of known ULXs based on a wealth of growing evidence, including the recent discoveries of pulsating neutron star ULXs (or PULXs). Among the key questions driving on-going research are whether a majority of ULXs contain neutron star accretors, and how such objects can overcome the Eddington limit. In this thesis, we examine the nature of ULXs in the context of super-Eddington accretion. We report the discovery of X-ray pulsations in an archetypal ULX, NGC 1313 X-2, which adds to the currently sparse number of PULXs. Notably, this object has a weaker pulsed fraction and a lower pulsation duty cycle compared to other sources, requiring frequent and long exposure observations to be detected with current facilities, but would be a key science driver for future missions like *Athena* (see chapter 3). Further, we undertake multi-band (near-infrared to X-ray) observations of NGC 1313 X-2 to discriminate between the proposed physical mechanisms responsible for its optical emission. This is likely to have contributions from multiple components, including the donor star and the X-ray irradiated accretion disc, and we use simultaneous *HST* and *XMM-Newton* data to disentangle these components. The results of this work are discussed in chapter 4. Finally, we perform a search for diffuse X-ray emission associated with shock-ionised ULX bubbles, driven by outflows launched from the ULX accretion disc. The aim was to investigate whether such a process can explain the narrow emission lines found in high-resolution *XMM-Newton* spectra of the particular ULX Holmberg IX X-1 (see chapter 2). We summarise our findings in chapter 5.

Contents

List of Figures

List of Tables

Declaration

The work in this thesis is based on research carried out in the Department of Physics at Durham University under the supervision of Prof. Timothy Roberts and Chris Done. No part of this thesis has been submitted elsewhere for any degree or qualification. Portions of this thesis have resulted in the following papers that have been published or are in preparation:

- Chapter 2: Sathyaprakash, R., Roberts, T. P., and Siwek, M. M. (2019a). Observational limits on the X-ray emission from the bubble nebula surrounding Ho IX X-1. MNRAS, 488(4):4614-4622.
- Chapter 3: Sathyaprakash, R., Roberts, T. P., Walton, D. J., et al. (2019b). The discovery of weak coherent pulsations in the ultraluminous X-ray source NGC 1313 X-2. MNRAS, 488(1):L35-L40.
- Chapter 4: Sathyaprakash, R., Roberts, T. P., Grisé F. et al. in preparation

Acknowledgements

First and foremost, I would like to thank my two supervisors Tim Roberts and Chris Done, without whom this thesis would not have come into fruition. I thank them for their guidance, enthusiasm, for being patient and tolerant of my mistakes, and for providing me the opportunity to interact with other members of the astronomy community. I hope that I have learned from your guidance for what lies ahead. I am thankful to my collaborators Ciro Pinto, Dom Walton, Fabien Grisé and Hannah Earnshaw for helping me with various aspects of X-ray and optical data analysis.

Next, I want to pay special thanks to Ra'ad and Lizelke for their friendship throughout my PhD and for all the memories we've had together. It's fair to say that I could not have come this far without their emotional support. Then, a special mention to my first two officemates Dan and Greg, the former for setting an example with his calm approach to research and helping me with various technical issues, and the latter for introducing me to fun board games that helped me to relax during times of stress. I am also grateful to my next set of officemates Carol, Arnau, Joaquin and Alex for our tennis sessions together, and enlightening discussions on topics outside academia.

Understandably, everyone has suffered from loneliness to some extent due to the COVID-19 pandemic. But, I've been lucky enough to have a great set of friends living near me who have kept me sane over the past few months: Alex A, Monika, Alex E, Gurpreet (a.k.a. the G-Man), Ecem and Abdul. Thanks for all the evenings of Frisbee, board games, dinner (before the pandemic) and banter! I've learnt a lot from being around you.

Of course, I cannot forget my parents and my sister for their persistent support in the face of difficulty, for inspiring me to do research in the first place, and setting an excellent example to follow.

Last but not least, I would like thank all those in the Durham astronomy department for having played a role in my PhD journey and for the fun coffee times (you know who you are!).

Chapter 1 | Introduction

The primary investigation of this thesis is directed towards the study of ultraluminous X-ray sources (ULXs). These are a class of extragalactic binary systems in which the compact remnant of a dead star, such as a neutron star or a black hole, feeds off matter from a neighbouring star at extreme rates, resulting in the emission of intense X-rays. Historically, ULXs were interpreted to be ideal candidates for intermediate mass black holes (IMBHs), thought to be the missing link between black holes formed from the death of massive stars and supermassive black holes residing in the centres of high mass galaxies. However, this picture has evolved in recent years to suggest that ULXs are a hybrid population of sources, mostly comprising neutron stars and stellar mass black holes accreting at rates in excess of the standard Eddington limit, with a few interesting IMBH candidates.

In this section, we begin with a brief introduction to the subject of accretion onto compact objects, highlighting how advances in X-ray astronomy have played an important role in observing such systems, the relevant physical processes of accretion, and the general concepts of sub-Eddington accretion. Then, we focus entirely on ULXs and briefly review the data-driven advances in this field, prior to discussing the main problems that are yet to be addressed, and state the aims of the thesis at the end of this chapter.

1.1 Accretion onto compact objects

1.1.1 The beginning of X-ray astronomy

The Earth's atmosphere is highly opaque to ultra-violet (UV), X-ray and gamma-ray photons, none of which can significantly penetrate below an altitude of 30 km from sea

level [1] (see Figure 1.1[2]). Clearly, this renders it impossible to observe cosmic X-ray sources using ground based detectors, so it is not greatly surprising that X-ray astronomy began with the inception of rocket borne instruments. The first of many such missions was launched in 1962, primarily to observe fluorescent X-rays from the Moon, produced by the irradiation of energetic solar wind particles onto its surface (see Bradt, Ohashi, and Pounds 1992 for details). Although this was unsuccessful, astronomers found another bright X-ray source near the constellation Scorpius, now known as Sco X-1 (Giacconi, Gursky, Paolini, and Rossi 1962). While its nature was not immediately realised, this discovery was crucial because it changed the popular perception that not many objects outside the Solar System would emit detectable amounts of X-rays. Therefore, the 1970s and 80s saw a steep increase in the development of X-ray satellites to explore a new window onto the most energetic astrophysical processes in the Universe, which gradually improved in sensitivity and angular resolution over the years. Some notable missions include *Uhuru* (Giacconi et al. 1971), the first orbiting satellite that scanned the entire sky in the 2-20 keV energy range, *Einstein* (Giacconi et al. 1979), which consisted of a multitude of instruments suitable for relatively deep imaging and spectroscopy, and *ROSAT* ((Pfeffermann et al., 1987)), another all sky survey that more than tripled the number of sources discovered prior to its launch. A detailed description of all the X-ray missions that took place in the early era of X-ray astronomy can be found in Seward and Charles 1995. Several of these satellites were placed on a low-Earth orbit (at altitudes below 500 km), giving them the advantage of being shielded from energetic solar wind particles by the Earth's magnetic field, which minimises a significant source of X-ray background. However, this also prevents exposure to a large fraction of the sky at any given time, which is not greatly problematic for satellites on an eccentric orbit. But, in the latter case, there is increased exposure to high energy radiation from the Sun and cosmic rays, sometimes resulting in background flares or complete interruptions during peak solar activity.

The initial X-ray surveys revealed a wide variety of astronomical sources, including active galaxies powered by accretion onto super-massive black holes residing in their centres

[1] thankfully, for the welfare of all life on the planet!

[2] http://www.icc.dur.ac.uk/ tt/Lectures/Galaxies/Images/Infrared/Windows/irwindows.html

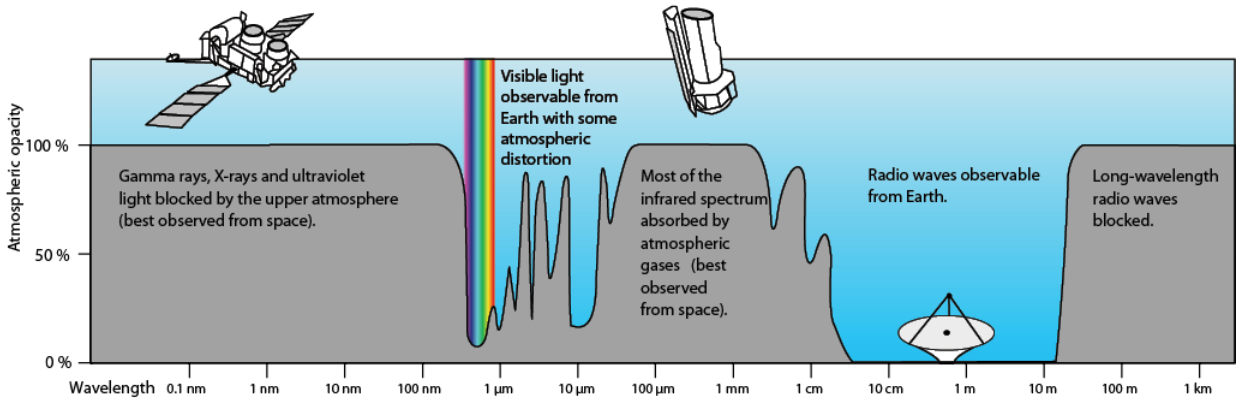

Figure 1.1: A general illustration of the Earth's atmospheric opacity to different regions of the electromagnetic spectrum. All radiation blueward of 100 nm (extreme UV - gamma rays) cannot penetrate below the upper atmosphere (i.e. an altitude of 30 km from sea level) even if the radiating source is directly overhead. This necessitates the use of rocket-borne detectors to observe high energy cosmic sources (Image credit: NASA).

(AGN; Friedman and Byram 1967), hot gas permeating clusters of galaxies (Bradt et al. 1967), which was critical to the inference of a large fraction of dark mass contributing to their gravitational potential, in addition to supernova remnants and X-ray binaries on smaller scales. We focus primarily on the latter as it is the main subject of this thesis, but first give an overview of the central engines of such sources.

1.1.2 The birth of neutron stars and black holes

The core of a main sequence star (including the Sun) is supported against collapsing under its self gravity by energy released from nuclear reactions, primarily from the fusion of hydrogen into Helium. Stars born with a mass larger than ~ 8 $M_\odot$ have cores that reach sufficiently large temperatures and densities to fuse heavier elements, up until the production of iron nuclei (Hirschi et al. 2008). But, nuclear fusion of iron is endothermic since it requires more energy than it produces, and thus cannot provide pressure support against inward gravity. As a result, the core contracts and liberates enormous amounts of gravitational energy, which causes the outer layers of the star to be expelled in a series of complex processes that lead to a supernova explosion. Meanwhile, as the core reaches extremely high densities exceeding that of a heavy atomic nucleus (i.e. $\sim 10^{15}$ g cm^{-3}), most of the protons are converted to neutrons (and neutrinos) via electron capture,

since this is energetically favoured to minimise Coulomb repulsion (Shapiro and Teukolsky 1983). Under these conditions, the neutrons are squeezed to such small volumes that they are forced to occupy higher energy states due to the Pauli exclusion principle, which gives rise to a degeneracy pressure that supports the core against gravitational collapse. Such an object is often referred to as a neutron star (NS). Similarly, white dwarfs (WDs) are the collapsed remnants of low-intermediate mass stars (< 8 $M_\odot$) that are held together by the pressure from degenerate electrons (Mukai 2017), provided that their mass is smaller than the *Chandrasekhar* limit (1.4 $M_\odot$; corresponding to the average molecular weight per electron $\mu_e = 2$).

As the radius of an NS shrinks to sizes much smaller than its progenitor during core collapse, it acquires a larger rotation velocity, conditional on angular momentum conservation of any material that remains bound to the NS after the supernova. In addition, if the surface magnetic flux of the NS's progenitor is also conserved, this can result in a newborn NS having a large magnetic field strength, in the range of $10^8 - 10^{15}$ Gauss (Ostriker and Gunn 1969). A combination of these two properties (fast rotation rates and strong magnetic fields) allows NSs to be observed as radio pulsars, first discovered by Bell and Hewish (1967). Pulsars emit beams of radio emission along their magnetic axis that periodically sweep the observer's line-of-sight, due to their misalignment with the rotational axis of the NS [3]. Currently, various types of radio and X-ray pulsars are known to exist (Manchester 2005; Caballero and Wilms 2012), which serve as extremely precise clocks that can be used to probe the effects of strong gravity. For example, a measurement of the infinitesimally small rate of orbital decay of a short period binary pulsar (i.e. 75 μs yr^{-1}; Hulse and Taylor 1975) enabled the first inference of gravitational waves (a recently confirmed prediction of general relativity; Abbott et al. 2016). Pulsar timing has also provided useful insights into another key unresolved issue, which pertains to the maximum mass that the core of an NS can be supported against gravitational collapse by degenerate nuclei (modulo its rotation). This depends on the poorly constrained equation of state of matter in its dense core (i.e. how its stiffness varies as a function of density). While it is beyond the scope of this chapter to discuss this in detail, we note that models for the equation of state can be mapped to two main observables of the NS:

[3] analogous to a lighthouse

its mass and radius. Among the principal aims of pulsar timing and X-ray observations of NSs are to provide precise measurements of these quantities, in order to make progress on understanding the composition of nuclear matter in their cores (e.g. Özel and Freire 2016).

Now, if the mass of an NS core breaches the threshold above which it can no longer be supported by degenerate nuclei, it collapses to an infinitely dense singularity known as a black hole (BH). The idea that such objects exist was formulated in Einstein's theory of general relativity (GR). In this framework, gravity is not treated as a force that acts instantaneously between two massive bodies, but is rather a consequence of the curvature in space and time induced by a massive object, on which external point masses (and photons) move along the shortest possible paths. Indeed, the curvature induced by black holes is thought to be so immense that within a special boundary, known as the event horizon, the escape velocity for an external point mass becomes larger than the speed of light, and no information from within this region can reach an outside observer. Furthermore, for a distant observer, the interval between two ticks of a clock will appear to be larger closer to a BH than further away due to the gravitational redshift of photons.

Using Einstein's theory, Karl Schwarzschild computed the event horizon for a non-spinning BH to be

$$R_{\rm s} = \frac{2GM}{c^2}, \tag{1.1.1}$$

where G is the gravitational constant, M is the BH mass and c is the speed of light. However, it is possible for the BH to have non-zero spin as it can retain some angular momentum from its progenitor, and in which case the event horizon is dragged inwards (Kerr 1963).

Based on the above description, it is clear that isolated black holes cannot be seen directly since they don't emit any observable amounts of radiation. But, their presence can be inferred indirectly through their influence on any surrounding material that might be devoured from a neighbouring star, or via their effect on the orbits of nearby stars. Indeed, usage of these and several other techniques has revealed concrete evidence for BHs populating two extreme mass ranges (e.g. Greene, Strader, and Ho 2019 and references therein). The first are thought to form via the direct collapse of massive stars at the end

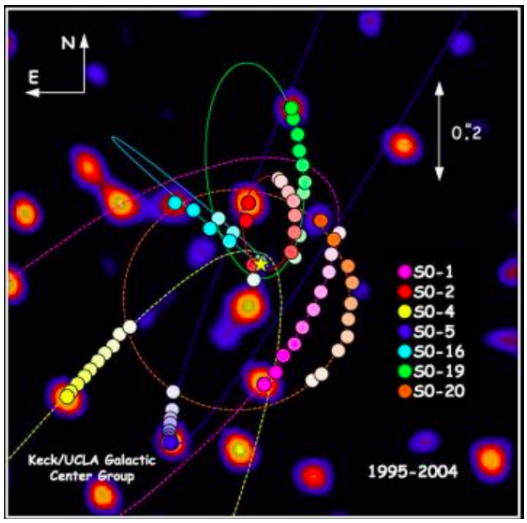

Figure 1.2: Annual averaged orbital positions of stars (coloured dots) near the Galactic centre using the 10-meter Keck telescope, which highlights the presence of an unseen supermassive BH named Sgr A∗ with $M \sim 4 \times 10^6$ $M_\odot$ (yellow star; Ghez et al. 2005). Increasingly darker shades of a given colour are used to depict the motion of the same star as a function of time (Image credit: UCLA Galactic Center Group).

of their evolution, which are observable as X-ray binaries if the BH is actively accreting material from a companion star (see next section). X-ray and optical observations of such sources in the Milky Way (MW) indicate that there are up to ~ 25 known stellar mass BH candidates, usually with $M \lesssim 20$ $M_\odot$ (see e.g. Charles and Coe 2006). However, it is possible to form slightly more massive BHs ($\lesssim 100$ $M_\odot$) in regions of lower metallicity, which allows their progenitor to lose less mass via stellar winds (e.g. Belczynski et al. 2010). Indeed, the existence of such massive stellar BHs is supported by the detection of gravitational waves (GWs) from merging binary BHs (Abbott et al. 2016), which have individual masses > 25 $M_\odot$. However, their origin is still debated since such massive BHs could also have formed via hierarchical mergers of smaller constituents in dense environments such as young star clusters (e.g. Fishbach et al. 2017).

On the other extreme, tracking multiple orbits of stars near the centre of the Milky Way (MW) revealed that they must be bound by an unseen massive object ($M \sim 10^6$ $M_\odot$) within a highly compact region of 10 - 50 AU (see Figure 1.2[4]; Ghez et al. 2005). This led to the likely conclusion that the central object is a supermassive BH (SMBH),

[4]https://phys.org/news/2006-01-astronomers-insights-massive-black-hole.html

which are currently thought to reside in the nucleus of all high mass galaxies. Indeed, the Event Horizon Telescope (EHT) built upon previous evidence for the existence of SMBHs using a series of synchronised radio interferometers around the world to reconstruct the radio image of the nearby SMBH Messier 87 with unprecedented angular resolution. This allowed for the first time to directly resolve the motions of material falling into the BH near its event horizon (see Event Horizon Telescope Collaboration et al. 2019). Some SMBHs are observed as active galactic nuclei (AGN) in which the SMBH feeds off material from its host, thus radiating energy at multiple wavelengths (radio - gamma rays). There is considerably less direct evidence for the existence of BHs linking the two extreme mass ranges discussed above. Such intermediate mass BHs are interesting to consider, since they could shed insights into the formation scenarios of the most massive SMBHs (e.g. Volonteri 2010 and references therein), and we discuss their implications briefly in section 1.3.1.

1.1.3 The discovery of X-ray binaries

Early X-ray observations of the Milky Way revealed numerous point sources located in the plane of the galaxy, with a few scattered in the bulge (Voges 1993). Their X-ray luminosities were observed to exceed the broadband solar power by many factors of ten thousand, and they showed variability over a wide range of timescales from fractions of a second to several days. The first major clues to understanding the emission mechanisms from these objects came from the launch of the *Uhuru* satellite. This led to the discovery of regular pulsations in several sources, with periods on the order of seconds to milliseconds, in addition to rhythmic X-ray eclipses on longer timescales (Giacconi et al 1971; Tananbaum et al. 1972). The stability of the X-ray pulsations implied that it must be connected with the rotation of a magnetised star, since no other mechanism was known to be capable of producing such an accurate clock. In some cases, the short (millisecond) pulsation periods implied rotation velocities too fast to be compatible with a spinning white dwarf, since this would lead to its break-up due to the centrifugal force. Instead, the X-ray source was more likely a neutron star, which would be able withstand more massive rotation rates due to its greater compactness. It was thus realised that the point sources observed by *Uhuru* could be well explained by the picture of a co-orbiting pair of

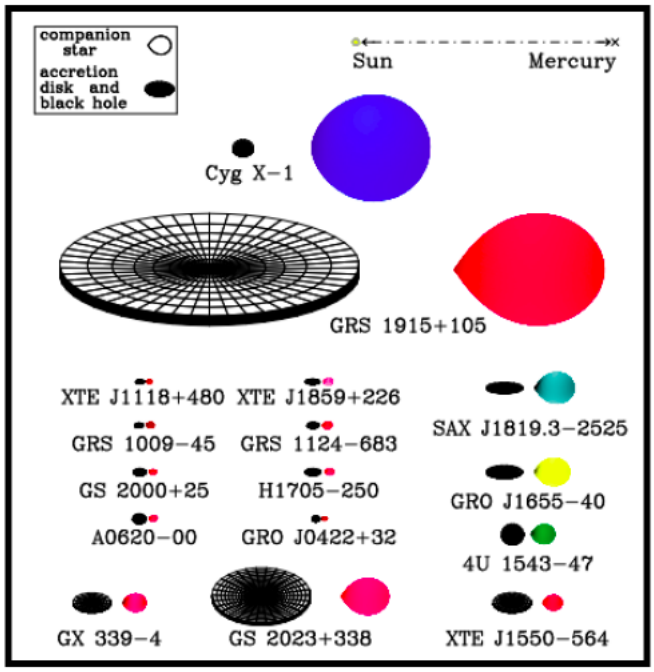

Figure 1.3: A pictorial list of 16 well known Galactic BH X-ray binary candidates, with the distance scale (between Sun and Mercury) illustrated by the black dashed line at the top. The colour of the donor star is a qualitative indication of its surface temperature (with hotter stars shown by blue and cooler stars by red; Image credit: Jerry Orosz)

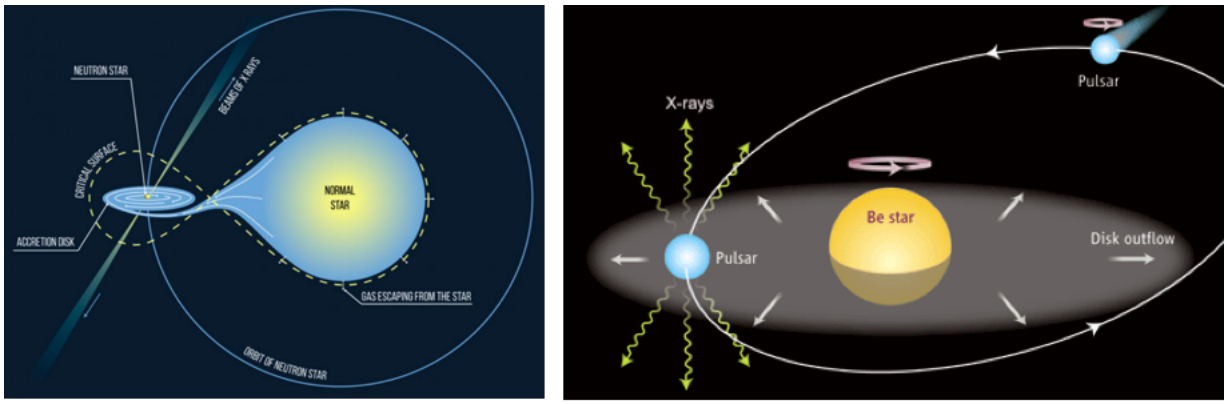

Figure 1.4: Two types of mass transfer mechanisms prevalent in X-ray binaries. *Left*: An illustration of Roche lobe overflow (RLOF) occurring when the donor's radius exceeds its own gravitational sphere of influence (yellow dashed line), which results in the formation of an accretion disc around the primary NS. Tidal forces acting on the donor distorts it into a tear-dropped shape. *Right*: An NS on a moderately eccentric orbit intercepting material from the equatorial disc of a Be star during certain orbital phases, leading to intermittent mass transfer in a Be XRB (Image credit: F. Mirabel)

stars that were close enough to be exchanging mass (i.e. a binary system). The strong gravitational potential of the accreting compact object (a WD, NS or a BH) heats the in-falling matter to temperatures near millions of Kelvin, which is sufficient to release energy at X-ray wavelengths. Notably, accretion is one of the most efficient ways of converting rest mass energy into radiation, even more so than the nuclear fusion of hydrogen into Helium in stellar cores. The accretion efficiency is parameterised by:

$$\eta = \frac{GM_{\rm BH}}{R_{\rm in}c^2} \tag{1.1.2}$$

where $R_{\rm in}$ is the innermost stable circular orbit and depends on the black hole mass and spin (relative to the spin of the accretion disc). For a non-spinning (Schwarzschild) BH, $R_{\rm in} = 6\frac{GM_{\rm BH}}{c^2}$ and thus $\eta = 1/6$. Below, we elaborate on the details of the mass transfer processes in these systems.

1.1.4 Mass transfer mechanisms

Classically, there are two main processes by which mass can be gravitationally captured by the accretor (also known as the primary). If the donor is of early O/B or Wolf-Rayet spectral type, it can undergo steady mass loss due to resonant absorption of UV photons by metals such as iron in its outer envelope. If a fraction of this ejected material traverses within the impact parameter of the compact object, it will be accreted via the Bondi-Hoyle process (see Bondi and Hoyle 1944). The typically high mass loss rates of O/B stars ($\sim 10^{-6}$ $M_\odot$ yr^{-1}) can account for the observed luminosities in several X-ray binaries. However, there are also X-ray luminous sources containing evolved low mass donors that are unlikely to be powering such strong winds. In these systems, an alternative means of fuelling mass onto the accretor is required (especially in cases where the radiative efficiency is small, as for non-spinning BHs). One proposed mechanism involves the tidal stripping of the donor's envelope when it overflows its Roche lobe (i.e. its gravitational region of influence) during certain stages of its evolution (e.g. Bhattacharya and van den Heuvel 1991; Tauris et al. 2000). This is highlighted in Figure 1.4[5], which shows the combined gravitational potential of two binary stars in their co-rotating frame of reference. The Roche Lobe intersects the Lagrangian point L1, where the net force acting on any external point mass is zero. The donor may begin to overfill its Roche lobe during the Hertzsprung gap [6] when its outer shell undergoes rapid expansion on the thermal (Klevin-Helmholtz) timescale, powered by energy release from multiple sources including hydrogen burning in the shell and gravitational contraction of the core. However, even when the donor's radius is stable during the main sequence, Roche lobe overflow may still be initiated due to a loss of orbital angular momentum from the binary (e.g. Podsiadlowski, Rappaport, and Pfahl 2001), or due to a decrease in orbital separation during mass transfer from a more massive to a less massive star. The latter can cause the size of the orbit and the Roche Lobe radius to shrink. To illustrate this, we can consider the simple case of conservative mass transfer, where all the mass transferred by the donor is accreted by its companion, so that the angular momentum of the binary system $\boldsymbol{J}$ is conserved. This can be expressed in

[5] https://science.sciencemag.org/content/335/6065/175.summary

[6] i.e. evolution just off the main-sequence

terms of the donor and accretor masses (M_1 and M_2) and orbital separation of the binary a as:

$$J = \frac{M_1 M_2}{M_1 + M_2} \sqrt{G(M_1 + M_2)a} \tag{1.1.3}$$

According to our assumptions, both $\dot{J} = 0$ and $\dot{M}_1 + \dot{M}_2 = 0$, which implies:

$$\dot{a} = 2a\dot{M}_1\Big(\frac{1 - M_2/M_1}{M_2/M_1}\Big) \tag{1.1.4}$$

From the above equation, it is clear that if $\dot{M}_1 < 0$ and $M_1 > M_2$ (i.e. mass is transferred from the more massive donor to the less massive companion), then $\dot{a} < 0$ and so the separation between the two stars will reduce. The gravitational region of influence of the donor reduces with decreasing orbital separation from its companion, which means that the Roche Lobe radius of the donor also decreases during the mass transfer. Meanwhile, as the donor loses mass due to Roche Lobe overflow, it is taken out of thermal and hydrostatic equilibrium, and this causes its radius to change (to restore equilibrium) in a manner that depends on its internal structure (i.e. whether it has a convective or radiative envelope; see Pavlovskii et al. 2017 for details). In some cases, the thermal equilibrium radius of the donor may be larger than its Roche Lobe radius, and in such cases the donor would expand to re-establish thermal equilibrium while its Roche Lobe radius decreases due to the shrinking orbital separation. This can lead to a period of unstable and short-lived mass transfer phase with $\dot{M} = M_1/t_{\rm KH}$, where $t_{\rm KH}$ is the timescale required for the donor to establish thermal equilibrium (i.e. the Kelvin-Helmholtz timescale):

$$t_{\rm KH} = \frac{GM_1^2}{R_1 L} \sim 3 \times 10^7 \left(\frac{M_1}{M_\odot}\right)^2 \left(\frac{R_1}{R_\odot}\right)\left(\frac{L_1}{L_\odot}\right)^{-1} \text{years} \tag{1.1.5}$$

Here, R_1 is the donor radius and L_1 is its bolometric luminosity. The mass transfer becomes more stable as the mass ratio of the system reverses until $M_1 < M_2$, at which point the donor's Roche Lobe starts to increase and the donor begins to re-attain thermal equilibrium. Then, the mass transfer occurs on the (much longer) nuclear timescale $t_{\rm nuclear}$ of the donor, when its expansion is powered mainly by nuclear processes in its interior:

$$t_{\rm nuclear} \sim 7 \times 10^9 \left(\frac{M_1}{M_\odot}\right)\left(\frac{L_1}{L_\odot}\right)^{-1} \text{years} \tag{1.1.6}$$

King et al. (2001) suggest that during thermal timescale mass transfer, the mass loss rate of the donor can be sufficiently large to account for the large X-ray luminosities of ultraluminous X-ray sources (see section 1.3) and is thus one possible way of powering such sources. Indeed, studying the range of parameter space (e.g. mass ratio, stellar structure, metallicity) over which the mass transfer due to Roche Lobe Overflow (RLOF) is stable is important, because this influences both the duration of the ULX phase (and hence its detectability; Wiktorowicz et al. 2017), and the likelihood of forming merging binary black hole and neutron star systems. Finally, we add that our arguments above are limited to the case of conservative mass transfer and angular momentum, which need not be adhered to in reality (Fragos et al. 2015). We refer the readers to Podsiadlowski (2014) for a detailed discussion on the mass transfer during such scenarios.

In summary, X-ray binary systems with compact stars accreting from the stellar wind are termed high mass X-ray binaries (HMXBs) due to the presence of a young massive companion powering the wind, and are likely to be found in regions where recent star formation has occurred (Grimm et al. 2002). On the other hand, those accreting from an evolved donor via RLOF are classified as low mass X-ray binaries (LMXBs). It is also worth highlighting a third type of mass transfer occurring in the so-called Be X-ray binaries, which usually contain an NS in a moderately eccentric orbit around a rapidly rotating B star (see Reig 2011 and references therein). The latter is surrounded by a thin disc of gas around its equator, as revealed by observations of highly variable Hα emission lines (see e.g. Reig et al. 2005). The disc is likely fuelled by episodes of mass ejection from the star, facilitated by its fast rotation, which can be periodically intercepted by the NS (Figure 1.4). This allows the NS to accrete large amounts of mass over short periods of time, giving rise to transient X-ray outbursts (Kretschmar et al. 2012). Finally, an additional mass transfer mechanism that could power ULXs, in which a strong wind from a supergiant or Wolf-Rayet donor is beamed towards the accretor in a moderately compact binary, is discussed in El Mellah et al. (2019).

1.1.5 Dynamical masses of compact objects

Optical spectroscopy of donor stars has provided crucial evidence in establishing the existence of stellar mass black holes via their dynamically measured masses. This method takes advantage of the periodic Doppler shifts displayed by the absorption and emission lines of the donor due to its orbital motion, which reveals information about the orbital period, while the amplitude of the Doppler shift indicates the projected orbital velocity of the star. These quantities are used to define the binary mass function

$$f(M) = \frac{P_{\rm orb} v_\star^3}{2\pi G} = \frac{M_{\rm BH}^3 \sin^3 i}{(M_{\rm BH} + M_\star)^2}, \tag{1.1.7}$$

where $P_{\rm orb}$ is the orbital period, $v_\star$ is the projected orbital velocity of the companion and G is the gravitational constant. The above expression is inferred using Kepler's third law and assuming that the centre of mass of the system is at the origin. If the mass of the donor star $M_\star$ is known from its spectral type (i.e. by comparing its optical spectrum with stellar templates), and if one assumes that the binary is viewed at a face-on inclination i, a lower limit on the black hole mass $M_{\rm BH}$ can be placed. Indeed, the first stellar mass black hole in our Galaxy (Cyg X-1) was discovered by applying this method, made possible by the identification of a supergiant counterpart to the X-ray source based on its optical spectrum (see Sowers et al. 1998). However, weighing black holes using this technique does introduce complexities, since it is not always trivial to disentangle the stellar emission from other sources of optical emission, such as from the accretion disc or X-ray reprocessing from outflowing material in the vicinity of the compact object. This is especially the case in LMXBs that usually have evolved, optically faint donors. Moreover, the inclination is usually unknown, and only in rare cases can it be inferred accurately due to the presence of X-ray eclipses. Despite the limitations of this method, it has been successfully used to constrain the black hole mass ranges for several Galactic X-ray binaries (see Figure 1.3[7]; Charles and Coe 2006).

[7] https://jorosz.sdsu.edu/

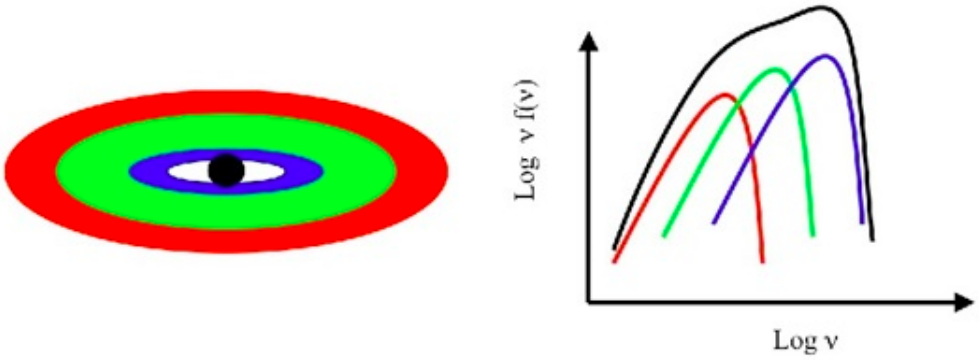

Figure 1.5: Each annulus of a standard geometrically thin, optically thick accretion disc radiates with a blackbody spectrum characterised by temperature T (Shakura and Sunyaev 1973), which scales with radial distance from the central object as $T \propto r^{-3/4}$. A combination of these individual spectra is used to construct a multi-colour blackbody spectrum, as shown in the right hand figure (solid black; Image credit: Jeanette Gladstone)

1.1.6 Accretion in the optically thick case

Any material expelled from the donor retains the orbital angular momentum of the binary, and hence does not initially fall radially inwards, but rather forms an accretion disc around the compact object. In order to be accreted, the material must lose its angular momentum, and the process by which this occurs was initially postulated by Shakura and Sunyaev (1973) in their α-disc model. The basic premise of their idea is that mass inflows radially as angular momentum is transported outwards due to frictional heating between different fluid elements of the disc. This friction is thought to arise due to the differential rotation of matter between neighbouring disc annuli, which results in a net viscous torque exerted on the inner annulus by the outer one, and this leads to a net transfer of angular momentum radially inwards. The viscous heating was assumed to be proportional to the sum of the disc gas ($\propto T$) and radiation pressures ($\propto T^4$), although a physical origin for the viscosity was not conceived until much later by Balbus and Hawley (1991). A detailed discussion of this mechanism is beyond the scope of this chapter.

The viscous torque forces the disc material to plunge in closer to the compact object, allowing it to liberate its gravitational potential energy, a fraction of which increases the internal energy of the gas while the rest is radiated away (according to the virial theorem;

Done 2010). Depending on the mass inflow rate, the emitted photons can thermalise (i.e. attain thermal equilibrium with the surrounding matter) to a temperature that is set by the balance between the viscous heating and radiative cooling rate. The disc temperature increases with decreasing radial distance from the compact object, as more energy is liberated over a smaller area. Hence, the observed energy spectrum is a sum of blackbodies emitted from infinitesimally thin circular annuli, each with a characteristic temperature (see Figure 1.5[8]). If the central object is a black hole, the disc extends inwards until the last stable circular orbit $R_{\rm in}$. The existence of $R_{\rm in}$ is a consequence of general relativity (Misner, Thorne, and Wheeler 1973), which predicts that the gravitational potential has an unstable inflection point at this radius, such that any small perturbation of a point mass forces it to rapidly infall beyond the event horizon. The expression for $R_{\rm in}$ depends on the BH mass and spin a, and on whether the disc's rotation is prograde (in the same sense) or retrograde (opposite sense) with respect to the latter. For a non-spinning (Schwarzschild) BH:

$$R_{\rm in} = \frac{6GM}{c^2} \tag{1.1.8}$$

while for a maximally spinning BH surrounded by a disc rotating in the same sense (prograde), the inner most stable orbit is dragged inwards with

$$R_{\rm in} = \frac{GM}{c^2} \tag{1.1.9}$$

or for a counter rotating disc (retrograde) around a maximally spinning BH:

$$R_{\rm in} = \frac{9GM}{c^2} \tag{1.1.10}$$

The total gravitational energy available for an accreting mass element as it plunges in from infinity to $R_{\rm in}$ is:

$$dU = \frac{GMdM}{R_{\rm in}} \tag{1.1.11}$$

If the flow is Keplerian, its orbital velocity at some arbitrary radius is $v(R) = \sqrt{GM/R}$, suggesting that half of the gravitational potential energy is used to increase its kinetic

[8]Image credit: https://sites.ualberta.ca/ jgladsto/Site/accretion.html

energy of the flow

$$dK = \frac{1}{2}v^2 dM = \frac{GMdM}{2R}, \tag{1.1.12}$$

while the other half is radiated away (in accordance with the Virial theorem). During steady state, the rate of mass flux $\dot{M}$ remains constant at each radius, implying that the total luminosity radiated by the fluid element is:

$$L_{\rm rad} = \frac{GM\dot{M}}{2R_{\rm in}} \tag{1.1.13}$$

If this energy thermalises, a relation between the disc luminosity and the peak temperature at the last stable orbit emerges, with

$$L_{\rm rad} \propto R_{\rm in}^2 T_{\rm max}^4, \tag{1.1.14}$$

where i is the inclination of the system. An observational test of this relation under the assumption of a constant inner disc radius (in accordance with General Relativity) was carried out by collating disc dominated spectra of an individual object (with a fixed BH mass) at differing luminosities (e.g. Kubota and Done 2004; Kolehmainen and Done 2010). These spectra confirm that the disc luminosity varies with peak temperature in the manner expected for a constant inner disc size scale (i.e. $L_{\rm rad} \propto T_{\rm max}^4$), thus confirming the behaviour predicted by GR in the strong field limit. If the BH mass is known (e.g. from the binary system parameters), a measurement of $R_{\rm in}$ may be used to infer the BH spin. However, determining $R_{\rm in}$ accurately for a given object is difficult due to uncertainties in the source distance and inclination, in addition to other caveats regarding the modification of the disc spectral shape due to incomplete thermalisation of the highest energy photons (known as colour temperature correction; see Gierliński and Done 2004 for details), and the associated relativistic corrections (see Zhang, Cui, and Chen 1997; Kubota et al. 1998).

Unlike BHs, neither white dwarfs nor neutron stars have a singularity, so one would expect that any accreted material deposits its kinetic energy on their surface, as apparent from unique observational phenomena. Indeed, many LMXBs are known to undergo periodically recurring X-ray bursts on hourly-daily timescales, thought to arise as a result of unstable thermonuclear burning on the surface of an NS (see Strohmayer and Bildsten 2003). In a simplified description of this process, hydrogen rich matter accumulates on

the surface and is compressed to sufficiently large densities and temperatures that it steadily fuses via the CNO cycle (as in the cores of massive stars), building up a thin layer of helium. This layer subsequently undergoes runaway thermonuclear burning due to the thin-shell instability (Galloway and Keek 2017), where energy input from nuclear reactions does not lead to a sufficiently fast expansion of the He shell to counteract the rising temperatures. The shell is thus ignited rapidly, producing an X-ray burst with a quasi-thermal spectrum. The entire process then recurs, as fresh hydrogen is accumulated, on a timescale that depends on the accretion rate. An examination of several X-ray burst lightcurves indicates that the peak emission usually stays below the Eddington luminosity of an NS, which allows these events to be used as standard candles to measure the distances to nearby sources (e.g. Chelovekov and Grebenev 2007).

1.1.7 The Eddington limit

The Eddington limit is an important baseline that determines the rate at which compact sources can grow in mass via accretion. Fundamentally, it arises because radiation emitted by the hot accreting plasma exerts an outward pressure on the surrounding material, thus opposing its gravitational infall. Originally, it was derived assuming that the infall of matter is spherically symmetric and that it is composed solely of ionised hydrogen, neither of which are always satisfied in real astrophysical systems (as we will discuss later). However, if these assumptions hold, one can determine the radiation pressure force acting on a proton-electron pair at some distance R from the compact object to be:

$$F_{\rm rad} = \frac{\sigma_T L}{4\pi c R^2} \tag{1.1.15}$$

where σ_T is the Thomson scattering cross section and L is the accretion luminosity. This force is mostly felt by the electrons since they have the larger cross section for photon scattering with respect to protons, and electrostatic attraction means that the protons are dragged along with the electrons. On the other hand, the dominant contribution to the gravitational force is from the protons:

$$F_{\rm g} = \frac{GMm_p}{R^2}, \tag{1.1.16}$$

where M is the mass of the central object. Hence, the critical luminosity at which radiation pressure balances the gravitational force is

$$L_{\rm Edd} = \frac{4\pi G M m_p c}{\sigma_T}, \tag{1.1.17}$$

which is the standard Eddington luminosity. The above expression implies that the growth rate of the compact object occurs exponentially, since $\dot{M}$ is proportional to M at any given time (although this does not account for the advection of radiative flux; see section 1.3.2.2 of this chapter and also chapter 4). This sets the timescale required to increase the BH mass by a factor of e (Salpeter timescale), which turns out to be $\sim 5\times10^7$ years (assuming an accretion efficiency of $1/6$ for a Schwarzschild BH). We note that the Eddington limit would be nearly twice as large for helium rich material, since it has a heavier nucleus compared to hydrogen.

1.1.8 Accretion disc instability

The assumption that the mass accretion rate is constant at each radius (Shakura and Sunyaev 1973) is generally not true, as the disc can be subject to the hydrogen ionisation instability. This is triggered during a steady build-up of material from the donor, which slowly increases the disc surface density and temperature, until it exceeds the temperature required for the collisional ionisation of hydrogen (i.e $\sim 10^{4-5}$ K; Hameury 2020). At this point, the highest energy photons (from the Wien tail of the thermal disc spectrum) begin to ionise some of the hydrogen, which leads to a steep rise in the electron scattering opacity. As a result, more photons are trapped in the disc, with their energy further increasing the local temperature until there is runaway heating. This causes the accretion rate to exceed the mass inflow rate from the donor, since viscous stresses responsible for angular momentum transport scale with the local disc temperature via the gas ($\propto T$) and radiation pressures ($\propto T^4$), in the α disc model of Shakura and Sunyaev (1973). Differences in mass accretion rate between neighbouring regions enables this local instability to propagate through the entire disc, causing it to be eaten away on the viscous timescale. As the material continues to be depleted, hydrogen begins to recombine and the disc temperatures decrease, thus completing a full outburst cycle (see Figure 1.5).

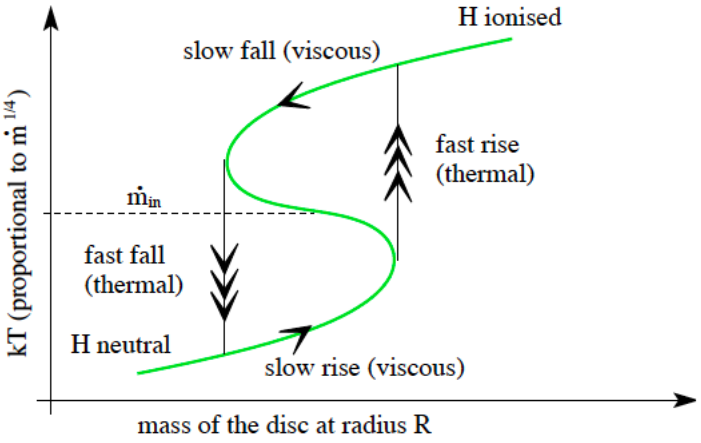

Figure 1.6: A schematic illustration of the hydrogen ionisation instability, operating at a given radius in the accretion disc. The local disc temperature rises steadily as matter accumulates from the companion, until a point at which hydrogen begins to ionise (bottom left). This triggers a steep rise in temperature and mass accretion rate, such that the matter is consumed much faster than it is fuelled ($\dot{m}_{\rm in}$) at this radius. Eventually, this leads to an increased mass accretion rate in the neighbouring regions, causing the entire disc to be consumed on a viscous timescale. As material is depleted, the disc temperature falls, hydrogen begins to recombine, and the source makes the transition back towards the quiescent state (Figure credit: Done 2007)

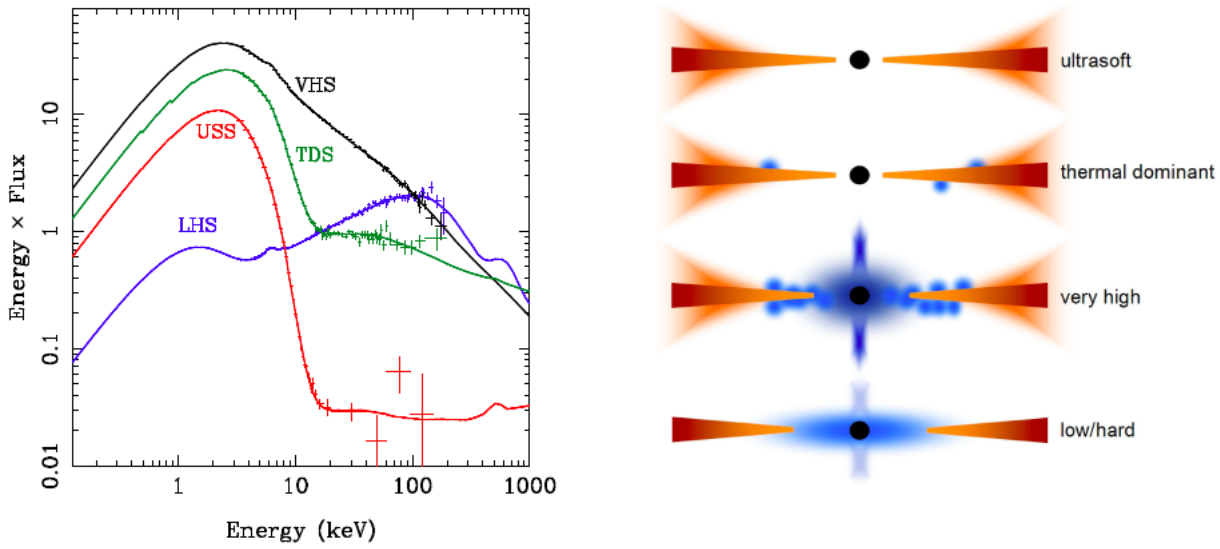

Figure 1.7: A range of spectral states observed in the sub-Eddington Galactic BH X-ray binary GRO J1655-40. *Left*: The expanded abbreviations are LHS (Low-hard state), USS (Ultra-soft/high-soft state), TDS (Thermal dominant state), VHS (Very high state). *Right*: The corresponding accretion disc geometries theorised for each spectral state, with an optically thick disc shown in red, an optically thin extended corona in blue, and its associated jet (blue arrows). This figure has been borrowed from Done, Gierliński, and Kubota 2007

1.1.9 Sub-Eddington accretion modes

Sub-Eddington X-ray binaries go through a plethora of accretion states as the disc cycles between periods of quiescence and outbursts, driven primarily by changes in the mass accretion rate. Here, we review the basic observational phenomenology of these states based on the much more detailed discussion in Remillard and McClintock (2006) and Done, Gierliński, and Kubota (2007). The specific values quoted below for various quantities can be found in the latter references.

- At low Eddington ratios, several black hole XRBs (e.g. Cyg X-1) show non-thermal energy spectra that clearly differ from a multi-colour blackbody (see Figure 1.7). These spectra are dominated by a power-law component (with > 80 % contribution) of the form

$$F(E) = F_0 E^{-\Gamma}, \tag{1.1.18}$$

usually with $\Gamma \sim 1.5 - 2.0$ and an exponential cut-off at the highest energies (~ 500 keV). A thermal component still exists below ~ 0.5 keV, but is much fainter than the power-law (Gierliński et al. 1999). This accretion state is generally seen at luminosities far lower than when the thermal emission dominates (but in some cases upto $\sim 70\%$ $L_{\rm Edd}$), and the spectra are also comparatively harder (i.e. peak flux well above 1 keV). It is thus referred to as the low hard state, and shows strong variability in the X-ray flux (rms > 10 %) on a wide range of timescales, with superposed (type C) low frequency quasi-periodic oscillations (LFQPOs; Motta 2016). This state is also accompanied by radio emission (Corbel et al. 2003) arising from the acceleration of non-thermal electrons within a jet (Markoff et al. 2005).

- Observations also reveal a second class of spectra belonging to the steep power-law (or very high/intermediate) state (Gierliński and Newton 2006), which contain roughly equal contributions from both the thermal and power-law components, and sometimes feature a relativistically broadened iron Kα line (see section 1.2.3). The power-law has a much steeper photon index ($\gtrsim 2.5$) than seen in the low-hard state. In terms of the timing properties, this state shows moderate broadband noise (with rms $\sim 5 - 10$ %) in addition to (type B) quasi-periodic oscillations (QPOs), which display enhanced variability on a narrow range of timescales (Ingram and Motta 2019).

- Finally, the third class of spectra are associated with the high/soft state, and are dominated by thermal emission from an optically thick accretion disc with a faint power-law tail (Mitsuda et al. 1984). They usually appear at the highest luminosities for a given object, and are characterised by weak (< 1 % rms) variability and the absence of radio emission. Observationally, these behaviours are best captured by a hardness-intensity diagram (HID), which uses the evolution in the intensity and spectral hardness (or hard-to-soft flux ratio) of a given source to illustrate its spectral state (see Figure 1.8).

In the low-hard state, the non-thermal component is thought to be powered by an optically thin accretion flow illuminated by photons from a standard disc truncated at a radius larger than the inner-most stable orbit of the BH (see right panel of Figure 1.7). Some measure of disc truncation radii in a few BH XRBs are provided by measurements

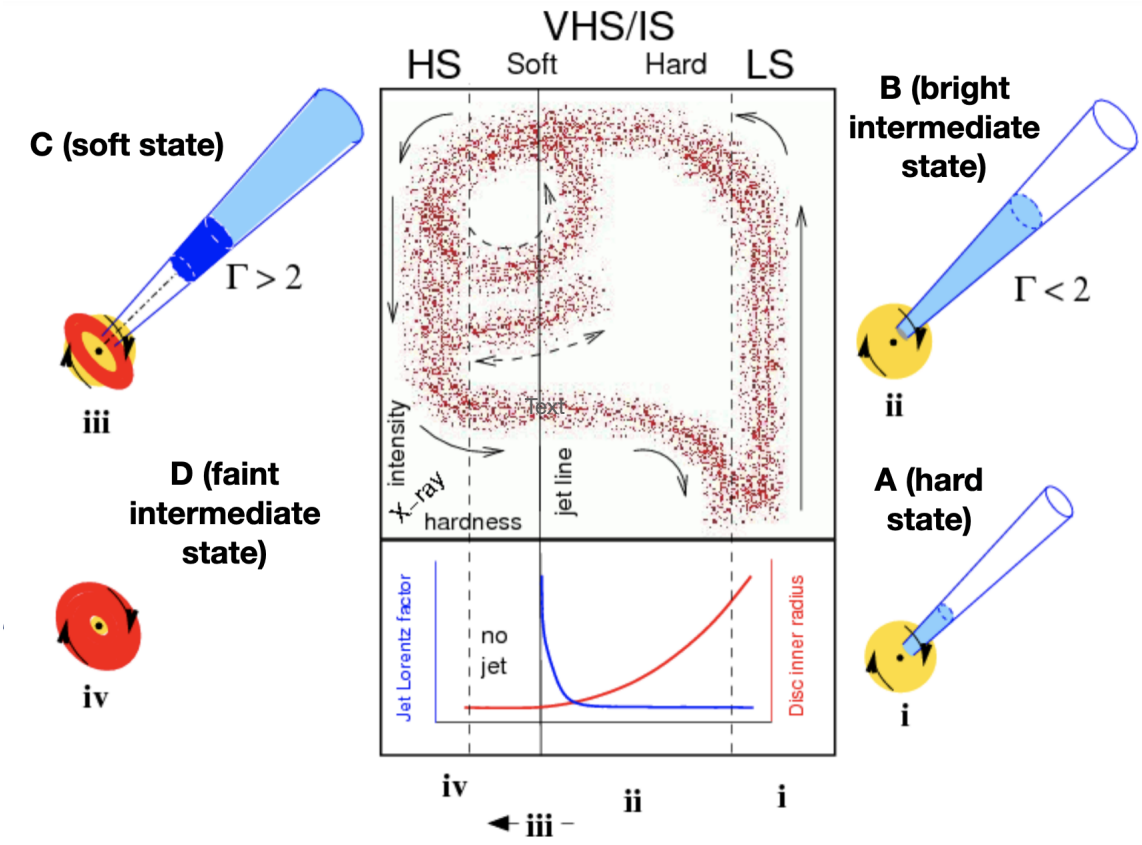

Figure 1.8: An illustration of transitions between various spectral states (shown by arrows from A-D) in the hardness-intensity plane of a BH X-ray binary. Key signatures of each state, including the appearance/disappearance of a radio jet, has been noted (Figure credit: Fender and Belloni 2004).

of thermal reverberation delays during the hard and intermediate states ($\sim 10 - 100\ R_g$; De Marco et al. 2017; Mahmoud, Done, and De Marco 2019). Although, the reader is pointed to De Marco and Ponti (2016) for a discussion of the systematics that could affect the measured lag amplitudes and hence the truncation radii (e.g. dilution of the intrinsic lag due to a contribution of the driving continuum in the energy range where the lagged continuum dominates).

During certain phases of the low-hard state, the mass accretion rate is thought to be sufficiently low that the density of the inner accretion flow becomes small enough for the protons and electrons to thermally decouple. That is, most of the gravitational energy is acquired by the protons due to their larger mass, but little of it is shared with the electrons via Coulomb collisions (e.g. Narayan and Yi 1995). Some electrons to which this energy is transferred cool more efficiently than the protons (due to their larger photon cross section) by radiating Bremsstrahlung X-rays, or by Compton up-scattering seed photons from the disc. The latter produces a power-law spectrum with a high energy cut-off at the mean thermal energy of the electron gas $3kT_e$, as seen in the spectra of BH XRBs (see also section 1.2.1 below). When the mass accretion rate rises during the outburst, so does the flux of seed photons incident on the flow, which leads to increased cooling of the electrons via Compton scattering. This lowers the radial extent of the hot flow as some electrons condense back into the disc, allowing the latter to move closer to the last stable orbit. The reduced mean thermal energy of the electrons causes the power-law emission to become softer, producing a spectrum similar to that seen during the very high/intermediate states. There is increased contribution from the standard disc in addition to some amount of reflected emission, which can be explained by the disc subtending a larger solid angle to emission from the hot flow. At even higher mass accretion rates, the source fully makes its transition to the disc dominated high-soft state. We note that these transitions are not continuous but triggered at some critical luminosity, which need not be the same for every outburst cycle. This occurrence in which the same spectrum can appear at two different accretion rates is known as hysteresis (Maccarone and Coppi 2003).

The above description of the truncated disc model is supported by the observed variability in the Type-C QPO frequency, which increases as the source evolves from the hard state to the thermal dominant state in the HID, suggesting a decrease in size scale of the hot inner flow (Motta 2016). However, some challenges to the truncated disc model are

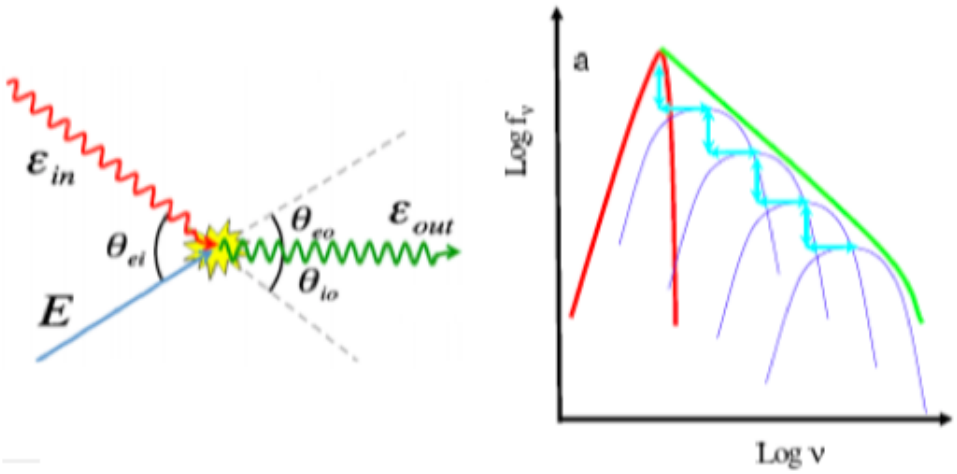

Figure 1.9: *Left*: Geometry of (inelastic) Compton-scattering of a high energy photon by a free electron, with the appropriate angles referred to in the text. *Right*: Seed thermal photons emitted by the disc undergo multiple orders of Compton scattering in an optically thin corona to produce a non-thermal power-law spectrum with a low and high energy cut-off. These figures have been borrowed from Done (2010).

presented by observations of extreme iron line broadening in the hard state of XTE J1650 − 500 (Miller et al. 2006; Reis et al. 2008), which would instead suggest a disc extending to the last stable orbit. Although, this suggestion is contested by Done and Gierliński (2006) who argue that these data could still be consistent with a truncated disc geometry if there is iron K line absorption from a disc wind, which could reduce the extent of the observed relativistic line smearing.

1.2 Radiative processes

Here, we discuss the fundamental physical processes responsible for the emission and absorption of X-ray radiation in the vicinity of compact objects, since they set the context for interpreting the analysis in subsequent chapters.

1.2.1 Comptonisation

Compton scattering is a process by which energy and momentum is exchanged during an inelastic collision between an electron and a photon. It is important to consider this

in a variety of astrophysical situations, with some examples including the scattering of ultra-relativistic cosmic rays by the cosmic microwave background, and the interaction between the disc and the corona in XRBs. After each scattering event, the energy of the photon $\epsilon_{\rm out}$ may change depending on its initial energy $\epsilon_{\rm in}$ and that of the electron, as the latter recoils. In full generality

$$\epsilon_{\rm out} = \frac{\epsilon_{\rm in}(1 - \beta\cos\theta_{ei})}{1 - \beta\cos\theta_{eo} + \epsilon_{\rm in}/\gamma(1 - \cos\theta_{io})}, \tag{1.2.19}$$

where β is the electron velocity (as a fraction of c) and $\gamma = (1 - \beta^2)^{-\frac{1}{2}}$ is the electron Lorentz factor, θ_{ei}, θ_{eo} and θ_{io} are the scattering angles pictured in Figure 1.9, and $\epsilon_{\rm in}$ is expressed as the ratio of the incoming photon and electron rest mass energy (Done 2010). The electrons populating a radiatively inefficient accretion flow in the low-hard state of XRBs (see previous section) are postulated to have a thermal distribution of velocities. Then, the mean velocity is set by the temperature of the gas cloud $v^2 = 3kT_e/m_e$, such that $\beta^2 = 3kT_e/m_ec^2 \equiv 3\Phi$. Over several encounters, the distribution of electron-photon momenta can be considered to be isotropic, such that the outgoing energy in equation 1.2.7 can be averaged over all angles (Rybicki and Lightman 1979). Combining this with the limit where $\epsilon_{\rm in} \ll 1$, we obtain

$$\epsilon_{\rm out} = (1 + 4\Phi)\epsilon_{\rm in} \tag{1.2.20}$$

This is the average energy of a photon after a single scattering event, but it may undergo several subsequent collisions where it is up-scattered by the same constant factor $(1 + 4\Phi)$. Indeed, the overall gain in energy is determined by the total number of scatterings, which cannot exceed the thermal energy of the electron gas (3Φ). This imposes a high energy cut-off to the spectrum of the scattered radiation field. The probability of a single electron-photon encounter depends on the interaction cross-section, which is given by the Thomson value σ_T for the limit considered above (although we note that σ_T changes if the electrons are relativistic; see Sunyaev and Titarchuk 1980). So, the total number of electrons (with density n) encountered by a photon travelling a path length R through the gas cloud is $\tau = nR\sigma_T$ (also known as the optical depth). Some photons are scattered away from the observer's line-of-sight, so the intensity decreases as a function of the distance traversed through the gas cloud. The change in intensity due to scattering dI is proportional to the optical depth τ and the incident flux I, which implies that the intensity

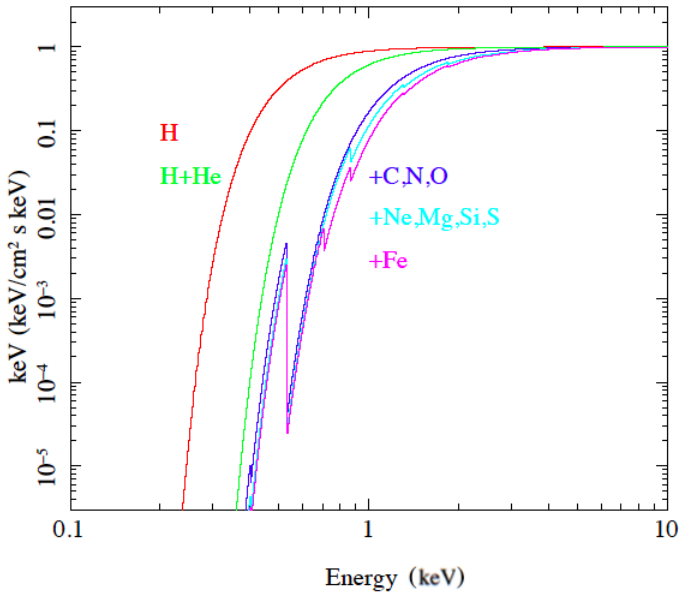

Figure 1.10: The effect of photoelectric absorption on an incident power-law spectrum (with photon index $\Gamma = 1$) by neutral hydrogen alone (red), and progressively heavier atoms (including Helium, Carbon and Iron). Figure credit: Done (2010)

attenuates by a factor of $\exp(-\tau)$. So, the fraction of photons scattered are $1 - \exp(-\tau)$, which simply reduces to τ for optical depths much less than unity.

The main implication of this derivation is that each scattering event induces a constant shift in the photon flux (τ) and energy ($1 + 4\Phi$). For this reason, Figure 1.9 shows how a seed photon spectrum (a blackbody) is distorted into a power-law shape after multiple orders of Compton scattering, similar to that observed during the low-hard state of XRBs.

1.2.2 Absorption

The intrinsic X-ray emission from a distant source can be absorbed by an intervening column of gas, located either within its host galaxy or the Milky Way, or by gas interspersed between galaxies [9]. The absorption results in the excitation of electrons in an atom to a higher (vacant) energy level, or their ejection via the photoelectric effect. In the former case (bound-bound), photons possessing energies equal to the difference between the electron's ground and excited states are absorbed, while in the second instance the energies must be larger than the binding energy of the electron (bound-free). Indeed, any thermal

[9] also known as the intergalactic medium

or turbulent motions of the absorbing gas broadens the range of energies that the photon must have to be absorbed. The absorption probability depends on the cross section $\sigma(E)$ of a given element/ion to the incident photon and its mean column density $N_{\rm X}$ along the line-of-sight. This is defined via the optical depth as $\tau = \sigma(E)N_{\rm X}$. For neutral hydrogen, the photoelectric cross section peaks at the binding energy of its electron (13.6 eV), but decreases above this energy as $\propto E^{-3}$. This results in the absorption edge shown in Figure 1.10. For heavier elements the edges occur at progressively higher energies, as their innermost (K-shell) electrons are more strongly bound. Some prominent examples are the carbon (0.4 keV), oxygen (0.53 keV) and iron edges (7.1 keV), although these elements are cosmologically less abundant than hydrogen and thus make a smaller contribution to the overall cross section. Now, atoms ionised via the photoelectric effect will recombine on a timescale that depends on the electron density n_e, its capture cross section and velocity distribution α. If this is larger than the photoionisation timescale ($\propto n_\gamma^{-1}$), the ions are likely to be irradiated by a photon before recombining, such that they make a non-negligible contribution to the X-ray absorption cross section. This is generally smaller than for neutral atoms, since ions contain less bound electrons (see Done 2010 for more details). The ionic state of a given element (i.e. the abundance of ion $\rm X^{+\mathit{i}}$, with i electrons removed, with respect to $\rm X^{(\mathit{i}+1)}$) is proportional to the ratios of the photon and electron densities, provided the photoionisation rate is in equilibrium with the recombination rate.

Absorption is a nuisance in interpreting the spectra of X-ray sources, especially in the Galactic plane where one views through a large column density of material. However, it provides useful information about the composition, ionisation states and kinematics of matter, both within the galaxy and in the vicinity of distant objects. For instance, the advent of high resolution grating instruments has enabled the detection of fast outflowing material from accretion discs around supermassive black holes, in the form of blue-shifted iron absorption lines (e.g. Pounds et al. 2003; Risaliti et al. 2005; Detmers 2011). Such winds are thought to be an important source of feedback, in terms of controlling the star formation activity of their host galaxy. Moreover, X-ray absorption spectroscopy may also have revealed a substantial fraction of hot diffuse baryons embedded in filaments connecting galaxies in the local universe (e.g. Nicastro et al. 2018), which were formerly thought to be missing since 2-3 billion years after the Big Bang.

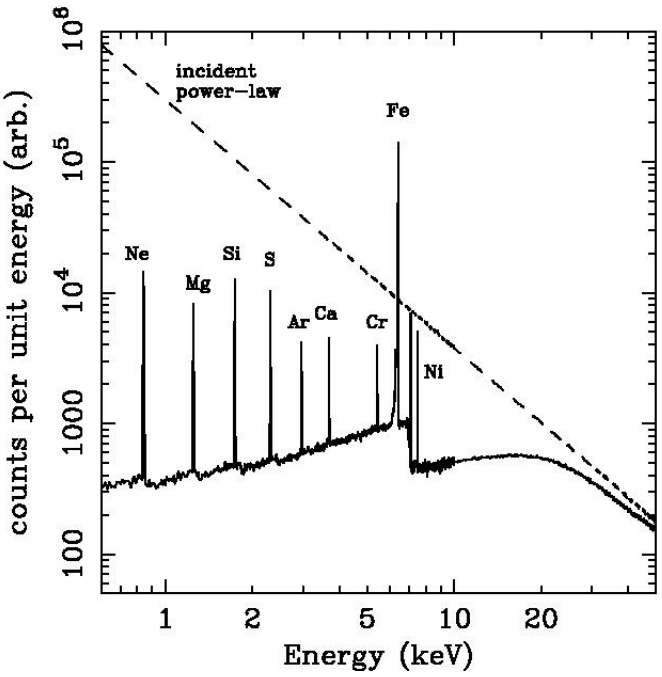

Figure 1.11: The reflection continuum (solid line), with a dominant iron line contribution, produced by the illumination of an incident power-law continuum (dashed line) onto a cold slab of material. This figure has been borrowed from Fabian et al. 2000.

1.2.3 Reflection

A reflection continuum emerges when Compton scattered emission from a large scale height corona irradiates the accretion disc during certain states (Fabian et al. 2000). These photons have some probability to be scattered back into the observer's line-of-sight (i.e. reflected), or to be absorbed via the photoelectric effect. In the latter case, the excited ion may decay back into the ground state either by emitting a fluorescence line (e.g. Kα for n=2 to n=1 transition) or via Auger de-excitation (i.e. by ejecting one of the bound electrons from the atom). Figure 1.11[10] shows the reflection spectrum produced when a slab of material is illuminated by non-thermal emission, with all elements except hydrogen and Helium assumed to be neutral (George and Fabian 1991; Done 2010). At low energies (< 2 keV) photoelectric absorption dominates, so the reflected emission is much weaker than the direct power-law continuum. As a result, any fluorescent lines are highly diluted at these energies, and the strongest line emission is seen at ~ 7 keV from

[10]https://ned.ipac.caltech.edu/level5/Fabian4/Fab2_1.html

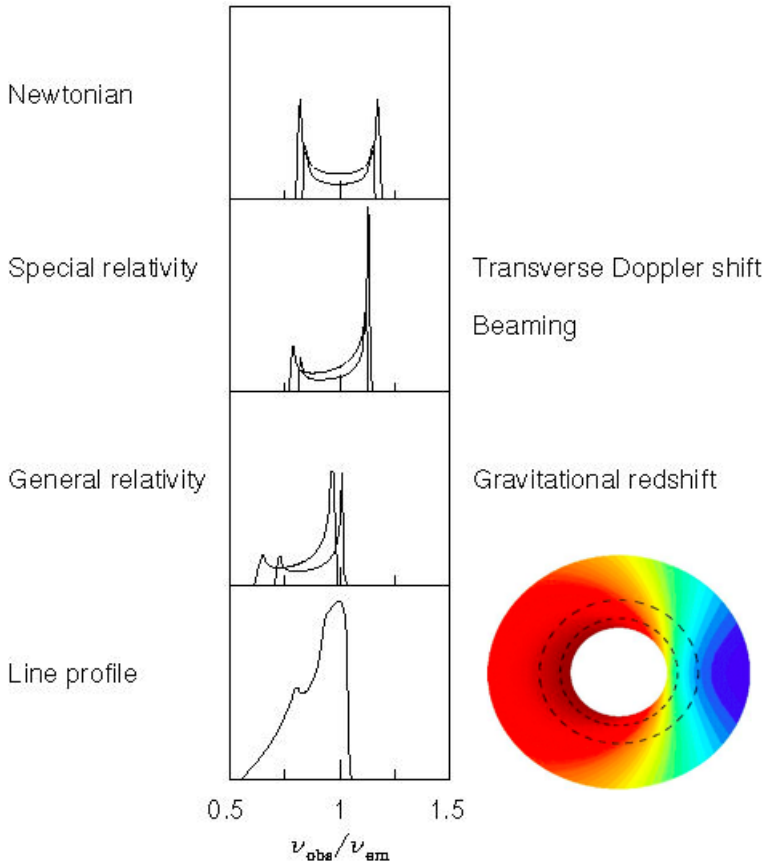

Figure 1.12: The top-most panel shows how Doppler shifted emission from the receding and approaching sides of the disc can produce two symmetric iron line peaks, provided the system is not viewed near face-on, and if the disc rotation velocities are non-relativistic. While this applies for regions farther away from the central object, it does not hold for radii closer to the last stable orbit, where line emission from the blue shifted side is enhanced (and the redshifted side is suppressed) due to relativistic beaming (second row). The observer also sees the emission from material moving perpendicular to the line-of-sight to be redshifted due to time dilation. Finally, the emission from each radius is subject to gravitational redshift, increasing in strength at smaller radii, which shapes the profile of the red wing (third row). The latter is thus sensitive to the location of the innermost stable orbit, which allows constraints on the BH spin. All these effects serve to produce the line profile shown in the bottom most row (Figure credit: Fabian et al. 2000)

iron, where the ratio of reflected to absorbed flux is larger. Above 10 keV, the reflection continuum increases as Compton scattering becomes more important, but the process is inelastic such that the scattered photons lose energy due to electron recoil (section 1.2.1). This gives a spectral break at high energies (above $\sim$ 50 keV) known as the reflection hump.

The iron line encodes information on the dynamics of the accretion flow in the vicinity of the compact object. The line profile is blurred as a result of special and general relativistic processes, which are explained in detail by the caption of Figure 1.12[11]. The extent of line broadening towards energies less than the rest frame is partly due to the gravitational redshift of photons, as they climb out of the strong potential well of the compact object. Hence, the red wing of the iron line is sensitive to the location of the innermost stable orbit, allowing constraints on the BH spin without a knowledge of its mass or distance. However, the line may also be smeared as a result of electron scattering in a partially ionised plasma, which would bias estimates of the inner disc radius unless this is taken into account with an appropriate model (Done 2010).

1.2.4 Shock heating

In this sub-section, we aim to give some background to the work carried out in chapter 2 by discussing the physics of shock-heating and thermal plasma emission. Radio, optical and X-ray observations have revealed cavities in the interstellar medium (ISM) on a wide range of spatial scales (Dubner et al. 1998; Predehl et al. 2020). Such bubbles are excavated by multiple processes including supernovae or winds from young massive stars situated within star clusters, winds launched from the accretion discs of active galaxies or that from low or high mass X-ray binaries on smaller scales. Interstellar bubbles are important in a variety of astrophysical problems, including the regulation of star formation rate in the host galaxy of an AGN and metal enrichment of the ISM.

According to the standard picture of wind inflated bubbles described in Weaver et al. (1977), the wind expands freely until its density becomes comparable to the density of the surrounding interstellar medium (ISM). Hereafter, the pressure exerted by the ISM slows down the expanding bubble to velocities less than the speed of sound, resulting in

[11] https://ned.ipac.caltech.edu/level5/Fabian4/Fab2_2.html

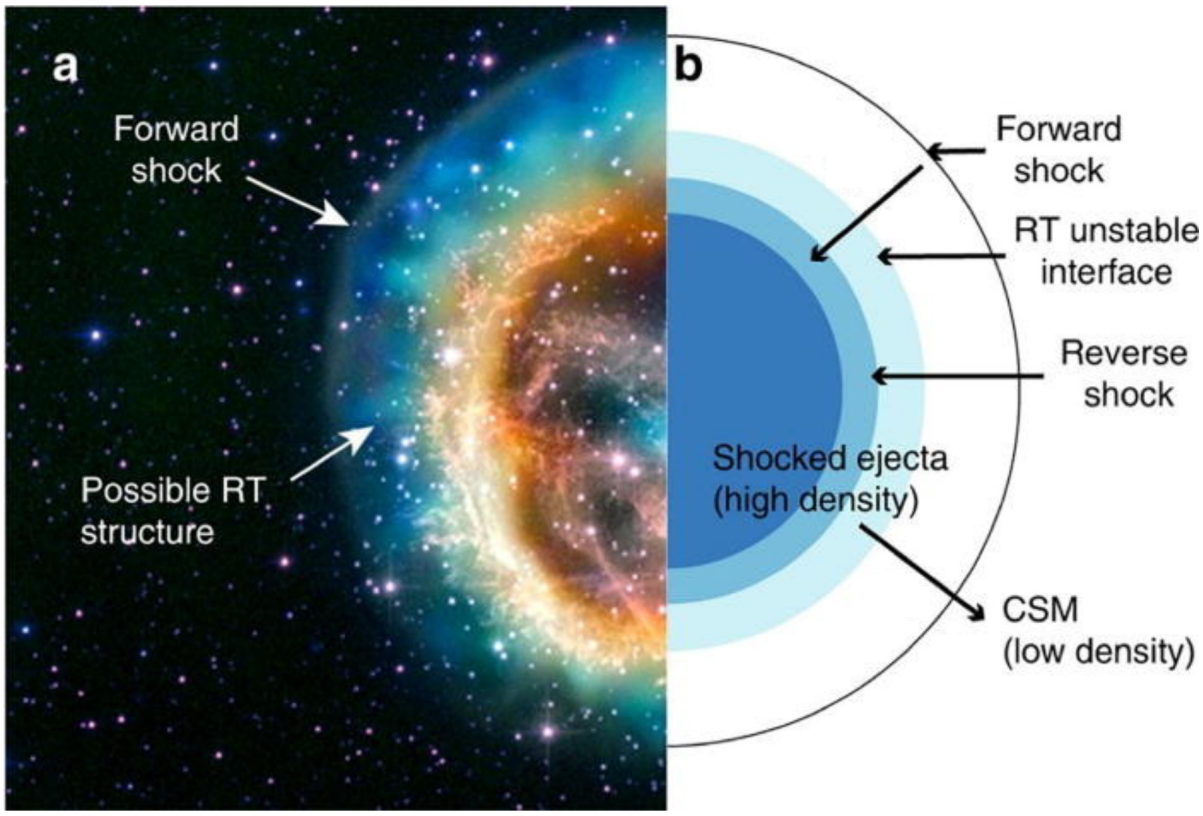

Figure 1.13: *Left*: A false colour X-ray and optical image of an interstellar bubble indicating the presence of a forward shock and a Rayleigh-Taylor (RT) unstable region. *Right*: A schematic of the structure of the bubble showing additional features discussed in the text. This figure has been reproduced from Zhou et al. (2019).

the formation of a reverse shock (that propagates inwards in the frame of the expanding ejecta). The acceleration of the ISM by the wind produces another shocked region at the forefront of the bubble (see Figure 1.13), known as the forward shock, which comprises a thin layer of swept-up ISM. This layer starts to become radiatively efficient when the cooling time of the ISM shell becomes comparable to the age of the bubble, thus influencing its dynamics. On the other hand, the shocked wind is assumed to be adiabatic for a large part of its expansion owing to its much longer cooling timescale (although this depends on its velocity), and is a thus a non-negligible source of X-ray emission (Siwek et al. 2017).

In order to model the X-ray emission from an optically thin collisionally ionised gas in the shocked wind region, we adopt the thermal plasma emission model `APEC` in chapter 2 (Smith et al. 2001). The X-ray continuum is characterised by the free electron temper-

ature, the emission measure of the plasma [12] and the elemental abundances. The X-ray spectral shape and emission line ratios serve as diagnostics of the electron temperature and plasma abundance. However, if the observed spectra are of sufficiently high resolution, the ion temperature and its turbulent velocity may also be inferred through their influence on the emission line widths. This could be useful for shock heated plasmas that are not in collisional ionisation equilibrium, such that the ion and electron temperatures are not necessarily the same (see [13] for further details).

We note that the above simple picture of bubble expansion makes several assumptions, including the homogeneity of the ISM, the absence of magnetic fields and the negligence of thermal conduction between the shocked wind and ISM regions. All these factors can affect the expansion velocity of the bubble, the observed spectral properties and the age of the bubble derived from its kinematic properties. While not considered in 1D simulations, it is also possible for the cool shocked ISM and the hot shocked wind regions to be susceptible to mixing due to Rayleigh-Taylor instabilities, which could shorten the adiabatic expansion phase of the shocked wind (Siwek et al. 2017), and the duration over which the X-ray emissivity is significant. Finally, within the shocked wind region the electrons and protons need not have the same temperatures (Faucher-Giguère and Quataert 2012) since electrons can cool more efficiently (via free-free and bound-free processes) than the protons (carrying most of the kinetic energy) if they only interact with each other via Coulomb collisions (Vink et al. 2003). This is another factor that can affect the effective duration of the adiabatic expansion phase of the shocked wind.

1.3 Ultraluminous X-ray sources

The launch of *Röntgensatellit* (ROSAT) in 1990 enabled precise localisations of X-ray point sources in nearby galaxies (at distances < a few Mpc), due to its vastly improved spatial resolution (~ 10 arcseconds) and sensitivity over its predecessors. This fostered the discovery of several X-ray sources found to be offset from the nucleus of their host galaxy with luminosities well above 10^{39} erg s^{-1} in less than ~ 20% of all galaxies surveyed

[12] The flux emitted by an optically thin plasma is proportional to its emission measure, which is the product of the electron and hydrogen densities integrated over the plasma volume: $\int n_e n_H dV$.

[13] https://ned.ipac.caltech.edu/level5/Sept08/Kaastra/Kaastra10.html#10.2

by ROSAT (Colbert and Mushotzky 1999; Roberts and Warwick 2000; Lira et al. 2000). These objects were aptly labelled as ultraluminous X-ray sources (ULXs), since they were more luminous than any known off-nuclear X-ray point source in the Milky Way. Although ULXs were initially observed by the X-ray satellite preceding ROSAT (namely *Einstein*), its poor angular resolution made it unclear whether ULXs were multiple point sources blended into one, or if they were even offset from the galactic nucleus, thus leaving their precise nature a mystery (Fabbiano and Trinchieri 1987). Presently, it is known that most ULXs are variable, sometimes on timescales as short as minutes (Strohmayer and Mushotzky 2003; Heil et al. 2009; Middleton et al. 2011), which affirms that they are powered by accretion onto a compact object.

If the most luminous ULXs were to radiate isotropically near or below the Eddington limit, this would imply accretion onto black holes more massive than currently known to exist in the Milky Way (i.e. > 20 $M_\odot$), but smaller than SMBHs found in the centres of galaxies. Such intermediate mass black holes are not predicted to form via direct stellar collapse in the local universe, and could represent the surviving seeds of SMBHs formed at high redshifts (Mezcua 2017), although very few ULXs are currently believed to contain IMBH candidates (see next section). An alternative scenario is that a majority of ULXs are undergoing extreme accretion onto stellar mass compact objects that somehow appear to violate the Eddington limit. This scenario has gained increasing support due to our growing understanding of their spectral and timing properties (see section 1.3.2), including the recent discovery of coherent pulsations in a few ULXs (see Bachetti et al. 2020 and references therein), which confirms that they contain an NS accretor with a mass below 3 $M_\odot$. Indeed, it is currently unclear whether a majority of ULXs are indeed powered by NSs, including those that have not yet been discovered to pulse (Brightman et al. 2018), or if some non-pulsing ULXs could contain relatively massive stellar BHs undergoing accretion moderately above the Eddington limit. For example, this could constitute BHs with masses in the range discovered by the LIGO collaboration (i.e. $\lesssim 50-60$ $M_\odot$; Abbott et al. 2020) that may form in metal poor regions (e.g. Zampieri and Roberts 2009) or via the hierarchical mergers in dense stellar clusters.

Accretion above the Eddington limit is thought to have played a crucial role in fuelling the growth of the most massive AGN discovered at high redshifts ($z \sim 6-7$; Mortlock et al. 2011; Fan 2006), which are difficult to observe directly with current instrumentation,

and could be aided by studies of local analogues such as tidal disruption events (TDEs) and ULXs. The former occur when the orbit of a star passes so close to a BH that tidal forces do enough work to overcome the binding energy of the star, thus shredding its outer layers. A significant fraction of the resulting debris is then accreted onto the BH at extreme rates, resulting in X-ray/UV/optical flares (Komossa 2015). Such rare and relatively short-lived events can be used to study a population of otherwise dormant IMBHs (Rees 1988), and are expected to be detected in large numbers in upcoming X-ray (*e-ROSITA*) and optical (LSST) surveys. Such events would be complemented by studies of ULXs, which represent a more persistent phase of super-Eddington accretion and is the main subject of this thesis. The remainder of this section briefly discusses the key observational and theoretical developments in the field of ULXs, highlighting how they have helped in furthering our knowledge of these enigmatic sources. For more detailed reviews, readers are referred to Kaaret, Feng, and Roberts (2017) or Feng and Soria (2011).

1.3.1 Intermediate mass black holes

Initial hypotheses on the nature of ULXs focussed on the possibility that they are powered by IMBHs accreting close to or below the Eddington luminosity (Colbert & Mushotzy 1999; Miller et al. 2003). Probing the existence of IMBHs with masses in the range of $10^2 - 10^4$ $M_\odot$ is an active area of research, and has implications for the formation of the most massive SMBHs in the centres of galaxies (see Volonteri 2010 for details). Some ideas for the formation of IMBHs include the direct collapse of metal poor population III stars (Madau and Rees 2001), or the runaway mergers of stars in dense stellar clusters that triggers their collapse to a massive black hole, which subsequently grows via gas accretion and mergers (e.g. Portegies Zwart et al. 2004). Indeed, some of the brightest sources of the ULX population, termed hyper luminous X-ray sources (HLXs) with $L_X > 5\times10^{40}$ erg s^{-1}, are difficult to explain with a model of super-critically accreting stellar mass BHs, and are thus good IMBH candidates. The best example of this is the object ESO 243-49 HLX-1 residing in the outskirts of a barred spiral galaxy (Farrell et al. 2009). It demonstrates X-ray spectral state transitions reminiscent of sub-Eddington accretion in Galactic BHs (Godet et al. 2009; Servillat et al. 2011), and also displays radio flares associated with jet

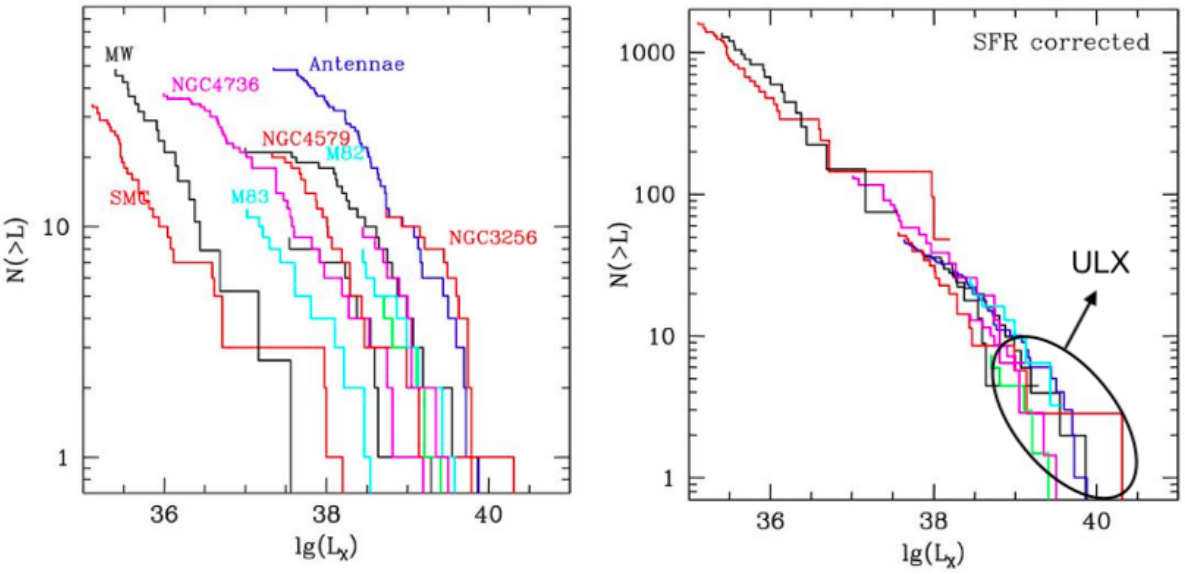

Figure 1.14: *Left*: The X-ray luminosity functions (i.e. number of sources with luminosity $> L$) of HMXBs in a few nearby galaxies as measured with *Chandra*. *Right*: The luminosity functions, scaled to the ratio of the host galaxy's star formation rate with respect to that of the Antennae, can be well modelled with a single power-law component, suggesting the most ULXs with $L \lesssim 2 \times 10^{40}$ erg s^{-1} belong to the same population as HMXBs (Figure credit: Grimm et al. 2003)

ejections that are thought to occur during such state transitions.

However, several observational results argue that the IMBH hypothesis is unlikely to hold for the entire ULX population. For instance, if the X-ray luminosity function (XLF) of ULXs in nearby star-forming galaxies is scaled to a constant star formation rate (SFR), it can be well modelled by a single power-law component with a fixed slope and a tentative cut-off at $\sim 2 \times 10^{40}$ erg s^{-1} (Swartz et al. 2004; Colbert et al. 2004; Walton et al. 2011; see also Figure 1.14). This turns out to be consistent with an extrapolation of the same XLF used to describe standard HMXBs, suggesting that these ULXs are likely to stem from a population of sources already known to host stellar mass compact objects. Secondly, if a large fraction of ULXs were indeed IMBHs accreting at sub-Eddington rates, one would expect their spectral properties to be similar to the well-studied sub-Eddington sources in our galaxy. However, the highest quality spectra of several ULXs show clear differences, featuring a cut-off at energies above ~ 4–7 keV (Stobbart et al. 2006; Gladstone et al. 2009; Bachetti et al. 2013), unlike Galactic XRBs that usually have a power-law tail extending

out to ∼ 100 keV (see section 1.1.9). In the case of ULXs, a smaller energy break maybe explained if the non-thermal coronal emission is cooler and has a larger optical depth, or via an entirely different mechanism (see below). In either case, the indications are that ULXs are in an accretion state distinct to sub-Eddington XRBs. As noted before, the discovery of pulsations clearly points to an NS accretor in a few ULXs, including one of the most luminous objects that was previously thought to be an IMBH candidate (NGC 5907 X-1; Israel et al. 2017a).

1.3.2 Towards super-Eddington accretion

Here, we elaborate on the evidence supporting the view that most ULXs are powered by accretion onto regular stellar mass compact objects that can overcome their Eddington limit. The superior sensitivity of *XMM-Newton* and *Chandra* (relative to their predecessors) has been instrumental in discovering additional ULXs and furthering our understanding of their behaviour. This is also complimented by the more recent launch of *NuSTAR*, which has significantly extended the energy range over which these sources are studied, helping to confirm the high energy spectral break alluded to above (Bachetti et al. 2013; Walton et al. 2015). The data combined from all these instruments has revealed a range of spectral properties of ULXs, which we summarise below.

1.3.2.1 Spectral properties

Generally, ULX spectra are well modelled by two thermal components in the 0.3 - 10 keV bandpass (see Figure 1.16). The soft emission (< 1 keV) is described by the same model used for a standard optically thick disc in Galactic XRBs (described in section 1.1.6), although a deeper analysis suggests that it is not commensurate with such an interpretation. For instance, Kajava and Poutanen (2009) studied a large sample of ULXs to find that the luminosity of the soft thermal component varies inversely with peak temperature ($L \propto T^{-3.5}$), contrary to the expectation for a standard disc with a constant inner radius (see Figure 1.15). The harder component (> 1 keV) is well fitted by a thermal comptonisation model, but requires smaller electron temperatures and larger optical depths than for Galactic XRBs. The balance between the hard and soft components varies between individual sources, with some transitioning between the two regimes over intra-observational

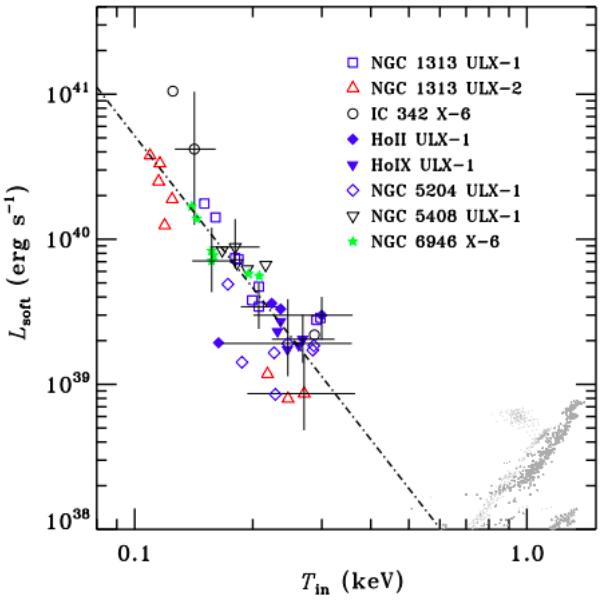

Figure 1.15: Kajava & Poutanen (2009) noted an inverse relationship between the luminosity of the soft thermal component in the spectra of several ULXs and its peak temperature ($L \propto T^{-3.5}$), with the relation for each ULX marked by a different symbol (see legend). This relation is not commensurate with the soft emission in ULXs arising from a standard thin disc (assuming that it has a constant inner radius for each source; Figure credit: Kajava and Poutanen 2009)

periods (e.g. Luangtip et al. 2016). Based on the dominance of a given component, ULX spectra are classified as hard or soft ultraluminous (HUL or SUL; Sutton, Roberts, and Middleton 2013). Interestingly, the hard component in SUL spectra is highly variable on short timescales of 100 - 1000 seconds, but is notably less variable in HUL spectra (Middleton et al. 2015a). Again, this is in contrast to Galactic XRBs, where the strongest variability is seen for the hardest spectral states (Belloni 2010). There are a third class of super-soft spectra in which a majority of the emission is dominated by a blackbody component below 2 keV, extending into far-UV wavelengths. Finally, a reasonable fraction of ULXs also show broadened disc spectra that require a flatter radial temperature profile than for standard thin discs in the high-soft state (for which $T(R) = R^{-0.75}$). The physical meaning of this property, in addition to the various spectral shapes described above, can be explained by a unified model in which a BH or an NS accretes above the Eddington limit. We discuss the former below, and leave the details of NS accretion to the next section.

1.3.2.2 A unified model of super-critical accretion

The discussion pertaining to the Eddington luminosity in section 1.1.7 was based on the assumption of spherical accretion, so does not hold for disc accretion, particularly if the disc is fuelled at rates exceeding Eddington. In the geometry of disc accretion, radiation diffuses primarily in the direction perpendicular to the plane of the disc, while matter inflows radially, so this could allow the global accretion rate to exceed the critical Eddington rate. For sufficiently high mass transfer rates, the disc flux approaches the *local* Eddington limit [14] at some critical radius (known as the spherisation radius $R_{\rm sph}$), where the disc is inflated to a large scale height ($\frac{H}{R} \sim 1$) by radiation pressure (Shakura and Sunyaev 1973; Poutanen et al. 2007; Middleton et al. 2015a). Indeed, $R_{\rm sph}$ increases

[14]The word *local* emphasises that the Eddington limit for disc accretion varies as a function of radial distance from the central object R and height above the disc mid-plane H. This is mainly because, for a thin disc, the radiation pressure force scales differently with R (i.e. R^{-3}; Shakura and Sunyaev 1973) relative to the gravitational force (modulo the centrifugal component), which scales as R^{-2}. By contrast, both forces scale as R^{-2} in the case of spherical accretion, so that the Eddington limit is independent on R in this case.

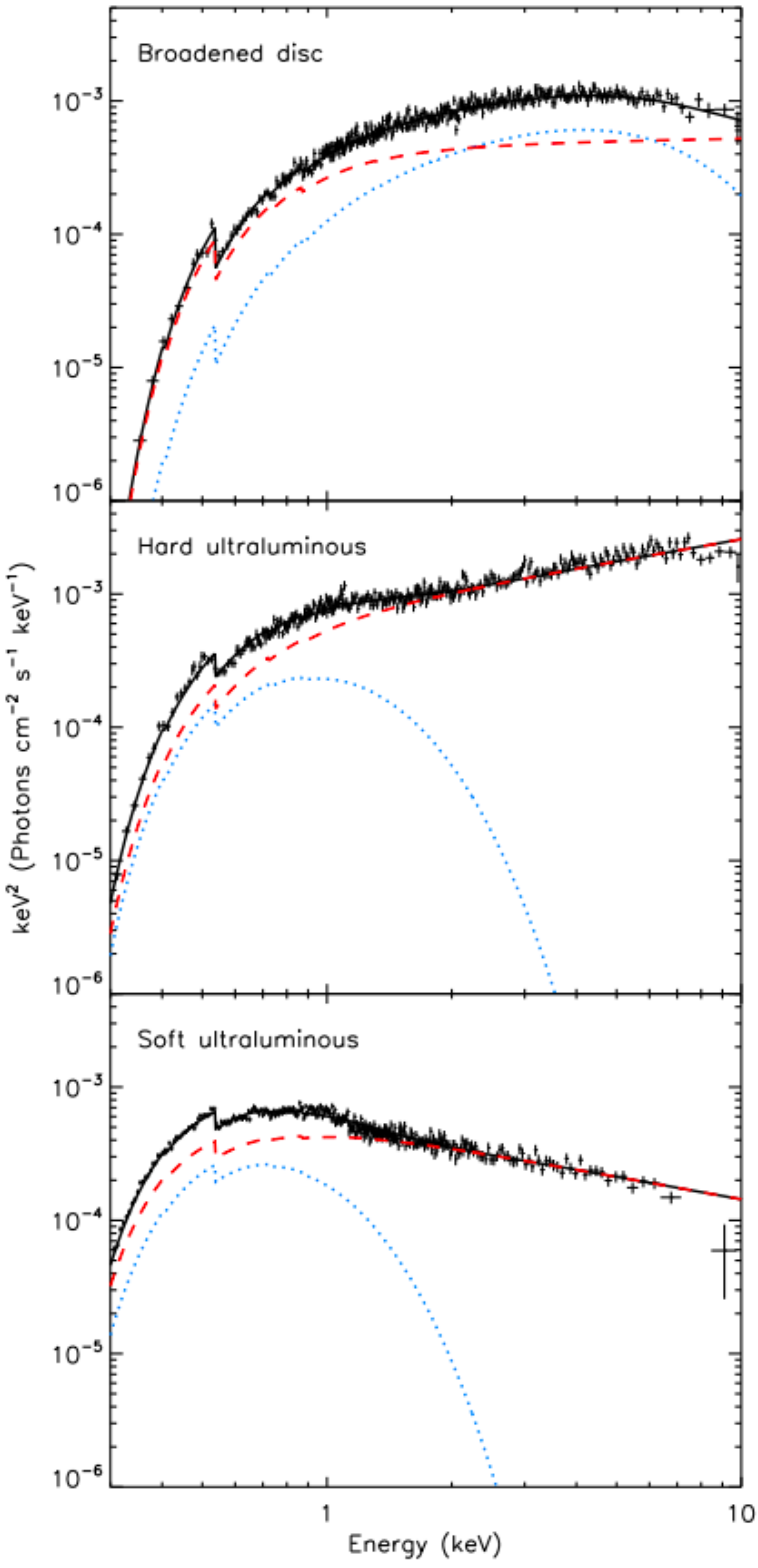

Figure 1.16: The three different classes of ULX spectra from Sutton et al. (2013) (*top*: broadened disc in NGC 1313 X-2, *middle*: hard ultraluminous in Ho IX X-1 and *bottom*: soft ultraluminous in NGC 5408 X-1), showing curvature above 5 keV in a manner distinct to Galactic XRBs (see text). The dashed blue and red lines mark the best-fitting multi-colour disc and power-law models (Figure credit: Sutton et al. 2013).

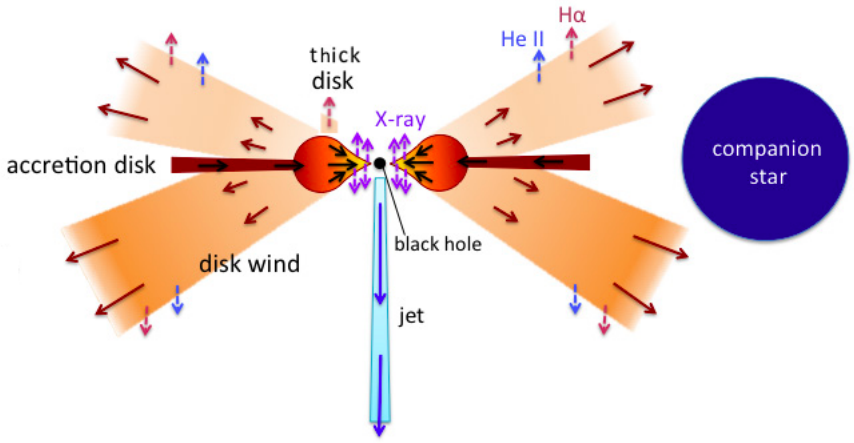

Figure 1.17: A simple schematic of the super-critical wind model hypothesised to explain the spectral and timing properties of ULXs. The accretion disc becomes geometrically thick at the spherisation radius and any loosely bound material on its surface is ejected by radiation pressure, resulting in relativistic outflows (red arrows). This introduces a viewing angle dependence on the observed spectral shape (Figure credit: ESA).

with larger mass accretion rate:

$$R_{\rm sph} = \dot{m} R_{\rm in} \tag{1.3.21}$$

since the Eddington limit is breached locally at a larger distance from the central object (Poutanen et al. 2007). In order that the accretion rate at each radius below $R_{\rm sph}$ is limited to $\lesssim$ the local Eddington rate, any excess material is thought to be ejected from the loosely bound surface layers of the thick disc (Shakura and Sunyaev 1973), which leads to the emission of strong winds that can become optically thick at high accretion rates. These winds can collimate the radiation emitted by the innermost regions of the disc, allowing it to escape preferentially along a narrow optically thin funnel enclosing the thick disc and wind (see Figure 1.17[15]). Hence, the inner disc emission is geometrically beamed towards the observer over a fraction b of the sky, which enhances the intrinsic luminosity by a factor b^{-1}. The combination of a super-Eddington accretion flow and geometric beaming (primarily) of hard X-ray photons from the central regions of this flow influences the apparent luminosity of a BH ULX, derived in King (2008) as:

$$L \propto \dot{m}^{-2} L_{\rm Edd} (1 + \ln \dot{m}), \tag{1.3.22}$$

[15]https://www.cosmos.esa.int/documents/332006/1402684/LZampieri_t.pdf

where $\dot{m}$ is the dimensionless mass accretion rate (in units of the Eddington rate) and L is the apparent radiative output. In the geometry of this model, the observed spectrum clearly depends on the viewing angle of the binary system. At low inclinations (face-on), the emission from the hot inner disc dominates, leading to the HUL class of spectra shown in Figure 1.16. For lines-of-sight grazing the wind, the softer emission begins to increase, since a fraction of the hard emission is Compton down-scattered by the outflowing material. Numerical simulations predict that the edge of the outflow becomes clumpy due to Rayleigh-Taylor instabilities (Takeuchi et al. 2013) and can thus imprint variability on the hard emission on short 100-1000 second timescales (Middleton et al. 2015a). At even higher inclinations, the observer sees the outer photosphere of the wind, which is expected to peak in the UV and heavily obscures the hard emission from the innermost regions, producing spectra consistent with the super-soft class of sources described above. Transitions between the different spectral regimes could be driven by a rise in the mass accretion rate, which causes the outflow to subtend a larger solid angle (as more mass is expelled), causing increased obscuration of the hard emission for a moderately face-on viewing angle. It could also occur due to bulk precession of the thick inner disc and wind (Middleton et al. 2018a), which changes the observer's view to different parts of the accretion flow. Hence, this model can successfully explain the diverse range of ULX spectral shapes (HUL, SUL and SSUL) and the transitions between them. One of its key predictions was confirmed recently by the discovery of blueshifted absorption (and ionised rest-frame emission) lines in the high resolution spectra of several ULXs (Pinto et al. 2016, Kosec et al. 2018a,b). The inferred magnitude of blueshift implies the presence of relativistically outflowing gas presumably launched from the accretion disc with speeds of ~ 0.1c, providing evidence in favour of ULXs being in a super-critical accretion state.

In super-critical discs, another important effect occurs at the spherisation radius $R_{\rm sph}$ where the disc has a large scale height. Here, the timescale for photons to diffuse from the disc mid-plane to the surface becomes longer than for the radial influx of matter (Abramowicz et al. 1988; Watarai et al. 2000; Czerny 2019). As a consequence, radiative flux is trapped or *advected* with the flow, and is lost beyond the event horizon in the case of accretion onto a BH. The temperature of such a radiatively inefficient, advective (or slim) disc decreases much more slowly with radius compared to a standard thin disc, since the energy of the photons is carried with the flow rather than being radiated away.

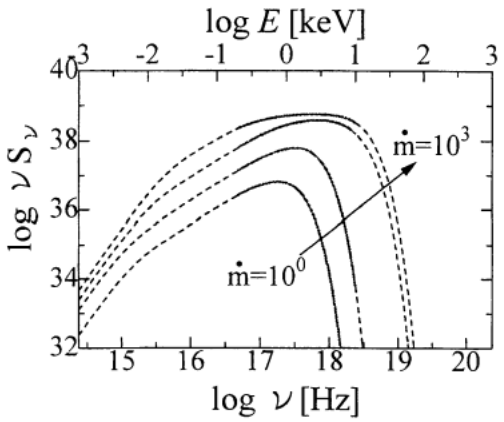

Figure 1.18: An illustration of how a standard optically thick disc spectrum is modified to a broadened disc (with increasing accretion rate), as the effects of photon trapping (or advection) become important (Figure credit: Watarai et al. 2000).

As a result, the emerging spectrum has a flatter shape (see Figure 1.18 and Watarai et al. 2000), and could be consistent with the broadened disc spectra of some ULXs. We explore this further in chapter 4.

1.3.3 A new twist: The discovery of pulsating ULXs

The first direct evidence that not all ULXs are powered by massive black holes came from the detection of X-ray pulsations in the *NuSTAR* data of M82 X-2 (Bachetti et al. 2014). The high coherence of the detected 1.4 second periodicity was ascribed to the stable rotation of a magnetised neutron star, with a canonical upper limit on its mass of < 3 $M_{\odot}$. Doppler modulations of the spin period were also found to occur on a timescale of 2.5 days, thought to arise due to the orbital motion of the NS, further strengthening the notion that the system is a high mass X-ray binary. Indeed, given the peak luminosity of M82 X-2 ($\sim 2 \times 10^{40}$ erg s^{-1}), this clearly suggests that the source is exceeding the Eddington limit by several factors of 10 - 100. Currently, there are at-least six known pulsating ULXs (PULXs; Fürst et al. 2016; Israel et al. 2017b,c; Carpano et al. 2018; Rodríguez Castillo et al. 2020), one of which was discovered as part of the work carried out in this thesis, and is discussed in chapter 3 (Sathyaprakash et al. 2019). These discoveries raise several key questions that drive ongoing research in this field, such as (i) whether a majority of ULXs are powered by NS accretors instead of BHs, (ii) whether they share

any observable differences with ULXs containing BHs and (iii) the mechanisms by which PULXs can overcome their Eddington limit. In particular, an insight into the relative populations of NS and BH ULXs may lead to better informed predictions for gravitational wave (GW) event rates, since ULXs are hypothesised to be possible progenitors of binary NS and BH mergers (see e.g. Fragos et al. 2015). To make further progress on these issues, expansion of the currently sparse population of PULXs is required, necessitating observational methods that can distinguish between ULXs containing NSs and BHs. This includes the detection of pulsations, in addition to other techniques that can probe the signatures of non-pulsing NS ULXs (see below).

1.3.3.1 Observational signatures

The X-ray spectral properties of the known PULXs are generally similar to the non-pulsing population, hinting that a majority of ULXs could be NSs, although PULXs tend to have slightly harder spectra (Pintore et al. 2017; Walton et al. 2018b). One property that could be unique to PULXs is that they demonstrate extreme variability by factors of a few hundred over periods of several months, in contrast to the usually persistent emission observed from other ULXs on those timescales. Such variability could be triggered by the *propeller effect*, in which accretion onto the poles of the NS is inhibited by its rotating magnetosphere, resulting in periods of distinct bright and faint X-ray fluxes (Tsygankov et al. 2016). It is thought to arise when the (variable) mass inflow rate from the donor temporarily decreases to an extent that the magnetospheric radius of the NS R_M (determined by a balance between the ram pressure of the infalling material and the magnetic pressure of the dipolar magnetic field) exceeds the co-rotation radius $R_{\rm co}$ (i.e. the radius at which the Keplerian velocity of the accretion flow equals the angular velocity of the NS). This forces the plasma at $R_{\rm M}$ to rotate faster than the local Keplerian velocity, causing the centrifugal force acting on it to overcome the local gravitational force, which temporarily halts accretion. Indeed:

$$R_M = 2.6 \times 10^8 q \dot{M}_{17}{}^{-2/7} M_{\rm NS}^{-1/7} \mu_{30}^{4/7} {\rm cm} \tag{1.3.23}$$

where $\dot{M}_{17}$ is the mass accretion rate in units of 10^{17} g s^{-1}, $M_{\rm NS}$ is the mass of the NS in $M_\odot$, μ_{30} is the dipole moment of the magnetic field in units of 10^{30} G cm^3 and $q(< 1)$

is a factor that accounts for the geometry of the accretion flow at R_M (and is ~ 0.5 for geometrically thin discs). The co-rotation radius is:

$$R_{\rm co} = \left(\frac{GM_{\rm NS}P^2}{4\pi^2}\right)^{1/3} \tag{1.3.24}$$

where P is the spin period of the NS. Based on these equations, it is clear that if one can determine the limiting luminosity at which the propeller regime is triggered (e.g. Campana et al. 2018), this would allow a constraint on the magnetic field of the NS at R_M. However, in the case of ULXs such an approach remains a challenge due to the sparsely sampled observations and efforts are mainly dedicated to determine whether the long term variability of ULXs can even be associated with the propeller effect. In this direction, Earnshaw et al. (2018) and Song et al. (2020) have combined *XMM-Newton*, *Chandra* and *Swift* catalogues to find ~ 15 NS ULX candidates based on their significant long-term variability, which may be followed-up with deeper X-ray observations for pulsation searches to confirm that they are NSs. As mentioned above, while this is an attractive method to find interesting targets, the poorly sampled light-curves of a majority of ULXs are often indistinguishable from other types of high amplitude variability aside from the propeller effect (e.g. due to a precessing flow; Middleton et al. 2018a; Brightman et al. 2019). Earnshaw et al. (2018) predicted that the successor to the *ROSAT* all sky-survey mission (*e-ROSITA*) would improve upon the observing cadence of ULXs, although a majority of those would be too distant (> 2.2 Mpc) to detect in the faint X-ray flux regime (i.e. below a luminosity 10^{38} erg s^{-1}), as needed to confirm the bi-modal X-ray flux distribution resulting from the propeller effect.

An additional signature of NS ULXs is the presence of cyclotron resonance lines in their spectra, thought to arise as a result of electron scattering in strongly magnetised plasma. Brightman et al. (2018) report such a feature in a hitherto non-pulsing ULX (M51 X-8). This is partly compelling due to the unexpected emission from other astrophysically abundant atomic/ionic species at the detected line centroid (4.5 keV), although a single detection in several years of observations suggests that it is marginally significant. Moreover, debates surrounding whether the feature is due to proton or electron scattering leads to large uncertainties in the derived magnetic field strength ($10^{11} - 10^{15}$ Gauss; but see Middleton et al. 2019a). Constraints on the magnetic field are important to determine

whether they play a crucial role in enabling the super-Eddington luminosities of PULXs, as we discuss below.

1.3.3.2 Accretion onto a magnetised neutron star

At distances sufficiently close to a magnetised NS, its magnetic pressure becomes strong enough to disrupt the radial infall of the surrounding accretion flow, which is subsequently channelled onto the poles of the NS along the field lines (see Figure 1.19[16]). The freely falling supersonic flow is decelerated to sub-sonic velocities by radiation pressure, resulting in the formation of a shock at some height above the NS surface (Basko and Sunyaev 1976b; Mushtukov et al. 2015). Below the shocked layer, the accretion flow is magnetically confined and has the structure of a column (see Figure 1.19 bottom). In this geometry, the Eddington limit can be exceeded by a factor of a few since photons can escape from the sides of the column in the direction of smallest optical depth, perpendicular to the direction of the inflowing stream of matter. Additional corrections to the Eddington limit arise if the field strength exceeds $\sim 10^{13}$ Gauss in the vicinity of the infalling plasma, since this can suppress the electron scattering cross section to values below the Thomson opacity (Herold 1979; Mushtukov et al. 2015). At distances far away from the magnetosphere, the structure of the flow is similar to the case for BH accretion as described in the previous section (King, Lasota, and Kluźniak 2017). If the disc is not truncated by the dipolar field at a radius larger than $R_{\rm sph}$, radiation pressure driven outflows are expected to form, thus collimating the emission from the central regions (e.g. Mushtukov et al. 2019).

Currently, we do not have a fully coherent picture of whether it is primarily the large magnetic fields of PULXs that allow them to accrete at super-Eddington rates, or whether this can be attributed to beaming from a geometrically thick flow (similar to BH accretion), or a combination of both. On one hand, large magnetic fields ($\sim 10^{14}$ Gauss) are favoured to explain the luminosities of the brightest PULXs (NGC 5907 X-1; $\sim 10^{41}$ erg s^{-1}), since they would otherwise require beaming factors too large to be compatible with their sinusoidal pulse profiles. However, such large (dipolar) fields also imply that steady state accretion would be inhibited by the propeller-effect, being inconsistent with the measured luminosity of NGC 5907 X-1. To avoid this issue, Israel et al. (2017) suggest

[16] http://www.issibern.ch/teams/observephysics/

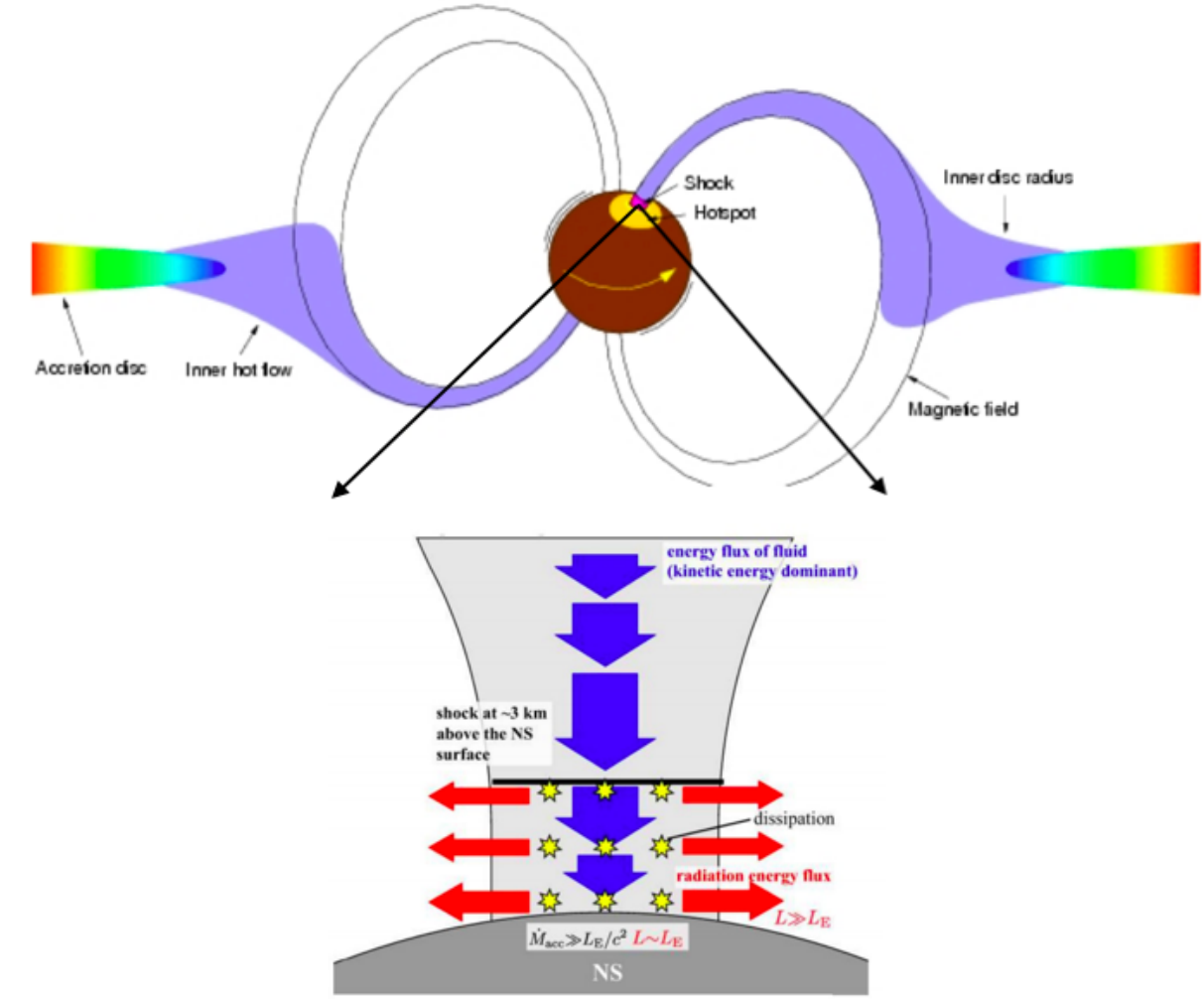

Figure 1.19: *Top*: Accretion onto a magnetised NS; the accretion flow is interrupted at the magnetospheric radius by the dipolar field of the NS and channeled onto its poles, giving rise to a shocked, magnetically confined column near the surface. *Bottom*: A magnified view of the accretion column, showing how this particular geometry allows accretion rates to exceed the Eddington rate for an NS (Figure credit: Kawashima et al. 2016).

that the magnetic field could be dominated by higher order components closer to the NS surface with values $\gtrsim 10^{14}$ Gauss, while the dipolar component at large radii could be small enough to enable steady-state accretion. However, there is no observational evidence for such multipolar fields as yet.

In principle, the secular spin-up rates of PULXs can be used as a probe of their dipolar magnetic field. The accretion flow applies a torque onto the NS by coupling with its magnetosphere, which has a positive sign if the Keplerian velocity of the disc is greater than the rotational velocity of the NS at the magnetospheric radius $R_{\rm M}$ (Ghosh and Lamb 1978). The applied torque causes the NS to spin-up at a rate that depends on the mass accretion rate and the dipolar field strength at $R_{\rm M}$ (acting as a 'lever arm'):

$$\dot{\nu} = \frac{\dot{M}(R_{\rm M})}{2\pi I_{\rm NS}} n(\omega_{\rm fast}) \sqrt{G M_{\rm NS} R_{\rm M}} \tag{1.3.25}$$

where $I_{\rm NS}$ is the NS moment of inertia and $n(\omega_{\rm fast})$ is a dimensionless function accounting for the fact that the accretion torque vanishes if there is no differential rotation between the disc and the NS. However, inverting the above equation to solve for the magnetic field leads to large uncertainties, mainly because the accretion torque varies depending on whether or not the source has reached spin equilibrium (i.e. when the relative rotation rates of the NS and the disc tends to zero at the radius $R_{\rm M}$). For example, Bachetti et al. (2014) inferred the magnetic field of M82 X-2 ($\gtrsim 10^{12}$ Gauss) by assuming the source to be far away from spin-equilibrium.

This assumption was contested by Eksi et al. (2015) on the basis of its short spin-up timescale ($\frac{P}{\dot{P}} \sim 300$ yrs), who instead suggest that the torque was overestimated and a larger field strength ($\sim 3 \times 10^{13}$ Gauss) is required to account for the spin-up rate of M82 X-2.

1.3.4 Optical counterparts

Initial surveys for optical counterparts to ULXs began with the intent of finding candidates for radial velocity measurements, which has been used to constrain the masses of compact objects in Galactic XRBs (see section 1.1.5). However, this presents several challenges in the case of ULXs. Firstly, the identification of unique counterparts is difficult since

ULXs tend to reside in distant crowded fields, although some progress has been made with combined HST and *Chandra* imaging owing to their high angular resolution. Tao et al. (2011) discovered ~ 10 counterparts in nearby galaxies (at distances $\lesssim 5-10$ Mpc), which was expanded upon by Gladstone et al. (2013). Most of these have blue colours (B - V ~ -0.6 to 0.4) and visual magnitudes (M_V ~ -3 to -8) that are superficially consistent with O/B stellar types. However, there are indications that the optical light is contaminated by additional processes, making it non-trivial to infer the stellar types of ULX donors by comparing their de-reddened colours and magnitudes with standard evolutionary tracks (e.g. Patruno and Zampieri 2008). For instance, stochastic variability in the optical fluxes are observed for some objects over short (monthly) timescales (Grisé et al. 2008), suggesting that the optical light could be dominated by reprocessing of variable X-ray emission from the outer accretion disc or from circum-stellar (outflowing) gas. This issue is also prevalent in LMXBs, although in this case any contribution from X-ray reprocessing can be removed by scheduling optical observations during periods of X-ray quiescence. This is difficult to do for ULXs since they tend to be persistently bright.

In some cases, ULX counterparts are found to be slightly offset from young stellar associations (Grisé et al. 2011), presumably having been ejected as a result of receiving a post-supernova kick. In this scenario, some constraints on the ULX donor can be obtained by determining the age of the stellar association, assuming that its constituent stars were born from the same gas cloud with a given metallicity. Such analyses tend to be consistent with the interpretation that ULXs are super-critically accreting HMXBs containing young, relatively massive donors.

ULX counterparts have also been followed-up with high resolution spectrographs to infer their stellar types, but there are very few sources for which stellar absorption lines are detected (Liu et al. 2013; Motch et al. 2014). Some spectra feature the high-excitation He II λ 4686 emission line, presumably emitted by the hot accretion disc, although the radial velocity variations derived from this line are not periodic, thus precluding any attempts to constrain the dynamical mass of the compact object (Roberts et al. 2011; Fabrika et al. 2015). More recently, searches for near infrared (NIR) counterparts to ULXs has gained popularity (López et al. 2017; Lau et al. 2017; Heida et al. 2019b), since the NIR band is expected to contain a smaller contribution from the disc and is less affected by dust extinction. This has resulted in the discovery of red supergiant donors associated with

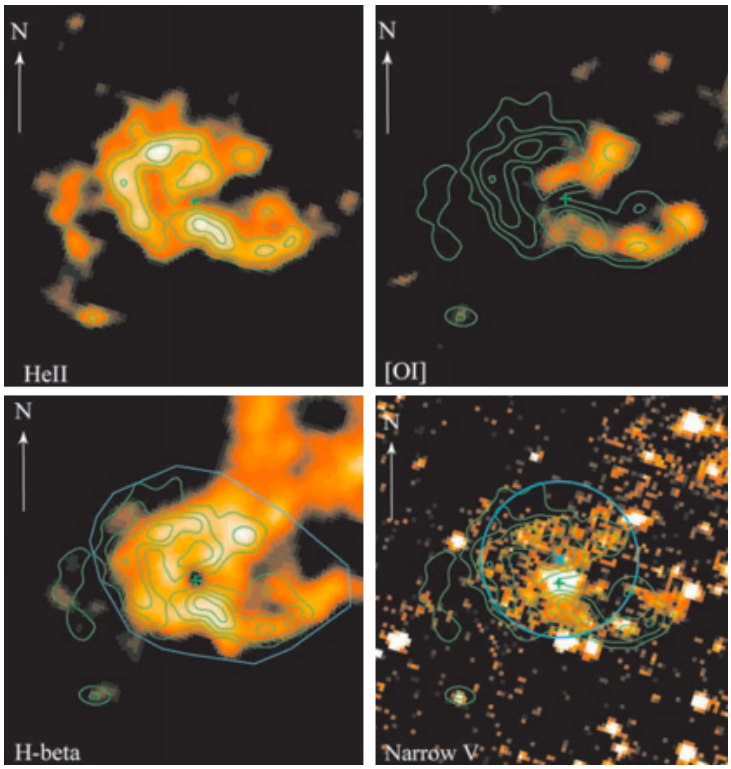

Figure 1.20: A collection of narrow-band optical images of the ULX Holmberg II X-1 from Kaaret, Ward, and Zezas (2004), with the ULX position marked by the green cross. The [He II] image (*top left*) illustrates the isotropic morphology of its photo-ionised nebula and [OI] (*top right*) shows regions dominated by shock-excitation. The point-like optical counterpart to the ULX is shown in the V-band image (*bottom right*).

several (P)ULXs (Heida et al. 2015; Heida et al. 2016; Heida et al. 2019).

1.3.5 Emission line nebulae

Optical studies have also been fruitful in revealing large bubble nebulae in the vicinity of ULXs, with diameters of a few hundred parsecs (Pakull and Mirioni 2002). These nebulae demonstrate signatures of ionisation both by the X-ray continuum of the ULX and shocks driven by relativistic disc winds or jets (Roberts et al. 2003; Pakull et al. 2006; Urquhart et al. 2018; López et al. 2019), providing additional support to the super-critical wind model. The presence of shock heated gas in the bubble outskirts is confirmed by the large fluxes of low-excitation emission lines such as [SII] and [OI] (Dopita and Sutherland 2003). Here, shocks compress the gas to sufficiently high densities that the recombination times of ionised sulphur are shorter than in strongly photo-ionised regions, where it mainly exists in

the S^{++} ionic state, thus producing weak [SII] emission (Gordon et al. 1998). The putative emission line-widths constrain the expansion velocities of ULX bubbles to be supersonic, and in combination with the observed size of the bubble, one can infer its lifetime and the average kinetic power driving its expansion (Castor et al. 1975). The latter tends to be consistent with the X-ray power output ($\sim 10^{40}$ erg s^{-1}) for several sources, implying that roughly half of the available accretion power is used to launch kinetic outflows or jets over long timescales ~ the age of the bubble (0.1 - 1 Myr). There are a few notable exceptions, such as the Galactic micro-quasar SS433 (e.g. Middleton et al. 2018b; Su et al. 2018) and the micro-quasar in NGC 7793 possessing an X-ray luminosity orders of magnitude lower than their super-Eddington jet power, which may suggest that their X-ray emission is beamed away from the line-of-sight or is heavily obscured (Pakull et al. 2010).

Evidence for photo-ionisation dominated nebulae has also emerged from the detection of extended He II λ 4686 recombination in the vicinity of ULXs. In order to be excited, the He II line requires a significant flux of ionising photons with energies larger than emitted even by the hottest O-type stars, which points to an X-ray ionising source. Since this line acts as a calorimeter to the soft X-ray emission from the ULX (Kaaret et al. 2004), this allows some insights into how strongly beamed the X-ray emission is. Indeed, photo-ionisation codes have been used to infer that the X-ray luminosities required to produce the nebular He II emission are consistent with the apparent X-ray luminosities to within a factor of ~ 3 (Abolmasov et al. 2008). This is usually taken to be evidence against significant beaming of the soft X-rays, together with the fact that the He II emission is largely isotropic (see Figure 1.20). However, this does not necessarily rule out the super-critical wind model, which predicts geometric beaming of only the hard thermal component (> 2 keV), while soft X-rays from the wind photosphere and the outer disc may still be emitted isotropically.

1.4 Thesis overview

Despite the success of the super-critical wind model in explaining much of the observed properties of ULXs, several issues are yet to be resolved. In this thesis, we continue the investigation of previous works into examining some of these issues by studying the detailed observational phenomenology of two ULXs in nearby galaxies, primarily using

X-ray data. Specifically:

- We build on the currently sparse number of NS ULXs by reporting and discussing the discovery of transient pulsations in an archetypal ULX, NGC 1313 X-2. We highlight the key questions raised by this discovery on the accretion geometry of NS ULXs (see chapter 3).

- We explore the information that multi-wavelength photometric observations can reveal about the UV/optical/near-infrared emission mechanisms of ULXs. Making use of simultaneous X-ray and optical observations of NGC 1313 X-2, we investigate whether the variability between the two components is correlated, and if this allows us to distinguish between the contributions from stellar and non-stellar sources of optical emission (see chapter 4).

- The work of Pinto et al. (2016) revealed the detection of wind absorption features in a handful of ULXs, which provides excellent support to the super-critical wind model, but their work also reported rest-frame emission lines from the same sources, whose origin is not well understood. We probe whether it is spatially associated with diffuse emission arising due to the interaction between outflows launched from the ULX accretion disc and the surrounding interstellar medium by analysing archival X-ray observations of the ULX Holmberg IX X-1 and its immediate surroundings (see chapter 2).

We summarise the results of the thesis in Chapter 5, and provide brief directions for future work.

Chapter 2 | Observational limits on the X-ray emission from the bubble nebula surrounding Holmberg IX X-1

2.1 Abstract

Optical and radio observations of shock-ionised bubble nebulae surrounding ultraluminous X-ray sources (ULXs) suggest that they are powered by jets or super-critical outflows presumably launched from the ULX accretion disc. Recent simulations of these systems (e.g. Siwek et al. 2017) have shown that the shocked wind can emit thermal X-rays with estimated luminosities $\lesssim 10^{36}$ erg s^{-1}. In this work, we investigated whether it is possible to detect and spatially resolve the X-ray emission from these systems using archival *Chandra* observations of the ULX Holmberg IX X-1. This source is an ideal target to study for two reasons: it is surrounded by an optical bubble nebula with a large spatial extent ($\sim$ 400 pc) that can easily be resolved with *Chandra*. Further, it has a hard X-ray continuum that is easily distinguishable from the expected soft thermal emission from the nebula. However, a spectral and photometric analysis on stacked *Chandra* observations of the source reveals that there is no strong evidence for an X-ray bubble associated with it, to a limiting luminosity of $\sim 2 \times 10^{36}$ erg s^{-1}. The detection of such X-ray nebulae may be possible with future X-ray missions such as *Athena*, which would provide useful constraints

on the kinematics of the outflow. Finally, our observations also emphasise that the nebular emission does not contribute significantly to the residuals in the X-ray spectrum of the source, which are more likely to be linked to processes localised to the ULX.

2.2 Introduction

The spectral properties of ULXs yield insights into the geometry of the accretion flow surrounding the compact object. The *XMM-Newton* spectra of bright ULXs (with $L_{\rm X} > 3\times10^{39}$ erg s^{-1}; Sutton et al. 2013) tend to feature two distinct thermal components, with the soft component clearly dominating over its hard counterpart (or vice versa) for some sources, while in others, the relative strengths of the two components are seen to vary on intra-observational timescales (Sutton et al. 2013). This behaviour is well explained by a unified model of super-Eddington accretion (Poutanen et al. 2007; Middleton et al. 2015c), whose key prediction is that StMBHs or low magnetic field NSs accreting above $L_{\rm Edd}$ launch strong radiatively driven winds from an advection dominated accretion flow. As discussed in chapter 1, the presence of such winds introduces a viewing angle dependence on the observed spectrum that is key to explaining the spectral and timing properties of ULXs (Roberts et al. 2015).

The *XMM-Newton* spectra of some ULXs also show residuals to the best-fit, dual thermal component models at energies below 2 keV (Middleton et al. 2014; Middleton et al. 2015b). In some cases, such features have been resolved into a complex of narrow, blue-shifted absorption and rest-frame emission lines (see Pinto et al. 2016, 2017 and Kosec et al. 2018a), with the former suggesting the presence of ionised, relativistically ouflowing gas (with $\frac{v}{c} \sim 0.2$), as per the expectations of the super-critical wind model. However, in sources with very weak detections of wind absorption features (Walton et al. 2017), the physical origin of the spectral residuals has remained unclear. Previous studies invoked various possibilities to account for their origin, including star-formation related diffuse emission in the host galaxy of the ULX (e.g. Strohmayer and Mushotzky 2009). Star-forming galaxies possess significant amounts of hot tenuous plasma thought to be heated by the combined effect of supernovae and winds from young massive stars (Mineo et al. 2012). While the residuals in ULX CCD spectra are well described by a thermal plasma emission model that could be ascribed to diffuse emission related to star-formation

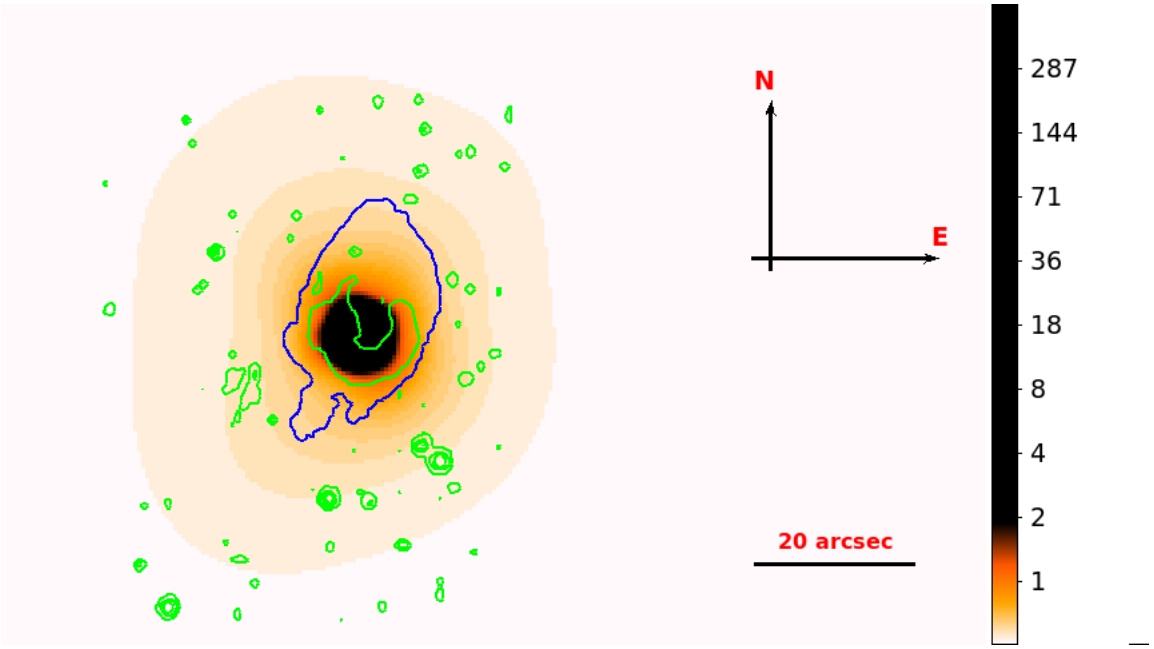

Figure 2.1: A stacked *Chandra* image of all five observations described in Table 2.1, with the contours of Hα emission (from the *SUBARU* FOCAS archive) overlaid. The colour-bar shows the smoothed X-ray counts per pixel in the (0.4 - 1.0) keV energy band (see text). The contour displayed in blue demarcates the edge of the expanding bubble and has a diameter of 37.6 and 24.5 arcsecs across its major and minor axis respectively, fully enclosing the brightest part of the PSF (see text). The image has been adaptively smoothed with `csmooth` (Ebeling, White, and Rangarajan, 2006), at a minimum significance of 3σ above the background.

ObsID	Exposure Time (ks)	Off-axis angle (arcsec)	Frame Time (s)	Detected count rate (photons/frame time)	Pileup fraction
4752	4.96	5.80	1.8	0.67 ± 0.02	0.21
4752	5.04	5.80	1.8	0.64 ± 0.02	0.19
9540	25.72	130.5	3.2	1.37 ± 0.01	0.39
13728	13.67	0.25	0.4	0.278 ± 0.004	0.10
14471	12.76	0.25	0.4	0.496 ± 0.004	0.18

Table 2.1: The five archival *Chandra* observations of Ho IX X-1 utilised in this study, with a combined exposure time of 62.15 ks. The ObsID column gives the observation identifier for each source. We also quote the off-axis angle of Ho IX X-1 in each exposure, assuming the WCS coordinates for the ULX given in Gladstone et al. (2013). The pile-up fractions specified in the final column are lower limits to the true values, since the *detected* (not the intrinsic) count rates of the source were used in calculating them. We calculated this with the PIMMS software provided by the *Chandra* Proposal Planning Toolkit.

activity, the luminosity in the residual component is far too large to be solely associated with such a process (Middleton et al. 2014). The evidence for this was strengthened by a spatial analysis of the source NGC 5408 X-1 with *Chandra* and HST observations, which indicate that it is displaced from the major sites of star-formation in its host galaxy (Sutton et al. 2015). Similarly, it has also been argued that the residuals are unlikely to be explained by collisional excitations of the low-density material in the nebulae surrounding some ULXs (Middleton et al. 2015b; Pinto et al. 2016), although this has not yet been confirmed observationally, and is the main scope of this chapter.

As discussed in section 2.2, ULX bubble nebulae (ULXBs) were first discovered in narrow-band optical images by Pakull and Mirioni (2002). Given the association of several ULXs with young star clusters, it was initially suggested that ULX bubbles are powered by multiple supernova explosions of massive early-type stars residing in those clusters. However, further studies have argued that that this alone is insufficient to account for the mechanical energy of ULXBs ($\gtrsim 10^{52}$ ergs; Roberts et al. 2003; Ramsey et al. 2006), and that their dynamics may be better explained by continual energetic input from jets or super-critical wide angle outflows launched from the ULX accretion disc (Pakull and Grisé, 2008). The evolution of wind-inflated bubbles has been the subject of several studies (Castor et al. 1975; Weaver et al. 1977), providing a generally accepted picture in which a supersonic outflow (launched from the ULX accretion disc) shocks the surrounding ISM gas and expands adiabatically at very early times, until the mass of the swept-up material becomes comparable to the mass of the ejected outflow. This is followed by the 'snow-plough' expansion phase, when the swept-up gas starts to become radiatively efficient and collapses into a thin dense shell just behind the forward shock. Beneath the cold layer of the swept-up ISM lies a more tenuous layer of hot shocked ejecta, which is continually heated by the mechanical energy of the outflow to temperatures in excess of 10^{6-7} K. It thus radiates as an optically thin plasma, producing line emission in the X-ray band with an underlying bremsstrahlung continuum. This general picture has been verified in recent numerical simulations of wind-inflated ULXBs by Siwek et al. (2017), who estimate a maximum X-ray luminosity from the shocked ejecta of $\sim 10^{36}$ erg s^{-1}. We note that this is also consistent with the X-ray luminosity observed from the Galactic micro-quasar SS433 (to within an order of magnitude), which is thought to be dominated by thermal Bremsstrahlung emission from hot plasma within a jet inflated bubble (e.g. Middleton et

al. 2018).

In this work, we investigate whether it is possible to detect the X-ray emission from ULXBs using archival *Chandra* observations of the ULX Ho IX X-1, and verify whether this makes a significant contribution to its X-ray spectral residuals. Ho IX X-1 resides at a distance of 3.6 Mpc in an irregular dwarf galaxy (Gerke et al. 2011), and consistently radiates with a (0.3 - 10 keV) X-ray luminosity above $\sim 10^{40}$ erg s^{-1} (Luangtip et al. 2016). We choose to study this source because (i) any potential X-ray emission from its large [300 pc × 470 pc] shock-ionised nebula can be spatially resolved with *Chandra* (Miller 1995), (ii) it has a notably hard X-ray spectrum (Walton et al. 2017) that may be distinguishable from the likely soft nebular emission on larger scales of $10 - 100$ pc, and finally (iii) among those ULXs with both a strong detection of spectral residuals and a spatially resolved bubble, Ho IX X-1 has the longest exposure *Chandra* data. This chapter is organised as follows: we describe the spatial analysis in section 2.3. The spectral properties of the source are examined in section 2.4, particularly focusing on searching for features of thermal plasma emission from the nebula. We then confirm whether the source is actually point-like at the spatial resolution of *Chandra* in section 2.5. Finally, we discuss the implications of our results and provide concluding statements in section 2.6.

2.3 Spatial analysis

The *Chandra* data were reprocessed and reduced using CIAO (v4.9)[1]. We first performed a visual check for any diffuse emission surrounding Ho IX X-1 by stacking the five observations listed in Table 2.1. We restricted the energy range of each observation to (0.4 - 1.0) keV. This was done in order to optimise the search for extended emission from an optically thin thermal plasma, whose luminosity is expected to peak close to a temperature of ~ 0.3 keV (Siwek et al. 2017). We do not consider events above 1 keV, since the power-law emission from the ULX dominates over the thermal plasma emission above this energy.

The individual aimpoints of each observation slightly differ from one another such

[1]http://cxc.harvard.edu/ciao/

that they do not all have identical positions in detector coordinates. We corrected for these offsets by shifting the positions of each exposure to a common tangent point via the `reproject_obs` task. We then checked for any external sources of contamination in the vicinity of the point source. Specifically, we removed ACIS readout streaks (McCollough and Rots, 2005) present in three of the five exposures (ObsIDs: 13728, 14471 and 9540) by running `acisreadcorr`. The latter was provided with a spectrum of the background extracted 50 arcseconds away from the position of the ULX. The algorithm removed any events that were not consistent with this spectrum, within the region containing the readout streak events. The cleaned event file was then adaptively smoothed by `csmooth` to produce the image shown in Figure 2.1, binned to native ACIS pixel resolution. The overlaid contours of Hα emission from *SUBARU* FOCAS[2] map the position of the ULXB relative to the X-ray source. We performed astrometric corrections of point sources in the *SUBARU* image by cross-matching their positions with seven sources from the USNO A2.0 catalogue[3]. This enabled us to account for any relative offset between the Hα nebula and the ULX. We note that the astrometric error was ~ 0.5 arc-seconds, which is very close to the spatial resolution of *Chandra*.

The stacked image in Figure 2.1 plainly does not suggest a strong evidence for any extended emission in the vicinity of the ULX. The X-ray emission appears point-like, with the regions surrounding the bubble nebula making a minor contribution to the total number of events. Prior to analysing the X-ray spectrum of the extended region, we ran the source detection algorithm `wavdetect` on the stacked image to ensure that no other point sources were detected within the extent of the bubble nebula. This would otherwise contaminate the spectrum in this region. The source detection is performed by correlating the input image with Mexican Hat functions at several scale sizes (i.e. 1,2,4,8 and 16 in pixel units). We used the default (CIAO) value for the detection significance parameter (`sigthresh` $= 1 \times 10^5$), which ensures no more than 1 false detection over the number of pixels in the image. As such, we found that the stacked image does not contain any resolved point sources within the Hα nebula aside from Ho IX X-1.

[2]http://smoka.nao.ac.jp/

[3]http://tdc-www.harvard.edu/catalogs/ua2.html

2.4 X-ray spectral properties

The X-ray emission in Figure 2.1 appears to be point-like, and therefore does not suggest a strong evidence for the presence of extended nebular emission. However, the radial profiles of some individual point sources indicate a hint of excess emission above the background beyond a 20 arcsecond radius (which is larger than the spatial extent of the ULXB; see Figure 2.5). Here, we analyse whether this is associated with the bubble nebula or is simply the emission in the PSF wings scattered off the *Chandra* mirrors. In particular, we investigate whether the spectrum of the extended region (as defined in Figure 2.2) contains some contribution from optically thin thermal plasma emission, which would support the former scenario. The X-ray emission from the shocked wind is not expected show significant variability over timescales as short as the duration between the first and the last *Chandra* observation. Therefore, we combine the spectra from all five exposures in order to enhance the signal-to-noise ratio (see below). One expects a greater (relative) contribution from the nebular emission in the wings of the PSF (where the ULX emission is fainter) than in the core, so we investigate whether this is satisfied by comparing the spectra from these two regions.

2.4.1 Spectral extraction

We proceeded to extract the ULX spectrum inside a circular aperture of 4 pixel radius for all exposures, as recommended for a point source in the relevant *Chandra* science thread[4]. The spectrum in the extended region was extracted using an annular aperture as shown in Figure 2.2. We set the outer radius of the annulus to 30 arcsec, ensuring that it extends well beyond the edge of the nebula, and the inner radius to the 98 percent encircled energy of the PSF. The motivation for this was to make sure that the extended source spectrum contains as little emission from the ULX as possible. We calculated the inner radius for each observation by making a curve-of-growth of the source events in a 5 arcsec circular aperture centered on the ULX. All the spectra were created by running `specextract` in CIAO, which automates the creation of the ancillary response

[4]http://cxc.harvard.edu/ciao/threads/pointlike/

Spectral region	XSPEC model	$N_{\rm H}$ [10^{22} cm^{-2}]	Γ	$kT_{\rm p}$ or $kT_{\rm in}$ (keV)	χ^2/dof.
ULX	tbabs × tbabs × (powerlaw)	0.16 ± 0.01	1.22 ± 0.02	N/A	459.7/386
ULX	tbabs × tbabs × (powerlaw + diskbb)	0.4 ± 0.1	1.33 ± 0.05	0.14 ± 0.01	437.2/384
Extended region	tbabs × tbabs × (powerlaw)	0.1 ± 0.1	1.3 ± 0.1	N/A	75.1/74
Extended region	tbabs × tbabs × (powerlaw + diskbb)	$0.1^{+0.3}_{-0.03}$	$1.2^{+0.2}_{-0.1}$	0.14*	75.1/73

Table 2.2: A summary of `xspec` models employed in fits to the combined ULX and extended source spectra. The quoted errors are at the 90 percent confidence level. Note that Γ is the photon index, $N_{\rm H}$ is the variable hydrogen column density, $kT_{\rm in}$ is the inner disc temperature (relevant for fits with the `diskbb` model) and $kT_{\rm p}$ is the temperature of the `apec` plasma. We were unable to constrain the temperature of either the `diskbb` or the `apec` models fit to the extended source spectrum, owing to a small number of counts at energies below 0.5 keV. So, these were fixed to the values indicated with an asterisk.

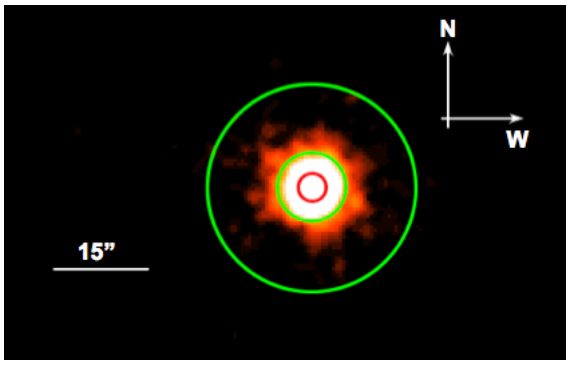

Figure 2.2: Stacked ACIS-S (0.3 - 6.0) keV image of Ho IX X-1 smoothed with a 2 arcsec Gaussian for display purposes. The red circle (with 4 pixel radius) marks the extraction region for the ULX spectrum, while the extended source spectra are extracted within the green annulus. The inner radius of this annulus varies for each observation, and corresponds to the radius demarcating the PSF core from the wings. The outer radius is fixed to 30 arcsec, which extends well beyond the edge of the bubble nebula (compare with Figure 2.1).

files (ARFs) and the response matrix files (RMFs). The background spectra were extracted within circular apertures of 20 arcsecond radius on the same chip as the X-ray source (but placed sufficiently far away to avoid any contamination from it), and were subtracted from the source events. When creating the ULX spectra, we did not generate weighted RMFs (`weight=no`) and corrected for events falling outside the extraction aperture (`correctpsf=yes`), as required for point source analysis. However, when extracting the extended source spectra the RMFs were weighted (`weight=yes`), in order to account for the spatial variation in the ACIS-S detector response. For each region, we stacked the spectra of all five observations and ensured that there were a minimum of 20 counts per energy bin, which validates the use of the χ^2 statistic in our fits.

2.4.2 A comparison of the ULX and extended emission

We began by fitting the stacked ULX spectrum with a doubly absorbed power-law model (i.e. `tbabs` × `tbabs` × `powerlaw`) in `xspec` using the abundances of Wilms et al. (2000), and restricted the energy range of the fit to (0.3 - 6.0) keV. We included two neutral absorption components, the first of which was fixed to the Galactic value in the direction of Ho IX X-1 (5.54×10^{20} cm^{-2}; Kalberla et al. 2005), while the second was chosen to

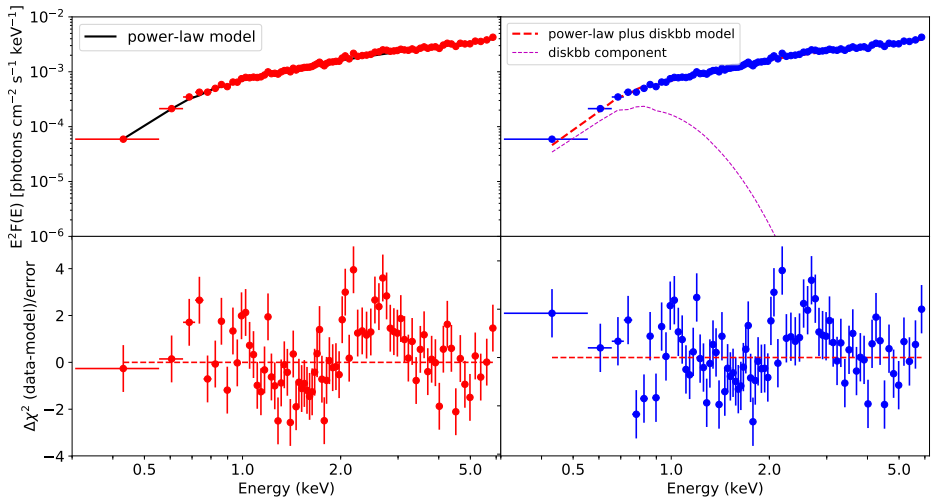

Figure 2.3: (Left): A stacked spectrum of the ULX, with the best-fit doubly absorbed power-law model plotted over the (0.3 - 6.0) keV energy range. A satisfactory fit to the data is obtained, with the best-fit parameters quoted in Table 2.2. (Right): The same spectrum now fitted with a doubly absorbed `diskbb` plus `powerlaw` model. This improves the goodness-of-fit significantly over just the single power-law component (see text).

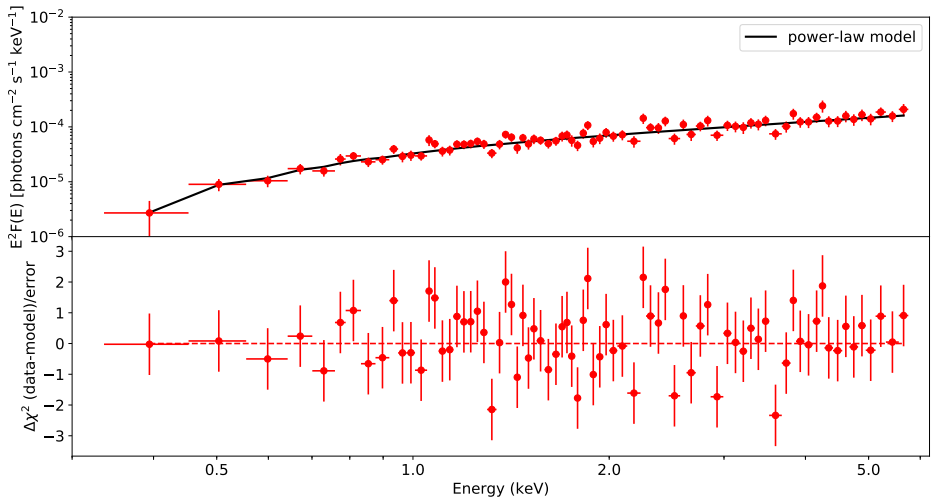

Figure 2.4: The stacked extended source spectrum extracted in the wings of the PSF and fitted with a doubly absorbed power-law model. The spectrum shows no evidence of any excess at energies below 1 keV, which would be expected if the emission from the shock-ionised nebula was significant.

account for any absorption intrinsic to the source and/or its host galaxy. This was allowed to vary together with the remaining parameters of the model.

A single power-law component alone did not provide a good fit to the stacked ULX spectrum, which shows some residuals at energies below 1 keV. However, the fit was substantially improved by the addition of a multi-colour disc model (i.e. $\Delta\chi^2 = 22.5$ for 2 additional degrees of freedom), which accounts for most of the residual emission. Previous analyses of the broadband spectrum of Ho IX X-1 have found a similarly strong evidence for the presence of a soft thermal component, which is thought to be emitted by the inner photosphere of a super-critical outflow. The peak emission temperatures found by those authors is in reasonable agreement with the value reported in Table 2.2 (i.e. ~ 0.1 keV). However, some *XMM-Newton* spectra (with sufficiently high signal-to-noise) show prominent residuals even after the inclusion of a soft thermal component (Gladstone, Roberts, and Done 2009; Middleton et al. 2015a). The residuals in these spectra are well modelled by emission from collisionally ionised plasma. There are very weak indications of such features in the stacked *Chandra* spectrum of Ho IX X-1 (below 1 keV). Namely, the addition of a thermal plasma emission model (on top of the pre-existing power-law and multi-colour disc components) leads to a very small change in the goodness-of-fit (i.e. $\Delta\chi^2 = 8$ for 2 additional degrees of freedom). We briefly comment on the possible origins of these features in the discussion.

We proceeded to check whether there is a stronger contribution from thermal plasma emission in the extended region by repeating the steps of analysis described above. However, the extended source spectrum appears to be featureless (Figure 2.4). It is very well fitted by a simple power-law model that cannot be rejected above a significance of 1σ. In this case, there is no strong requirement for an additional `diskbb` component, and the spectrum is dominated by the hard emission from the ULX (see Table 2.2). This is consistent with the fact that the photon indices of the ULX and extended source spectra are fully within error. Even though the radial profiles of the individual observations of Ho IX X-1 indicate some excess emission above the background in the extended region, this is unlikely to be attributed to emission from an X-ray nebula, since there are no strong features of thermal plasma emission in the extended source spectrum. Rather, it is likely to be dominated by the scattered emission of the ULX in the wings of the PSF. As an aside, we note that since four of the five *Chandra* exposures suffer from pile-up (see Table

2.1), the accuracy of the best-fit parameters in Table 2.2 cannot be guaranteed. But, this does not affect the main goal of the analysis performed here. That is, we are not interested in characterising the spectral properties of the source, but rather in searching for features of diffuse emission from the bubble nebula in the PSF wings, where pile-up is negligible.

We set an upper limit on the nebular emission by fitting the extended source spectrum with three additive model components. Namely, the (absorbed) `powerlaw` plus `diskbb` model sets the baseline for the soft emission in the extended region (which is dominated by the ULX), and we add a thermal plasma emission model `APEC` (see chapter 1 and Smith et al. 2001) to calculate any excess nebular emission. Owing to an insufficient number of counts at energies below 1 keV, we could not constrain the plasma temperature in our fits. However, the simulations of bubble nebulae (Siwek et al. 2017) estimate plasma temperatures from the shocked wind to be $\lesssim 0.5$ keV. So, we fixed the temperature to a range of different values between (0.2 - 0.5) keV and computed the upper limit separately for each value. As such, the largest limiting luminosity of the `52` component (in the 0.1 - 10.0 keV energy range) was found to be 10^{36} erg s^{-1} (corresponding to a plasma temperature of 0.4 keV), which constitutes less than 5 percent of the total flux. As a caveat, we note that the upper limit was calculated by extrapolating the `52` model flux to energies below 0.3 keV, since the bandpass of *Chandra* does not extend below this energy. The observed (0.3 - 10.0) keV upper limit is slightly lower (i.e. $\sim 5 \times 10^{35}$ erg s^{-1}). This is reasonably consistent with the estimates from Siwek et al. (2017), although we caution that they only compute this at a single energy (2 keV).

2.5 Photometry

As a final test of whether Ho IX X-1 is truly point-like at the spatial resolution of *Chandra*, we examined the radial profile of each observation (Figure 2.5). We calculated these by using a stack of concentric annuli centered on the source, out to a radius of 27 arcsecs. Figure 2.5 illustrates that in three of the four cases, the surface brightness does not significantly exceed the background level beyond a radius of ~ 15 arcsec, which is well within the extent of the ULXB. The only exception to this is Obs 9540. This observation has the largest offset from the nominal aimpoint of the instrument (see Table 2.1), which

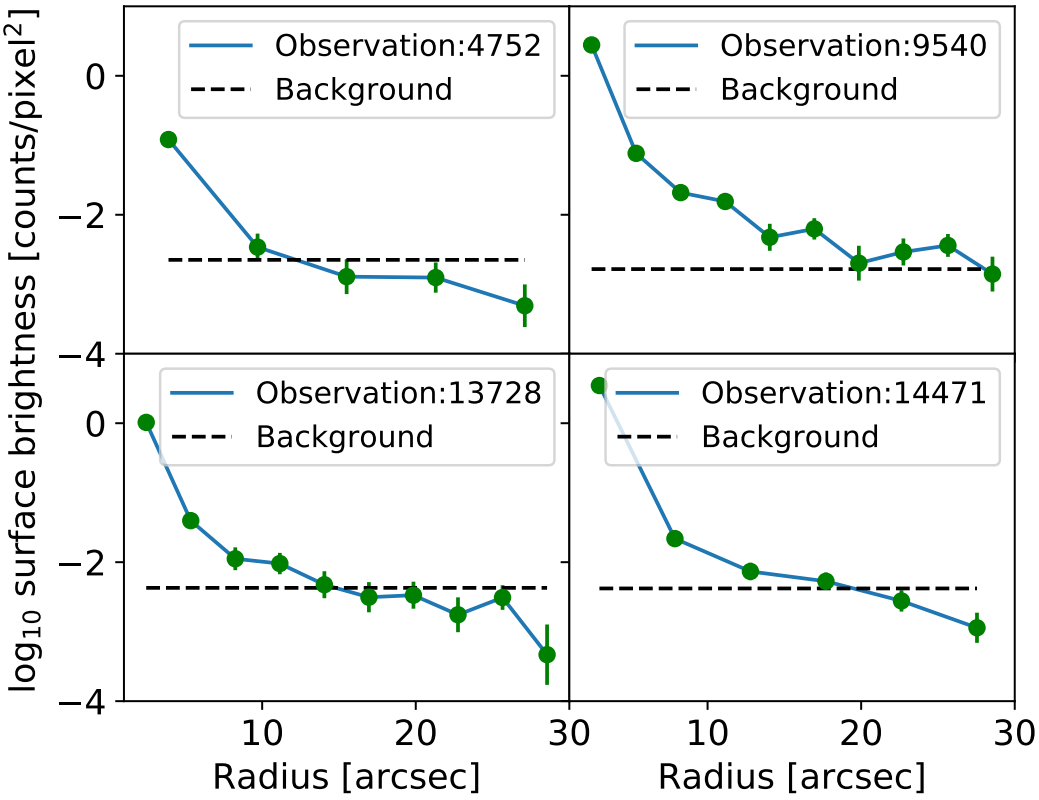

Figure 2.5: Surface brightness profiles of the four longest exposure *Chandra* observations of Ho IX X-1. The surface brightness stays below the background level beyond a radius of 20 arcsec in three of the four cases (see text). We have not shown the radial profile of Obs 4751, since it displays virtually the same behaviour as Obs 4752.

broadens the PSF thus giving rise to a greater number of counts in the PSF wings. However, it still does not show any excess emission in the vicinity of the bubble.

We extended this analysis by comparing the observed PSF with a realistic (ray-tracing) simulation of the *Chandra* point source via the MARX (Model of the AXAF [5] Response to X-rays; Davis et al. 2012) software suite (v5.3.2). We selected the observation that was least piled-up (i.e. Obs 13728; Table 2.1) to compare the observed number of counts in the wings of the PSF (i.e. in the annular aperture in Figure 2.2) with the corresponding MARX simulation. As inputs to the latter, we provided the off-axis angle of the observation and its energy spectrum, both of which influence the encircled energy fraction of the PSF. In summary, we find that the predicted number of counts in the PSF wings (250 ± 20) is in very good agreement with the observed counts (240 ± 20). Given that Obs: 13728 is the faintest of the five observations and the most on-axis, one would expect the extended nebular emission to be most strongly detected in this exposure due to a comparative reduction in the number of counts from the point-like ULX. But, this does not appear to be the case, further confirming the point-like nature of the source and the lack of an extended X-ray nebulosity.

2.6 Discussion and conclusion

In summary, we do not find any evidence for an extended X-ray nebula surrounding the ULX Ho IX X-1 after performing a spectral and photometric analysis of the source with archival *Chandra* data. We estimate an upper-limit on the thermal plasma emission from the shocked wind to be $< 10^{36}$ erg s^{-1} (at the 3σ confidence level). This implies that the simulations of Siwek et al. (2017) do not under-estimate the X-ray emission from ULXBs. Our result also highlights that the soft residuals in the *XMM-Newton* spectrum of Ho IX X-1 are likely to be attributed to processes spatially localised to the source, and not to an extended X-ray nebula. As discussed in section 2.1, there is strong evidence that the spectral residuals are associated with absorption/emission by a fast-moving outflow in at-least four other ULXs (Pinto et al. 2016,17). But, there are very weak detections

[5]The *Chandra* X-ray Observatory (CXO) was previously known as Advanced X-ray Astrophysics Facility (AXAF)

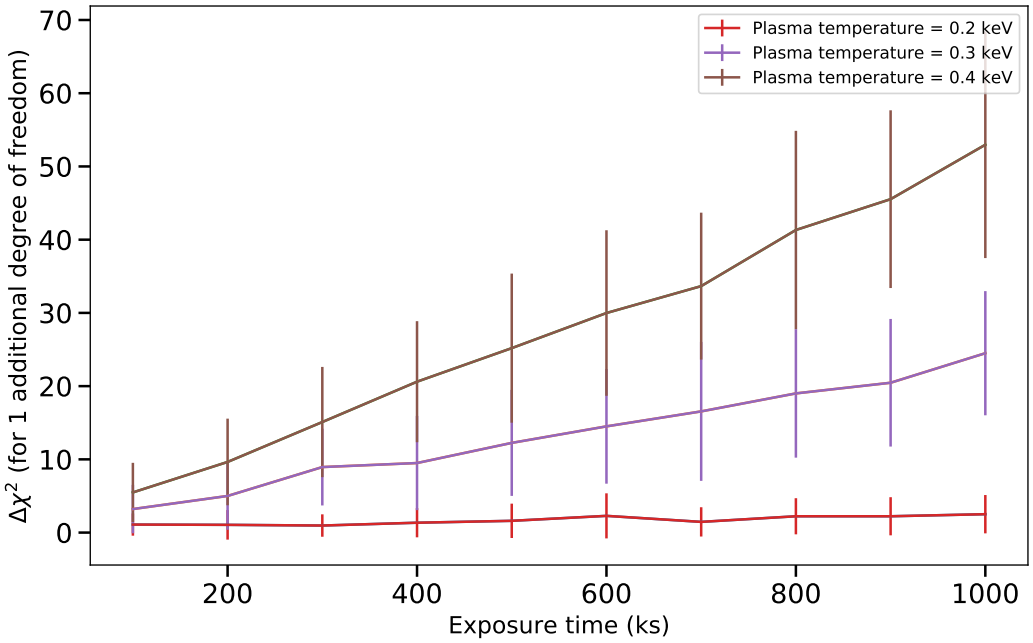

Figure 2.6: The exposure time required to detect the faint ($\sim 10^{35}$ erg s^{-1}) X-ray emission from the bubble nebula with the *Athena* X-IFU micro-calorimeter. We generate mock spectra of the X-IFU for a range of different exposure times. We model the X-ray emission from the bubble nebula with a thermal plasma emission (`apec`) component, considering three different plasma temperatures. The ULX emission is modelled with a standard multi-colour disc plus power-law component. The vertical axis indicates the difference in the chi-squared value when the mock spectrum is fitted with and without the `apec` component. Clearly, the nebular emission can only be detected to a high significance for plasma temperatures larger than 0.2 keV, and for exposure times greater than ~ 400 ks. Each point represents an average over 100 iterations to eliminate statistical fluctuations in the goodness of fit.

of wind absorption features in the RGS spectrum of Ho IX X-1 (Kosec et al. 2018), even though it plainly shows residuals in the broadband continuum at energies below 1 keV. According to the super-critical wind model, the non-detection of wind-absorption features implies that we are viewing this source at very small inclinations, which is consistent with its very hard X-ray spectrum. However, the residuals may still arise due to emission from a partially ionised outflow at *large distances* from the compact object ($\gtrsim 10^3$ gravitational radii; Middleton et al. 2014) as it expands and becomes optically thin.

Deep X-ray observations of bubble nebulae with future instruments could provide additional insights into the kinematics of the outflow. The X-ray emissivity of the shocked wind depends on the density of material in the wind n and on the gas temperature T, scaling as $n^2T^{0.5}$. The simulations predict that both of these quantities are sensitive to the unshocked outflow velocity (see Figure 7 of Siwek et al. 2017). A faster unshocked wind leads to a hotter X-ray emitting plasma, causing it to radiate with a greater emissivity. At the same time, for a given kinetic wind power, a faster wind also implies a smaller mass outflow rate (and hence electron density). This acts to decrease the X-ray emissivity overall, since the latter depends more strongly on electron density rather than temperature. Siwek et al. (2017) find that the X-ray luminosity peaks at wind velocities of ~ 0.003c, whilst being almost negligible (i.e. $< 10^{33}$ erg s^{-1}) for velocities that are ten times larger. Therefore, if limits can be placed on the X-ray emission of ULXBs with more sensitive instruments, this would enable independent constraints on the unshocked outflow velocity, which is a key input parameter of magnetohydrodynamic (MHD) simulations of accretion flows around BHs and NSs. We note that this would add to the constraints already derived from the analysis of atomic features in the RGS spectra of some ULXs (Pinto et al. 2016,17).

We investigate the viability of such an experiment by estimating the exposure time required to detect the faint nebular emission with *Chandra*, and compare this to the expectations from the X-IFU micro-calorimeter on-board *Athena* (Nandra et al. 2016). Mock spectra of both instruments are generated using the `fakeit` tool in `xspec`. We adapt the best-fit continuum model from section 2.4 in order to account for the broadband ULX emission, which comprises two distinct multi-colour disc and power-law components. We add an `52` component in order to model collisionally ionised X-ray emission from the shocked wind, and assign to it a luminosity of 10^{35} erg s^{-1}. This is typical of the estimated

X-ray luminosities from the shocked wind by Siwek et al. (2017). We test the significance of the `52` component against the broadband ULX continuum for a range of different exposure times. Since the effective areas of both *Chandra* and *Athena* vary quite strongly between (0.3 - 1.0) keV, we expect the detection significance to also depend on the plasma temperature. Hence, the procedure is repeated for three different temperatures (0.2 - 0.4 keV). Unfortunately, we find that even for exposure times larger than 1 mega-second, the nebular emission is not strongly detected with *Chandra* (i.e. detection significance $< 2\sigma$). A statistically significant detection may be possible with the X-IFU for gas temperatures exceeding 0.3 keV and integration times larger than ~ 400 ks (see Figure 2.6).

In deriving the estimates above, we conservatively assume that the nebula cannot be spatially resolved by the X-IFU, although this might be unrealistic. Whilst its angular resolution is expected to be ten times lower than *Chandra* (i.e. ~ 5 arc-seconds), this might still be sufficient to resolve bubble nebulae with diameters $\gtrsim$ (20 - 25) arc-seconds. In that case, the required detection exposure times will be smaller than shown in Figure 2.6 owing to a much lower contribution from the spatially point-like ULX emission. The strength of the X-ray emission is also sensitive to the age of the bubble. During the very early stages of its evolution, the shocked wind is nearly adiabatic and radiates with an approximately ten times larger X-ray luminosity than during the snow-plough phase (i.e. after ~ 0.2 Myrs; see Figure 3 of Siwek et al. 2017). However, the inferred ages of a majority of ULXBs are ~ 1 Myr (Pakull and Mirioni 2002), such that their X-ray luminosities would be consistent with the value we use to estimate the detection exposure times (i.e. $\sim 10^{35}$ erg s^{-1}). Finally, we note that numerous ULXs are found to reside in star-forming and starburst galaxies with strong diffuse X-ray emission extending several kpc from their centres. This is expected to be brighter than the intrinsic X-ray emission from ULXBs, posing further problems to their detection. Therefore, dwarf galaxies like Holmberg IX with negligible amounts of diffuse emission are more realistic targets for future X-ray observations of bubble nebulae.

Chapter 3 The discovery of weak coherent pulsations in the ultraluminous X-ray source NGC 1313 X-2

3.1 Abstract

We report the detection of weak pulsations from the archetypal ultraluminous X-ray source (ULX) NGC 1313 X-2. Acceleration searches reveal transient pulsations in individual segments of two out of six new deep observations of this object, with a period of ~ 1.5 seconds and a pulsed fraction of ~ 5%. We use Monte Carlo simulations to demonstrate that the two detections are unlikely to be false positives caused by Poisson noise, especially given their very close frequencies. Moreover, their strong similarity to the sinusoidal pulsations detected from other ULXs also argues for their validity. The presence of a large bubble nebula surrounding NGC 1313 X-2 implies an age of order 1~ Myr for the accreting phase of the ULX, suggesting that the neutron star's magnetic field has not been suppressed over time by accreted material, nor has the neutron star collapsed into a black hole, despite an average energy output into the nebula two orders of magnitude above Eddington. This argues that most of the accreted material has been expelled over the lifetime of the ULX, favouring accretion models that invoke the emission of strong winds and/or jets for neutron star ULXs.

3.2 Introduction

The discovery of pulsations in a few ULXs has led to an unexpected twist in this field, since much of the initial debate was focussed on whether they are powered by stellar or intermediate mass black holes (e.g. Colbert & Mushotzky 1999) accreting close to the Eddington limit. As discussed in chapter 1, the key questions for ULXs now revolve around whether a majority of the population host neutron stars, and how they can overcome the Eddington limit in the presence of a strong magnetic field. Further progress on these issues can only be made by expanding on the currently sparse number of PULXs (see Bachetti et al. 2020 and references therein), which have steadily grown since the first discovery including the first detection of a Galactic pulsating ULX (Wilson-Hodge et al. 2018). In this chapter, we report and discuss the detection of pulsations from an archetypal extragalactic ULX, NGC 1313 X-2. This PULX is located on the outskirts of the barred spiral galaxy NGC 1313, and is historically amongst the best studied ULXs in terms of its X-ray properties (e.g Feng and Kaaret 2007; Pintore and Zampieri 2012), optical counterpart and environment (e.g. Pakull and Mirioni 2002; Grisé et al. 2008). In particular, a lack of radial velocity variations in its optical spectrum (Roberts et al. 2011) and the patterns of change in its hard X-ray spectrum and flux variability could suggest that it is viewed at a low inclination angle (Sutton et al. 2013; Middleton et al. 2015a), thus affording a direct view of the central regions of its accretion flow.

3.3 Observations and data analysis

The barred spiral galaxy NGC 1313 was observed by *XMM-Newton* seven times between 2017 June 16 and 2017 September 24, as part of a Large Programme observing both ULXs in the galaxy: NGC 1313 X-1 and X-2 (see Pinto et al. in prep. for a summary of the data obtained). The latter is the target of this study, and it lies ~ 7 arcminutes off-axis from the nominal aim-point of the observations. The observations were carried out with the EPIC-pn and MOS detectors in full-frame imaging mode. The raw observation data files (ODF) were processed with the Science Analysis Software (SAS)v.16. We excluded observation 0803990701 from further analysis at this stage as it contained only ~ 15 ks of exposure; all other observations were exposed for > 120 ks. Source events were extracted

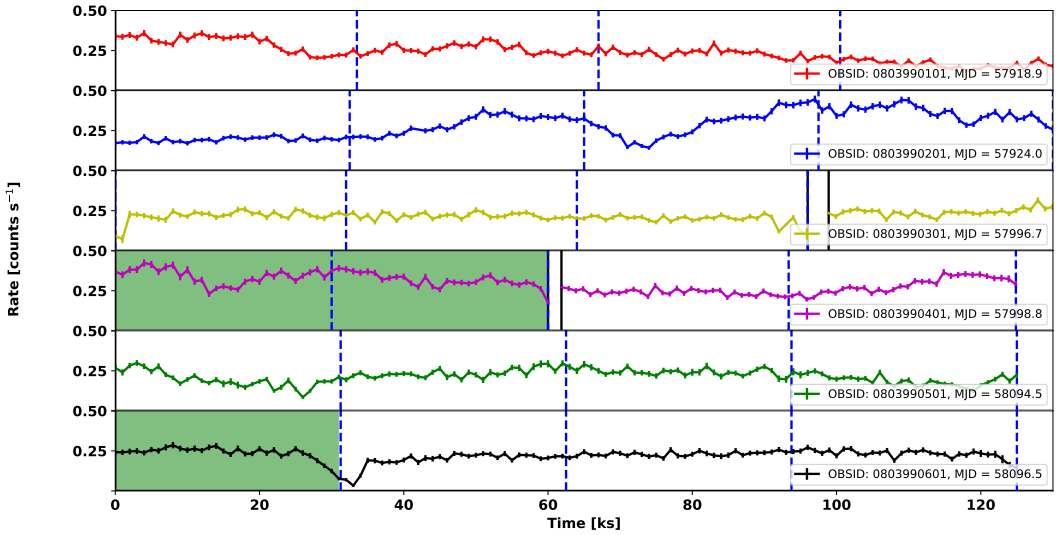

Figure 3.1: The EPIC-pn light curves of the six *XMM-Newton* observations of NGC 1313 X-2 in time bins of 1000 seconds. Each light curve is split first into (i) four segments of ~ 30 ks exposure length (indicated by the dashed blue lines) and then into (ii) two longer segments ~ 60 ks exposure length, as explained in the text. The acceleration search is run on each individual segment. The shaded green regions correspond to epochs during which the pulsations were detected, and the black lines separate the non-contiguous segments (owing to a pause in exposure) of the fourth and sixth observation. The legend specifies the observation identifier for each source.

Table 3.1: Observation log for the NGC 1313 campaign.

Data set (Obs. ID)	Start date (MJD)	Effective exposure (ks)
0803990101	57918.9	134.1
0803990201	57924.0	130.8
0803990301	57996.7	129.8
0803990401	57998.8	125.0
0803990501	58094.5	125.9
0803990601	58096.5	125.9

in a circular aperture of 25 arcsecond radius centred on the target, while the background region was chosen to be adjacent to the source on the same chip. We then used the the SAS task `evselect` to derive the background-subtracted 0.3-10 keV light curves in 73 ms time bins, which corresponds to the maximal time resolution of the EPIC-pn camera (in full-frame mode). We did not utilise data from the MOS detectors, since they do not have sufficient time resolution to be able to detect pulsations with frequencies close to what we measure with the EPIC-pn detectors. This is fundamentally because of the Nyquist theorem, which states that if a signal is sampled at a rate below twice its maximum frequency, such a sampling rate would be inadequate to capture the information on the highest frequency components of the signal (see for e.g. [1]). It follows that, given the time resolution of the MOS detectors (i.e. 2.6 seconds), only signals with frequencies $< 0.5 \times (2.6)^{-1}$ Hz (i.e. < 0.2 Hz) can be fully resolved.

We implemented the standard filtering of events as recommended in the *XMM-Newton* science threads. Namely, we selected only single or double patterned events (`PATTERN <= 4`) and used the standard flagging criteria (i.e. `#XMMEA_EP`) that ensures the exclusion of hot pixels and events falling outside the field of view. In some observations the source emission was spread over more than one chip, and in such circumstances, we combined the data from both chips to construct the light curves.

[1] https://www.themusictelegraph.com/268

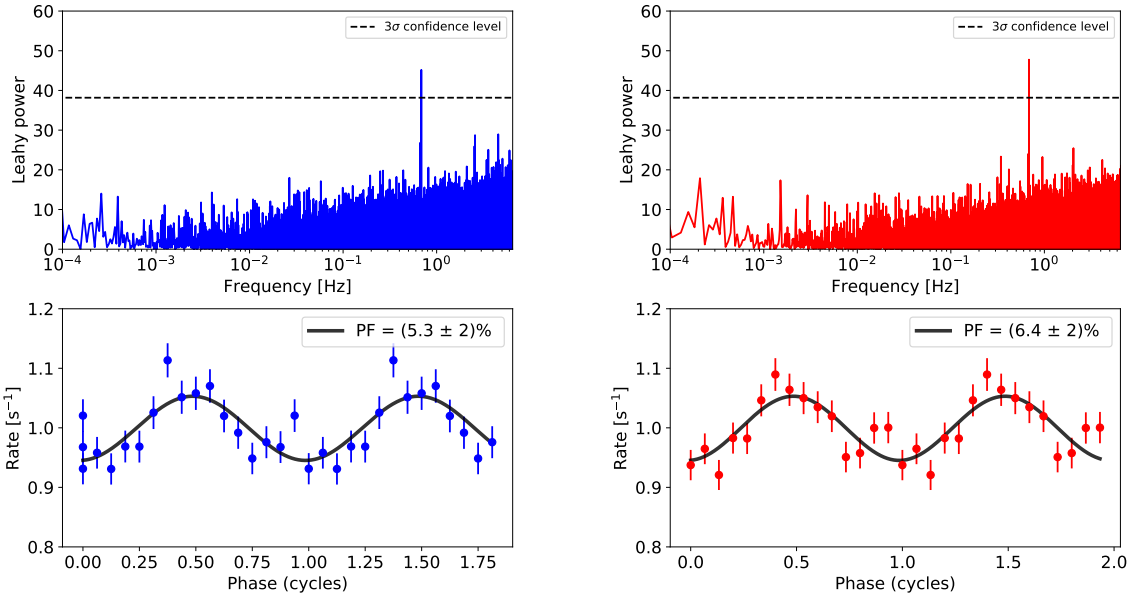

Figure 3.2: (*Top row*) The power spectral densities of the two *XMM-Newton* observations during which coherent pulsations were detected. The dotted line overlaid on each plot shows the 3σ confidence level, taking into account the number of Fourier frequencies. (*Bottom row*) The pulse profiles of the corresponding observations folded on the period and period derivative quoted in Table 3.2.

3.3.1 Discovery of coherent pulsations

As the starting point of our timing analysis, we converted the event times from the EPIC-pn detector to the barycentre of the Solar System with the SAS task `barycen`, using the *Chandra* source position (RA = 49.594 degrees, DEC = -66.601 degrees) and the DE-200 Solar System ephemeris (Standish 1990). We computed the discrete power spectral densities (PSDs) of the six remaining observations using the HEASARC (v6.22) tool `powspec`. A discrete PSD represents the decomposition of a signal into multiple frequency components with varying amplitudes (e.g. van der Klis 1989), and is defined as the sum of the square of the Fourier amplitudes as follows:

$$P_j = \frac{2 \mid a_j \mid^2}{N_\gamma} \qquad \text{and} \qquad a_j = \sum_{k=0}^{N-1} x_k \exp\left(2\pi i jk/N\right) \tag{3.3.1}$$

where a_j is the Fourier amplitude corresponding to a distinct frequency bin j, x_k is the (background subtracted) count-rate in the $k^{\rm th}$ time series bin, N_γ is the total number of counts, and $2/N_\gamma$ is the PSD normalisation factor (also referred to as the Leahy normalisation; Leahy et al. 1983). Even if the time series is devoid of inherent (quasi) periodicities, the PSD will have non-zero values at each frequency bin due to noisy fluctuations in the count-rate characterised by some mean and variance. Indeed, if these fluctuations obey a Poisson distribution, Leahy et al. (1983) show that the PSD will have an equally large mean and variance of two (for the adopted normalisation). However, this only refers to one particular frequency bin in the PSD, while one must consider the total number of frequency bins (or number of trials) when computing the probability of detecting a signal against a background of noise with some confidence level (see section 3.3 of van der Klis 1989).

Initially, the PSDs of the six observations did not indicate any signals peaking above the 1σ white-noise threshold (van der Klis 1989). However, if the source has a relatively strong period derivative $\dot{f}$, this causes the signal to drift across multiple Fourier bins in the power spectrum, with the number of bins scaling as $\dot{f}T_{\rm obs}^2$ for observations of length $T_{\rm obs}$, thus reducing the amplitude of the signal power and the sensitivity of any given search. In order to correct for such an effect, we implemented the Fourier domain acceleration search method by using the PRESTO software (Ransom, Eikenberry, and Middleditch 2002). This method is optimised if the acceleration (or the period derivative) of the source is constant throughout the observation, which is best satisfied if the exposure time is smaller than a tenth of the orbital period of the system. Therefore, we split the light curve of each observation, first into (i) contiguous 30 ks segments, which accounts for the strongest period derivative measured so far in PULXs (i.e. $\sim 10^{-7}$ Hz s^{-1}; Carpano et al. 2018), and later into (ii) larger 60 ks segments, which allows for a stronger detection of candidates with smaller period derivatives. We show the full light curves, and their segmentation, in Figure 3.1; in all cases we ran the search separately on each segment.

This resulted in the detection of coherent pulsations in a 30 ks and a 60 ks segment of two separate observations, out of the total of six, indicating that NGC 1313 X-2 is a new addition to the class of PULXs. Both of these detections were found to occur at similar Fourier frequencies and with a statistical significance larger than 3σ (see Figures 3.2

and **??**)[2]. We folded the light curves of these two segments on the best-fit values of the pulse frequency and its derivative (determined using PRESTO) in order to obtain the pulse profiles (Larsson 1996; Figure 3.2). These appear sinusoidal, as per other PULXs, but the pulsed fractions at $\sim 5\%$ are notably smaller than previously seen (e.g. Bachetti et al. 2014; Fürst et al. 2016). We further verified our timing analysis through an epoch folding search on the two light curve segments shown in Figure 3.1 by using the HENDRICS tool `HENzsearch` (Bachetti 2018). Here, a test for periodicity was performed by evaluating the Z^2 statistic over a grid of $f - \dot{f}$ values (c.f. Buccheri et al. 1983 for further details). The results of the test are shown in Figure 3.3, with the peak Z^2 values in both observations being larger than the 3σ significance level, consistent with the results obtained through PRESTO. As a caveat, we note that in the two *XMM-Newton* observations during which pulsations were detected, there were also periods of intense background flaring, but these periods were not excluded to prevent the loss of genuine signal counts, which otherwise results in a non-detection of the pulsed signal. Indeed, we emphasise that background flares are also seen to occur in an archival observation of another PULX NGC 5907 X-1, such that excluding these periods results in a notable reduction of the pulsation significance (from 10σ to 4.5σ), even though a strong pulsation detection cannot not be disputed when all events are considered.

We calculated the unabsorbed 0.3-10 keV X-ray luminosity for each observation by fitting a simple power-law plus multi-colour disc model to the EPIC-pn spectra in XSPEC and correcting for both the Galactic and intrinsic absorption columns. The X-ray spectra were extracted by following the standard procedure outlined in Walton et al. (2018b). We tabulate these luminosities alongside the characteristics of the detected pulses in Table 3.2. Finally, we note that we do not detect pulsations in any archival observations with similar quality of data and exposure as in the six observations from our programme.

3.3.2 Verifying the detection significance with Monte Carlo simulations

In van der Klis (1989), the significance level for the detection of a coherent signal (above a given threshold) is evaluated by considering the distribution of the noise powers and

[2]Here, we refer to the significance reported by the `accelsearch` routine in PRESTO, which accounts for the total number of trials

Table 3.2: Characteristics of the detected pulsations.

Data set	Date[a]	f[b]	$\dot{f}$[c]	PRESTO significance	Pulsed fraction	$L_{\rm X}^{\rm d}$
Obs.ID	(MJD)	(Hz)	(Hz s^{-1})	(σ)	(%)	(10^{40} erg s^{-1})
0803990401	57998.0	0.68624(8)	6.5(5) $\times 10^{-9}$	3.00	5.3(2)	1.99
0803990601	58096.0	0.68458(2)	1.6(2) $\times 10^{-8}$	4.12	6.4(2)	1.44

Notes: [a] mid-point of the observation; [b] detected frequency; [c] detected frequency derivative; [d] intrinsic X-ray luminosity in units of 10^{40} erg s^{-1} in the 0.3-10 keV band.

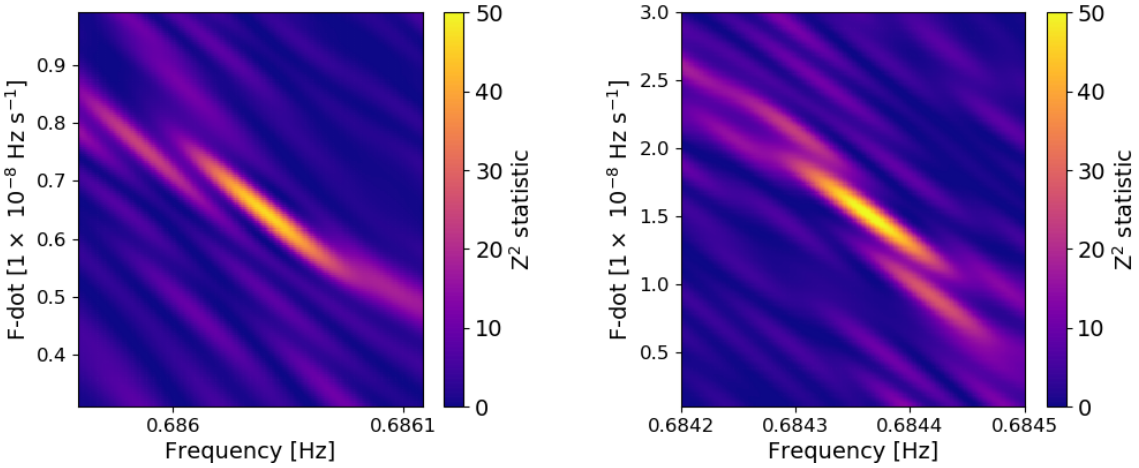

Figure 3.3: Epoch-folding search results for the two observations revealing pulsations. This re-affirms the results obtained through PRESTO. The colour bar shows the Z^2 statistic with peak values being above the 3σ significance level (i.e. > 40).

the number of Fourier bins in the power spectrum. The significance given by PRESTO is calculated in the same manner. However, it does not consider the fact that we split each light curve into several segments, and also searched for signals dispersed over an initially unknown number of Fourier bins $z_{\max}$. Searching over a range of different $z_{\max}$ values for each segmented light curve vastly increases the parameter space, making it more likely to obtain a false positive. Therefore, Monte Carlo simulations are required in order to account for these factors and derive an estimate of the true significance of our detections.

We simulated 10000 fake light curves containing pure Poisson noise with exposure times set to match those of the real observations, and mean count rates sampled randomly from the range of count rates observed in archival *XMM-Newton* and *Swift* observations of NGC 1313 X-2 (with the latter converted to equivalent count rates in *XMM-Newton* using PIMMS). Each light curve was split in the same manner as the real data (including the addition of GTI timing gaps), and was searched for pulsations using PRESTO as described in section 3.3.1. We then picked 12 simulated light curves at random to match the 12 long observations in the actual data (including archival observations). We looked for two detections of pulsations within these simulated observations with statistical significances equal to or larger than those measured for the real data, and detected pulse frequencies differing by no more than the difference between our two detections (i.e. $< 1.5 \times 10^{-3}$ Hz).

We repeated this random sampling of our simulated light curves 10000 times. We found a false positive rate of 1 in 10000, implying that our detections are significant to more than 3.5σ even after accounting for the "look elsewhere" effect.

3.3.3 Constraints on orbital parameters

In order to set preliminary constraints on the orbital parameters of the system, we will conservatively assume that any variation in the pulsation frequency is dominated by an orbital modulation (although see section 4.4). In this case, the line-of-sight acceleration of the source α can be expressed in terms of the spin parameters as $\alpha = c(\dot{f}/f)$. The value of $\dot{f}$ measured in the sixth observation is $1.6(2) \times 10^{-8}$ Hz s^{-1}, which corresponds to $\alpha = 7(1)$ m s^{-2}. In order to produce such a large acceleration, the companion mass M_c and the orbital period $P_{\rm orb}$ must be restricted to the range of values illustrated in the top panel of Figure 3.4. Moreover, if the observed pulse frequency shift between the two observations is solely due to the orbital motion of the source, this imposes further limits on the orbital parameters (as illustrated in the bottom panel of Figure 3.4). In deriving these estimates we have assumed that the pulsations indicate the presence of a NS primary in the binary system with a mass $\sim 1.4 M_{\odot}$. We also assume a circular orbit, which appears to be the case for several other PULXs likely due to the action of strong tidal torques (Bachetti et al. 2014, Israel et al. 2017a, Fürst et al. 2016). We consider the constraints on the orbital parameters for two separate inclination angles, and find that it is particularly difficult to explain the observed frequency shift if the system is viewed moderately face-on (i.e. $<$ 30 degrees; second figure in the bottom panel). However, since the source is classified to be hard ultraluminous from its X-ray spectrum, its central regions are likely to be seen close to face-on rather than edge-on (Sutton, Roberts & Middleton 2013). This apparent contradiction could be reconciled if the spin and orbital angular momenta of the system are misaligned, possibly due to a kick received by the NS after an asymmetric supernova explosion of its progenitor (see e.g Lai 2000; Kaspi et al. 1996).

Further, Grisé et al. (2008) have derived an upper limit on the mass of the companion star from studies of the young OB association in its vicinity. By fitting stellar isochrones to the *HST* optical magnitudes of these stars, they were able to measure the cluster age to be $\sim$ 20 Myrs. This limits the maximum mass of the companion star of the ULX to be

$\lesssim 12 M_{\odot}$, provided that it is associated with the star cluster. A typical B-type companion consistent with this mass limit has a radius of $\sim 4 R_{\odot}$ and must overflow its Roche-Lobe during the ULX phase. In such a scenario, the period-density relation (Frank et al. 2002) independently constrains the orbital period, which we find to be consistent with the range of values inferred from X-ray timing (provided that there is some spin-orbit misalignment). Finally, we can use the constraints derived from this analysis to verify that our definition of a false positive in the previous section (i.e. any two detections with pulse frequencies differing by $\sim 1.5 \times 10^{-3}$ Hz or less) is not physically unreasonable. Indeed, for the allowed set of parameters shown in Figure 3.4, the expected change in the pulse frequency in a single orbital cycle will not exceed 5×10^{-3} Hz. If we re-run the Monte Carlo simulations by allowing the pulse frequencies to differ by as much as the latter value, we find that this does not change the false positive rate quoted in the previous section.

3.3.4 The pulsed spectrum

In between the epochs of pulse minima and maxima, variability in the hard X-ray continuum (> 1 keV) has been confirmed for some of the known PULXs (e.g. Brightman et al. 2016; Israel et al. 2017; Walton et al. 2018), and is in agreement with the idea that the pulsations are caused by a modulation of the emission from a magnetically channelled accretion column. Here, we attempt explore whether the X-ray spectrum of NGC 1313 X-2 displays a similar hardening between the phases of pulse minima and maxima. We only use the second observation since it has a larger pulsed fraction compared to the first, which should strengthen any variations in the X-ray spectrum between the two extremal pulse phases.

We began by converting the (barycentered) time-of-arrival of each event to a rotational phase, using the best-fit pulse frequency and its derivative $\dot{f}$ obtained from the Z^2 search (see Table 3.2). We assigned this phase to one of the 16 equally spaced phase bins (comprising a full pulse cycle) via the HENDRICS tool `HENphasetag` (see Walton et al. 2018a). We then extracted the source spectrum during the brightest (pulse-on) and faintest (pulse-off) quarters of the pulse cycle by filtering on the phase of each event via the `evselect` task in SAS (see Figure 3.6). These spectra were subtracted from the background spectra extracted during the same periods. As reference, we repeated the above steps to obtain

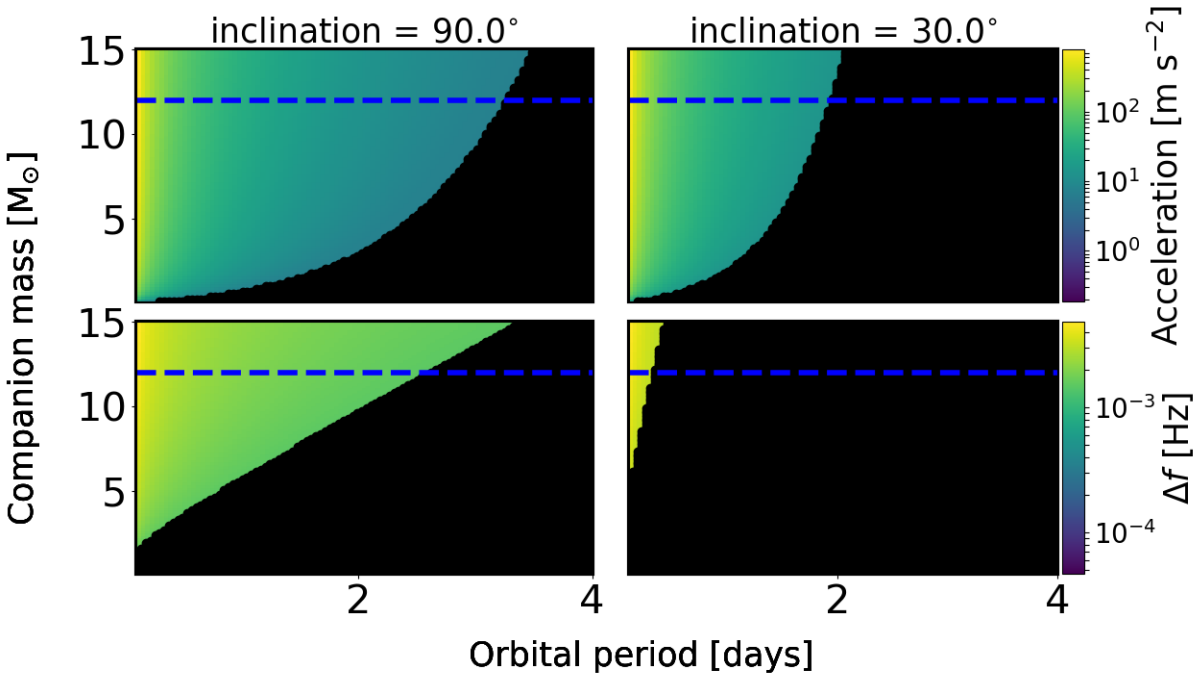

Figure 3.4: Constraints on the orbital parameters of NGC 1313 X-2. In the top panel, we plot the expected line-of-sight acceleration (shown by the colour-bar) of a 1.4 $M_\odot$ neutron star in a circular orbit around a companion with varying masses and orbital periods. In the bottom panel, the colour-bar indicates the expected pulse frequency shift in a single orbital cycle (in Hz) as a function of the companion mass and orbital period. In both cases, the black shaded regions correspond to an area of the parameter space that do not give rise to accelerations (top-panel) or pulse frequency shifts (bottom-panel) as large as the value actually observed (see Table 3.2), and are therefore ruled-out. The blue dashed line marks the upper limit on the companion star mass inferred through stellar population studies by Grisé et al. (2008).

Table 3.3: Best-fit parameters to the pulse on and pulse off spectra of four different PULXs, modelled simultaneously with the `xspec` model: `TBABS` × `TBABS` × (`DISKBB` + `POWERLAW`). The hydrogen column density is linked to a constant value between the pulse-off and pulse-on phases (and thus does not have any errors). All errors are quoted at the 90% confidence level, and any unconstrained parameters are indicated with a −.

Source	Phase	$N_{\rm H}$[a] $[10^{22}$ cm$^{-2}]$	$kT_{\rm in}$[b] [keV]	norm$_{\rm d}$	Γ[c]	norm$_{\rm PL}$ $[1\times10^{-4}]$	χ^2/dof[d]
NGC 5907 X-1	On	1.2	0.1 ± 0.05	2800^{+90000}_{-2700}	1.6 ± 0.1	1.0 ± 0.1	153.1/148
	Off		$0.1^{+0.1}_{-0.04}$	$7^{+60}_{-6}\times10^5$	2.2 ± 0.1	1.2 ± 0.1	
M51 X-7	On	0.1	-	-	1.7 ± 0.1	0.3 ± 0.01	106.5/92
	Off		-	-	1.9 ± 0.1	0.23 ± 0.01	
NGC 7793 P13	On	0.15	0.18 ± 0.04	6^{+10}_{-4}	1.0 ± 0.05	1.2 ± 0.1	249.6/215
	Off		0.19 ± 0.04	5^{+6}_{-3}	1.1 ± 0.1	0.91 ± 0.07	
NGC 1313 X-2	On	0.5	$(4.0\pm0.1)\times10^{-2}$	$(5.7\pm0.2)\times10^6$	2.3 ± 0.1	2.0 ± 0.1	75.9/89
	Off		$(4.9\ ^{+0.03}_{-0.1})\times10^{-2}$	$3^{+8}_{-1}\times10^5$	2.3 ± 0.1	1.3 ± 0.1	

Notes: [a] Hydrogen column density; [b] Inner disc temperature; [c] Photon index; [d] The reduced chi-squared per degrees of freedom (quoted only once since fits are simultaneous)

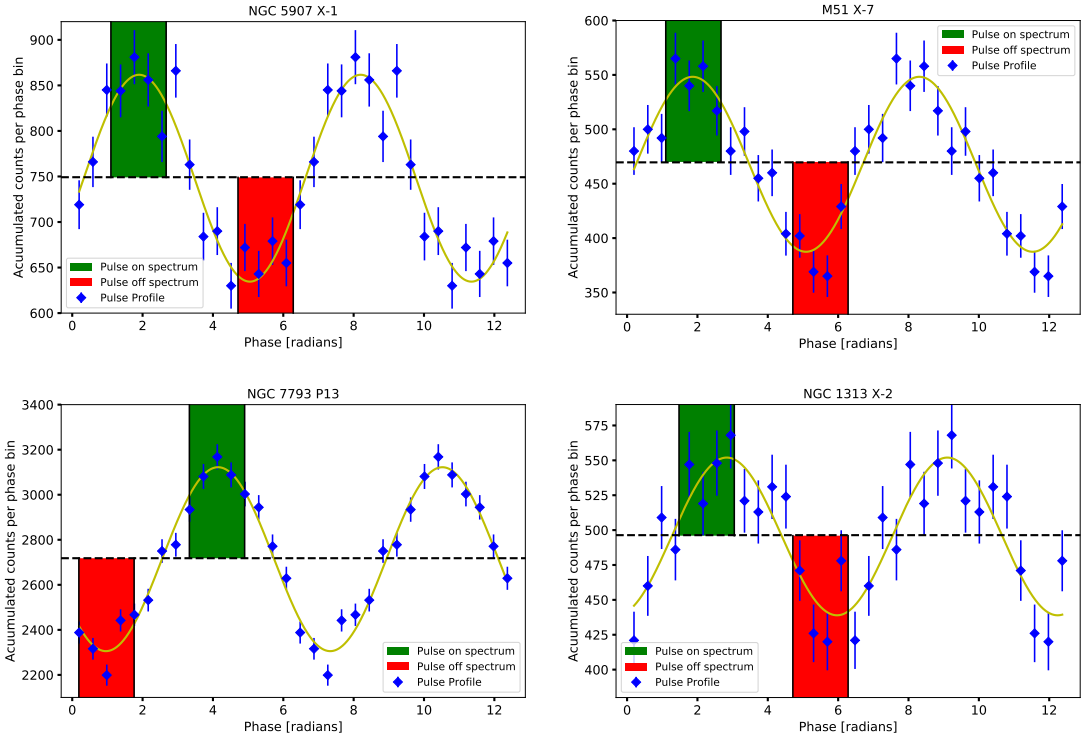

Figure 3.5: The pulse profiles of four different PULXs, showing epochs of pulse minima (red shaded region) and maxima (green shaded region) during which the spectra shown in Figure 3.6 were extracted.

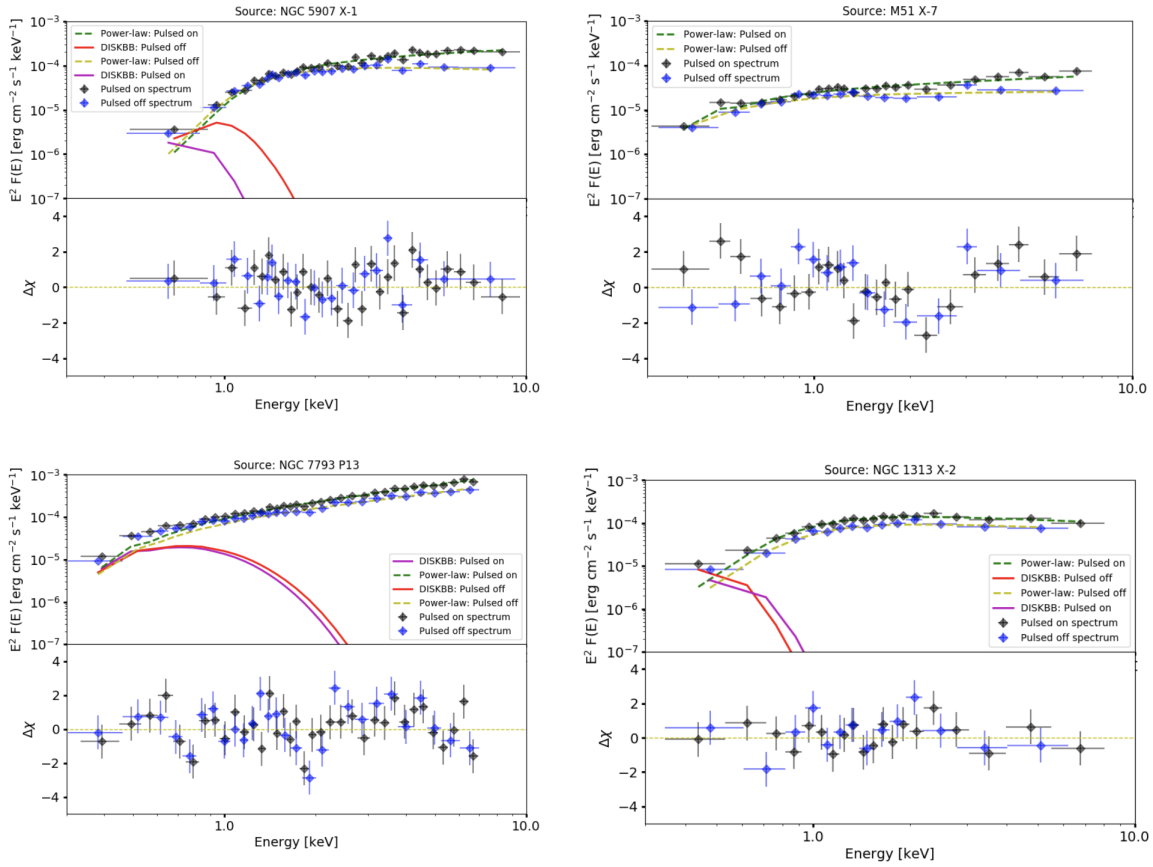

Figure 3.6: The X-ray continuum of four different PULXs during phases of pulse minima (blue diamond) and maxima (black diamond), with the best-fit powerlaw and `DISKBB` models overlaid, and labelled according to the legend in each plot. The residuals to these model fits are shown in the bottom panel. The best-fit parameters corresponding to each model are specified in Table 3.3.

the pulse-on and pulse-off spectra for three other PULXs. All spectra were re-binned to have a signal-to-noise of at-least 5, such that the errors are close to Gaussian to permit the use of χ^2 fitting. The final spectra for all sources are shown in Figure 3.6. For each source, we fitted its pulse-on and pulse-off spectra simultaneously in `xspec` with a doubly absorbed multi-colour disc plus power-law model, with the aim of seeing which of the two components vary more significantly. We adopted a common hydrogen column density between the pulse-on and pulse-off epochs, and fixed it to a value obtained from fitting the above model to the phase averaged spectrum. We highlight the fit results in Table 3.3 and overlay the best fit models alongside the data in Figure 3.6.

In accordance with previous studies, we find that two of the four ULXs (NGC 5907 X-1 and M51 X-7) show a notable hardening of the power-law emission between the pulse-off and pulse-on epochs, while their soft emission (< 1 keV) remains unchanged (within errors). Such hardening is less pronounced for NGC 7793 P13 and appears even less so for NGC 1313 X-2; the latter shows weak evidence for any variation in the photon index between the pulse minima and maxima, but rather suggests an increase in the powerlaw and `DISKBB` normalisation. This hints that the pulsed fraction has a flatter energy dependence for NGC 1313 X-2 relative to other PULXs, which has also been found to occur in some observations of M51 X-7 (c.f. Figure 2 of Rodríguez Castillo et al. 2020). We do not further speculate on the physical origin of this relation here, but note that it presents an interesting point that could be explored in future studies.

3.4 Discussion

We report the detection of coherent pulsations in individual segments of two *XMM-Newton* observations of NGC 1313 X-2 (out of a total of twelve). The detected pulsations are notably weaker than for previous PULXs, with the measured pulsed fractions ($\sim 5\%$) being roughly a factor of two smaller. As a result, each individual detection is only marginally significant at $\sim 3-4\sigma$; however the two detections have remarkably similar pulsation frequencies, and we confirm using Monte Carlo simulations that the chance of detecting two false positives with such similar frequencies is extremely low, so we are confident that we are observing a *bona fide* new member of the PULX class. This is supported by the detected frequencies (that can be associated with the spin of the neutron

star) and their derivatives, in addition to the sinusoidal pulse profiles, all of which are very similar to those of previously discovered sources (Bachetti et al. 2014; Israel et al. 2017b,c). The pulsations are transient on intra-observational timescales, which is reminiscent of the behaviour seen in M82 X-2 (Bachetti et al. 2014), although the physical mechanism for this behaviour remains poorly understood.

We were unable to measure an orbital modulation of the rotational frequency f given the sparse number of pulsation detections. However, given the constraints on orbital acceleration provided by the frequency derivatives we were able to calculate the dependency of orbital period on mass of the companion to the NS; it is notable that we rule out periods as large as the 6.1 day period reported by Liu et al. (2009) on the basis of *HST* data for the optical counterpart to NGC 1313 X-2 (although the veracity of this period was questioned by Zampieri et al. 2012 on the basis of a wider dataset). The lack of constraints on the orbital modulation of the pulsations means that we cannot estimate secular (i.e. accretion-driven) changes in the pulsation frequency with any great certainty. Although, we can at least state that the observed frequency reduction of ~ 1 mHz over 100 days between the two pulse detections suggests a spin down rate $\dot{f} \sim -1.2 \times 10^{-10}$ Hz s^{-1}, which is notable as other PULXs all show secular spin increases. However, the instantaneous values of $\dot{f}$ measured during both epochs have the opposite sign and are significantly larger (see Table 3.2). Therefore, we caution that the observed frequency variation may well be dominated by orbital motion. We note that if the source is indeed spinning-down between the two observations, then this is probably not due to a transition to the propeller regime (Illarionov and Sunyaev 1975), as this is naturally accompanied by a dramatic decline in the X-ray luminosity by several orders of magnitude. Unlike other PULXs (Tsygankov et al. 2016; see also Earnshaw et al. 2018) no such diminution of luminosity has been seen for NGC 1313 X-2 (cf. Figure 3.1; also Weng and Feng 2018).

NGC 1313 X-2 is unusual amongst PULXs as the presence of a shock-ionised bubble (with ~ 400 pc diameter) around it means that we can infer an age for the active phase of the ULX. Pakull and Grisé (2008) calculate this age as ~ 1 Myr for NGC 1313 X-2. This appears to contradict the assertion of King, Lasota, and Kluźniak (2017) that PULXs are rare because the accretion of material onto the surface of the neutron star acts to rapidly diminish its magnetic field; NGC 1313 X-2 demonstrates that this is not the case. Indeed, current binary evolution models show that there are only a small number of scenarios

in which stable Roche Lobe overflow persists for more than $\sim$ 1 Myr onto a NS (e.g. Wiktorowicz et al. 2017). This likely implies that NGC 1313 X-2 is close to the end of its lifetime as a ULX, and yet it is still pulsating. As the bubble nebula requires an average input energy of $\sim 10^{40}$ erg s^{-1} over its entire lifetime to inflate, from the kinetic output of the ULX wind/jets, this also suggests that NGC 1313 X-2 has sustained extreme ($\sim$ 100 times Eddington) accretion rates from its secondary stellar companion. It is likely that the majority of this matter was expelled in radiatively driven outflows, as if this amount of matter were retained by the NS it would have accreted $\gtrsim 1 M_{\odot}$ of material and potentially collapsed to a black hole, resulting in a cessation of pulsations. This necessity for both a strong outflow and a pulsating compact object supports the recent hybrid models for PULXs, such as described by Mushtukov et al. (2019) and is consistent with the recent detection of outflowing material from a PULX (Kosec et al., 2018b).

We attempt to obtain a rough estimate of the dipolar field strength of the NS, which could be used (in a future work) to compare with models that predict the extent of magnetic field decay as a function of accreted mass over the lifetime of the ULX, starting from a range of initial values (e.g. Wijers 1997; Cumming et al. 2004; Cruces et al. 2019). Limits on the field strength can be derived based on two main constraints that (i) the magnetospheric radius R_M of the NS (see equation 1.3.23) is likely to be smaller than the disc spherisation radius $R_{\rm sph}$ (see equation 1.3.21) given the presence of a wind inflated bubble in its vicinity, and (ii) that the magnetospheric radius is larger than the NS radius since the source is observed to be pulsing. Indeed, we use the approach of King et al. (2017) to determine the mass inflow rate $\dot{m}$ onto the NS (see equation 1.3.22 of chapter 1), which is defined in units of the Eddington rate:

$$\dot{m}^2 (1 + \ln \dot{m}) - \frac{4500 L_{40}}{m_{\rm NS}} = 0 \tag{3.4.2}$$

where L_{40} is the apparent X-ray luminosity (in units of 10^{40} erg/s), $m_{\rm NS}$ is the NS mass (in what follows, we assume this to have a canonical value of 1.4 $M_{\odot}$; Özel & Freire 2016). We caution that this does not account for the advection of radiative flux at the spherisation radius, and hence may overestimate the degree of geometric beaming (e.g. Poutanen et al. 2007). Regardless, we use the above equation to compute the two radii R_M and $R_{\rm sph}$, and based on the first of the two constraints above, we arrive at the following expression for

an upper limit on the dipolar field:

$$B < 3.2 \times 10^{12} \left(q^{-7/4} R^3_{\rm NS,\ 10km} \right) \rm Gauss \tag{3.4.3}$$

where $q(< 1.0)$ is a factor that depends on the details of the interaction between the disc and magnetosphere (Ghosh and Lamb 1979) and $R_{\rm NS,\ 10km}$ is the NS radius in units of 10 km. For the lower limit we have:

$$B > 2.2 \times 10^{9} \left(q^{-7/4} R^3_{\rm NS,\ 10km} \right) \rm Gauss \tag{3.4.4}$$

This appears to suggest that the NS in this object is unlikely to be as strongly magnetised as some other PULXs (with $B > 10^{14}$ Gauss), as sometimes invoked to explain their large X-ray luminosities (e.g. Israel et al. 2017b).

Finally, we note that NGC 1313 X-2 is an archetype for the 'hard ultraluminous' X-ray spectral class for ULXs, in which the object is thought to be viewed directly down the wind-delimited funnel to its central engine (Sutton et al. 2013). This observational configuration is obviously well-suited to detecting pulsations as the emission of the central regions is visible and/or beamed into an observer's line of sight; notwithstanding the transient nature of the detected pulsations, or their faintness, the advanced age of NGC 1313 X-2 as a ULX offers some encouragement that observations with sufficient depth and baseline should detect pulsations from all those ULXs with a face-on aspect, if they contain NSs.

Chapter 4

A multi-wavelength view of different accretion regimes in the ultraluminous X-ray pulsar NGC 1313 X-2

4.1 Introduction

Dedicated X-ray monitoring campaigns on some ULXs have revealed that they show quasi-periodic variations in the X-ray flux on timescales larger than a few weeks (e.g. Grisé et al. 2013; Fürst et al. 2017; Walton et al. 2016). These variations seem to disappear over sufficiently long baselines and are hence difficult to interpret as the orbital period of the system. Recently, Weng and Feng (2018) have reported that at least four ULXs display a strong quasi-periodic modulation in the hard X-ray band, with little variability at energies below 1 keV. These ULXs also show a bimodal distribution on the hardness-intensity plane, with the brightest sources appearing to have a slightly harder spectrum. This is consistent with the proposition that long-term trends in the X-ray variability are driven by the precession of a super-critical accretion flow (Luangtip et al. 2016; **?**), rather than a genuine variation in the mass accretion rate.

One of the objects that demonstrates this behaviour is the archetypal ULX, NGC 1313 X-2 (Weng and Feng 2018). Being one of the best-studied ULXs in X-rays (e.g. Feng and Kaaret 2007; Gladstone et al. 2009; Bachetti et al. 2013), it has spectral behaviour in

common with some other bright ULXs that show hard ultraluminous spectra at moderate luminosities, which evolve to broadened disc spectra at peak luminosities (cf. Middleton et al. 2015c; Luangtip et al. 2016). The broadened disc regime appears very similar to the dominant spectra observed in the pulsating ULXs (PULXs) that host a neutron star (Walton et al., 2018b). Indeed, NGC 1313 X-2 is very notable for being a PULX, with the discovery of faint pulsations in the recent long *XMM-Newton* observations, as discussed in chapter 3. Its phenomenology is therefore of the utmost interest as we begin to observationally disentangle the mystery of the emission mechanisms in such objects.

NGC 1313 X-2 is also one of the best studied ULXs at optical wavebands. Mucciarelli et al. (2005) identified two potential optical counterparts to the X-ray source, although improved *HST* and *Chandra* astrometry have shown that only one of these is a plausible candidate. The true counterpart is known to be variable in the optical waveband, with short timescale ($\sim$ days) periodic modulations initially reported by Liu et al. (2007). They interpreted this as arising due to X-ray heating of the donor's surface. This can produce periodic variations in the observed intensity as the X-ray heated (more luminous) face of the star moves in and out of the observer's line-of-sight over a complete orbital cycle (provided the system is not viewed too close to face on; Motch et al. 2014). However, these periodic variations were absent in subsequent observations of X-2, perhaps having been masked out by a stronger contribution from the accretion disc, which is expected to vary stochastically (Grisé et al. 2008). Further spectroscopic monitoring of the ULX counterpart with Gemini-South revealed a broad and variable He II λ4686 emission line. The variations in its central wavelength were found to be non-periodic, thus unlikely to be associated with the orbital motion of the donor (Roberts et al. 2011). Instead, the variability is stochastic, suggesting an origin in the reprocessing of X-rays in the outer accretion disc or a radiatively accelerated outflow (Grisé et al. 2008; Fabrika et al. 2015). Previous works analysing the broadband spectral energy distributions (SEDs) of ULXs have been unable to distinguish unambiguously between an irradiated disc and donor star models (e.g. Grisé et al. 2012). However, quasi-simultaneous X-ray and optical monitoring of X-2 showed that its B-band magnitude displays larger amplitude variability during periods of high X-ray flux levels (Grisé et al. 2008), giving some credence to irradiation scenarios. Studying correlated changes between the X-ray and optical emission could therefore be the key to breaking the degeneracy in the emission mechanisms associated

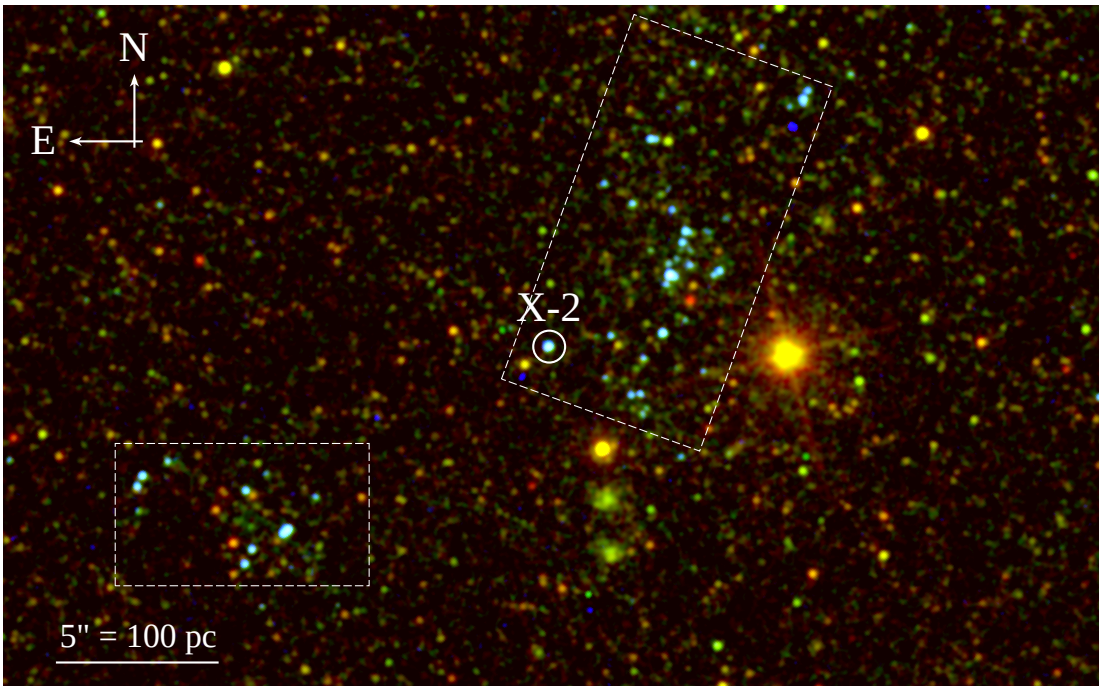

Figure 4.1: An *HST*/WFC3 composite image of the field containing the ULX NGC 1313 X-2 (whose position is marked by a circle of radius 0.5 arcseconds). Red, green and blue colours represent intensities in the F814W, F555W and F225W filters, respectively. The dashed boxes highlight the approximate location of two OB associations in the vicinity of the ULX. The image has been smoothed with a Gaussian kernel with σ = 1.5 pixels (≈0.06 arcseconds).

with the optical counterpart. They could also provide further insight into the physical process(es) driving the transition between the bimodal hardness-intensity regimes in X-2 and by extension other ULXs showing similar behaviour.

In order to investigate this problem further, we obtained simultaneous *XMM-Newton* and *HST* observations of NGC 1313 X-2. We describe the data reduction procedure in Section 2, before presenting the X-ray and optical results and modelling of the X-ray-to-optical Spectral Energy Distributions (SEDs) in Section 3. We discuss these results in Section 4 before concluding the paper in Section 5.

4.2 Data reduction

In *XMM-Newton* programme 076477 (PI: Grisé) we obtained observations of NGC 1313 X-2 in two distinct phases of its behaviour (see Section 3). This provided simultaneous X-ray spectroscopy of the ULX from the *XMM-Newton* EPIC cameras and photometry of the optical counterpart in several bands (ranging from the near-IR to near-UV) from the *HST* WFC3 and ACS cameras.

4.2.1 XMM-Newton X-ray observations

The *XMM-Newton* observations were carried out with the EPIC-pn and MOS detectors in full-frame imaging mode, and were reduced using the Science Analysis Software (SAS)v.16.[1] We summarise the essential features of these observations in Table 4.1. After examining the radial profile to confirm there were no extended components to the point spread function, we extracted source events within an aperture of 30 arcseconds centred on the *Chandra* source position (RA = 49.592, DEC = -66.601; Zampieri et al. 2004). The background region was chosen to lie adjacent to the source on the same chip. Care was taken to avoid areas with a large internal quiescent background in the EPIC-pn detector, which is primarily traced by the intensity of the Copper-Kα emission line (at $\sim$ 8 keV). We excluded events associated with bad pixels by implementing the standard flagging criteria (`FLAG==0`) and grade selection (`PATTERN` $\leq$ 12 for MOS and `PATTERN` $\leq$ 4 for PN). We extracted light curves in the 10 - 12 keV energy band using the `evselect` task from chips devoid of a large number of point sources, in order to inspect and remove periods of intense soft proton flares. We ran the SAS task `bkgoptrate` to determine a safe count rate threshold below which the background level remains steady. As such, periods during which the count rates exceeded this threshold (in the 10 - 12 keV band) were excluded; this resulted in a loss of up to $\sim$ 46% of the original exposure for the pn camera in the March 24 observation, with other losses being smaller. Finally, using the cleaned event files we extracted the source and background spectra in the 0.3 - 10.0 keV energy range for each instrument. The spectra were grouped into a minimum of 25 background subtracted

[1] https://www.cosmos.esa.int/web/xmm-newton/xsa

Table 4.1: A log of the *XMM-Newton* X-ray observations.

Dataset (Obs. ID)	Start date (dd-mm-yy)	GTI-corrected exposure (pn/MOS1/MOS2, in ks)	Combined EPIC count-rate (s^{-1})
0764770101	05-12-15	50.1/68.7/68.4	0.247 ± 0.002
0764770401	24-03-16	16.4/21.5/21.0	0.422 ± 0.005

counts per energy bin (yielding a signal-to-noise > 5), ensuring not to oversample the intrinsic detector resolution by a factor larger than 3. Hence, it was acceptable to use χ^2 statistics to characterise the goodness-of-fit. Finally, in order to deconvolve the energy spectrum through the detector response, we generated the auxillary response files and redistribution matrix files using the `arfgen` and `rmfgen` tasks respectively.

4.2.2 HST optical and UV observations

The field containing the counterpart to the ULX was observed during two separate HST visits with the WFC3 and ACS detectors in seven independent filters. We summarise the details of these observations in Table 4.2. We first ran the `calwf3` pipeline (version 3.3[2]) on the raw event files of all WFC3 observations using the latest calibration files available in the STScI website[3]. The pipeline produces event files that have been bias subtracted, flat fielded and corrected for the effect of charge transfer inefficiency (CTI). We ensured that all sub-exposures were aligned to within 0.1" accuracy (using the `drizzlepac` tool `TweakReg`v1.4). This is especially important for the near-infrared (NIR) image, in which the ULX counterpart resides in a crowded environment, such that any misalignments between individual sub-exposures could compromise the photometric accuracy. We then implemented the PSF-fitting technique to derive instrumental magnitudes for the ULX counterpart in all six WFC3 filters using the `DOLPHOT`v1.2 software (Dolphin 2000). This method identifies point sources above a preset detection threshold from a stack of flat-fielded and cosmic-ray cleaned images. It then uses the `TinyTim` PSF models (Krist 1995; Hook et al. 2008) to simultaneously fit the PSF of each source and the local background.

[2]https://hst-crds.stsci.edu/

[3]The equivalent pipeline `calacs` was used to reduce the ACS data

Table 4.2: *HST* optical, UV and IR magnitudes of the ULX counterpart.

Start date (dd-mm-yy)	Instrument	Filter[a]	Exposure time (s)	Aperture corrected magnitude[bc] (Vega mag)	Aperture correction[c] (Vega mag)
05-12-15	ACS/SBC	F140LP	1200.0	20.56 ± 0.07	0.2
	WFC/UVIS	F225W	1440.0	21.34 ± 0.05	0.25 ± 0.04
	WFC/UVIS	F336W	1017.0	21.93 ± 0.08	0.24 ± 0.07
	WFC/UVIS	F438W	1050.0	23.35 ± 0.06	0.26 ± 0.05
	WFC/UVIS	F555W	1170.0	23.41 ± 0.05	0.69 ± 0.05
	WFC/UVIS	F814W	1740.0	23.46 ± 0.06	0.34 ± 0.06
	WFC/IR	F125W	1796.9	23.30 ± 0.08	0.41 ± 0.08
24-03-16	ACS/SBC	F140LP	1200.0	20.65 ± 0.07	0.2
	WFC/UVIS	F225W	1440.0	21.25 ± 0.05	0.18 ± 0.04
	WFC/UVIS	F336W	1017.0	21.90 ± 0.05	0.18 ± 0.04
	WFC/UVIS	F438W	1050.0	23.43 ± 0.05	0.19 ± 0.05
	WFC/UVIS	F555W	1170.0	23.50 ± 0.04	0.20 ± 0.04
	WFC/UVIS	F814W	1740.0	23.57 ± 0.05	0.29 ± 0.05
	WFC/IR	F125W	1796.9	23.63 ± 0.08	0.49 ± 0.08

Notes: [a] W and LP refer to wide-band and long-pass filters respectively; [b] The uncertainties on the magnitudes are weighted by the errors on the aperture correction [c] These magnitudes have not been corrected for extinction

This approach is preferred over aperture photometry in scenarios where the crowding is severe (e.g. in the near infra-red waveband), which causes the PSFs of closely spaced point sources to overlap. The software performs all the necessary pre-processing steps prior to running the photometry routine (including the masking of bad pixels affected by cosmic rays and image combination). The instrumental magnitudes were initially measured using a circular aperture of 3 pixel radius, and converted to an equivalent 10 pixel (or 0.4") magnitude by applying aperture corrections. To do this, we selected relatively bright and well isolated stars in the field-of-view, with signal-to-noise ratios larger than the ULX counterpart. The vertical axis intercept of a linear fit to the 3 pixel versus 10 pixel magnitude of the selected objects yields the aperture correction δ. Here, we emphasise that a fitting function accounting for uncertainties in both the independent and dependent variables (equivalent to the `fit_exy` routine in IDL; see also Press et al. 1992) was used to ensure that the errors in δ are not underestimated.

The initial reduction steps were similar for the ACS/SBC data. We used the few bright and well resolved stars in the field of view to align the drizzled SBC image with the F225W and F336W filters, to confirm that the brightest object in the F140LP image is the ULX counterpart. However, we were unable to perform PSF fitting on the ACS/SBC data due to the lack of both a model ACS/SBC PSF in `DOLPHOT`, and of a sufficient number of well resolved stars in the field of view. Hence aperture photometry was used within an aperture of radius 0.4 arcseconds (equivalent to the 80% encircled energy for ACS/SBC). We were also hampered by the lack of bright resolved stars in calculating an aperture correction, hence we resorted to using that provided by the instrument manual [4]. The results of the photometry are quoted in Table 4.2, and we show a cleaned, 3-colour image of the field that highlights the position of the ULX counterpart in Figure 4.1.

4.3 Spectral analysis

NGC 1313 X-2 was regularly monitored by the Neil Gehrels *Swift* Observatory over a baseline of several years. This has allowed us to construct its long-term X-ray lightcurve (see Figure 4.2), which suggests a bimodality in the flux distribution

[4] http://www.stsci.edu/hst/acs/documents/isrs/isr1605.pdf

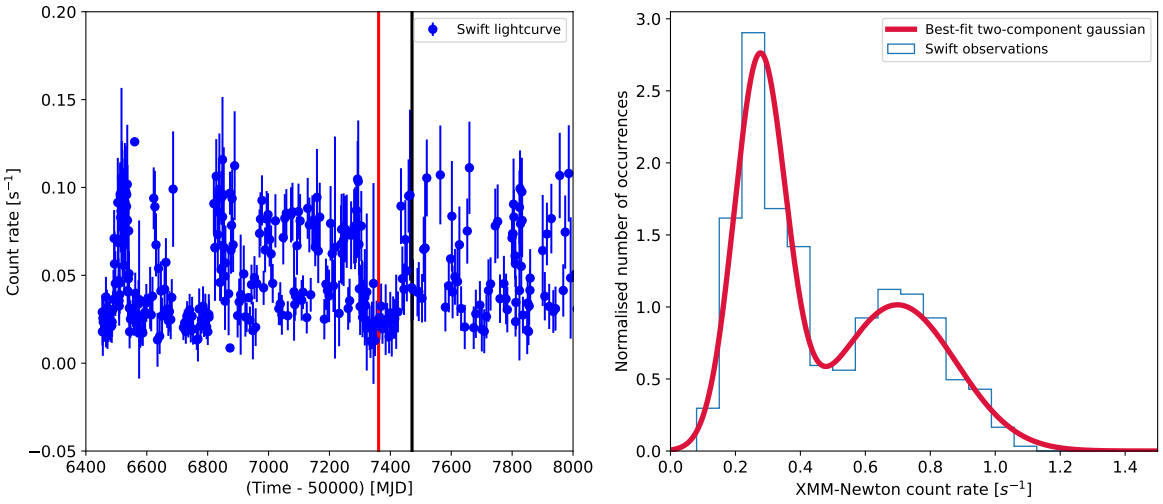

Figure 4.2: *Left*: The long-term *Swift* light-curve of X-2, with the vertical axis plotting the 0.3-10 keV count rate. The source appears to switch between periods of two distinct behaviours on timescales of several weeks, a relatively low flux and stable regime, and a higher mean flux regime with much more variability. The red and black solid lines indicate the two epochs when *XMM-Newton* and *HST* observations were triggered and taken simultaneously. *Right*: An illustration of the bi-modality in the source X-ray flux across the entire *Swift* monitoring period of X-2. The horizontal axis specifies the count rate scaled to the *XMM-Newton* EPIC detectors combined.

(see also Weng and Feng 2018). The data allows us to define two distinct behaviour regimes: in the first the ULX has a relatively low count rate and the source displays very limited variability on timescales of ∼ days. In the second the source shows much higher amplitude variability over a range of timescales from ∼ hours to days, while its mean flux level also increases. In the second of these regimes, there is marginal evidence for a change in the hardness ratio when the ULX is at its brightest (see Figure 6 of Weng and Feng 2018), which becomes more prominent when the count rates are corrected for absorption.

One set of our observations was taken in each of these behaviour regimes. Our first observation was taken when the source count rate was relatively low and stable (red solid line in Figure 4.2); we then followed up with our second set of observations when the source had begun to show more variable behaviour, with a higher mean count rate (black solid line in Figure 4.2).

4.3.1 X-ray characterisation

We began by fitting the *XMM-Newton* spectra of both observations separately. In order to obtain an understanding of the spectral shape in each observation, and any changes between observations, we fitted the data with a simple two-component model used previously to characterise ULX spectra, comprising an absorbed multicolour disc (`diskbb`; see for e.g. Mitsuda et al. 1984; Makishima et al. 1986) plus power-law in `xspec`. X-ray absorption was modelled using two instances of the Tuebingen-Boulder ISM component (`tbabs`; Wilms et al. 2000). We fixed the first component to the Galactic extinction value in the direction of the source (3.97×10^{20} cm^2) using the `heasarc` tool N_H[5], and allowed the second to vary. We added cross normalisation factors to account for any differences in calibration between the EPIC and MOS detectors, but these were found to be consistent to within 5 percent. The model provides a good fit to the data as indicated in Table 4.3. As can be seen in Figure 4.3 the ratios of the power-law and disc fluxes, in addition to the disc temperatures, suggest that the source spectrum changes from being in the hard ultraluminous regime (in the first observation) to a broadened disc spectrum

[5]https://heasarc.gsfc.nasa.gov/cgi-bin/Tools/w3nh/w3nh.pl

Table 4.3: The best-fit parameters of the two component power-law plus multi-colour disc model, fitted to the two *XMM-Newton* spectra of X-2.

Date	$n_{\rm H}^{\rm a}$	$kT_{\rm in}^{\rm b}$	$\Gamma_{\rm pl}^{\rm c}$	$\log_{10} L_{\rm disc}^{\rm d}$	$\log_{10} L_{\rm power}^{\rm e}$	Spectral regime	χ^2/Dof$^{\rm f}$
[dd-mm-yy]	[10^{22} cm^{-2}]	[keV]		[erg s^{-1}]	[erg s^{-1}]		
05-12-15	0.18 ± 0.02	0.28 ± 0.01	1.7 ± 0.4	39.20 ± 0.01	39.69 ± 0.01	HUL	282.1/311
24-03-16	0.14 ± 0.01	0.73 ± 0.04	$1.7^{+0.1}_{-0.2}$	39.51 ± 0.02	39.86 ± 0.01	Broadened disc	235.4/212

Notes: [a] Hydrogen column density (see text); [b] Inner disc temperature; [c] Photon index; [d] Disc component luminosity (0.3 - 10.0 keV); [e] Power-law component luminosity (0.3 - 10.0 keV); [f] Reduced χ^2 of the fit

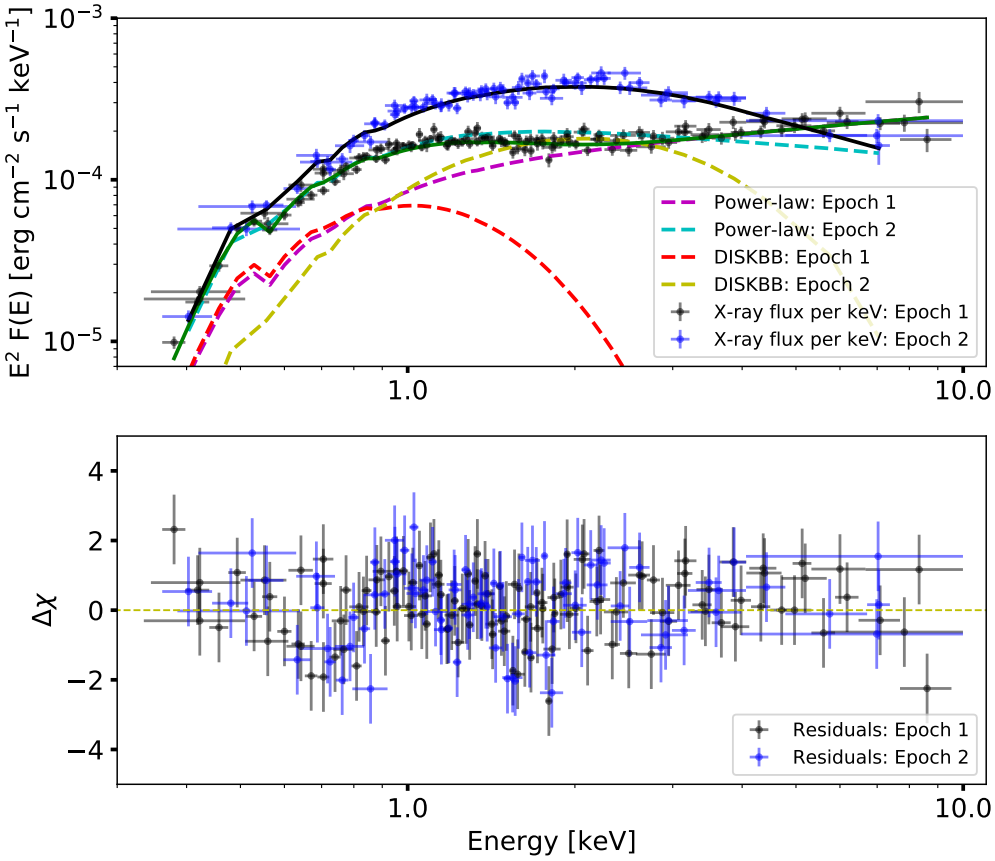

Figure 4.3: The *XMM-Newton* X-ray spectra of X-2 with the observed data on December 2015 (black points) and March 2016 (blue points). The best-fitting multi-colour disc and power-law model to each spectrum are overlaid, with the legend specifying the label to each component. The residuals are shown in the bottom panel, indicating a good fit to the data. The spectral shape changes between the observations

(see Sutton, Roberts, and Middleton, 2013). Critically, this change in spectrum supports the notion that the ULX is changing between the low, stable flux behaviour in December 2015 and the higher flux, more variable periods in March 2016.

As an aside, we note that the (0.3 - 1) keV flux of the power-law component can be influenced by the degeneracy between the photon index and the hydrogen column density. To avoid this, we constrained $N_{\rm H}$ separately by fitting the two X-ray spectra above with a multi-colour blackbody and a thermal comptonisation model (`comptt`; Titarchuk 1994). The latter is not unphysically extrapolated to energies below that of the seed disc photons and thus does not influence the best-fit value of $N_{\rm H}$ as much as the power-law component. Then, when modelling the X-ray spectra with the previous multi-colour blackbody plus power-law component (in order to classify them as per Sutton, Roberts & Middleton 2013), the hydrogen column density was fixed to the values obtained from fitting the same spectra with `diskbb` plus `comptt`.

In the remainder of this work, we will investigate how the observed variability in the X-ray spectra affects the multi-wavelength properties of the system, and and whether this sheds any insights on the physical cause of the spectral variability. For the sake of convenience we will hereafter refer to the December 2015 observations as epoch 1, and March 2016 observations as epoch 2.

4.3.2 Does the optical emission vary?

In Section 3.1 we demonstrated that the X-ray emission varies between epoch 1 and epoch 2. The *HST* data were obtained simultaneously in two different epochs specifically to test how the UV/optical/IR colours change with the X-ray emission. We present the observed fluxes in each filter at each epoch (converted from the magnitudes given in Table 4.2) in Table 4.4, alongside the ratio of the fluxes. We also present the X-ray flux separated into three bands; this again demonstrates the variability of the X-ray emission, with the largest variations occurring at medium X-ray energies (1-4 keV).

There appears to be no statistically significant variation exceeding the 3σ error range between the epochs in the UV bands. However, there is some evidence for variability at longer wavelengths, with amplitude increasing with wavelength. This appears strongest in the NIR bands, with the F125W band in particular showing a drop of about 25%

Table 4.4: UV/optical/IR (*HST*) and X-ray (*XMM-Newton*) fluxes of X-2 as measured in December 2015 and March 2016.

HST fluxes			
Pivot wavelength [Angstrom]	Source flux (epoch low) [10^{-18} erg s^{-1} cm^{-2} Å^{-1}]	Source flux (epoch high) [10^{-18} erg s^{-1} cm^{-2} Å^{-1}]	Ratio[a]
1528.0	38.0 ± 2.0	35.0 ± 2.0	0.92 ± 0.07
2375.0	12.0 ± 1.0	13.3 ± 0.6	1.1 ± 0.1
3356.0	5.5 ± 0.4	5.6 ± 0.2	1.0 ± 0.1
4327.0	3.1 ± 0.2	2.8 ± 0.1	0.9 ± 0.1
5307.0	1.7 ± 0.1	1.57 ± 0.04	0.92 ± 0.06
8048.0	0.47 ± 0.02	0.42 ± 0.02	0.89 ± 0.06
12486.0	0.15 ± 0.01	0.11 ± 0.01	0.73 ± 0.08
XMM-Newton fluxes			
X-ray energy range [keV]	Source flux (epoch low) [10^{-13} erg s^{-1} cm^{-2} Å^{-1}]	Source flux (epoch high) [10^{-13} erg s^{-1} cm^{-2} Å^{-1}]	Ratio[a]
0.3 - 1.0	3.8 ± 0.1	4.0 ± 0.1	1.05 ± 0.04
1.0 - 4.0	4.2 ± 0.1	8.1 ± 0.2	1.90 ± 0.1
4.0 - 10.0	3.1 ± 0.1	2.4 ± 0.1	0.77 ± 0.04

Notes: [a] Ratio of source flux between the two epochs

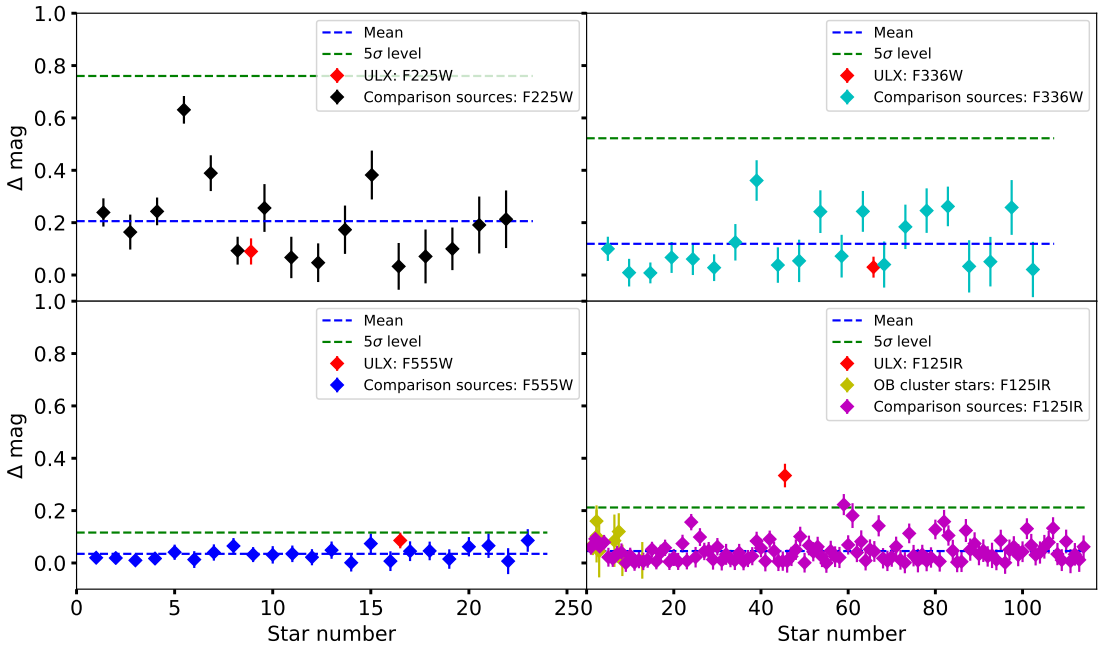

Figure 4.4: The observed change in the UV/optical/NIR magnitudes (Δ mag) of the ULX counterpart, selected comparison sources and stars belonging to the OB association, between December 2015 and March 2016. The particular *HST* filter in each case is indicated by the legend. The mean Δ mag of all the reference sources (dashed blue) and the corresponding 5σ scatter (dashed green) are also shown. The level of variability of the ULX is clearly consistent with most invariant stars in the field of view for all except the NIR waveband.

(0.33 ± 0.04 mags) in its flux as the X-ray emission increases from epoch 1 to epoch 2. To validate this result we carefully cross-matched relatively bright and well-isolated sources in both observations in the WFC/IR filter images, and in three other filters. We rejected objects that were too saturated, or those with too many bad pixels (due to cosmic ray hits), by applying a flag threshold within `dolphot`. Aside from the ULX, our final selection included a number of stars belonging to the OB association, which should be intrinsically invariant on monthly timescales[6]. In any case, the bottom right panel of Figure 4.4 shows that the ULX counterpart has the largest NIR variability (defined as Δ mag) among all the reference sources; its Δ mag value is clearly an outlier, easily exceeding the 5σ level (where σ is the standard deviation in Δ mag of all the comparison sources). This marks the first detection of NIR variability from this object, which had only been observed at UV/optical wavelengths prior to this work. We will elaborate on the possible origin of the NIR emission in the discussion.

4.3.3 Optical colours & stellar models

Given that the optical emission appears to be relatively invariant between the two epochs, we examine whether the UV/optical/IR emission of the source is consistent with arising solely from the donor star. The ULX counterpart is thought to be associated with a young OB star cluster in its vicinity, since it has a similarly large UV/optical luminosity and a distinctly blue colour, as per other members of the cluster (cf. Figure 4.1). By fitting stellar isochrones to the colour magnitude diagrams (CMDs) of its member stars, Grisé et al. (2008) inferred the cluster age to be 20 ± 5 Myrs, implying that the mass of the ULX donor is $< 16 M_{\odot}$. Given this constraint on the counterpart, in addition to its absolute visual magnitude ($M_{\rm V} \sim -5$) and colour index ($B - V \sim -0.25$), a range of possible OB spectral types were suggested. Here, we attempt to refine these constraints by re-fitting the *HST* magnitudes (see Table 4.2) with a grid of O/B type stellar templates from Castelli and Kurucz (2003). The temperature of individual spectral types were

[6] Although we note that B stars are sometimes surrounded by circumstellar excretion discs due to their fast rotation, which can enhance variability in the infrared.

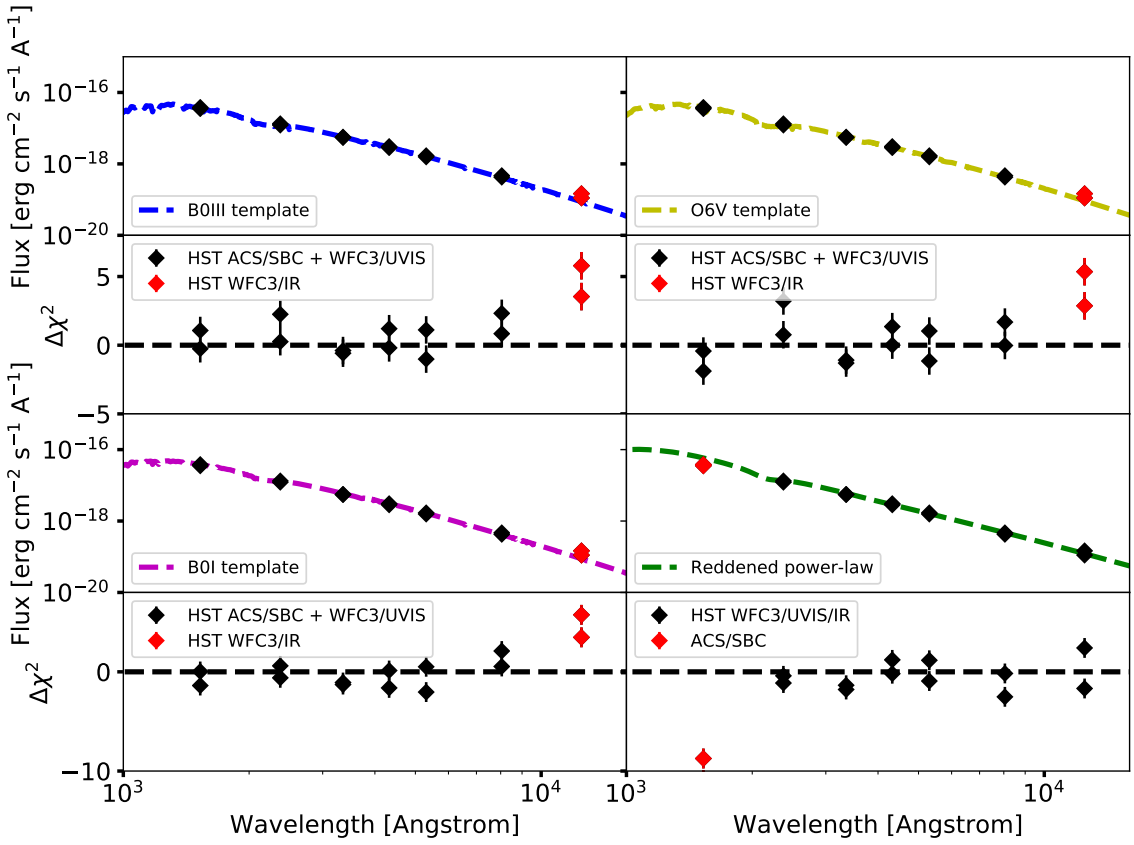

Figure 4.5: A collection of O/B stellar templates and a reddened power-law model fit (dashed lines) to the UV/optical/NIR photometry (black diamonds) of the ULX. In all cases, the data points discrepant with respect to the best-fitting model are highlighted by the red diamond. A slight NIR excess is seen in all the stellar fits, whereas the reddened power-law model over-predicts the far UV emission.

Table 4.5: A collection of stellar templates and a reddened power-law model fit to the UV/optical/NIR spectrum of X-2.

Model	E(B-V)[a]	T_{eff} [b] [K]	log g[c]	R_* [d] [$R_\odot$]	log Z[e]	Γ [f]	power-law norm[g] [1×10^{-8}]	χ^2/dof
B0III[h]	0.14 ± 0.01	29000†	3.5†	12.4 ± 0.3	-0.5	-	-	14.5/9.0
O6V[h]	0.19 ± 0.01	38867†	4.0†	10.5 ± 0.2	0.5	-	-	24.6/9.0
B0Ia[h]	0.11 ± 0.01	26000†	3.0†	13.4 ± 0.3	-1.5	-	-	13.9/9.0
Power-law[i]	0.12 ± 0.04	-	-	-	-	3.3 ± 0.2	5.0 ± 0.8	11.3/9.0

Notes: [a] Dust reddening; [b] Effective temperature (from Martins, Scharer & Hiller 2005); [c] Surface gravity (from Martins, Scharer & Hiller 2005); [d] Stellar radius; [e] Metallicity (these are values are for the best fitting model from a grid of five trial metallicities per stellar type); [f] Exponent of power-law fit; [g] Power-law normalisation; [h] Obtained with the NIR data points excluded; [i] Obtained with the FUV data points excluded; † Parameter fixed.

adopted from Martins, Schaerer, and Hillier (2005)[7] and Straizys and Kuriliene (1981)[8]. The normalisation of each template depends on the stellar radius and the source distance, where we allowed the former to vary and fixed the latter to a value of 4.0 Mpc (based on a weighted average of the distances to NGC 1313 in the SIMBAD database [9]). We included two additional free parameters, namely the metallic abundance and interstellar reddening (using the Cardelli et al. 1989 extinction curve). We fit the data from both epochs simultaneously given that we have seen little or no change in the flux between epochs in most bands.

The best fitting stellar templates are shown in Figure 4.5, and the fits are summarised in Table 4.5. A B0III giant provides the most reasonable fit (i.e. $\chi^2 = 14.5$ for 9 degrees of freedom), but only if the NIR data points are excluded, with the fit otherwise worsening by $\Delta\chi^2 = 20$ for 2 degrees of freedom. A B0Ia supergiant may have a better reduced χ^2, but the best-fit stellar radius is at least a factor of 2.5 smaller than expected for a star of this type (Straizys and Kuriliene 1981). A main-sequence O6V star can provide a reasonable fit, but it is a worse fit to the data than B-star models with $\chi^2 = 24.9$ for 9 degrees of freedom.

We also attempted a reddened power-law model as a fit to the data. It strongly over-predicts the far UV flux, but provides an acceptable fit at larger wavelengths, with the slope being consistent with the B0III stellar type below 10000 angstroms. This is intriguing for interpreting the optical emission, as reprocessed emission will have a power-law-like spectrum at optical wavelengths. Hence it is clear from the optical data alone we cannot unambiguously identify the physical origin of the counterpart's emission.

4.3.4 Irradiation of the outer accretion disc

Using *VLT* observations, Grisé et al. (2008) reported that the optical counterpart to the ULX shows significant variability in the B-band (by ~ 0.2 mag) on timescales ranging from several hours to days, with respect to other invariant stars in the field. These timescales are much faster than that at which the mass accretion rate varies at the outer disc, which

[7] for O-type stars

[8] for all other spectral types

[9] http://simbad.u-strasbg.fr/simbad/

occurs on the viscous timescale:

$$\tau_{\rm visc} = \alpha^{-1}\Big(\frac{H}{R}\Big)^{-2} t_{\rm dyn}, \tag{4.3.1}$$

where α is the viscosity coefficient, H is the disc scale-height at radius R and $t_{\rm dyn}$ is the Keplerian dynamical timescale. We can crudely estimate that $\tau_{\rm visc}$ is of order several hundred years assuming $\alpha \sim H/R \sim 0.1$ for a geometrically thin outer disc, whose size is determined by the orbital period of the system containing a neutron star accretor (which we assume is ~ 2 days; Sathyaprakash et al. 2019). The latter is not tightly constrained, but even if it is taken to be two orders of magnitude smaller, $\tau_{\rm visc}$ remains much larger than the B-band flickering timescale. Variation of the outer disc itself cannot therefore explain the previous reports of optical variability.

A possible alternative is to explain this is via a disc reprocessing model: variable X-rays from the inner accretion flow can illuminate the outermost regions of the disc (Gierliński, Done, and Page 2009), where a fraction of the incident X-rays are absorbed and heat the underlying disc material. The highest energy photons penetrate deeper into the disc atmosphere and can thermalise with the surrounding material, re-emerging with a blackbody continuum peaking in the UV/optical band (depending on the local temperature). In this scenario, the longer wavelength emission should vary coherently with the inner X-ray emission across a broad range of timescales, although the variability will be suppressed on the shortest timescales due to a finite propagation time between the two regions. In particular, it will be limited by the light travel time in the simple picture of X-rays directly illuminating a geometrically thin outer disc. If the disc is tidally truncated with an outer radius $R_{\rm out}$ of ~ 0.7 times the orbital separation, the light travel time is $\lesssim$ a minute (for the orbital period estimate used above). Thus, one might expect changes in the UV/optical and X-ray fluxes to be correlated over the much longer three month (inter-observational) timescale. However, a comparison of the fluxes in the two separate bands demonstrates no evidence for such a correlation. The broadband 0.3-10.0 keV flux increases by $\sim 30\%$ between the two observations, while the UV/optical fluxes are mostly consistent between the two epochs and only change significantly (and in the opposite sense) for the longest wavelength filters (see Table 4.4 and Figure 4.4). This presents a strong argument against any correlated X-ray-to-optical long-term variability in the system, at least between the two epochs at which our new observations were taken. Nevertheless

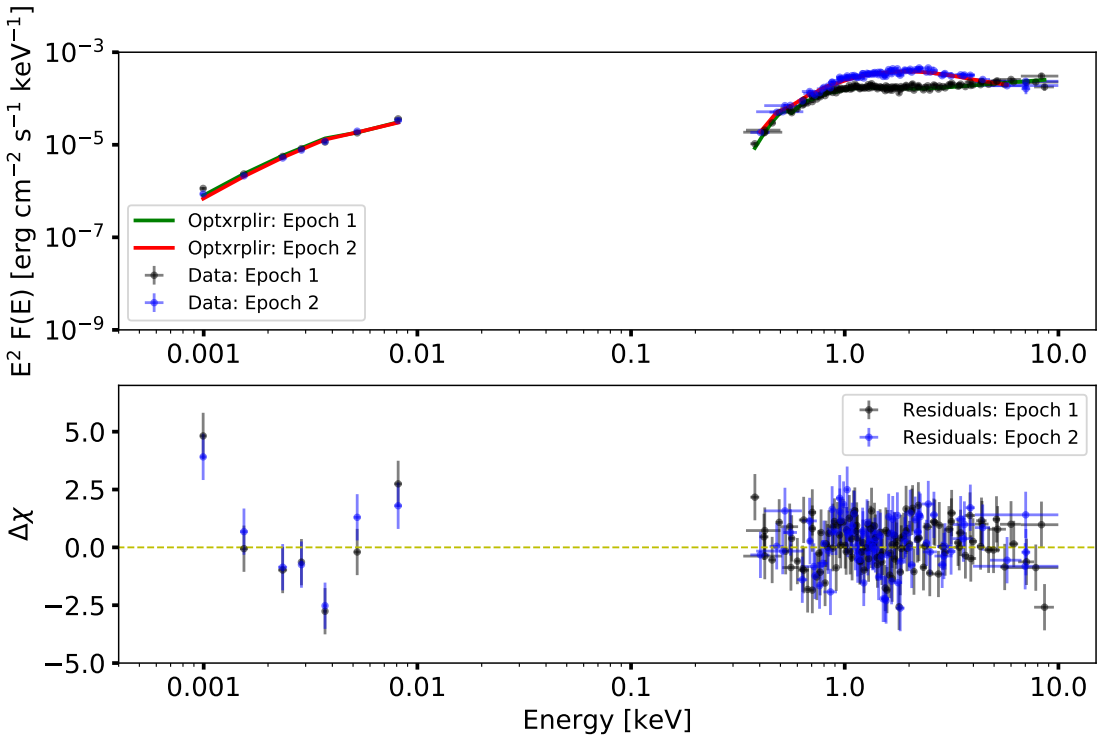

Figure 4.6: The X-ray to optical SED of NGC 1313 X-2 taken during epoch 1 (black dots) and epoch 2 (blue dots). The broadband (0.3-10.0 keV) X-ray flux is seen to vary by ∼ 30% between the two epochs, but there is no evidence for corresponding UV/optical variability. The best-fitting (absorbed) models are indicated by the legend. The bottom panel shows the residuals to the best-fitting models.

given the previous evidence we cannot rule out X-ray reprocessing as a contributor to the optical emission, and so seek to constrain its presence using further techniques.

4.3.4.1 X-ray irradiation model

Previous work by Sutton et al. (2014) constrained the fraction of photons emitted in the inner accretion flow that were reprocessed in its outer regions for a small number of ULXs with broadened disc spectra, including NGC 1313 X-2. For this they used standard disc irradiation models developed for sub-Eddington accretors, on the basis that they disregarded the details of the X-ray part of the joint X-ray to optical fits as unphysical; but could trust the calculated reprocessed fractions as a reliable output of the model, given the energy distribution of the irradiating X-rays was broadly correct. We take a

Table 4.6: The best-fitting parameters of the irradiated disc model for both epochs.

Epoch	$N_{\rm H}$[a]	E(B-V)[b]	$\log_{10}\frac{L}{L_{\rm Edd}}$[c]	$f_{\rm out}$[d]	$R_{\rm cor}$[e]	Γ[f]	Mass[g]	$\log R_{\rm out}$[h]	χ^2/Dof[i]
	[10^{22} cm^{-2}]	(vega mag)			[$R_{\rm g}$]		[$M_\odot$]	[$R_{\rm g}$]	
1	0.18 ± 0.02	0.15 ± 0.02	$-0.03^{+0.2}_{-0.1}$	> 0.87	72^{+11}_{-7}	1.7 ± 0.1	49^{+8}_{-12}	5.3 ±0.1	573.3/522
2	0.14 ± 0.02	0.12 ± 0.02	$-0.2^{+0.25}_{-0.1}$	> 0.86	20^{+9}_{-3}	$2.5^{+0.3}_{-0.5}$			

Notes: [a] Hydrogen column density; [b] Dust reddening; [c] Eddington ratio; [d] Reprocessed fraction; [e] Coronal radius; [f] Photon index; [g] Calculated compact object mass (which is known to be incorrect as this ULX contains a neutron star); [h] Outer disc radius (NB – the compact object mass and outer disc radius were held constant for both fits; other parameters were left free to fit individual spectra) ; [i] Reduced chi-squared for the simultaneous fit of both SEDs

similar tack here.

We adopted a state-of-the-art irradiated disc model (`optxrplir`; Shidatsu et al. 2016), which assumes that the gravitational power released by the accretion flow is dissipated via the standard Novikov-Thorne emissivity, giving rise to two distinct spectral components. This includes thermal emission from an optically thick accretion disc and a warm comptonisation component emitted by a cool, optically thick corona comprising a thermal population of electrons with optical depth τ and temperature $kT_{\rm es}$. These components are thought to be emitted in two distinct regions of the accretion flow, with the size of the corona denoted by $R_{\rm cor}$. We neglected the contribution from the third component, corresponding to hot comptonised emission from an optically thin corona (characterised by photon index $\Gamma_{\rm pl}$ and electron temperature $kT_{\rm eh}$), since it is expected to be dominant far above the energy band probed by *XMM-Newton*. All these X-ray spectral components illuminate the outer disc, producing reprocessed emission in the UV/optical band. The strength of the irradiation $f_{\rm out}$ depends on the scale-height of the outer disc and its albedo. The former is influenced by the shape of the incident X-ray spectrum, which is self consistently accounted for by the model. We note that the reprocessed fraction is defined differently in previous irradiated disc models as compared to `optxrplir`, which separates it into a geometry dependent factor $f_{\rm out}$ and the albedo α: i.e. $f_{\rm out,\ old} = f_{\rm out,\ new}(1-\alpha)$. Furthermore, the shape of the reprocessed emission depends on the outer disc radius $R_{\rm out}$; a larger $R_{\rm out}$ allows the emission to thermalise over a larger area, thus decreasing the outer disc temperature and increasing the luminosity at longer wavelengths.

Additional parameters of the model include a black hole mass $M_{\rm BH}$ and spin a^*, the Eddington ratio $\dot{m}_{\rm Edd}$ and the distance to the object $d_{\rm Mpc}$. Obviously as NGC 1313 X-2 is a neutron star and not a black hole we immediately have at least a semantic issue in using this model to describe the physical reality of the system. More critically, the model cannot provide realistic solutions for the accretor mass and spin once the Eddington limit is locally exceeded in the accretion disc, as the Novikov-Thorne emissivity requires modification. Hence the values of these parameters (and the linked Eddington ratio) are largely physically irrelevant for these fits of NGC 1313 X-2. We fixed the black hole mass and spin values to be constant between observations, but otherwise simply allowed the parameters to find values that allow us to trace the X-ray spectrum as accurately as possible, as this affects $f_{\rm out}$, but do not comment further on their best-fitting values.

We fixed the electron temperature and optical depth of the warm comptonisation component to arbitrary values ($kT_{\rm es}$ = 0.2 keV and τ = 10 respectively, consistent with previous observations of ULXs cf. Gladstone et al. 2009), since these could not be constrained with the current quality of data. However, we note that varying these parameters even over a range of three dex does not have a noticeable effect on the spectral fit. The albedo was set to 0.9 assuming a highly ionised outer disc (see Kimura and Done 2019; Gierliński, Done, and Page 2009). We treated dust extinction in the same manner as in section 4.3.3, but adopted `phabs` to model the gas phase absorption intrinsic to the source. The model normalisation is determined from $M_{\rm BH}$, $\dot{m}_{\rm Edd}$ and the inclination angle i, where the latter was set to a moderately face-on view of 30 degrees (given the detection of pulsations and the X-ray spectrum of X-2). Finally, we adopted a distance of 4.0 ± 0.8 Mpc towards the galaxy NGC 1313 and allowed the remaining parameters to vary between both observations.

We fitted this model to the X-ray to optical Spectral Energy Distributions (SEDs) of both epochs. The fits were performed simultaneously with some parameters held to the same value at each epoch. We detail the best fitting parameters in Table 4.6 and show the data and best-fitting model in Figure 4.6. This model is formally an acceptable fit to the data, as it cannot be rejected above a significance of 2σ. However, the fit is obviously statistically dominated by the X-ray data (which itself shows some residuals, consistent with features described by Middleton et al. 2015b and thought to be linked with absorption in an outflowing wind), and the shape of the optical spectrum is not well described as possible excesses are clear in both the IR and UV wings of the spectrum.

The inferred reprocessed fractions are unphysically large (i.e. close to unity), clearly inconsistent with the fact that both the donor star and the outer disc only cover a small fraction of the sky. They are also comparatively much larger than found previously for this object (and several other ULXs) by Sutton et al. (2014). This is initially surprising, since neither the ULX optical fluxes nor the X-ray spectral shapes greatly differ between the two studies. However, the reprocessed fraction depends on the choice of the albedo α (i.e. thermalisation fraction) of the outer disc, among other things (see below). In the version of the irradiated disc model used by Sutton et al. (2014), both α and $f_{\rm out}$ are combined into a single free parameter, while here the former is fixed to a desired value. In principle, re-fitting the SED with a smaller albedo (0.3) yields a best-fit $f_{\rm out}$ that is more

consistent with Sutton et al. (2014). However, this is disfavoured on physical grounds since an albedo close to unity is expected due to a highly ionised outer disc resulting from X-ray irradiation (van Paradijs and McClintock 1994; Gierliński, Done, and Page 2009).

It is difficult to pinpoint a single reason for the resulting large reprocessed fractions, since this depends on several factors. However, we try to outline a few points that could explain such an occurrence. One critical reason is linked to the negligence of advection and mass loss by the irradiated disc model, which are important when the accretion rate is larger than Eddington (see next section). The model uses an emissivity applicable to a sub-Eddington geometrically thin disc, for which the luminosity at each radius scales linearly with the mass accretion rate ($L = \eta \dot{M} c^2$). For an advection dominated slim disc, this only applies to the outermost UV/optically emitting regions where advection is not important. The luminosity of the inner X-ray emitting region saturates when $\dot{M}$ exceeds a critical value, due to photon trapping and mass loss from a large scale height flow (see e.g. Czerny 2019). Hence, the true mass accretion rate at the outer disc (and the UV/optical flux) can be severely underestimated if the standard linear scaling between $\dot{M}$ and L is used (as this model does). This could easily over-predict the reprocessed fraction required to produce the observed UV/optical flux through X-ray irradiation alone. Further, the reprocessing geometry is not as simple in ULXs as assuming that X-rays from the inner flow directly irradiate the outer disc. The emergence of a radiatively driven wind (when the local disc flux is larger than Eddington) can influence the reprocessed fraction in at-least two distinct ways. Photons scattering off the optically thick regions of the wind (close to the spherisation radius) may lose enough energy as to not thermalise with material in the outer disc (Kaaret and Corbel 2009). However, some photons can also scatter off the optically thin phase of the wind at larger distances from the compact object (Middleton et al. 2014), which can enhance the scattering of the hard X-ray flux onto the outer regions. We cannot account for these complexities with the current model. But, Sutton et al. (2014) speculated that since the reprocessed fractions of several ULXs were comparable to that inferred for sub-Eddington X-ray binaries, these opposing effects could cancel out. They do not appear to do so for this current model, so we conclude that it does not provide any physically meaningful constraints on this system and move on to seek out a model that can.

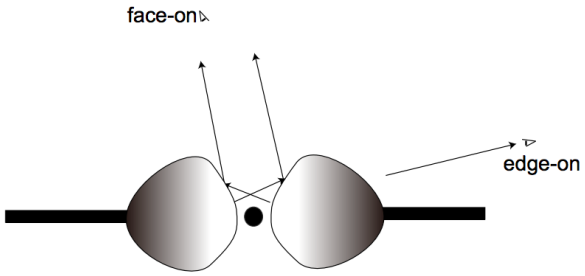

Figure 4.7: The accretion geometry adopted to model the multi-wavelength emission from the PULX (figure borrowed from Kubota & Done 2019).

4.3.5 Composite model including a slim disc

We have seen that the X-ray emission changes between epochs but that the UV/optical/IR largely doesn't; that the optical emission alone could be described by either stellar light or reprocessed X-ray emission; but that a state-of-the-art sub-Eddington irradiation model does not provide a meaningful constrain on the possible reprocessing. We therefore attempt to construct a new model that takes into account the super-Eddington nature of the central regions and that can also account for the optical light.

Our prime means of achieving this is to replace the multi-colour disk blackbody component in the X-ray spectrum with the physically-motivated slim disc model of Kubota and Done 2019. In previous modelling of two-component ULX X-ray spectra this component has been interpreted as the photospheric region at the base of the wind (Kaaret et al. 2017 and references therein) although more recent models based on magnetic neutron stars have more classically attributed it to the outer accretion disc (Koliopanos et al., 2017); in broadened disc spectra this component has frequently been attributed to an advection-dominated slim disc (Soria et al., 2015). Here we use this model as it should be applicable for a neutron star ULX with accretion rates well above Eddington, when the advection of radiative flux becomes important (Czerny 2019; Chashkina et al. 2017; Poutanen et al. 2007). Specifically, when the disc flux exceeds the Eddington limit at some critical radius r_c, the disc inflates to a large enough scale height that the timescale for photons to escape perpendicular to the plane of the disc exceeds the timescale for the accretion flow to move radially inwards. Hence, some unknown fraction of the radiated energy is advected with the flow, while some fraction of the inflowing mass may also be

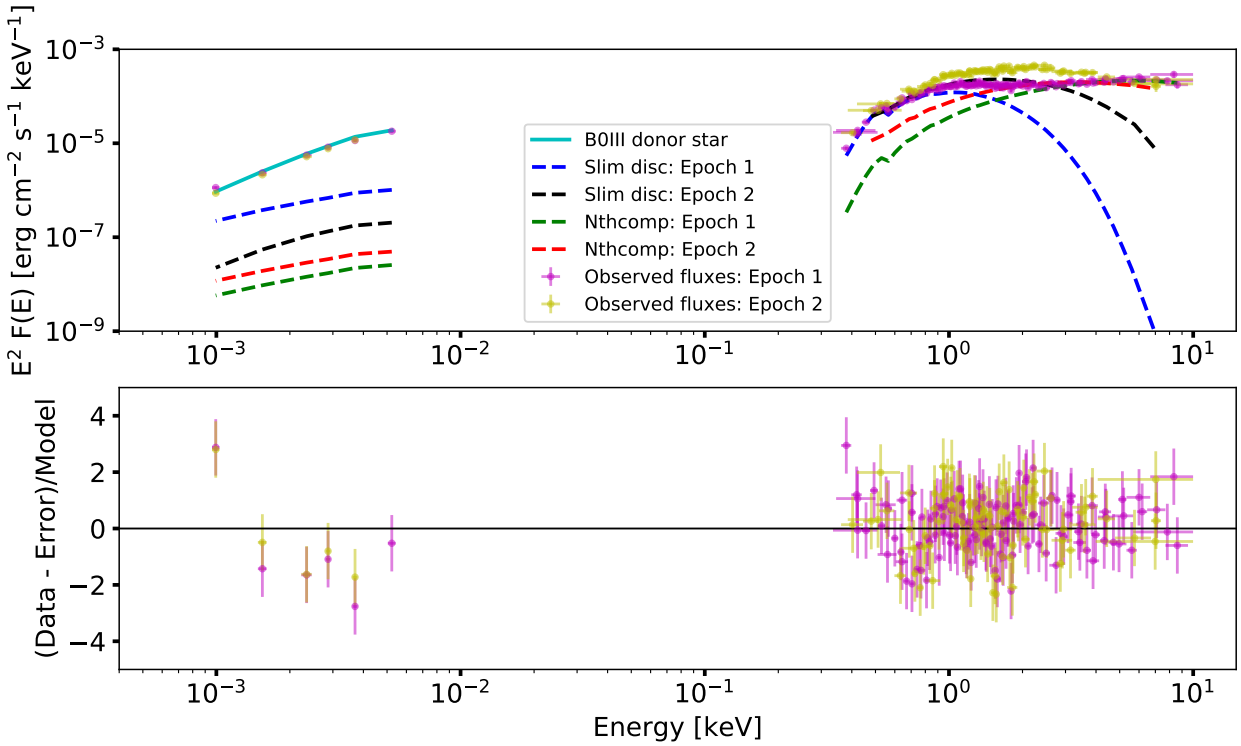

Figure 4.8: The SED of NGC 1313 X-2 fitted with a composite slim disc and thermal comptonisation model, including the contribution from the donor star (solid cyan line). The best-fitting slim disc component is indicated by the dashed blue (epoch 1) and black (epoch 2) lines, and the corresponding thermal comptonisation component is shown by the dashed green and red lines. The residuals to the best-fitting model are shown in the bottom panel, indicating that a good fit is obtained to most of the data points.

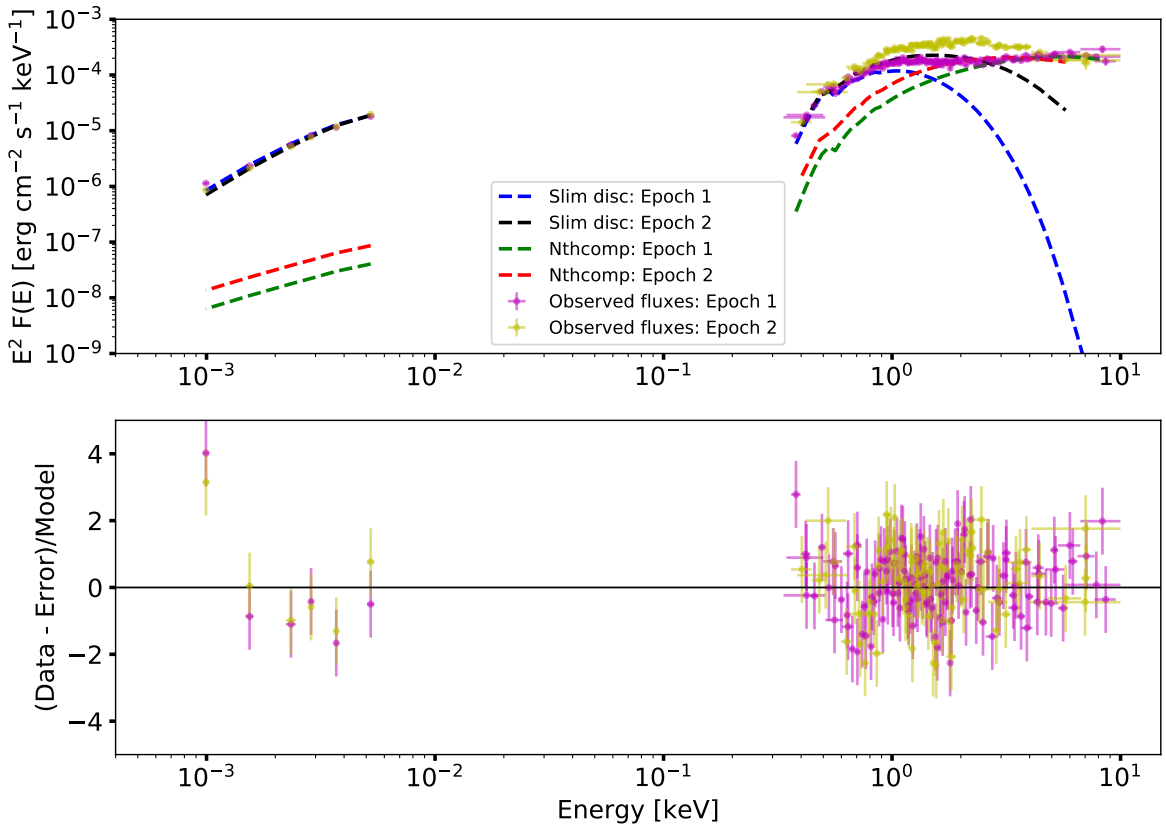

Figure 4.9: The same plot as in Figure 4.8, excluding the contribution from a donor star. The slim disc component alone provides a good fit to the UV/optical emission, although predictably this requires a substantial increase in the mass accretion rate compared to the case where the donor emission is considered.

ejected from the system due to radiation pressure [10] (Shakura and Sunyaev 1973). To account for these complications, the model replaces the standard Novikov-Thorne emissivity with a less effective parametric emissivity below a critical radius r_c where advection is important. This suppresses the luminosity released by the inner accretion flow, relative to that predicted by the accretion rate $\dot{M}_{in}$ through the outer disc. Hence, beyond some critical value of $\dot{M}_{in}$ the intrinsic X-ray luminosity of a slim disc saturates to $\sim 10\ L_{Edd}$ (due to photon trapping and mass loss from a large scale height flow). Finally, the model retains the same three-radial zone structure as `optxrplir`, with two distinct (warm and hot) coronal regions. However, a critical assumption is that the puffed-up disc at the radius r_c self-shields the hard X-ray emission from the inner accretion flow, such that any reprocessed emission from the outer disc is negligible (see Figure 4.7 for a visualisation of this effect).

We made slight adjustments to some of the model parameters before it was appropriate for fitting the multi-wavelength spectrum of a neutron star ULX. These sources can have strong magnetic fields that impart an opposing pressure to the inward ram pressure of the infalling material, thus halting the accretion flow at a radius R_M much larger than the innermost stable orbit R_{isco}. The value of R_M depends on the dipolar field strength and the mass accretion rate at that radius (see King et al. 2017). So, we enforced the inner disc radius of `agnslim` to take on values much larger than R_{isco} (while still allowing it to vary). Moreover, any advected material should re-radiate its kinetic energy at the (hard) surface of the NS, in contrast to the case of a BH where it disappears beneath the event horizon and adds to its mass. Indeed, it is classically understood that most of the accretion power is released near the neutron star surface in a shock-heated column (Basko and Sunyaev 1976a). Mushtukov et al. (2017) argued that some fraction of this hard emission can be reprocessed by matter inflowing along the dipolar field lines, which can become optically thick to electron scattering at super-Eddington accretion rates, forming a toroidal envelope around the central object. The envelope radiates with an approximately multi-colour blackbody spectrum, with peak temperature depending on the accretion luminosity and the size of the envelope (dictated by a balance between the magnetic and ram pressure at R_m). For typical ULX luminosities, the envelope temperature can be $\gtrsim 1$

[10] Although the latter is not considered here.

Table 4.7: The best-fit parameters of the multi-component model including a slim disc. Parameters (c-i) were free to vary, while the dust reddening was linked to the value derived from Grisé et al. (2008).

With stellar contribution (using $T_* = 29000$ K and $R = 11.0 R_\odot$)							
Epoch	E(B-V)[a] [Vega mag]	n_H[b] [10^{22} cm^{-2}]	$\log(\dot{m})$[c]	R_{in}[d] [R_g]	$\log R_{out}$[e] [R_g]	kT_{bb}[f] [keV]	χ^2/dof
1	0.09 ± 0.01	0.16 ± 0.02	1.22 ± 0.1	129 ±14	6.0*	1.68 ± 0.2	283.01/310
2	0.12 ± 0.01	0.15 ± 0.02	1.17 ± 0.04	24^{+12}_{-10}	6.0*	0.9 ± 0.1	258.4/212
Without stellar contribution							
Epoch	E(B-V)[a] [Vega mag]	n_H[b] [10^{22} cm^{-2}]	$\log(\dot{m})$[c]	R_{in}[d] [R_g]	$\log R_{out}$[e] [R_g]	kT_{bb}[f] [keV]	χ^2/dof
1	$0.16^{+0.01}_{-0.05}$	0.25 ± 0.01	> 4.3	133^{+11}_{-10}	$6.4^{+0.1}_{-0.02}$	$1.6^{+0.1}_{-0.05}$	266.3/309
2	0.1*	0.24 ± 0.01	$3.86^{+0.02}_{-0.04}$	25^{+12}_{-11}	6.6 ± 0.03	0.86 ± 0.1	253.5/211

Notes: [a] Dust reddening; [b] Hydrogen column density; [c] Dimensionless mass accretion rate (equivalent to the Eddington ratio); [d]Inner-disc radius; [e] Outer-disc radius; [f] Temperature of seed (blackbody) photons to non-thermal electrons; * Parameter frozen because it is insensitive to the fit.

keV, thus concurrent with the hard thermal component of the ULX energy spectrum. We modelled the emission from the envelope using the thermal comptonisation model (`nthcomp`) following Middleton et al. (2019a). Further, we adopted a canonical NS mass of 1.5 $M_\odot$, and retained the same neutral gas absorption and dust reddening components as in the previous section.

In Table 4.7, we present the best-fit parameters for the two cases where (i) we fit the multi-wavelength SED of X-2 with a composite model including `agnslim`, `nthcomp` and a single-temperature blackbody (`bbodyrad`) to account for the donor star's emission, and (ii) when the latter is ignored. Discarding any stellar contribution in the UV/optical yields an upper limit to $\dot{m}$ that we annotate as $\dot{M}_0$. But, we emphasise that due to uncertainties in the donor spectral type and any other contributions to the *HST* spectrum, the latter will invariably have some unknown systematic uncertainty. We set the temperature and

normalisation of `bbodyrad` to match a B0III spectral type, since this gives the most reasonable (although not an ideal) fit to the UV/optical magnitudes in section 4.3.3. We illustrate the fits to the SED of NGC 1313 X-2 with this new model both with and without a stellar contribution in Figures 4.8 and 4.9 respectively.

Although the models generally provide good fits across the SED, it is noticeable that the IR datapoint presents an outlier to both models. This is because the stellar blackbody does not produce sufficient flux in at this longer wavelength to match the data, and the accretion disc cannot become large enough (given the suspected orbital constraints) for its outer radii to radiate with a characteristic temperature in this band. We must therefore seek a different explanation for the flux in this band, and do so in the Discussion section.

Table 4.7 shows that statistically acceptable fits are obtained for both cases (i) and (ii), with the major difference being the requirement of a substantially larger $\dot{M}_0$ when the stellar emission is not considered (i.e. $\gtrsim 6000$ times the Eddington value). One reason to disfavour this solution is that such a large value of $\dot{M}_0$ implies an extremely small beaming factor b according to the King (2009) model, in which $b \propto \dot{m}^{-2}$. This scaling simply reflects that an increase in the mass accretion rate enhances the mass loading in the wind, causing it to occupy a larger solid angle (see Jiang et al. 2019). The predicted value of b means that the intrinsic accretion luminosity of the object $L_{\rm acc} = bL_{\rm obs}$ would be well below Eddington, in conflict with the requirement of a thick inner disc for geometric collimation in the first place, given that a large scale height disc only forms if the local Eddington limit is breached at some radius (for e.g. Fig. 1 of Kubota and Done 2019 illustrates that this occurs at $\sim 20R_g$ for $\dot{m} \sim 2.5$). However, it is possible that the geometrical thickness of a fully advection dominated disc saturates above a critical value of $\dot{m} \gtrsim 2$ (see Fig. 1 of Lasota et al. 2016), thus preventing the occurrence of strong beaming. In this case, a second strong argument mitigates against a very large $\dot{M}_0$. For a neutron star accretor, any advected energy must be released near their surface (unlike the case of a black hole, where it falls beyond the event horizon). In the absence of strong disc winds (as the Lasota et al. 2016 prediction implies), we can estimate the luminosity radiated near the surface to be $\sim 5 \times 10^{41}$ erg s^{-1}, using the accretion efficiency applicable to a neutron star ($\eta = \frac{GM_{\rm NS}}{R_{\rm NS}c^2} \sim 0.2$) and the lower best-fit $\dot{M}_0 \sim 6000\dot{M}_{\rm Edd}$. This is clearly at odds with the much smaller observed luminosity of the thermal comptonisation component (3×10^{39} erg s^{-1}), implying that the outflow rate must be more than than 95% of the accretion rate

through the outer disc, and that implausibly strong winds are required[11]. Admittedly, we could be underestimating the luminosity from the accretion column above 10 keV, with analyses of the pulsed emission of other NS ULXs indicating that it peaks above the bandpass of *XMM-Newton*. However, this discrepancy is likely to be well within a factor of 2 (see e.g. Walton et al. 2018b). Therefore, the best-fit mass inflow rate inferred by only considering the slim disc contribution at UV/optical wavelengths leads to inconsistencies on two fronts: (i) the implication of too small a beaming factor (adopting the King 2009 model), or (ii) the prediction of an unreasonably large luminosity from the NS surface and/or an implausibly powerful wind. We note that the best-fit $\dot{m}$ is also influenced by the inclination i, since the projected emission from the accretion flow scales as $\cos i$ (i.e. larger viewing angles will require an increase in $\dot{m}$ to fit a given spectrum). Setting the inclination to an extremal 0 degrees (fully face on view) does reduce the best-fit $\dot{m}$, but not to the extent that the above problems are alleviated. Hence, we strongly favour the fits including a stellar component on a physical basis. We note they obtain a more reasonable value of $\dot{m}$ that requires only $\sim$ 10% of the inflowing mass to be ejected, such that the accretion luminosity from the neutron star surface is consistent with that observed. However, we cannot be very precise about the outflow rate, given uncertainties in the beaming, the donor spectral type, and the contribution of the accretion column.

The derived mass accretion rate $\dot{m}$ hardly changes between the two observations. This is expected given a lack of observed variability in the UV/optical bands, which correspond to emission from the outermost regions of the disc that are much more sensitive to changes in $\dot{m}$ (since photon trapping effects are unimportant here). Despite an unchanged mass accretion rate, the inner disc radius takes on a much smaller value in the second epoch (decreasing by a factor ~ 5), which allows `agnslim` to account for an increase in the 1.0 - 6.0 keV flux. This is difficult to understand if $R_{\rm in}$ is interpreted as the magnetospheric radius, which scales primarily with the mass accretion rate and magnetic field strength as $\dot{M}^{-\frac{2}{7}}B^{\frac{4}{7}}$ (Ghosh and Lamb 1979). Unless the field strength decreases considerably (by a factor ~ 10) on the three month timescale, there is no reason to expect any variation in $R_{\rm M}$. We note that repeating the fit by linking the inner disc radius between the two

[11]Estimates from ULX bubbles, including for NGC 1313 X-2, are that winds carry $\lesssim 10^{40}$ erg s^{-1} of kinetic energy (e.g. Roberts et al. 2003), over an order of magnitude smaller than required here.

observations causes $\dot{m}$ to become fully unconstrained. In the discussion, we allude to a possible scenario that could explain this X-ray spectral behaviour, and its apparent lack of correlation with the UV/optical emission.

4.3.6 A possible UV excess?

We now discuss a subtle point regarding the modelling of the gas phase absorption for all the simultaneous X-ray and UV/optical spectral fits. We use the `phabs` component to do this, which appears to be preferred by the data over the alternative model `tbabs`. The difference between the two is that the former neglects absorption below the rest-frame hydrogen ionisation energy (e.g. from Fe I), which may be applicable for sight-lines dominated by a column of highly ionised gas. If the spectra in Figs. 4.6 and 4.8 are instead fitted with the `tbabs` model, the FUV fluxes are clearly seen to exceed the best-fitting continua, thus worsening the fit significantly. We demonstrate this visually in Fig 4.10.

The stellar fits (in Fig. 4.5) do not show any strong residuals in the FUV, because we only include the dust reddening component in this case (the neutral gas absorption model is difficult to integrate with other components outside of `xspec`). But, if we approximate the stellar emission with a single temperature blackbody within `xspec`, then we also see residuals in the UV. This could partly be attributed to the fact that `bbodyrad` does not capture the upturn that genuine stellar templates (from Castelli & Kurucz 2004) have over the UV bandpass. But, the magnitude of this upturn is still not sufficient to yield an adequate fit. So, unless the sight-line to NGC 1313 X-2 fortuitously excludes any cold, neutral material, then the observed FUV excess warrants a separate explanation. We discuss this below.

4.4 Discussion

We have presented the results of simultaneous X-ray and optical (actually UV - optical - NIR) photometry of the pulsating ULX NGC 1313 X-2. This shows that when the X-ray emission appeared to transit from a low, stable flux regime to a higher, more variable flux regime the X-ray spectral shape changed, but the optical emission remained largely the same, excepting a diminution in the NIR flux. In this section we will discuss what we can

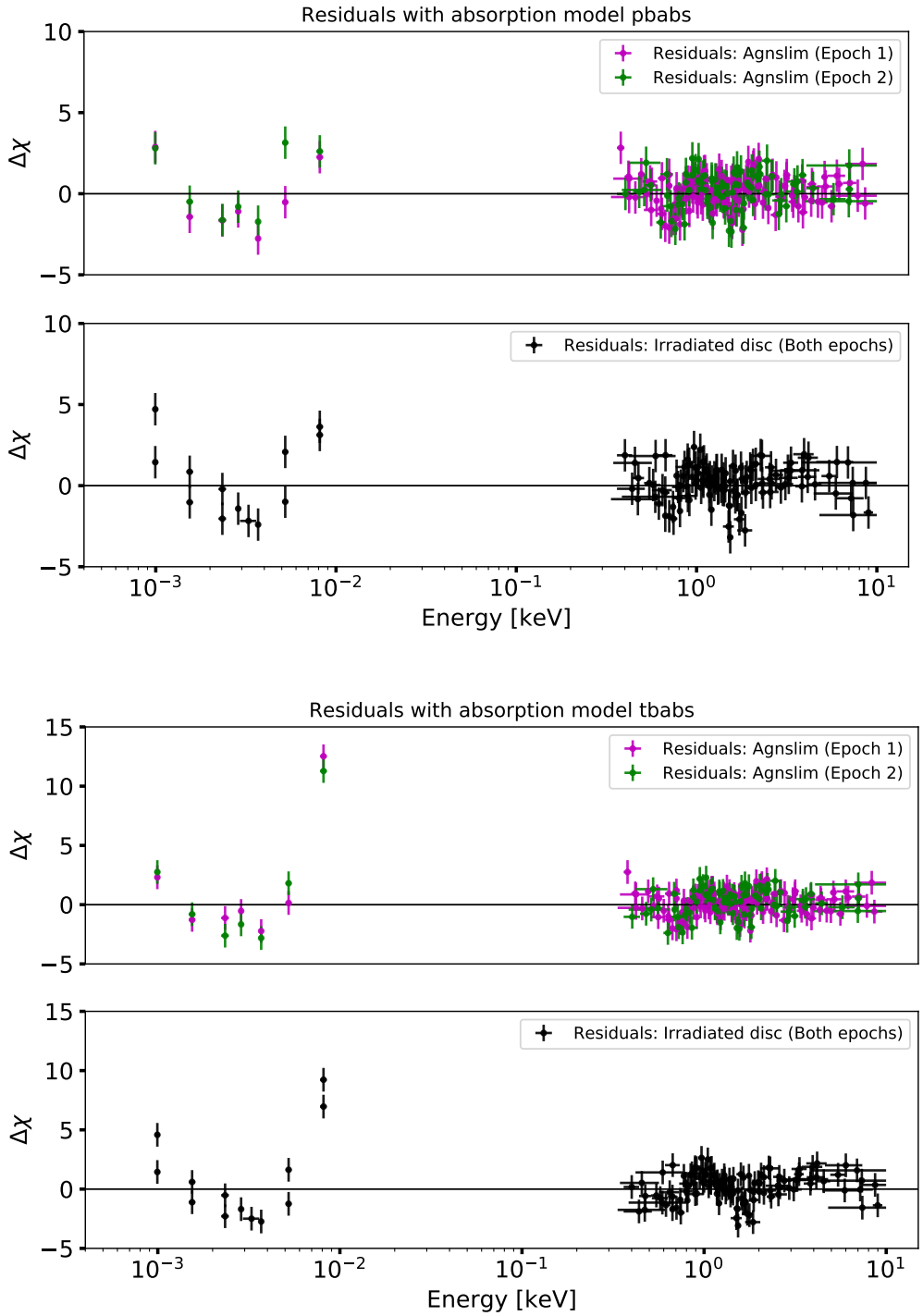

Figure 4.10: A demonstration of the absorption-model-dependent UV excess. *Top panels:* fitting residuals for the NGC 1313 X-2 SEDs fitted to both the irradiated disc and the composite slim disc model, with the absorption fitted by the phabs model. *Bottom panels:* as above, but using the tbabs absorption model.

learn about the physical processes in this object, and its optical counterpart, on the basis of these observations.

4.4.1 The big picture

NGC 1313 X-2 is remarkable in that it is one of the half-dozen known PULXs, albeit one with the faintest pulsations (Sathyaprakash et al., 2019). The presence of a large bubble nebula around this object strongly argues for the presence of outflows and/or jets, in expectation with supercritical accretion models. In this work, we explored whether the two distinct modes of X-ray spectral behaviour it shows (as described in section 4.3.1) are also consistent with such models, derived originally from Shakura and Sunyaev (1973) and adapted for the presence of a magnetic neutron star by Mushtukov et al. (2019). We note that to fully understand this, continual monitoring in X-rays and at other wavelengths is necessary, rather than the two snapshots we have obtained; however we will proceed with this caveat in mind.

We notice that the change in X-ray spectral shape between the two observations occurs primarily through an increase in the 1.0-6.0 keV flux, while the lowest ($<$ 1 keV) and highest energy ($>$ 6 keV) components remain stable. Such an occurrence is qualitatively similar to at least two other ULXs (Holmberg IX X-1 and NGC 1313 X-1; Luangtip et al. 2016; Walton et al. 2020), and is difficult to reconcile with an intrinsic change in the mass accretion rate alone (see Table 4.7). This is supported by the seemingly invariant UV/optical and soft X-ray fluxes, which are (in part) emitted by the outermost regions of the disc, implying that $\dot{M}_0$ through the outer disc remains steady over the three month timescale. As noted by Luangtip et al. (2016), the observed X-ray spectral transitions may instead be caused by a bulk precession of the thick inner disc and wind, plausibly due to the Lense-Thirring (or frame dragging) effect (Middleton et al. 2018a). This naturally changes the observer's viewing angle to different parts of the accretion flow; a line-of-sight corresponding to the inner-most regions presents a view of the highest energy photons, which are geometrically collimated by the ultra-fast wind. Conversely, a view of the outer wind photosphere reduces the hard X-ray flux, as the highest energy photons are Compton down-scattered by the outflowing material and/or scattered out of the line-of-sight. This picture is supported both by observational studies of how the soft X-ray spectral residuals

correlate with luminosity (Middleton et al. 2015b), in addition to numerical simulations of super-critical discs (Ohsuga and Mineshige 2011; Sądowski and Narayan 2016).

Clearly, the precession scenario also predicts a stronger modulation in the hard X-ray band over long timescales, since the soft X-rays are less geometrically beamed and distributed over a larger solid angle, and should thus be less variable as the wind moves in/out of the observer's sight line. Indeed, recent studies have reported quasi-periodic hard X-ray variability in several (P)ULXs on weekly-monthly timescales (e.g. Weng and Feng 2018; Brightman et al. 2019; Vasilopoulos et al. 2020), invoking the above precession model as a possible explanation. In the particular case of X-2, Weng and Feng (2018) conclude that the variability is strongly periodic, although they do not consider red noise into their significance estimation, and the periodicity is not fully obvious in their folded light curve. In any case, Ogilvie and Dubus (2001) discuss that a radiatively warped disc may undergo unstable precession, which need not induce strictly periodic modulations on the X-ray flux (although it is unclear whether this mechanism is preferred over the general relativistic Lense-Thirring effect for ULXs).

So, can a precession scenario explain the combination of raised X-ray flux and variability, in addition to the spectral changes we observe? Is it also consistent with the lack of optical variability? The answer on both counts is plausibly yes. If the periods of higher flux are generally due to a more face-on view of the ULX, then the increased short-term X-ray variability (as seen in Figure 4.2) could be an effect of discrete clumps of material at the edge of the wind passing through the line-of-sight, as described by Middleton et al. (2011). Then, the lower flux and variability at higher viewing angles is a damping effect of many more clouds passing through the line-of-sight, effectively providing an opaque layer to the hard X-rays. The key question is why, if the X-ray emission changes, the optical does not? Our analysis suggests that this may be due to the optical emission being dominated by the companion star, with a weaker contribution from an irradiated outer disc (although other factors may also play a role, as we discuss below). Indeed, this is perhaps not unexpected if the hard X-rays are collimated away from the accretion disc and (presumably) the companion star, and so cannot be reprocessed. Hence, precession cannot affect the optical appearance of the PULX in the same way that it can affect the X-ray emission.

However, we do note that there are previous reports of rapid optical variability for

this object (Grisé et al., 2008) (and others, cf. Thongpoyai et al. 2019) that are difficult to interpret in a simple supercritical wind model geometry, given the lack of opportunity for reprocessing. We leave the reconciliation of these results and the model as an open question for future work.

4.4.2 The nature of the optical emission

Our analysis of the optical light from the ULX counterpart shows it to be largely invariant between the two observational epochs, despite a change in the X-ray flux. Using the magnitudes obtained in each of the different *HST* filters we can obtain a coarse spectrum of the counterpart, finding that its shape is broadly consistent with a B0III giant (if the NIR data point is ignored), but is also well explained by a power-law model (if the far UV data point is ignored), which is reminiscent of reprocessed X-rays. We therefore attempted to fit the broadband X-ray - UV/optical SED with a disc reprocessing model, but this provided an unreasonably large reprocessed fraction (> 80% of the X-ray flux), although this is partly attributable to the unsuitability of the model to fitting super-Eddington accretion flows. While a 'slim' disc model is more justified in this respect, it does not consider X-ray reprocessing, and implicitly assumes that the outer disc is largely shielded from hard X-rays by the inflated inner disc. However, usage of this model implied that either unreasonably high accretion rates are required to account for the observed levels of UV/optical emission, or that an additional stellar component (dominating the UV/optical flux) is necessary. We emphasise that, while the light from the star dominating the counterpart appears probable from our results, we cannot fully rule out reprocessing since it is not accounted for by the slim disc model.

Even if the optical light were to arise in reprocessed X-ray emission, changes in the reprocessed fraction may be difficult to observe in our case, given that the broadband X-ray flux increases only by $\sim 25\%$ between the observations probed by *XMM-Newton*. In the simple disc geometry applicable to sub-Eddington low mass X-ray binaries with a geometrically thin disc, $f_{\rm out}$ can be predicted analytically. It is a function of the X-ray flux irradiating the outer disc $f_{\rm out} \propto (L_{\rm X})^{1/7}$ (Cunningham 1976), for a given compact object mass and disc size. This relation implies that a 25% increase in $L_{\rm X}$ should lead only to a 3% increase in $f_{\rm out}$, which cannot be demonstrated given the current quality of

our data (see Table 4.6). While this is consistent with the lack of variability we see, our accretion disc should not be in a geometrically thin configuration (as emphasised before). Indeed, it is noted above that in supercritical discs one might expect the hard X-rays to be funnelled away from the disc, making large reprocessing fractions unlikely.

In addition to disc reprocessing, we should also consider other effects contributing to any UV/optical modulations. If the donor is tidally distorted by the NS, its apparent size and projected flux would vary as a function of orbital phase (unless the system is seen near face-on). Similarly, if the star is irradiated by photons from the accretion disc (although see the above point on hard X-rays being funnelled), the bright X-ray heated face would only be visible during certain orbital phases, which presents another source of variability. In principle, a combination of these effects (referred to as ellipsoidal modulations) may have negated any increase in the UV/optical flux caused by X-ray reprocessing. Indeed, there has been a previous report of periodic optical modulations from this object, thought to be consistent with ellipsoidal modulations (Liu et al., 2007), but it was subsequently shown to be of low statistical significance (Zampieri et al., 2012).

A final point to consider on reprocessing is that the longer wavelength emission may respond to changes in the X-ray flux with a time delay that is much larger than the duration of the snapshot *HST* observations ($15-20$ mins). This would clearly mask any correlated variability between these bands, although a crude estimate of the light-travel time between the X-ray and optically emitting regions of the disc may suggest that it is unlikely (see section 4.3.4). Indeed, our estimate does not account for the emergence of an ultrafast wind at accretion rates above Eddington (Pinto et al. 2016, Kosec et al. 2018b). The lag between the X-ray and UV/optical flux could then be influenced by the photon diffusion timescales across across the outflow, which will partly depend on the density of material within it. Some evidence for such lags is already emerging within the X-ray regime (Heil et al. 2009; Middleton et al. 2019b; Kara et al. 2020).

Our modelling does however favour the optical emission arising in the companion star. It is worth noting that the best-fitting stellar model reported here may not reflect the true donor spectral type, partly due to reasons outlined in Patruno and Zampieri (2008). They demonstrate that the luminosity-temperature evolution of an isolated star can substantially differ from one in a binary. For example, an isolated star on the main sequence will tend to become more luminous as its radius expands. By contrast, a binary

main sequence star (of the same initial mass) cannot expand above its Roche Lobe radius, and tends to decrease both in luminosity and temperature at the onset of Roche Lobe overflow. It will thus appear cooler and fainter than an isolated star at the same stage of its evolution, posing problems for a direct comparison of the observed magnitudes and colours with standard stellar templates. In addition, the donor star can also be irradiated by X-ray photons from the accretion flow, further affecting its brightness and colour (e.g. Motch et al. 2014, although see comments above). Hence, our attempts at identifying the stellar type may not be very accurate.

Finally, we note that this result presents an intriguing link to other PULXs. The first ULX for which the counterpart was unambiguously demonstrated to be stellar was NGC 7793 P13, also a PULX (Motch et al., 2014). A red supergiant companion has now been revealed for a second PULX, NGC 300 X-1 (Heida et al., 2019b), although attempts to uncover the counterparts for two more PULXs have proven inconclusive due to their distance, being heavily affected by obscuration and/or residing in crowded locations (Heida et al., 2019a). Thus at least half of the PULXs have plausible stellar-dominated counterparts. This contrasts strongly with the remainder of the ULX population where reprocessed X-ray emission remains a strong explanation for the optical counterpart (Tao et al., 2011). This could perhaps support the strong hard X-ray beaming in NS ULXs predicted by King (2008), and seems consistent with the notion that NS ULXs would have smaller accretion discs than in their black hole equivalents (Heida et al., 2019a).

4.4.3 What is the origin of the NIR excess?

In almost all of our modelling, the NIR data point from the *HST* F125W filter appears to sit above the expected model emission, demonstrating a likely NIR excess in this ULX. It is also notable that this filter shows the strongest evidence for variability in any of the *HST* data between the two observational epochs, with a $\sim 35\%$ decrease in NIR flux observed. This is in stark contrast to an increase in X-ray flux between the same two epochs.

The fact that this variability occurs only in the NIR (whilst being absent in the UV/optical) immediately rules out an origin due to X-ray reprocessing, or arbitrary changes in the line-of-sight interstellar extinction. It is also unlikely to come from the

counterpart being a red supergiant star, which appears to be excluded by the observed SED[12]. We speculate that it may instead be attributed to transient jet emission, although we require additional evidence to confirm this. Classical Galactic black hole binaries (GBHBs) sometimes show NIR flaring episodes during accretion state transitions, from the low-hard state (featuring a persistent radio jet) to the high-soft/thermal dominant state (when jet emission is suppressed). These episodes are hypothesised to be caused by ejections of material from the hot inner flow. Similar potentially explosive jet formation has also been seen in more than one ULX, for example in Ho II X-1 (Cseh et al., 2015) and in a transient ULX in M31 (Middleton et al., 2013). One key signature of jet emission is a break in the power-law spectrum usually seen at mid-IR wavelengths in GBHBs (e.g. GX 339-4; Gandhi et al. 2011; Corbel and Fender 2002). The energy break separates the flat synchrotron self absorbed emission emerging from optically thick regions of the jet, from the optically thin non-thermal emission at larger distances, as the jet material is accelerated by internal shocks (e.g. Blandford and Königl 1979; Markoff et al. 2003). The possible presence of such a break in the ULX Holmberg IX X-1 (Dudik et al. 2016) strengthens the notion that its variable mid-IR emission is associated with jet activity (e.g. Lau et al. 2019). Of course, we have no evidence for a spectral break in X-2 as yet (as the current HST data do not cover the mid-IR band), and this would be interesting to explore in future works.

An alternative explanation for excess NIR emission in ULXs is the presence of a disc of circumbinary material. Such a disc is strongly suggested for Ho II X-1 on the basis of mid-IR observations (Lau et al., 2017). Several more candidates for circumbinary discs are presented in Lau et al. (2019), which also extensively discusses the physics of these bodies. One pertinent point they make is that the dust in these discs may be sublimated by the X-ray emission of the ULX, if either the disc comes too close to the ULX, or if the ULX luminosity increases significantly. We note that the coincidence of an increase in X-ray emission and a decrease in NIR emission is seen in X-2, which might be suggestive of the

[12]We note that López et al. (2020) catalogue a possible red supergiant companion to X-2. However, this object (their object B) is only just within their formal error region. They also detect the object we regard as the counterpart (their object A) much closer to the centre of their error region, and derive magnitudes from the *HST* data consistent with ours.

destruction of the innermost edge of a circumbinary disc by dust sublimation. However, we have argued above that the increase in luminosity may primarily be a line-of-sight effect associated with precession of the inner disc; in such a scenario we would not expect a sustained intrinsic luminosity change, and so the sublimation of the inner edge of the circumbinary disc would not be expected. Whether a sublimation scenario is the case may also rely on the geometry of the outer part of the accretion disc - the circumbinary disc is likely to be equatorial to the secondary star, as will the outer disc be, hence if it is significantly flared the circumbinary disc will likely be shielded from even the soft X-ray emission, which is likely to cover a wider solid angle than the beamed hard X-rays. Hence, although we cannot rule out a circumbinary disc as a possible origin for the NIR excess, its variability is more difficult to explain.

4.4.4 What is the origin of the putative UV excess?

We have shown that there is a possible UV excess present for NGC 1313 X-2, although this result is strongly model-dependent and relies on the presence of cold and neutral material along the line-of-sight to the ULX. However, this does not seem entirely unreasonable given that the X-rays from X-2 must pass through both the outer regions of its host galaxy, and our own Galaxy, to reach us.

Indeed, previous studies have claimed that some ULXs have UV fluxes larger than predicted by the extrapolation of a standard multi-colour disc component (usually fitted to their X-ray spectra between 0.3 - 1.0 keV). For instance, Abolmasov et al. (2008) reconstructed the SED of NGC 6946 X-1 by estimating the UV quanta from the ULX required to account for the photoionized emission line fluxes (including He II λ4686) from the surrounding X-ray ionized nebula. Their result suggests $L_{\rm UV} > 10^{40}$ erg s^{-1}, which was subsequently confirmed by direct *HST* observations of the same object by Kaaret et al. (2010). One possible explanation for this phenomenon is that the UV emission emerges from the outer photosphere of the radiatively driven wind in a supercritical disc. In fact, the wind photospheres of the most extreme, down-scattered sources, when viewed at large inclinations, are expected to be seen primarily in the UV (Poutanen et al., 2007). While X-2 may be accreting at a sufficiently high rate to drive a wind substantial enough to downscatter copious X-rays into the UV, it is not obvious how much of this emission

would be visible for a ULX that is aligned close to face-on, as is expected to be the case for X-2, rather than close to edge-on. Hence, we cannot rule out a real UV excess present in this object, but do not regard the evidence as strong.

4.5 Conclusions

We detect clear X-ray spectral variations in NGC 1313 X-2 between *XMM-Newton* observations taken in December 2015, when *Swift* monitoring suggested the PULX was in a low flux, low variability mode, and subsequent observations in March 2016 when the PULX was in a higher flux and variability regime. However, simultaneous optical/UV observations taken with *HST* demonstrate no correlated multi-wavelength variability, with the exception of an anti-correlation to the NIR emission of the counterpart: this fades as the X-ray emission rises between the two observation epochs.

We have discussed the X-ray and optical characteristics of this PULX in the context of a supercritical disc model, where a massive radiatively-driven wind is launched from the inner regions of the accretion disc as the disc becomes locally super-Eddington. We find that the behaviour is consistent with this notion, with the changing X-ray properties plausibly the result of precession of the inner regions of the accretion flow. The lack of optical variability is consistent with both a lack of reprocessing in the outer accretion disc/companion star due to the hard X-rays being collimated away from these media, and the optical counterpart being likely dominated by the stellar light; however this cannot explain previous reports of short-term ($\sim$ hours) optical variability in this object. We also caution that our conclusions are drawn from a pair of snapshots; a much clearer picture of behaviour would emerge from longer-term simultaneous multi-wavelength monitoring of objects like X-2.

We also find evidence for other interesting phenomenology in this PULX, most notable of which is the variable NIR excess. Possible explanations for this include a jet or a circumbinary disc, with the former perhaps the more plausible for this object. Weaker, model-dependent evidence is presented for a UV excess; if present this may originate in the outer photosphere of the disc wind.

This work shows both the power and the pitfalls of simultaneous, multi-wavelength observations of interesting objects such as ULXs. The simultaneity of the data puts clear

constraints on the physics of the observed system; however to access such data requires the investment of observing time from the world's leading observatories, which is a scarce commodity, leading to limited datasets. Obtaining the further monitoring data required to constrain the key behavioural characteristics of interesting objects such as the PULX NGC 1313 X-2 is therefore an expensive pursuit. However, the continual development of new and future observatories with the capability for monitoring at a variety of wavelengths promises that this science will become more accessible with time, and so our understanding of objects such as PULXs should grow.

Chapter 5 | Conclusions

In this section, we summarise our work on understanding the spectral and timing signatures of ULXs in the context of super-Eddington accretion, and provide brief directions for future work.

5.0.1 Chapter 2

In chapter 2, we began by investigating whether it is possible to detect and spatially resolve diffuse X-ray emission associated with shock ionised ULX nebulae. The general aim was to obtain constraints on the kinematics of the bubble, complementary to that derived from optical and radio studies (Pakull and Mirioni 2002). We chose the ULX Holmberg IX X-1 as an ideal target, on the basis of its hard X-ray spectrum, the quality of *Chandra* data, and the open question surrounding the origin of its spectral residuals below 1 keV (Middleton et al. 2014; Middleton et al. 2015b; Pinto et al. 2016). While our spectral and photometric analysis did not provide any significant evidence for extended diffuse emission, we briefly discussed the prospects that *Athena* would offer for studies of this type. We note that reports of X-ray emission associated with ULX bubbles are presently rare, with only one recent work claiming evidence for extended X-ray emission surrounding the PULX NGC 5907 X-1, during its dim X-ray state (see Belfiore et al. 2020). Even in this case, the question of whether the diffuse emission is genuinely linked to a shock ionised bubble or is the result of dust scattering remains open, but it provides some encouragement that detecting such extended emission is not impossible if the conditions are favourable.

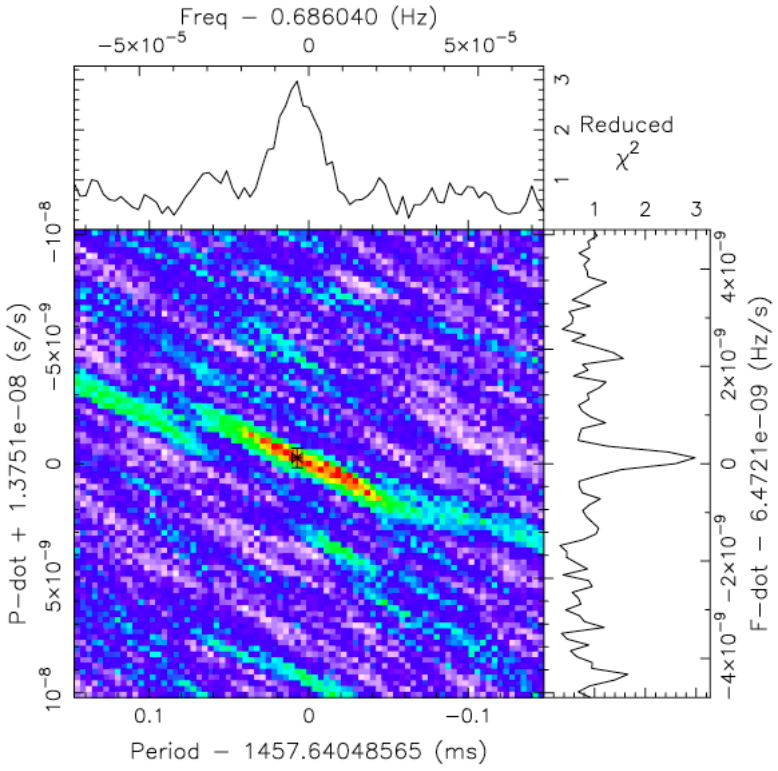

Figure 5.1: Accelerated epoch folding search on an *XMM-Newton* observation of NGC 1313 X-2, highlighting the detection of a periodic signal at a significance of $\sim 3.5\sigma$. The light-curve is folded on the best-fit frequency and its derivative in the manner described in Chapter 3.

5.0.2 Chapter 3

In chapter 3, we presented the discovery of weak pulsations in the ultraluminous X-ray source NGC 1313 X-2. Indeed, since the first PULX was detected by Bachetti et al. (2014), the number of such sources has grown in the recent years, posing questions on the genuine fraction of ULXs that host NS accretors. While there are continued efforts to reveal the potentially distinct signatures of NS ULXs that could separate them from BH ULXs (see e.g. Walton et al. 2018; Brightman et al. 2018; Earnshaw et al. 2018; Middleton et al. 2018), the detection of coherent pulsations remains one of the few robust ways of distinguishing between the two populations. Among the ~ 6 PULXs discovered so far, NGC 1313 X-2 has the smallest pulsed fraction ($< 8\%$), requiring more than ~ 15000 counts with *XMM-Newton* to be detected to a significance of at-least $3.5 - 4\sigma$ (given its X-ray count-rate and period derivative). Presently, less than 5% of all known ULXs have sufficient data quality for pulsations to be detected in them with current generation instruments, provided they share the typical pulsed fractions and period derivatives of the known PULXs (Rodríguez Castillo et al. 2020). This is assuming that the pulsed fraction remains above the detection threshold for the entire lifetime of the source, while in reality the pulsations can be transient (Sathyaprakash et al. 2019; Bachetti et al. 2020). Thus, it is relevant to ask whether the recently launched and upcoming X-ray missions such as *e-ROSITA* and *Athena* will have the requisite sensitivity to detect the weak pulsations found in NGC 1313 X-2 to the same (or higher) significance. We analyse this briefly below.

We simulate a fake light-curve containing a constant and a periodic component (with the same properties as observed for the PULX), with Poisson noise added to both. Mathematically, the count rate expected in each time bin is:

$$s(t) = r[1 + q\sin(2\pi f(t)t + \phi)] \tag{5.0.1}$$

,

where r is the non-periodic count rate (including the background), q is the pulsed fraction, $f(t)$ is the time-dependent spin frequency of the pulsar and ϕ is an arbitrary rotational phase offset. The NS spin frequency varies with time due to Doppler shifts of

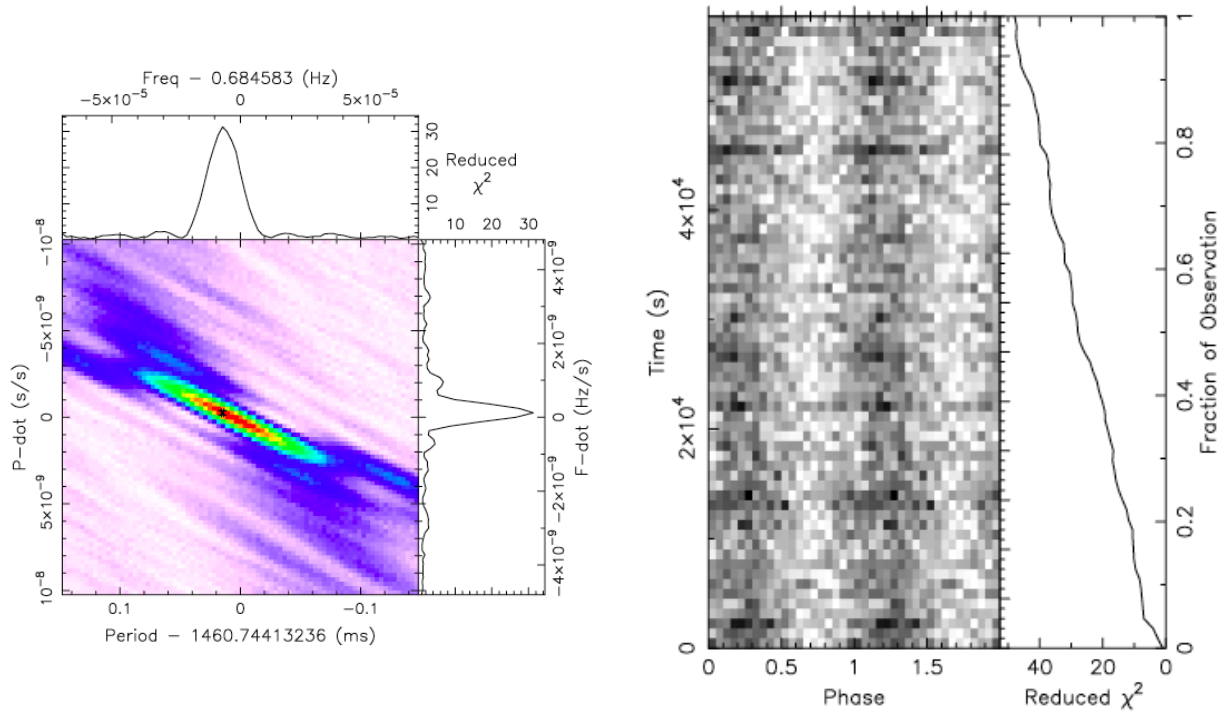

Figure 5.2: *Top left*: An accelerated epoch folding search on the simulation of a periodic signal (with $\dot{f} = 0$) from the PULX NGC 1313 X-2, with the count-rate scaled to that expected from *Athena*, but all other parameters (pulsed fraction and spin frequency) set to the observed values. A measure of the improvement in detection signifcance afforded by *Athena* can be gained by comparing the peak reduced χ^2 values with those measured in the real search with *XMM-Newton* (see Figure 5.1). *Top right*: A phaseogram of the mock data, highlighting how the phase corresponding to the peak amplitude of the pulsed signal (shown by the darker colours) evolves as a function of time. It remains constant in this case since $\dot{f} = 0$.

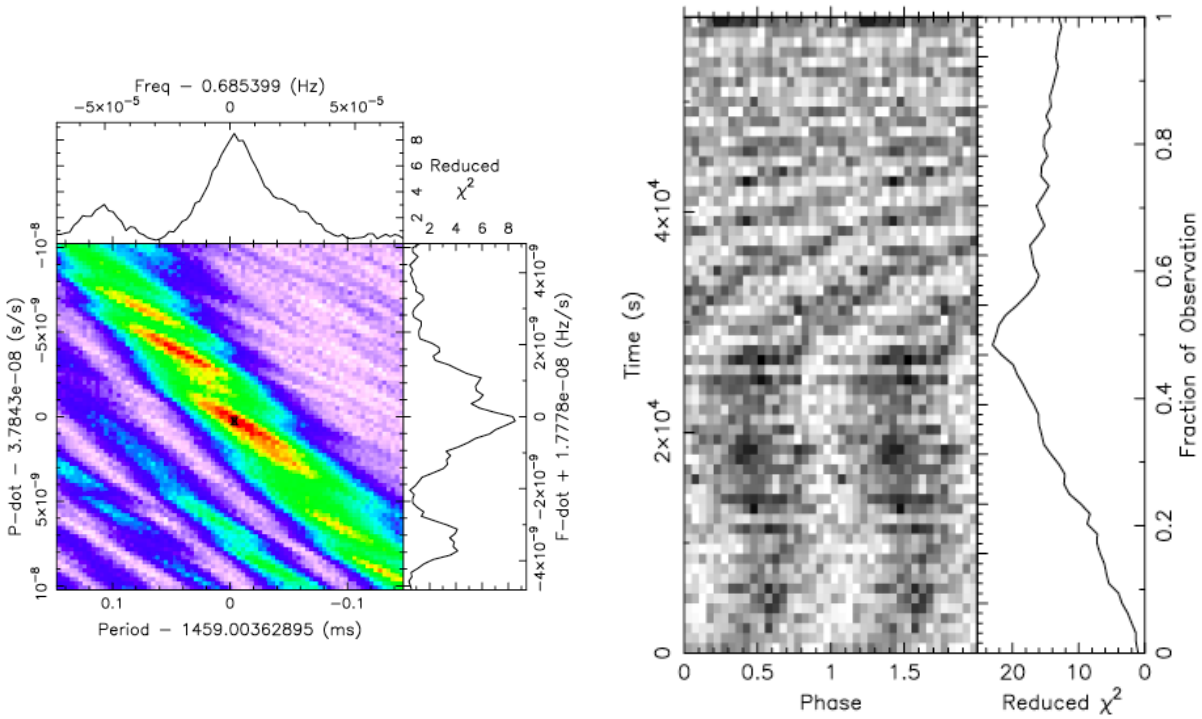

Figure 5.3: These figures show the same information as above, except for the simulation in which the pulse frequency is allowed to evolve with time.

the pulsations induced by the orbital motion of the NS around its companion, in addition to the NS's own spin-up via accretion of material. We consider two instances in which the spin frequency is (i) constant and (ii) evolves periodically as per the expectations of an NS in a Keplerian orbit with a period of ∼ 3 days and a companion mass ∼ 12 $M_\odot$ (i.e. within the allowed values of the orbital constraints derived in Chapter 3). In order to convert the mean count rate r measured with *XMM-Newton* to the count-rate expected from *Athena*, one needs to assume a model for the energy spectrum, since the detector response varies as a function of energy. We assume a composite (absorbed) disc plus power-law model, adopting the same parameters as measured for the real spectrum. Then, we use the available response matrices and auxiliary response files[1] to obtain the *Athena* equivalent mean count-rate for NGC 1313 X-2. We add Poisson noise by drawing $g(t)$ randomly from a Poisson distribution, where

$$g(t) = \frac{\mathrm{Po}[s(t)\Delta t]}{\Delta t} \tag{5.0.2}$$

,

[1] https://www.the-athena-x-ray-observatory.eu/resources/simulation-tools.html

and Δt is the instrumental time resolution. Finally, we implement the acceleration search software `PRESTO` on the fake light-curve in the same manner as described in Chapter 3. Figure 5.2 (5.3) highlights the expected improvement in the pulsation detection significance afforded by the XIFU-detector onborad *Athena* compared to *XMM-Newton*, when the pulsed signal has a (non) zero period-derivative. Thus, *Athena* is expected to discover many more PULXs including those that are weakly pulsating, and will be crucial to understand the heterogeneous ULX population.

In the case of *e-ROSITA*, its lightcurve will comprise of 8 snapshots covered over 4 years with a total duration of ~ 2 ks (on average), while areas lying closer to the poles of *e-ROSITA's* orbit (constituting $\lesssim 1\%$ of the total sky area) are expected to receive about 10 ks of total exposure. Since *e-ROSITA's* lightcurve will not be uniformly sampled, the use of Lomb-Scargle periodograms (e.g. VanderPlas 2018) may be better suited to search for periodic signals as opposed to the standard acceleration searches used in this work, and would be worth exploring in future studies. For the purposes of this chapter, however, we crudely assume that the lightcurve is continuous (with a typical exposure time of ~ 2 ks), and repeat the same analysis as above. Given a broadband source count-rate of 0.07 s^{-1} (corresponding to an apparent luminosity of 1.5×10^{40} erg s^{-1} at 4.0 Mpc), we find that *e-ROSITA* will only be able to detect pulsations from PULXs (at the 3σ level) if the pulsed fraction is $\gtrsim 55-60\%$, which is higher than measured for almost all of the current objects (except NGC 300 X-1; Carpano et al. 2018). We note that the effect of the period derivative on the detection significance is not important due to the small exposure time of each scan. For regions of the sky receiving ~ 10 ks exposure, pulsations can be detected from sources with much smaller pulsed fractions ($\gtrsim 25\%$).

While *e-ROSITA* may not play as big a role as *Athena* in the direct detection of pulsations from PULXs, its vast improvement in sky coverage and sensitivity [2] over previous X-ray missions will be crucial to unveiling new ULXs. These can later be followed-up with *XMM-Newton* and *NuSTAR* for detecting pulsations. Moreover, *e-ROSITA* will play an important role in other aspects of ULX science, such as the discovery of X-ray transients associated with propeller-phase NS ULXs (Earnshaw et al. 2018) and IMBH candidates undergoing X-ray outbursts (Webb et al. 2014). Indeed, *e-ROSITA* recently completed

[2] expected to reach a depth of 10^{39} erg s^{-1} out to ~ 9 Mpc after 8 scans

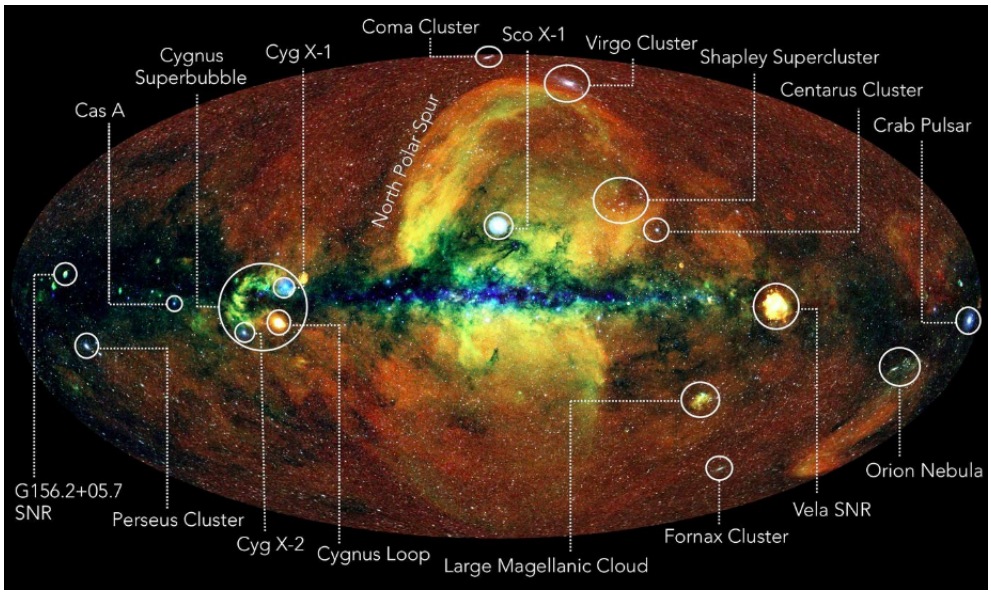

Figure 5.4: The first all sky map of the hot universe from *e-ROSITA* (projected onto an ellipse) released in June 2020. The X-ray photon energies are colour coded according to: red - 0.3 - 0.6 keV, green - 0.6 - 1.0 keV, blue - 1 - 2.3 keV. The most important Galactic and extra-galactic sources have been highlighted.

its first scan of the entire sky and is underway to achieving its goals in the next four years (see Figure 5.4).

5.0.3 Chapter 4

In chapter 4, we performed simultaneous X-ray and UV/optical/NIR monitoring of the pulsating ULX, NGC 1313 X-2. The aim was to investigate the source of its optical emission, the mechanism driving its X-ray variability on weekly timescales, and whether this is correlated with its rapid optical variability seen in previous observations. However, during our most recent campaign, the ULX did not demonstrate significant optical variability with respect to other non-variable stars in the field, but this was insufficient to rule out an X-ray reprocessing origin for the optical emission. On the other hand, we observed notable variability in the X-ray band, with changes in the energy spectrum hinting that it could be caused by bulk precession of a super-critical accretion flow, in line with the proposed explanations for super-orbital variability in other PULXs (e.g. Walton et al. 2017). We emphasise that these conclusions are drawn from snapshot X-ray and optical data, while longer cadence observations may yield more insights into the puzzling

relationship between the X-ray and optical emission bands[3]. Modelling the broadband (X-ray to optical) SED of the source suggested that it requires both stellar and non-stellar (irradiated disc) components in the UV/optical regime, with the former likely dominating the optical light, in a similar vein to other PULXs. Finally, we presented evidence for NIR variability from NGC 1313 X-2 that could be attributed to sublimation of a dust shell its vicinity, or transient jet emission linked to ejection of material from the accretion disc.

Future optical surveys such as *LSST* are expected to provide longer baselines that would allow deeper investigations into the link between X-ray and optical variability in ULXs. It would help to discriminate between the proposed scenarios for the optical emission processes in such objects (e.g. donor star, reprocessing from outer disc and surrounding material). In order to reach the required detection sensitivities of the distant, optically faint ULX counterparts, co-adding of multiple *LSST* visits would be essential. Despite this, the latter could still sample each object hundreds of times, providing a vast improvement over current facilities used to study optical variability in ULX counterparts. We emphasise that multi-wavelength studies of ULXs also aim to infer the properties of its donor and the orbital parameters of the binary. This is important to understand the fraction of (P)ULXs that may evolve to become merging double compact objects that emit gravitational waves (e.g. Mondal et al. 2020), thus helping to ascertain whether ULXs constitute a significant channel for the formation of GW sources.

Indeed, the field of ULXs has progressed greatly since the decade during which they were initially discovered with key progress being made in the era of *Chandra*, *XMM-Newton* and *NuSTAR*. The recent discoveries of pulsating ULXs has brought about an unexpected twist in this field, and there is plenty to look forward to with the wealth of X-ray and other multi-wavelength facilities that are set to begin operation in this decade.

[3]http://astro.u-strasbg.fr/ motch/ulx2016/06_06_Zampieri.pdf

Bibliography

Abbott, B. P., R. Abbott, T. D. Abbott, M. R. Abernathy, F. Acernese, K. Ackley, C. Adams, T. Adams, P. Addesso, R. X. Adhikari, V. B. Adya, C. Affeldt, M. Agathos, K. Agatsuma, N. Aggarwal, O. D. Aguiar, L. Aiello, A. Ain, P. Ajith, B. Allen, A. Allocca, P. A. Altin, S. B. Anderson, W. G. Anderson, K. Arai, M. C. Araya, C. C. Arceneaux, J. S. Areeda, N. Arnaud, K. G. Arun, S. Ascenzi, G. Ashton, M. Ast, S. M. Aston, P. Astone, P. Aufmuth, C. Aulbert, S. Babak, P. Bacon, M. K. M. Bader, P. T. Baker, F. Baldaccini, G. Ballardin, S. W. Ballmer, J. C. Barayoga, S. E. Barclay, B. C. Barish, D. Barker, F. Barone, B. Barr, L. Barsotti, M. Barsuglia, D. Barta, J. Bartlett, I. Bartos, R. Bassiri, A. Basti, J. C. Batch, C. Baune, V. Bavigadda, M. Bazzan, M. Bejger, A. S. Bell, B. K. Berger, G. Bergmann, C. P. L. Berry, D. Bersanetti, A. Bertolini, J. Betzwieser, S. Bhagwat, R. Bhandare, I. A. Bilenko, G. Billingsley, J. Birch, R. Birney, O. Birnholtz, S. Biscans, A. Bisht, M. Bitossi, C. Biwer, M. A. Bizouard, J. K. Blackburn, C. D. Blair, D. G. Blair, R. M. Blair, S. Bloemen, O. Bock, M. Boer, G. Bogaert, C. Bogan, A. Bohe, C. Bond, F. Bondu, R. Bonnand, B. A. Boom, R. Bork, V. Boschi, S. Bose, Y. Bouffanais, A. Bozzi, C. Bradaschia, P. R. Brady, V. B. Braginsky, M. Branchesi, J. E. Brau, T. Briant, A. Brillet, M. Brinkmann, V. Brisson, P. Brockill, J. E. Broida, A. F. Brooks, D. A. Brown, D. D. Brown, N. M. Brown, S. Brunett, C. C. Buchanan, A. Buikema, T. Bulik, H. J. Bulten, A. Buonanno, D. Buskulic, C. Buy, R. L. Byer, M. Cabero, L. Cadonati, G. Cagnoli, C. Cahillane, J. Calderón Bustillo, T. Callister, E. Calloni, J. B. Camp, K. C. Cannon, J. Cao, C. D. Capano, E. Capocasa, F. Carbognani, S. Caride, J. Casanueva Diaz, C. Casentini, S. Caudill, M. Cavaglià, F. Cavalier, R. Cavalieri, G. Cella, C. B. Cepeda, L. Cerboni Baiardi, G. Cerretani, E. Cesarini, S. J. Chamberlin, M. Chan, S. Chao, P. Charlton, E. Chassande-Mottin, B. D. Cheeseboro, H. Y. Chen, Y. Chen, C. Cheng, A. Chincar-

ini, A. Chiummo, H. S. Cho, M. Cho, J. H. Chow, N. Christensen, Q. Chu, S. Chua, S. Chung, G. Ciani, F. Clara, J. A. Clark, F. Cleva, E. Coccia, P. F. Cohadon, A. Colla, C. G. Collette, L. Cominsky, M. Constancio, A. Conte, L. Conti, D. Cook, T. R. Corbitt, N. Cornish, A. Corsi, S. Cortese, C. A. Costa, M. W. Coughlin, S. B. Coughlin, J. P. Coulon, S. T. Countryman, P. Couvares, E. E. Cowan, D. M. Coward, M. J. Cowart, D. C. Coyne, R. Coyne, K. Craig, J. D. E. Creighton, J. Cripe, S. G. Crowder, A. Cumming, L. Cunningham, E. Cuoco, T. Dal Canton, S. L. Danilishin, S. D'Antonio, K. Danzmann, N. S. Darman, A. Dasgupta, C. F. Da Silva Costa, V. Dattilo, I. Dave, M. Davier, G. S. Davies, E. J. Daw, R. Day, S. De, D. DeBra, G. Debreczeni, J. Degallaix, M. De Laurentis, S. Deléglise, W. Del Pozzo, T. Denker, T. Dent, V. Dergachev, R. De Rosa, R. T. DeRosa, R. DeSalvo, R. C. Devine, S. Dhurand har, M. C. Díaz, L. Di Fiore, M. Di Giovanni, T. Di Girolamo, A. Di Lieto, S. Di Pace, I. Di Palma, A. Di Virgilio, V. Dolique, F. Donovan, K. L. Dooley, S. Doravari, R. Douglas, T. P. Downes, M. Drago, R. W. P. Drever, J. C. Driggers, M. Ducrot, S. E. Dwyer, T. B. Edo, M. C. Edwards, A. Effler, H. B. Eggenstein, P. Ehrens, J. Eichholz, S. S. Eikenberry, W. Engels, R. C. Essick, T. Etzel, M. Evans, T. M. Evans, R. Everett, M. Factourovich, V. Fafone, H. Fair, S. Fairhurst, X. Fan, Q. Fang, S. Farinon, B. Farr, W. M. Farr, M. Favata, M. Fays, H. Fehrmann, M. M. Fejer, E. Fenyvesi, I. Ferrante, E. C. Ferreira, F. Ferrini, F. Fidecaro, I. Fiori, D. Fiorucci, R. P. Fisher, R. Flaminio, M. Fletcher, H. Fong, J. D. Fournier, S. Frasca, F. Frasconi, Z. Frei, A. Freise, R. Frey, V. Frey, P. Fritschel, V. V. Frolov, P. Fulda, M. Fyffe, H. A. G. Gabbard, J. R. Gair, L. Gammaitoni, S. G. Gaonkar, F. Garufi, G. Gaur, N. Gehrels, G. Gemme, P. Geng, E. Genin, A. Gennai, J. George, L. Gergely, V. Germain, Abhirup Ghosh, Archisman Ghosh, S. Ghosh, J. A. Giaime, K. D. Giardina, A. Giazotto, K. Gill, A. Glaefke, E. Goetz, R. Goetz, L. Gondan, G. González, J. M. Gonzalez Castro, A. Gopakumar, N. A. Gordon, M. L. Gorodetsky, S. E. Gossan, M. Gosselin, R. Gouaty, A. Grado, C. Graef, P. B. Graff, M. Granata, A. Grant, S. Gras, C. Gray, G. Greco, A. C. Green, P. Groot, H. Grote, S. Grunewald, G. M. Guidi, X. Guo, A. Gupta, M. K. Gupta, K. E. Gushwa, E. K. Gustafson, R. Gustafson, J. J. Hacker, B. R. Hall, E. D. Hall, H. Hamilton, G. Hammond, M. Haney, M. M. Hanke, J. Hanks, C. Hanna, M. D. Hannam, J. Hanson, T. Hardwick, J. Harms, G. M. Harry, I. W. Harry, M. J. Hart, M. T. Hartman, C. J. Haster, K. Haughian, J. Healy, A. Heidmann, M. C. Heintze, H. Heitmann, P. Hello,

G. Hemming, M. Hendry, I. S. Heng, J. Hennig, J. Henry, A. W. Heptonstall, M. Heurs, S. Hild, D. Hoak, D. Hofman, K. Holt, D. E. Holz, P. Hopkins, J. Hough, E. A. Houston, E. J. Howell, Y. M. Hu, S. Huang, E. A. Huerta, D. Huet, B. Hughey, S. Husa, S. H. Huttner, T. Huynh-Dinh, N. Indik, D. R. Ingram, R. Inta, H. N. Isa, J. M. Isac, M. Isi, T. Isogai, B. R. Iyer, K. Izumi, T. Jacqmin, H. Jang, K. Jani, P. Jaranowski, S. Jawahar, L. Jian, F. Jiménez-Forteza, W. W. Johnson, N. K. Johnson-McDaniel, D. I. Jones, R. Jones, R. J. G. Jonker, L. Ju, Haris K, C. V. Kalaghatgi, V. Kalogera, S. Kandhasamy, G. Kang, J. B. Kanner, S. J. Kapadia, S. Karki, K. S. Karvinen, M. Kasprzack, E. Katsavounidis, W. Katzman, S. Kaufer, T. Kaur, K. Kawabe, F. Kéfélian, M. S. Kehl, D. Keitel, D. B. Kelley, W. Kells, R. Kennedy, J. S. Key, F. Y. Khalili, I. Khan, S. Khan, Z. Khan, E. A. Khazanov, N. Kijbunchoo, Chi-Woong Kim, Chunglee Kim, J. Kim, K. Kim, N. Kim, W. Kim, Y. M. Kim, S. J. Kimbrell, E. J. King, P. J. King, J. S. Kissel, B. Klein, L. Kleybolte, S. Klimenko, S. M. Koehlenbeck, S. Koley, V. Kondrashov, A. Kontos, M. Korobko, W. Z. Korth, I. Kowalska, D. B. Kozak, V. Kringel, B. Krishnan, A. Królak, C. Krueger, G. Kuehn, P. Kumar, R. Kumar, L. Kuo, A. Kutynia, B. D. Lackey, M. Land ry, J. Lange, B. Lantz, P. D. Lasky, M. Laxen, A. Lazzarini, C. Lazzaro, P. Leaci, S. Leavey, E. O. Lebigot, C. H. Lee, H. K. Lee, H. M. Lee, K. Lee, A. Lenon, M. Leonardi, J. R. Leong, N. Leroy, N. Letendre, Y. Levin, J. B. Lewis, T. G. F. Li, A. Libson, T. B. Littenberg, N. A. Lockerbie, A. L. Lombardi, L. T. London, J. E. Lord, M. Lorenzini, V. Loriette, M. Lormand, G. Losurdo, J. D. Lough, C. O. Lousto, H. Lück, A. P. Lundgren, R. Lynch, Y. Ma, B. Machenschalk, M. MacInnis, D. M. Macleod, F. Magaña-Sandoval, L. Magaña Zertuche, R. M. Magee, E. Majorana, I. Maksimovic, V. Malvezzi, N. Man, I. Mandel, V. Mandic, V. Mangano, G. L. Mansell, M. Manske, M. Mantovani, F. Marchesoni, F. Marion, S. Márka, Z. Márka, A. S. Markosyan, E. Maros, F. Martelli, L. Martellini, I. W. Martin, D. V. Martynov, J. N. Marx, K. Mason, A. Masserot, T. J. Massinger, M. Masso-Reid, S. Mastrogiovanni, F. Matichard, L. Matone, N. Mavalvala, N. Mazumder, R. McCarthy, D. E. McClelland, S. McCormick, S. C. McGuire, G. McIntyre, J. McIver, D. J. McManus, T. McRae, S. T. McWilliams, D. Meacher, G. D. Meadors, J. Meidam, A. Melatos, G. Mendell, R. A. Mercer, E. L. Merilh, M. Merzougui, S. Meshkov, C. Messenger, C. Messick, R. Metzdorff, P. M. Meyers, F. Mezzani, H. Miao, C. Michel, H. Middleton, E. E. Mikhailov, L. Milano, A. L. Miller, A. Miller, B. B. Miller, J. Miller, M. Millhouse, Y. Minenkov,

J. Ming, S. Mirshekari, C. Mishra, S. Mitra, V. P. Mitrofanov, G. Mitselmakher, R. Mittleman, A. Moggi, M. Mohan, S. R. P. Mohapatra, M. Montani, B. C. Moore, C. J. Moore, D. Moraru, G. Moreno, S. R. Morriss, K. Mossavi, B. Mours, C. M. Mow-Lowry, G. Mueller, A. W. Muir, Arunava Mukherjee, D. Mukherjee, S. Mukherjee, N. Mukund, A. Mullavey, J. Munch, D. J. Murphy, P. G. Murray, A. Mytidis, I. Nardecchia, L. Naticchioni, R. K. Nayak, K. Nedkova, G. Nelemans, T. J. N. Nelson, M. Neri, A. Neunzert, G. Newton, T. T. Nguyen, A. B. Nielsen, S. Nissanke, A. Nitz, F. Nocera, D. Nolting, M. E. N. Normandin, L. K. Nuttall, J. Oberling, E. Ochsner, J. O'Dell, E. Oelker, G. H. Ogin, J. J. Oh, S. H. Oh, F. Ohme, M. Oliver, P. Oppermann, Richard J. Oram, B. O'Reilly, R. O'Shaughnessy, D. J. Ottaway, H. Overmier, B. J. Owen, A. Pai, S. A. Pai, J. R. Palamos, O. Palashov, C. Palomba, A. Pal-Singh, H. Pan, C. Pankow, F. Pannarale, B. C. Pant, F. Paoletti, A. Paoli, M. A. Papa, H. R. Paris, W. Parker, D. Pascucci, A. Pasqualetti, R. Passaquieti, D. Passuello, B. Patricelli, Z. Patrick, B. L. Pearlstone, M. Pedraza, R. Pedurand, L. Pekowsky, A. Pele, S. Penn, A. Perreca, L. M. Perri, H. P. Pfeiffer, M. Phelps, O. J. Piccinni, M. Pichot, F. Piergiovanni, V. Pierro, G. Pillant, L. Pinard, I. M. Pinto, M. Pitkin, M. Poe, R. Poggiani, P. Popolizio, A. Post, J. Powell, J. Prasad, V. Predoi, T. Prestegard, L. R. Price, M. Prijatelj, M. Principe, S. Privitera, R. Prix, G. A. Prodi, L. Prokhorov, O. Puncken, M. Punturo, P. Puppo, M. Pürrer, H. Qi, J. Qin, S. Qiu, V. Quetschke, E. A. Quintero, R. Quitzow-James, F. J. Raab, D. S. Rabeling, H. Radkins, P. Raffai, S. Raja, C. Rajan, M. Rakhmanov, P. Rapagnani, V. Raymond, M. Razzano, V. Re, J. Read, C. M. Reed, T. Regimbau, L. Rei, S. Reid, D. H. Reitze, H. Rew, S. D. Reyes, F. Ricci, K. Riles, M. Rizzo, N. A. Robertson, R. Robie, F. Robinet, A. Rocchi, L. Rolland, J. G. Rollins, V. J. Roma, J. D. Romano, R. Romano, G. Romanov, J. H. Romie, D. Rosińska, S. Rowan, A. Rüdiger, P. Ruggi, K. Ryan, S. Sachdev, T. Sadecki, L. Sadeghian, M. Sakellariadou, L. Salconi, M. Saleem, F. Salemi, A. Samajdar, L. Sammut, E. J. Sanchez, V. Sandberg, B. Sandeen, J. R. Sand ers, B. Sassolas, B. S. Sathyaprakash, P. R. Saulson, O. E. S. Sauter, R. L. Savage, A. Sawadsky, P. Schale, R. Schilling, J. Schmidt, P. Schmidt, R. Schnabel, R. M. S. Schofield, A. Schönbeck, E. Schreiber, D. Schuette, B. F. Schutz, J. Scott, S. M. Scott, D. Sellers, A. S. Sengupta, D. Sentenac, V. Sequino, A. Sergeev, Y. Setyawati, D. A. Shaddock, T. Shaffer, M. S. Shahriar, M. Shaltev, B. Shapiro, P. Shawhan, A. Sheperd, D. H. Shoemaker, D. M. Shoemaker, K. Siellez,

X. Siemens, M. Sieniawska, D. Sigg, A. D. Silva, A. Singer, L. P. Singer, A. Singh, R. Singh, A. Singhal, A. M. Sintes, B. J. J. Slagmolen, J. R. Smith, N. D. Smith, R. J. E. Smith, E. J. Son, B. Sorazu, F. Sorrentino, T. Souradeep, A. K. Srivastava, A. Staley, M. Steinke, J. Steinlechner, S. Steinlechner, D. Steinmeyer, B. C. Stephens, S. P. Stevenson, R. Stone, K. A. Strain, N. Straniero, G. Stratta, N. A. Strauss, S. Strigin, R. Sturani, A. L. Stuver, T. Z. Summerscales, L. Sun, S. Sunil, P. J. Sutton, B. L. Swinkels, M. J. Szczepańczyk, M. Tacca, D. Talukder, D. B. Tanner, M. Tápai, S. P. Tarabrin, A. Taracchini, R. Taylor, T. Theeg, M. P. Thirugnanasamband am, E. G. Thomas, M. Thomas, P. Thomas, K. A. Thorne, E. Thrane, S. Tiwari, V. Tiwari, K. V. Tokmakov, K. Toland, C. Tomlinson, M. Tonelli, Z. Tornasi, C. V. Torres, C. I. Torrie, D. Töyrä, F. Travasso, G. Traylor, D. Trifirò, M. C. Tringali, L. Trozzo, M. Tse, M. Turconi, D. Tuyenbayev, D. Ugolini, C. S. Unnikrishnan, A. L. Urban, S. A. Usman, H. Vahlbruch, G. Vajente, G. Valdes, M. Vallisneri, N. van Bakel, M. van Beuzekom, J. F. J. van den Brand, C. Van Den Broeck, D. C. Vand er-Hyde, L. van der Schaaf, J. V. van Heijningen, A. A. van Veggel, M. Vardaro, S. Vass, M. Vasúth, R. Vaulin, A. Vecchio, G. Vedovato, J. Veitch, P. J. Veitch, K. Venkateswara, D. Verkindt, F. Vetrano, A. Viceré, S. Vinciguerra, D. J. Vine, J. Y. Vinet, S. Vitale, T. Vo, H. Vocca, C. Vorvick, D. V. Voss, W. D. Vousden, S. P. Vyatchanin, A. R. Wade, L. E. Wade, M. Wade, M. Walker, L. Wallace, S. Walsh, G. Wang, H. Wang, M. Wang, X. Wang, Y. Wang, R. L. Ward, J. Warner, M. Was, B. Weaver, L. W. Wei, M. Weinert, A. J. Weinstein, R. Weiss, L. Wen, P. Weßels, T. Westphal, K. Wette, J. T. Whelan, B. F. Whiting, R. D. Williams, A. R. Williamson, J. L. Willis, B. Willke, M. H. Wimmer, W. Winkler, C. C. Wipf, H. Wittel, G. Woan, J. Woehler, J. Worden, J. L. Wright, D. S. Wu, G. Wu, J. Yablon, W. Yam, H. Yamamoto, C. C. Yancey, H. Yu, M. Yvert, A. Zadrożny, L. Zangrando, M. Zanolin, J. P. Zendri, M. Zevin, L. Zhang, M. Zhang, Y. Zhang, C. Zhao, M. Zhou, Z. Zhou, X. J. Zhu, M. E. Zucker, S. E. Zuraw, J. Zweizig, M. Boyle, D. Hemberger, L. E. Kidder, G. Lovelace, S. Ossokine, M. Scheel, B. Szilagyi, S. Teukolsky, LIGO Scientific Collaboration and VIRGO Collaboration (2016), "GW151226: Observation of Gravitational Waves from a 22-Solar-Mass Binary Black Hole Coalescence." *prl*, 116, 241103.

Abbott, R., T. D. Abbott, S. Abraham, F. Acernese, K. Ackley, C. Adams, R. X. Ad-

hikari, V. B. Adya, C. Affeldt, M. Agathos, K. Agatsuma, N. Aggarwal, O. D. Aguiar, A. Aich, L. Aiello, A. Ain, P. Ajith, S. Akcay, G. Allen, A. Allocca, P. A. Altin, A. Amato, S. Anand, A. Ananyeva, S. B. Anderson, W. G. Anderson, S. V. Angelova, S. Ansoldi, S. Antier, S. Appert, K. Arai, M. C. Araya, J. S. Areeda, M. Arène, N. Arnaud, S. M. Aronson, K. G. Arun, Y. Asali, S. Ascenzi, G. Ashton, S. M. Aston, P. Astone, F. Aubin, P. Aufmuth, K. AultONeal, C. Austin, V. Avendano, S. Babak, P. Bacon, F. Badaracco, M. K. M. Bader, S. Bae, A. M. Baer, J. Baird, F. Baldaccini, G. Ballardin, S. W. Ballmer, A. Bals, A. Balsamo, G. Baltus, S. Banagiri, D. Bankar, R. S. Bankar, J. C. Barayoga, C. Barbieri, B. C. Barish, D. Barker, K. Barkett, P. Barneo, F. Barone, B. Barr, L. Barsotti, M. Barsuglia, D. Barta, J. Bartlett, I. Bartos, R. Bassiri, A. Basti, M. Bawaj, J. C. Bayley, M. Bazzan, B. Bécsy, M. Bejger, I. Belahcene, A. S. Bell, D. Beniwal, M. G. Benjamin, J. D. Bentley, F. Bergamin, B. K. Berger, G. Bergmann, S. Bernuzzi, C. P. L. Berry, D. Bersanetti, A. Bertolini, J. Betzwieser, R. Bhandare, A. V. Bhandari, J. Bidler, E. Biggs, I. A. Bilenko, G. Billingsley, R. Birney, O. Birnholtz, S. Biscans, M. Bischi, S. Biscoveanu, A. Bisht, G. Bissenbayeva, M. Bitossi, M. A. Bizouard, J. K. Blackburn, J. Blackman, C. D. Blair, D. G. Blair, R. M. Blair, F. Bobba, N. Bode, M. Boer, Y. Boetzel, G. Bogaert, F. Bondu, E. Bonilla, R. Bonnand, P. Booker, B. A. Boom, R. Bork, V. Boschi, S. Bose, V. Bossilkov, J. Bosveld, Y. Bouffanais, A. Bozzi, C. Bradaschia, P. R. Brady, A. Bramley, M. Branchesi, J. E. Brau, M. Breschi, T. Briant, J. H. Briggs, F. Brighenti, A. Brillet, M. Brinkmann, P. Brockill, A. F. Brooks, J. Brooks, D. D. Brown, S. Brunett, G. Bruno, R. Bruntz, A. Buikema, T. Bulik, H. J. Bulten, A. Buonanno, R. Buscicchio, D. Buskulic, R. L. Byer, M. Cabero, L. Cadonati, G. Cagnoli, C. Cahillane, J. Calderón Bustillo, J. D. Callaghan, T. A. Callister, E. Calloni, J. B. Camp, M. Canepa, K. C. Cannon, H. Cao, J. Cao, G. Carapella, F. Carbognani, S. Caride, M. F. Carney, G. Carullo, J. Casanueva Diaz, C. Casentini, J. Castañeda, S. Caudill, M. Cavaglià, F. Cavalier, R. Cavalieri, G. Cella, P. Cerdá-Durán, E. Cesarini, O. Chaibi, K. Chakravarti, C. Chan, M. Chan, K. Chandra, S. Chao, P. Charlton, E. A. Chase, E. Chassande-Mottin, D. Chatterjee, M. Chaturvedi, K. Chatziioannou, H. Y. Chen, X. Chen, Y. Chen, H.-P. Cheng, C. K. Cheong, H. Y. Chia, F. Chiadini, R. Chierici, A. Chincarini, A. Chiummo, G. Cho, H. S. Cho, M. Cho, N. Christensen, Q. Chu, S. Chua, K. W. Chung, S. Chung, G. Ciani, P. Ciecielag, M. Cieślar, A. A. Ciobanu, R. Ciolfi, F. Cipriano, A. Cirone, F. Clara, J. A. Clark,

P. Clearwater, S. Clesse, F. Cleva, E. Coccia, P.-F. Cohadon, D. Cohen, M. Colleoni, C. G. Collette, C. Collins, M. Colpi, M. Constancio, L. Conti, S. J. Cooper, P. Corban, T. R. Corbitt, I. Cordero-Carrión, S. Corezzi, K. R. Corley, N. Cornish, D. Corre, A. Corsi, S. Cortese, C. A. Costa, R. Cotesta, M. W. Coughlin, S. B. Coughlin, J.-P. Coulon, S. T. Countryman, P. Couvares, P. B. Covas, D. M. Coward, M. J. Cowart, D. C. Coyne, R. Coyne, J. D. E. Creighton, T. D. Creighton, J. Cripe, M. Croquette, S. G. Crowder, J.-R. Cudell, T. J. Cullen, A. Cumming, R. Cummings, L. Cunningham, E. Cuoco, M. Curylo, T. Dal Canton, G. Dálya, A. Dana, L. M. Daneshgaran-Bajastani, B. D'Angelo, S. L. Danilishin, S. D'Antonio, K. Danzmann, C. Darsow-Fromm, A. Dasgupta, L. E. H. Datrier, V. Dattilo, I. Dave, M. Davier, G. S. Davies, D. Davis, E. J. Daw, D. DeBra, M. Deenadayalan, J. Degallaix, M. De Laurentis, S. Deléglise, M. Delfavero, N. De Lillo, W. Del Pozzo, L. M. DeMarchi, V. D'Emilio, N. Demos, T. Dent, R. De Pietri, R. De Rosa, C. De Rossi, R. DeSalvo, O. de Varona, S. Dhurandhar, M. C. Díaz, M. Diaz-Ortiz, T. Dietrich, L. Di Fiore, C. Di Fronzo, C. Di Giorgio, F. Di Giovanni, M. Di Giovanni, T. Di Girolamo, A. Di Lieto, B. Ding, S. Di Pace, I. Di Palma, F. Di Renzo, A. K. Divakarla, A. Dmitriev, Z. Doctor, F. Donovan, K. L. Dooley, S. Doravari, I. Dorrington, T. P. Downes, M. Drago, J. C. Driggers, Z. Du, J.-G. Ducoin, P. Dupej, O. Durante, D. D'Urso, S. E. Dwyer, P. J. Easter, G. Eddolls, B. Edelman, T. B. Edo, O. Edy, A. Effler, P. Ehrens, J. Eichholz, S. S. Eikenberry, M. Eisenmann, R. A. Eisenstein, A. Ejlli, L. Errico, R. C. Essick, H. Estelles, D. Estevez, Z. B. Etienne, T. Etzel, M. Evans, T. M. Evans, B. E. Ewing, V. Fafone, S. Fairhurst, X. Fan, S. Farinon, B. Farr, W. M. Farr, E. J. Fauchon-Jones, M. Favata, M. Fays, M. Fazio, J. Feicht, M. M. Fejer, F. Feng, E. Fenyvesi, D. L. Ferguson, A. Fernandez-Galiana, I. Ferrante, E. C. Ferreira, T. A. Ferreira, F. Fidecaro, I. Fiori, D. Fiorucci, M. Fishbach, R. P. Fisher, R. Fittipaldi, M. Fitz-Axen, V. Fiumara, R. Flaminio, E. Floden, E. Flynn, H. Fong, J. A. Font, P. W. F. Forsyth, J.-D. Fournier, S. Frasca, F. Frasconi, Z. Frei, A. Freise, R. Frey, V. Frey, P. Fritschel, V. V. Frolov, G. Fronzè, P. Fulda, M. Fyffe, H. A. Gabbard, B. U. Gadre, S. M. Gaebel, J. R. Gair, S. Galaudage, D. Ganapathy, A. Ganguly, S. G. Gaonkar, C. García-Quirós, F. Garufi, B. Gateley, S. Gaudio, V. Gayathri, G. Gemme, E. Genin, A. Gennai, D. George, J. George, L. Gergely, S. Ghonge, Abhirup Ghosh, Archisman Ghosh, S. Ghosh, B. Giacomazzo, J. A. Giaime, K. D. Giardina, D. R. Gibson, C. Gier, K. Gill, J. Glanzer, J. Gniesmer,

P. Godwin, E. Goetz, R. Goetz, N. Gohlke, B. Goncharov, G. González, A. Gopakumar, S. E. Gossan, M. Gosselin, R. Gouaty, B. Grace, A. Grado, M. Granata, A. Grant, S. Gras, P. Grassia, C. Gray, R. Gray, G. Greco, A. C. Green, R. Green, E. M. Gretarsson, H. L. Griggs, G. Grignani, A. Grimaldi, S. J. Grimm, H. Grote, S. Grunewald, P. Gruning, G. M. Guidi, A. R. Guimaraes, G. Guixé, H. K. Gulati, Y. Guo, A. Gupta, Anchal Gupta, P. Gupta, E. K. Gustafson, R. Gustafson, L. Haegel, O. Halim, E. D. Hall, E. Z. Hamilton, G. Hammond, M. Haney, M. M. Hanke, J. Hanks, C. Hanna, M. D. Hannam, O. A. Hannuksela, T. J. Hansen, J. Hanson, T. Harder, T. Hardwick, K. Haris, J. Harms, G. M. Harry, I. W. Harry, R. K. Hasskew, C.-J. Haster, K. Haughian, F. J. Hayes, J. Healy, A. Heidmann, M. C. Heintze, J. Heinze, H. Heitmann, F. Hellman, P. Hello, G. Hemming, M. Hendry, I. S. Heng, E. Hennes, J. Hennig, M. Heurs, S. Hild, T. Hinderer, S. Y. Hoback, S. Hochheim, E. Hofgard, D. Hofman, A. M. Holgado, N. A. Holland, K. Holt, D. E. Holz, P. Hopkins, C. Horst, J. Hough, E. J. Howell, C. G. Hoy, Y. Huang, M. T. Hübner, E. A. Huerta, D. Huet, B. Hughey, V. Hui, S. Husa, S. H. Huttner, R. Huxford, T. Huynh-Dinh, B. Idzkowski, A. Iess, H. Inchauspe, C. Ingram, G. Intini, J.-M. Isac, M. Isi, B. R. Iyer, T. Jacqmin, S. J. Jadhav, S. P. Jadhav, A. L. James, K. Jani, N. N. Janthalur, P. Jaranowski, D. Jariwala, R. Jaume, A. C. Jenkins, J. Jiang, G. R. Johns, N. K. Johnson-McDaniel, A. W. Jones, D. I. Jones, J. D. Jones, P. Jones, R. Jones, R. J. G. Jonker, L. Ju, J. Junker, C. V. Kalaghatgi, V. Kalogera, B. Kamai, S. Kandhasamy, G. Kang, J. B. Kanner, S. J. Kapadia, S. Karki, R. Kashyap, M. Kasprzack, W. Kastaun, S. Katsanevas, E. Katsavounidis, W. Katzman, S. Kaufer, K. Kawabe, F. Kéfélian, D. Keitel, A. Keivani, R. Kennedy, J. S. Key, S. Khadka, F. Y. Khalili, I. Khan, S. Khan, Z. A. Khan, E. A. Khazanov, N. Khetan, M. Khursheed, N. Kijbunchoo, Chunglee Kim, G. J. Kim, J. C. Kim, K. Kim, W. Kim, W. S. Kim, Y.-M. Kim, C. Kimball, P. J. King, M. Kinley-Hanlon, R. Kirchhoff, J. S. Kissel, L. Kleybolte, S. Klimenko, T. D. Knowles, E. Knyazev, P. Koch, S. M. Koehlenbeck, G. Koekoek, S. Koley, V. Kondrashov, A. Kontos, N. Koper, M. Korobko, W. Z. Korth, M. Kovalam, D. B. Kozak, V. Kringel, N. V. Krishnendu, A. Królak, N. Krupinski, G. Kuehn, A. Kumar, P. Kumar, Rahul Kumar, Rakesh Kumar, S. Kumar, L. Kuo, A. Kutynia, B. D. Lackey, D. Laghi, E. Lalande, T. L. Lam, A. Lamberts, M. Landry, B. B. Lane, R. N. Lang, J. Lange, B. Lantz, R. K. Lanza, I. La Rosa, A. Lartaux-Vollard, P. D. Lasky, M. Laxen, A. Lazzarini, C. Lazzaro, P. Leaci, S. Leavey, Y. K.

Lecoeuche, C. H. Lee, H. M. Lee, H. W. Lee, J. Lee, K. Lee, J. Lehmann, N. Leroy, N. Letendre, Y. Levin, A. K. Y. Li, J. Li, K. li, T. G. F. Li, X. Li, F. Linde, S. D. Linker, J. N. Linley, T. B. Littenberg, J. Liu, X. Liu, M. Llorens-Monteagudo, R. K. L. Lo, A. Lockwood, L. T. London, A. Longo, M. Lorenzini, V. Loriette, M. Lormand, G. Losurdo, J. D. Lough, C. O. Lousto, G. Lovelace, H. Lück, D. Lumaca, A. P. Lundgren, Y. Ma, R. Macas, S. Macfoy, M. MacInnis, D. M. Macleod, I. A. O. MacMillan, A. Macquet, I. Magaña Hernandez, F. Magaña Sandoval, R. M. Magee, E. Majorana, I. Maksimovic, A. Malik, N. Man, V. Mandic, V. Mangano, G. L. Mansell, M. Manske, M. Mantovani, M. Mapelli, F. Marchesoni, F. Marion, S. Márka, Z. Márka, C. Markakis, A. S. Markosyan, A. Markowitz, E. Maros, A. Marquina, S. Marsat, F. Martelli, I. W. Martin, R. M. Martin, V. Martinez, D. V. Martynov, H. Masalehdan, K. Mason, E. Massera, A. Masserot, T. J. Massinger, M. Masso-Reid, S. Mastrogiovanni, A. Matas, F. Matichard, N. Mavalvala, E. Maynard, J. J. McCann, R. McCarthy, D. E. McClelland, S. McCormick, L. McCuller, S. C. McGuire, C. McIsaac, J. McIver, D. J. McManus, T. McRae, S. T. McWilliams, D. Meacher, G. D. Meadors, M. Mehmet, A. K. Mehta, E. Mejuto Villa, A. Melatos, G. Mendell, R. A. Mercer, L. Mereni, K. Merfeld, E. L. Merilh, J. D. Merritt, M. Merzougui, S. Meshkov, C. Messenger, C. Messick, R. Metzdorff, P. M. Meyers, F. Meylahn, A. Mhaske, A. Miani, H. Miao, I. Michaloliakos, C. Michel, H. Middleton, L. Milano, A. L. Miller, M. Millhouse, J. C. Mills, E. Milotti, M. C. Milovich-Goff, O. Minazzoli, Y. Minenkov, A. Mishkin, C. Mishra, T. Mistry, S. Mitra, V. P. Mitrofanov, G. Mitselmakher, R. Mittleman, G. Mo, K. Mogushi, S. R. P. Mohapatra, S. R. Mohite, M. Molina-Ruiz, M. Mondin, M. Montani, C. J. Moore, D. Moraru, F. Morawski, G. Moreno, S. Morisaki, B. Mours, C. M. Mow-Lowry, S. Mozzon, F. Muciaccia, Arunava Mukherjee, D. Mukherjee, S. Mukherjee, Subroto Mukherjee, N. Mukund, A. Mullavey, J. Munch, E. A. Muñiz, P. G. Murray, A. Nagar, I. Nardecchia, L. Naticchioni, R. K. Nayak, B. F. Neil, J. Neilson, G. Nelemans, T. J. N. Nelson, M. Nery, A. Neunzert, K. Y. Ng, S. Ng, C. Nguyen, P. Nguyen, D. Nichols, S. A. Nichols, S. Nissanke, A. Nitz, F. Nocera, M. Noh, C. North, D. Nothard, L. K. Nuttall, J. Oberling, B. D. O'Brien, G. Oganesyan, G. H. Ogin, J. J. Oh, S. H. Oh, F. Ohme, H. Ohta, M. A. Okada, M. Oliver, C. Olivetto, P. Oppermann, Richard J. Oram, B. O'Reilly, R. G. Ormiston, L. F. Ortega, R. O'Shaughnessy, S. Ossokine, C. Osthelder, D. J. Ottaway, H. Overmier, B. J. Owen, A. E. Pace, G. Pagano,

M. A. Page, G. Pagliaroli, A. Pai, S. A. Pai, J. R. Palamos, O. Palashov, C. Palomba, H. Pan, P. K. Panda, P. T. H. Pang, C. Pankow, F. Pannarale, B. C. Pant, F. Paoletti, A. Paoli, A. Parida, W. Parker, D. Pascucci, A. Pasqualetti, R. Passaquieti, D. Passuello, B. Patricelli, E. Payne, B. L. Pearlstone, T. C. Pechsiri, A. J. Pedersen, M. Pedraza, A. Pele, S. Penn, A. Perego, C. J. Perez, C. Périgois, A. Perreca, S. Perriès, J. Petermann, H. P. Pfeiffer, M. Phelps, K. S. Phukon, O. J. Piccinni, M. Pichot, M. Piendibene, F. Piergiovanni, V. Pierro, G. Pillant, L. Pinard, I. M. Pinto, K. Piotrzkowski, M. Pirello, M. Pitkin, W. Plastino, R. Poggiani, D. Y. T. Pong, S. Ponrathnam, P. Popolizio, E. K. Porter, J. Powell, A. K. Prajapati, K. Prasai, R. Prasanna, G. Pratten, T. Prestegard, M. Principe, G. A. Prodi, L. Prokhorov, M. Punturo, P. Puppo, M. Pürrer, H. Qi, V. Quetschke, P. J. Quinonez, F. J. Raab, G. Raaijmakers, H. Radkins, N. Radulesco, P. Raffai, H. Rafferty, S. Raja, C. Rajan, B. Rajbhandari, M. Rakhmanov, K. E. Ramirez, A. Ramos-Buades, Javed Rana, K. Rao, P. Rapagnani, V. Raymond, M. Razzano, J. Read, T. Regimbau, L. Rei, S. Reid, D. H. Reitze, P. Rettegno, F. Ricci, C. J. Richardson, J. W. Richardson, P. M. Ricker, G. Riemenschneider, K. Riles, M. Rizzo, N. A. Robertson, F. Robinet, A. Rocchi, R. D. Rodriguez-Soto, L. Rolland, J. G. Rollins, V. J. Roma, M. Romanelli, R. Romano, C. L. Romel, I. M. Romero-Shaw, J. H. Romie, C. A. Rose, D. Rose, K. Rose, D. Rosińska, S. G. Rosofsky, M. P. Ross, S. Rowan, S. J. Rowlinson, P. K. Roy, Santosh Roy, Soumen Roy, P. Ruggi, G. Rutins, K. Ryan, S. Sachdev, T. Sadecki, M. Sakellariadou, O. S. Salafia, L. Salconi, M. Saleem, F. Salemi, A. Samajdar, E. J. Sanchez, L. E. Sanchez, N. Sanchis-Gual, J. R. Sanders, K. A. Santiago, E. Santos, N. Sarin, B. Sassolas, B. S. Sathyaprakash, O. Sauter, R. L. Savage, V. Savant, D. Sawant, S. Sayah, D. Schaetzl, P. Schale, M. Scheel, J. Scheuer, P. Schmidt, R. Schnabel, R. M. S. Schofield, A. Schönbeck, E. Schreiber, B. W. Schulte, B. F. Schutz, O. Schwarm, E. Schwartz, J. Scott, S. M. Scott, E. Seidel, D. Sellers, A. S. Sengupta, N. Sennett, D. Sentenac, V. Sequino, A. Sergeev, Y. Setyawati, D. A. Shaddock, T. Shaffer, S. Sharifi, M. S. Shahriar, A. Sharma, P. Sharma, P. Shawhan, H. Shen, M. Shikauchi, R. Shink, D. H. Shoemaker, D. M. Shoemaker, K. Shukla, S. ShyamSundar, K. Siellez, M. Sieniawska, D. Sigg, L. P. Singer, D. Singh, N. Singh, A. Singha, A. Singhal, A. M. Sintes, V. Sipala, V. Skliris, B. J. J. Slagmolen, T. J. Slaven-Blair, J. Smetana, J. R. Smith, R. J. E. Smith, S. Somala, E. J. Son, S. Soni, B. Sorazu, V. Sordini, F. Sorrentino, T. Souradeep, E. Sow-

ell, A. P. Spencer, M. Spera, A. K. Srivastava, V. Srivastava, K. Staats, C. Stachie, M. Standke, D. A. Steer, M. Steinke, J. Steinlechner, S. Steinlechner, D. Steinmeyer, S. Stevenson, D. Stocks, D. J. Stops, M. Stover, K. A. Strain, G. Stratta, A. Strunk, R. Sturani, A. L. Stuver, S. Sudhagar, V. Sudhir, T. Z. Summerscales, L. Sun, S. Sunil, A. Sur, J. Suresh, P. J. Sutton, B. L. Swinkels, M. J. Szczepańczyk, M. Tacca, S. C. Tait, C. Talbot, A. J. Tanasijczuk, D. B. Tanner, D. Tao, M. Tápai, A. Tapia, E. N. Tapia San Martin, J. D. Tasson, R. Taylor, R. Tenorio, L. Terkowski, M. P. Thirugnanasambandam, M. Thomas, P. Thomas, J. E. Thompson, S. R. Thondapu, K. A. Thorne, E. Thrane, C. L. Tinsman, T. R. Saravanan, Shubhanshu Tiwari, S. Tiwari, V. Tiwari, K. Toland, M. Tonelli, Z. Tornasi, A. Torres-Forné, C. I. Torrie, I. Tosta e Melo, D. Töyrä, F. Travasso, G. Traylor, M. C. Tringali, A. Tripathee, A. Trovato, R. J. Trudeau, K. W. Tsang, M. Tse, R. Tso, L. Tsukada, D. Tsuna, T. Tsutsui, M. Turconi, A. S. Ubhi, R. Udall, K. Ueno, D. Ugolini, C. S. Unnikrishnan, A. L. Urban, S. A. Usman, A. C. Utina, H. Vahlbruch, G. Vajente, G. Valdes, M. Valentini, N. van Bakel, M. van Beuzekom, J. F. J. van den Brand, C. Van Den Broeck, D. C. Vander-Hyde, L. van der Schaaf, J. V. Van Heijningen, A. A. van Veggel, M. Vardaro, V. Varma, S. Vass, M. Vasúth, A. Vecchio, G. Vedovato, J. Veitch, P. J. Veitch, K. Venkateswara, G. Venugopalan, D. Verkindt, D. Veske, F. Vetrano, A. Viceré, A. D. Viets, S. Vinciguerra, D. J. Vine, J.-Y. Vinet, S. Vitale, Francisco Hernandez Vivanco, T. Vo, H. Vocca, C. Vorvick, S. P. Vyatchanin, A. R. Wade, L. E. Wade, M. Wade, R. Walet, M. Walker, G. S. Wallace, L. Wallace, S. Walsh, J. Z. Wang, S. Wang, W. H. Wang, R. L. Ward, Z. A. Warden, J. Warner, M. Was, J. Watchi, B. Weaver, L.-W. Wei, M. Weinert, A. J. Weinstein, R. Weiss, F. Wellmann, L. Wen, P. Weßels, J. W. Westhouse, K. Wette, J. T. Whelan, B. F. Whiting, C. Whittle, D. M. Wilken, D. Williams, A. Williamson, J. L. Willis, B. Willke, W. Winkler, C. C. Wipf, H. Wittel, G. Woan, J. Woehler, J. K. Wofford, I. C. F. Wong, J. L. Wright, D. S. Wu, D. M. Wysocki, L. Xiao, H. Yamamoto, L. Yang, Y. Yang, Z. Yang, M. J. Yap, M. Yazback, D. W. Yeeles, Hang Yu, Haocun Yu, S. H. R. Yuen, A. K. Zadrożny, A. Zadrożny, M. Zanolin, T. Zelenova, J.-P. Zendri, M. Zevin, J. Zhang, L. Zhang, T. Zhang, C. Zhao, G. Zhao, M. Zhou, Z. Zhou, X. J. Zhu, A. B. Zimmerman, M. E. Zucker and J. Zweizig (2020), "Gw190521: A binary black hole merger with a total mass of 150 $M_{\odot}$." *Phys. Rev. Lett.*, 125, 101102, URL `https://link.aps.org/doi/10.1103/PhysRevLett.125.101102`.

Abolmasov, Pavel, S. Fabrika, O. Sholukhova and Taro Kotani (2008), "Optical Spectroscopy of the ULX-Associated Nebula MF16." *arXiv e-prints*, arXiv:0809.0409.

Abramowicz, M. A., B. Czerny, J. P. Lasota and E. Szuszkiewicz (1988), "Slim Accretion Disks." *apj*, 332, 646.

Bachetti, M. (2018), "HENDRICS: High ENergy Data Reduction Interface from the Command Shell." Astrophysics Source Code Library.

Bachetti, M., F. A. Harrison, D. J. Walton, B. W. Grefenstette, D. Chakrabarty, F. Fürst, D. Barret, A. Beloborodov, S. E. Boggs, F. E. Christensen, W. W. Craig, A. C. Fabian, C. J. Hailey, A. Hornschemeier, V. Kaspi, S. R. Kulkarni, T. Maccarone, J. M. Miller, V. Rana, D. Stern, S. P. Tendulkar, J. Tomsick, N. A. Webb and W. W. Zhang (2014), "An ultraluminous X-ray source powered by an accreting neutron star." *nature*, 514, 202–204.

Bachetti, Matteo, Thomas J. Maccarone, Murray Brightman, McKinley C. Brumback, Felix Fürst, Fiona A. Harrison, Marianne Heida, Gian Luca Israel, Matthew J. Middleton, John A. Tomsick, Natalie A. Webb and Dominic J. Walton (2020), "All at Once: Transient Pulsations, Spin-down, and a Glitch from the Pulsating Ultraluminous X-Ray Source M82 X-2." *apj*, 891, 44.

Bachetti, Matteo, Vikram Rana, Dominic J. Walton, Didier Barret, Fiona A. Harrison, Steven E. Boggs, Finn E. Christensen, William W. Craig, Andrew C. Fabian, Felix Fürst, Brian W. Grefenstette, Charles J. Hailey, Ann Hornschemeier, Kristin K. Madsen, Jon M. Miller, Andrew F. Ptak, Daniel Stern, Natalie A. Webb and William W. Zhang (2013), "The Ultraluminous X-Ray Sources NGC 1313 X-1 and X-2: A Broadband Study with NuSTAR and XMM-Newton." *apj*, 778, 163.

Balbus, Steven A. and John F. Hawley (1991), "A Powerful Local Shear Instability in Weakly Magnetized Disks. I. Linear Analysis." *apj*, 376, 214.

Basko, M. M. and R. A. Sunyaev (1976a), "The limiting luminosity of accreting neutron stars with magnetic fields." *mnras*, 175, 395–417.

Basko, M. M. and R. A. Sunyaev (1976b), "The role of the Alfvén surface in forming x-ray pulses in accreting pulsars." *sovast*, 20, 537.

Belczynski, Krzysztof, Tomasz Bulik, Chris L. Fryer, Ashley Ruiter, Francesca Valsecchi, Jorick S. Vink and Jarrod R. Hurley (2010), "On the Maximum Mass of Stellar Black Holes." *apj*, 714, 1217–1226.

Belfiore, Andrea, Paolo Esposito, Fabio Pintore, Giovanni Novara, Ruben Salvaterra, Andrea De Luca, Andrea Tiengo, Patrizia Caraveo, Felix Fürst, Gian Luca Israel, Danilo Magistrali, Martino Marelli, Sandro Mereghetti, Alessandro Papitto, Guillermo A. Rodríguez Castillo, Chiara Salvaggio, Luigi Stella, Dominic J. Walton, Anna Wolter and Luca Zampieri (2020), "Diffuse X-ray emission around an ultraluminous X-ray pulsar." *Nature Astronomy*, 4, 147–152.

Bell, S. J. and A. Hewish (1967), "Angular Size and Flux Density of the Small Source in the Crab Nebula at 81.5 Mc/s." *nature*, 213, 1214–1216.

Belloni, Tomaso M. (2010), "Fast variability from X-ray binaries." *arXiv e-prints*, arXiv:1007.5404.

Bhattacharya, D. and E. P. J. van den Heuvel (1991), "Formation and evolution of binary and millisecond radio pulsars." *physrep*, 203, 1–124.

Blandford, R. D. and A. Königl (1979), "Relativistic jets as compact radio sources." *apj*, 232, 34–48.

Bondi, H. and F. Hoyle (1944), "On the mechanism of accretion by stars." *mnras*, 104, 273.

Bradt, H., W. Mayer, S. Naranan, S. Rappaport and G. Spada (1967), "Evidence for X-Radiation from the Radio Galaxy M87." *apjl*, 150, L199.

Bradt, Hale V. D., Takaya Ohashi and Kenneth A. Pounds (1992), "X-ray astronomy missions." *araa*, 30, 391–427.

Brightman, M., F. A. Harrison, F. Fürst, M. J. Middleton, D. J. Walton, D. Stern, A. C. Fabian, M. Heida, D. Barret and M. Bachetti (2018), "Magnetic field strength of a neutron-star-powered ultraluminous X-ray source." *Nature Astronomy*, 2, 312–316.

Brightman, Murray, Fiona A. Harrison, Matteo Bachetti, Yanjun Xu, Felix Fürst, Dominic J. Walton, Andrew Ptak, Mihoko Yukita and Andreas Zezas (2019), "A 60 day

Super-orbital Period Originating from the Ultraluminous X-Ray Pulsar in M82." *apj*, 873, 115.

Buccheri, R., K. Bennett, G. F. Bignami, J. B. G. M. Bloemen, V. Boriakoff, P. A. Caraveo, W. Hermsen, G. Kanbach, R. N. Manchester, J. L. Masnou, H. A. Mayer-Hasselwander, M. E. Özel, J. A. Paul, B. Sacco, L. Scarsi and A. W. Strong (1983), "Search for pulsed gamma-ray emission from radio pulsars in the COS-B data." *aap*, 128, 245–251.

Caballero, I. and J. Wilms (2012), "X-ray pulsars: a review." *memsai*, 83, 230.

Campana, Sergio, Luigi Stella, Sandro Mereghetti and Domitilla de Martino (2018), "A universal relation for the propeller mechanisms in magnetic rotating stars at different scales." *aap*, 610, A46.

Cardelli, Jason A., Geoffrey C. Clayton and John S. Mathis (1989), "The Relationship between Infrared, Optical, and Ultraviolet Extinction." *apj*, 345, 245.

Carpano, S., F. Haberl, C. Maitra and G. Vasilopoulos (2018), "Discovery of pulsations from NGC 300 ULX1 and its fast period evolution." *mnras*, 476, L45–L49.

Castelli, F. and R. L. Kurucz (2003), "New Grids of ATLAS9 Model Atmospheres." In *Modelling of Stellar Atmospheres* (N. Piskunov, W. W. Weiss, and D. F. Gray, eds.), volume 210 of *IAU Symposium*, A20.

Castor, J., R. McCray and R. Weaver (1975), "Interstellar bubbles." *apjl*, 200, L107–L110.

Charles, P. A. and M. J. Coe (2006), *Optical, ultraviolet and infrared observations of X-ray binaries*, volume 39, 215–265.

Chashkina, Anna, Pavel Abolmasov and Juri Poutanen (2017), "Super-Eddington accretion on to a magnetized neutron star." *mnras*, 470, 2799–2813.

Chelovekov, I. V. and S. A. Grebenev (2007), "Detection of the first thermonuclear X-ray burst from AX J1754.2-2754." *Astronomy Letters*, 33, 807–813.

Colbert, E. J. M. and R. F. Mushotzky (1999), "The Nature of Accreting Black Holes in Nearby Galaxy Nuclei." *apj*, 519, 89–107.

Colbert, Edward J. M., Timothy M. Heckman, Andrew F. Ptak, David K. Strickland and Kimberly A. Weaver (2004), "Old and Young X-Ray Point Source Populations in Nearby Galaxies." *apj*, 602, 231–248.

Corbel, S. and R. P. Fender (2002), "Near-Infrared Synchrotron Emission from the Compact Jet of GX 339-4." *apjl*, 573, L35–L39.

Corbel, S., M. A. Nowak, R. P. Fender, A. K. Tzioumis and S. Markoff (2003), "Radio/X-ray correlation in the low/hard state of GX 339-4." *aap*, 400, 1007–1012.

Cruces, Marilyn, Andreas Reisenegger and Thomas M. Tauris (2019), "On the weak magnetic field of millisecond pulsars: does it decay before accretion?" *mnras*, 490, 2013–2022.

Cseh, D., J. C. A. Miller-Jones, P. G. Jonker, F. Grisé, Z. Paragi, S. Corbel, H. Falcke, S. Frey, P. Kaaret and E. Körding (2015), "The evolution of a jet ejection of the ultraluminous X-ray source Holmberg II X-1." *mnras*, 452, 24–31.

Cumming, Andrew, Phil Arras and Ellen Zweibel (2004), "Magnetic Field Evolution in Neutron Star Crusts Due to the Hall Effect and Ohmic Decay." *apj*, 609, 999–1017.

Cunningham, C. (1976), "Returning radiation in accretion disks around black holes." *apj*, 208, 534–549.

Czerny, Bozena (2019), "Slim Accretion Disks: Theory and Observational Consequences." *Universe*, 5, 131.

Davis, J. E., M. W. Bautz, D. Dewey, R. K. Heilmann, J. C. Houck, D. P. Huenemoerder, H. L. Marshall, M. A. Nowak, M. L. Schattenburg, N. S. Schulz and R. K. Smith (2012), "Raytracing with MARX: x-ray observatory design, calibration, and support." In *Space Telescopes and Instrumentation 2012: Ultraviolet to Gamma Ray*, volume 8443 of *procspie*, 84431A.

De Marco, B., G. Ponti, P. O. Petrucci, M. Clavel, S. Corbel, R. Belmont, S. Chakravorty, M. Coriat, S. Drappeau, J. Ferreira, G. Henri, J. Malzac, J. Rodriguez, J. A. Tomsick, F. Ursini and A. A. Zdziarski (2017), "Evolution of the reverberation lag in GX 339-4 at the end of an outburst." *mnras*, 471, 1475–1487.

De Marco, Barbara and Gabriele Ponti (2016), "The Reverberation Lag in the Low-mass X-ray Binary H1743-322." *apj*, 826, 70.

Detmers, Robertus G. (2011), *Outflow and feedback in active galactic nuclei: high-resolution X-ray spectroscopy and variability*. Ph.D. thesis, Utrecht University.

Dolphin, Andrew E. (2000), "WFPC2 Stellar Photometry with HSTPHOT." *pasp*, 112, 1383–1396.

Done, Chris (2010), "Observational characteristics of accretion onto black holes." *arXiv e-prints*, arXiv:1008.2287.

Done, Chris and Marek Gierliński (2006), "Truncated disc versus extremely broad iron line in XTE J1650-500." *mnras*, 367, 659–668.

Done, Chris, Marek Gierliński and Aya Kubota (2007), "Modelling the behaviour of accretion flows in X-ray binaries. Everything you always wanted to know about accretion but were afraid to ask." *aapr*, 15, 1–66.

Dopita, M. A. and R. S. Sutherland (2003), *Astrophysics of the diffuse universe*.

Dubner, G. M., M. Holdaway, W. M. Goss and I. F. Mirabel (1998), "A High-Resolution Radio Study of the W50-SS 433 System and the Surrounding Medium." *aj*, 116, 1842–1855.

Dudik, R. P., C. T. Berghea, T. P. Roberts, F. Grisé, A. Singh, R. Pagano and L. M. Winter (2016), "Spitzer IRAC Observations of IR Excess in Holmberg IX X-1: A Circumbinary Disk or a Variable Jet?" *apj*, 831, 88.

Earnshaw, H. P., T. P. Roberts and R. Sathyaprakash (2018), "Searching for propeller-phase ULXs in the XMM-Newton Serendipitous Source Catalogue." *mnras*, 476, 4272–4277.

Ebeling, H., D. A. White and F. V. N. Rangarajan (2006), "ASMOOTH: a simple and efficient algorithm for adaptive kernel smoothing of two-dimensional imaging data." *mnras*, 368, 65–73.

Eksi, K. Y., I. C. Andac, S. Cikintoglu, A. A. Gencali, C. Gungor and F. Oztekin (2015), "The ultraluminous X-ray source NuSTAR J095551+6940.8: a magnetar in a high-mass X-ray binary." *mnras*, 448, L40–L42.

El Mellah, I., J. O. Sundqvist and R. Keppens (2019), "Wind Roche lobe overflow in high-mass X-ray binaries. A possible mass-transfer mechanism for ultraluminous X-ray sources." *aap*, 622, L3.

Event Horizon Telescope Collaboration, Kazunori Akiyama, Antxon Alberdi, Walter Alef, Keiichi Asada, Rebecca Azulay, Anne-Kathrin Baczko, David Ball, Mislav Baloković, John Barrett, Dan Bintley, Lindy Blackburn, Wilfred Boland, Katherine L. Bouman, Geoffrey C. Bower, Michael Bremer, Christiaan D. Brinkerink, Roger Brissenden, Silke Britzen, Avery E. Broderick, Dominique Broguiere, Thomas Bronzwaer, Do-Young Byun, John E. Carlstrom, Andrew Chael, Chi-kwan Chan, Shami Chatterjee, Koushik Chatterjee, Ming-Tang Chen, Yongjun Chen, Ilje Cho, Pierre Christian, John E. Conway, James M. Cordes, Geoffrey B. Crew, Yuzhu Cui, Jordy Davelaar, Mariafelicia De Laurentis, Roger Deane, Jessica Dempsey, Gregory Desvignes, Jason Dexter, Sheperd S. Doeleman, Ralph P. Eatough, Heino Falcke, Vincent L. Fish, Ed Fomalont, Raquel Fraga-Encinas, William T. Freeman, Per Friberg, Christian M. Fromm, José L. Gómez, Peter Galison, Charles F. Gammie, Roberto García, Olivier Gentaz, Boris Georgiev, Ciriaco Goddi, Roman Gold, Minfeng Gu, Mark Gurwell, Kazuhiro Hada, Michael H. Hecht, Ronald Hesper, Luis C. Ho, Paul Ho, Mareki Honma, Chih-Wei L. Huang, Lei Huang, David H. Hughes, Shiro Ikeda, Makoto Inoue, Sara Issaoun, David J. James, Buell T. Jannuzi, Michael Janssen, Britton Jeter, Wu Jiang, Michael D. Johnson, Svetlana Jorstad, Taehyun Jung, Mansour Karami, Ramesh Karuppusamy, Tomohisa Kawashima, Garrett K. Keating, Mark Kettenis, Jae-Young Kim, Junhan Kim, Jongsoo Kim, Motoki Kino, Jun Yi Koay, Patrick M. Koch, Shoko Koyama, Michael Kramer, Carsten Kramer, Thomas P. Krichbaum, Cheng-Yu Kuo, Tod R. Lauer, Sang-Sung Lee, Yan-Rong Li, Zhiyuan Li, Michael Lindqvist, Kuo Liu, Elisabetta Liuzzo, Wen-Ping Lo, Andrei P. Lobanov, Laurent Loinard, Colin Lonsdale, Ru-Sen Lu, Nicholas R. MacDonald, Jirong Mao, Sera Markoff, Daniel P. Marrone, Alan P. Marscher, Iván Martí-Vidal, Satoki Matsushita, Lynn D. Matthews, Lia Medeiros, Karl M. Menten, Yosuke Mizuno, Izumi Mizuno, James M. Moran, Kotaro Moriyama, Monika Moscibrodzka, Cornelia

Müller, Hiroshi Nagai, Neil M. Nagar, Masanori Nakamura, Ramesh Narayan, Gopal Narayanan, Iniyan Natarajan, Roberto Neri, Chunchong Ni, Aristeidis Noutsos, Hiroki Okino, Héctor Olivares, Gisela N. Ortiz-León, Tomoaki Oyama, Feryal Özel, Daniel C. M. Palumbo, Nimesh Patel, Ue-Li Pen, Dominic W. Pesce, Vincent Piétu, Richard Plambeck, Aleksandar PopStefanija, Oliver Porth, Ben Prather, Jorge A. Preciado-López, Dimitrios Psaltis, Hung-Yi Pu, Venkatessh Ramakrishnan, Ramprasad Rao, Mark G. Rawlings, Alexander W. Raymond, Luciano Rezzolla, Bart Ripperda, Freek Roelofs, Alan Rogers, Eduardo Ros, Mel Rose, Arash Roshanineshat, Helge Rottmann, Alan L. Roy, Chet Ruszczyk, Benjamin R. Ryan, Kazi L. J. Rygl, Salvador Sánchez, David Sánchez-Arguelles, Mahito Sasada, Tuomas Savolainen, F. Peter Schloerb, Karl-Friedrich Schuster, Lijing Shao, Zhiqiang Shen, Des Small, Bong Won Sohn, Jason SooHoo, Fumie Tazaki, Paul Tiede, Remo P. J. Tilanus, Michael Titus, Kenji Toma, Pablo Torne, Tyler Trent, Sascha Trippe, Shuichiro Tsuda, Ilse van Bemmel, Huib Jan van Langevelde, Daniel R. van Rossum, Jan Wagner, John Wardle, Jonathan Weintroub, Norbert Wex, Robert Wharton, Maciek Wielgus, George N. Wong, Qingwen Wu, Ken Young, André Young, Ziri Younsi, Feng Yuan, Ye-Fei Yuan, J. Anton Zensus, Guangyao Zhao, Shan-Shan Zhao, Ziyan Zhu, Juan-Carlos Algaba, Alexander Allardi, Rodrigo Amestica, Jadyn Anczarski, Uwe Bach, Frederick K. Baganoff, Christopher Beaudoin, Bradford A. Benson, Ryan Berthold, Jay M. Blanchard, Ray Blundell, Sandra Bustamente, Roger Cappallo, Edgar Castillo-Domínguez, Chih-Cheng Chang, Shu-Hao Chang, Song-Chu Chang, Chung-Chen Chen, Ryan Chilson, Tim C. Chuter, Rodrigo Córdova Rosado, Iain M. Coulson, Thomas M. Crawford, Joseph Crowley, John David, Mark Derome, Matthew Dexter, Sven Dornbusch, Kevin A. Dudevoir, Sergio A. Dzib, Andreas Eckart, Chris Eckert, Neal R. Erickson, Wendeline B. Everett, Aaron Faber, Joseph R. Farah, Vernon Fath, Thomas W. Folkers, David C. Forbes, Robert Freund, Arturo I. Gómez-Ruiz, David M. Gale, Feng Gao, Gertie Geertsema, David A. Graham, Christopher H. Greer, Ronald Grosslein, Frédéric Gueth, Daryl Haggard, Nils W. Halverson, Chih-Chiang Han, Kuo-Chang Han, Jinchi Hao, Yutaka Hasegawa, Jason W. Henning, Antonio Hernández-Gómez, Rubén Herrero-Illana, Stefan Heyminck, Akihiko Hirota, James Hoge, Yau-De Huang, C. M. Violette Impellizzeri, Homin Jiang, Atish Kamble, Ryan Keisler, Kimihiro Kimura, Yusuke Kono, Derek Kubo, John Kuroda, Richard Lacasse, Robert A. Laing, Erik M. Leitch, Chao-Te Li, Lupin C. C. Lin,

Ching-Tang Liu, Kuan-Yu Liu, Li-Ming Lu, Ralph G. Marson, Pierre L. Martin-Cocher, Kyle D. Massingill, Callie Matulonis, Martin P. McColl, Stephen R. McWhirter, Hugo Messias, Zheng Meyer-Zhao, Daniel Michalik, Alfredo Montaña, William Montgomerie, Matias Mora-Klein, Dirk Muders, Andrew Nadolski, Santiago Navarro, Joseph Neilsen, Chi H. Nguyen, Hiroaki Nishioka, Timothy Norton, Michael A. Nowak, George Nystrom, Hideo Ogawa, Peter Oshiro, Tomoaki Oyama, Harriet Parsons, Scott N. Paine, Juan Peñalver, Neil M. Phillips, Michael Poirier, Nicolas Pradel, Rurik A. Primiani, Philippe A. Raffin, Alexandra S. Rahlin, George Reiland, Christopher Risacher, Ignacio Ruiz, Alejandro F. Sáez-Madaín, Remi Sassella, Pim Schellart, Paul Shaw, Kevin M. Silva, Hotaka Shiokawa, David R. Smith, William Snow, Kamal Souccar, Don Sousa, T. K. Sridharan, Ranjani Srinivasan, William Stahm, Anthony A. Stark, Kyle Story, Sjoerd T. Timmer, Laura Vertatschitsch, Craig Walther, Ta-Shun Wei, Nathan Whitehorn, Alan R. Whitney, David P. Woody, Jan G. A. Wouterloot, Melvin Wright, Paul Yamaguchi, Chen-Yu Yu, Milagros Zeballos, Shuo Zhang and Lucy Ziurys (2019), "First M87 Event Horizon Telescope Results. I. The Shadow of the Supermassive Black Hole." *apjl*, 875, L1.

Fabbiano, G. and G. Trinchieri (1987), "X-Ray Observations of Spiral Galaxies. II. Images and Spectral Parameters of 13 Galaxies." *apj*, 315, 46.

Fabian, A. C., K. Iwasawa, C. S. Reynolds and A. J. Young (2000), "Broad Iron Lines in Active Galactic Nuclei." *pasp*, 112, 1145–1161.

Fabrika, Sergei, Yoshihiro Ueda, Alexander Vinokurov, Olga Sholukhova and Megumi Shidatsu (2015), "Supercritical accretion disks in ultraluminous X-ray sources and SS 433." *Nature Physics*, 11, 551–553.

Fan, Xiaohui (2006), "Evolution of high-redshift quasars." *New Astronomy Reviews*, 50, 665–671.

Farrell, Sean A., Natalie A. Webb, Didier Barret, Olivier Godet and Joana M. Rodrigues (2009), "An intermediate-mass black hole of over 500 solar masses in the galaxy ESO243-49." *nature*, 460, 73–75.

Faucher-Giguère, Claude-André and Eliot Quataert (2012), "The physics of galactic winds driven by active galactic nuclei." *mnras*, 425, 605–622.

Fender, Rob and Tomaso Belloni (2004), "GRS 1915+105 and the Disc-Jet Coupling in Accreting Black Hole Systems." *araa*, 42, 317–364.

Feng, H. and P. Kaaret (2007), "Spectral Evolution of NGC 1313 X-2: Evidence against the Cool Disk Model." *apjl*, 660, L113–L116.

Feng, Hua and Roberto Soria (2011), "Ultraluminous X-ray sources in the Chandra and XMM-Newton era." *nar*, 55, 166–183.

Fishbach, Maya, Daniel E. Holz and Ben Farr (2017), "Are LIGO's Black Holes Made from Smaller Black Holes?" *apjl*, 840, L24.

Fragos, Tassos, Tim Linden, Vicky Kalogera and Panos Sklias (2015), "On the Formation of Ultraluminous X-ray Sources with Neutron Star Accretors: the Case of M82 X-2." In *IAU General Assembly*, volume 29, 2256674.

Friedman, H. and E. T. Byram (1967), "X-rays from Sources 3C 273 and M 87." *Science*, 158, 257–259.

Fürst, F., D. J. Walton, F. A. Harrison, D. Stern, D. Barret, M. Brightman, A. C. Fabian, B. Grefenstette, K. K. Madsen, M. J. Middleton, J. M. Miller, K. Pottschmidt, A. Ptak, V. Rana and N. Webb (2016), "Discovery of Coherent Pulsations from the Ultraluminous X-Ray Source NGC 7793 P13." *apjl*, 831, L14.

Fürst, F., D. J. Walton, D. Stern, M. Bachetti, D. Barret, M. Brightman, F. A. Harrison and V. Rana (2017), "Spectral Changes in the Hyperluminous Pulsar in NGC 5907 as a Function of Super-orbital Phase." *apj*, 834, 77.

Galloway, Duncan K. and Laurens Keek (2017), "Thermonuclear X-ray bursts." *arXiv e-prints*, arXiv:1712.06227.

Gandhi, P., A. W. Blain, D. M. Russell, P. Casella, J. Malzac, S. Corbel, P. D'Avanzo, F. W. Lewis, S. Markoff, M. Cadolle Bel, P. Goldoni, S. Wachter, D. Khangulyan and A. Mainzer (2011), "A Variable Mid-infrared Synchrotron Break Associated with the Compact Jet in GX 339-4." *apjl*, 740, L13.

George, I. M. and A. C. Fabian (1991), "X-ray reflection from cold matter in Active Galactic Nuclei and X-ray binaries." *mnras*, 249, 352.

Gerke, J. R., C. S. Kochanek, J. L. Prieto, K. Z. Stanek and L. M. Macri (2011), "A Study of Cepheids in M81 with the Large Binocular Telescope (Efficiently Calibrated with Hubble Space Telescope)." *apj*, 743, 176.

Ghez, A. M., S. Salim, S. D. Hornstein, A. Tanner, J. R. Lu, M. Morris, E. E. Becklin and G. Duchêne (2005), "Stellar Orbits around the Galactic Center Black Hole." *apj*, 620, 744–757.

Ghosh, P. and F. K. Lamb (1978), "Disk accretion by magnetic neutron stars." *apjl*, 223, L83–L87.

Ghosh, P. and F. K. Lamb (1979), "Accretion by rotating magnetic neutron stars. II. Radial and vertical structure of the transition zone in disk accretion." *apj*, 232, 259–276.

Giacconi, R., J. Bechtold, G. Branduardi, W. Forman, J. P. Henry, C. Jones, E. Kellogg, H. van der Laan, W. Liller, H. Marshall, S. S. Murray, J. Pye, E. Schreier, W. L. W. Sargent, F. Seward and H. Tananbaum (1979), "A high-sensitivity X-ray survey using the Einstein Observatory and the discrete source contribution to the extragalactic X-ray background." *apjl*, 234, L1–L7.

Giacconi, R., H. Gursky, E. Kellogg, E. Schreier and H. Tananbaum (1971), "Discovery of Periodic X-Ray Pulsations in Centaurus X-3 from UHURU." *apjl*, 167, L67.

Giacconi, Riccardo, Herbert Gursky, Frank R. Paolini and Bruno B. Rossi (1962), "Evidence for x Rays From Sources Outside the Solar System." *prl*, 9, 439–443.

Gierliński, M., A. A. Zdziarski, P. S. Coppi, J. Poutanen, K. Ebisawa and W. N. Johnson (1999), "Thermal/non-thermal model of Cyg X-1 in the soft state." *Nuclear Physics B Proceedings Supplements*, 69, 312–315.

Gierliński, Marek and Chris Done (2004), "Black hole accretion discs: reality confronts theory." *mnras*, 347, 885–894.

Gierliński, Marek, Chris Done and Kim Page (2009), "Reprocessing of X-rays in the outer accretion disc of the black hole binary XTE J1817-330." *mnras*, 392, 1106–1114.

Gierliński, Marek and Jo Newton (2006), "X-ray spectral transitions of black holes from RXTE All-Sky Monitor." *mnras*, 370, 837–844.

Gladstone, Jeanette C., Chris Copperwheat, Craig O. Heinke, Timothy P. Roberts, Taylor F. Cartwright, Andrew J. Levan and Mike R. Goad (2013), "Optical Counterparts of the Nearest Ultraluminous X-Ray Sources." *apjs*, 206, 14.

Gladstone, Jeanette C., Timothy P. Roberts and Chris Done (2009), "The ultraluminous state." *mnras*, 397, 1836–1851.

Godet, O., D. Barret, N. A. Webb, S. A. Farrell and N. Gehrels (2009), "First Evidence for Spectral State Transitions in the ESO 243-49 Hyperluminous X-Ray Source HLX-1." *apjl*, 705, L109–L112.

Gordon, Shawn M., Robert P. Kirshner, Knox S. Long, William P. Blair, Nebojsa Duric and R. Chris Smith (1998), "A New Optical Sample of Supernova Remnants in M33." *apjs*, 117, 89–133.

Greene, Jenny E., Jay Strader and Luis C. Ho (2019), "Intermediate-Mass Black Holes." *arXiv e-prints*, arXiv:1911.09678.

Grimm, H. J., M. Gilfanov and R. Sunyaev (2002), "The Milky Way in X-rays for an outside observer. Log(N)-Log(S) and luminosity function of X-ray binaries from RXTE/ASM data." *aap*, 391, 923–944.

Grimm, H. J., M. Gilfanov and R. Sunyaev (2003), "High-mass X-ray binaries as a star formation rate indicator in distant galaxies." *mnras*, 339, 793–809.

Grisé, F., P. Kaaret, S. Corbel, D. Cseh and H. Feng (2013), "A long-term X-ray monitoring of the ultraluminous X-ray source NGC 5408 X-1 with Swift reveals the presence of dips but no orbital period." *mnras*, 433, 1023–1038.

Grisé, F., P. Kaaret, S. Corbel, H. Feng, D. Cseh and L. Tao (2012), "Optical Emission of the Ultraluminous X-Ray Source NGC 5408 X-1: Donor Star or Irradiated Accretion Disk?" *apj*, 745, 123.

Grisé, F., P. Kaaret, M. W. Pakull and C. Motch (2011), "Optical Properties of the Ultraluminous X-Ray Source Holmberg IX X-1 and Its Stellar Environment." *apj*, 734, 23.

Grisé, F., M. W. Pakull, R. Soria, C. Motch, I. A. Smith, S. D. Ryder and M. Böttcher (2008), "The ultraluminous X-ray source NGC 1313 X-2. Its optical counterpart and environment." *aap*, 486, 151–163.

Hameury, J. M. (2020), "A review of the disc instability model for dwarf novae, soft X-ray transients and related objects." *Advances in Space Research*, 66, 1004–1024.

Heida, M., F. A. Harrison, M. Brightman, F. Fürst, D. Stern and D. J. Walton (2019a), "Searching for the Donor Stars of ULX Pulsars." *apj*, 871, 231.

Heida, M., P. G. Jonker, M. A. P. Torres, T. P. Roberts, D. J. Walton, D. S. Moon, D. Stern and F. A. Harrison (2016), "Keck/MOSFIRE spectroscopy of five ULX counterparts." *mnras*, 459, 771–778.

Heida, M., R. M. Lau, B. Davies, M. Brightman, F. Fürst, B. W. Grefenstette, J. A. Kennea, F. Tramper, D. J. Walton and F. A. Harrison (2019b), "Discovery of a Red Supergiant Donor Star in SN2010da/NGC 300 ULX-1." *apjl*, 883, L34.

Heida, M., M. A. P. Torres, P. G. Jonker, M. Servillat, S. Repetto, T. P. Roberts, D. J. Walton, D. S. Moon and F. A. Harrison (2015), "Discovery of a red supergiant counterpart to RX J004722.4-252051, a ULX in NGC 253." *mnras*, 453, 3510–3518.

Heil, L. M., S. Vaughan and T. P. Roberts (2009), "A systematic study of variability in a sample of ultraluminous X-ray sources." *mnras*, 397, 1061–1072.

Herold, H. (1979), "Compton and Thomson scattering in strong magnetic fields." *prd*, 19, 2868–2875.

Hirschi, Raphael, Cristina Chiappini, Georges Meynet, André Maeder and Sylvia Ekström (2008), "Stellar Evolution at Low Metallicity." In *Massive Stars as Cosmic Engines* (F. Bresolin, P. A. Crowther, and J. Puls, eds.), volume 250 of *IAU Symposium*, 217–230.

Hook, R., F. Stoehr and J. Krist (2008), "Tiny Tim PSF simulator - now with WFC3 support." *Space Telescope European Coordinating Facility Newsletter*, 44, 11.

Hulse, R. A. and J. H. Taylor (1975), "Discovery of a pulsar in a binary system." *apjl*, 195, L51–L53.

Illarionov, A. F. and R. A. Sunyaev (1975), "Why the Number of Galactic X-ray Stars Is so Small?" *aap*, 39, 185.

Ingram, Adam R. and Sara E. Motta (2019), "A review of quasi-periodic oscillations from black hole X-ray binaries: Observation and theory." *nar*, 85, 101524.

Israel, G. L., A. Belfiore, L. Stella, P. Esposito, P. Casella, A. De Luca, M. Marelli, A. Papitto, M. Perri, S. Puccetti, G. A. R. Castillo, D. Salvetti, A. Tiengo, L. Zampieri, D. D'Agostino, J. Greiner, F. Haberl, G. Novara, R. Salvaterra, R. Turolla, M. Watson, J. Wilms and A. Wolter (2017a), "An accreting pulsar with extreme properties drives an ultraluminous x-ray source in NGC 5907." *Science*, 355, 817–819.

Israel, G. L., A. Belfiore, L. Stella, P. Esposito, P. Casella, A. De Luca, M. Marelli, A. Papitto, M. Perri, S. Puccetti, G. A. R. Castillo, D. Salvetti, A. Tiengo, L. Zampieri, D. D'Agostino, J. Greiner, F. Haberl, G. Novara, R. Salvaterra, R. Turolla, M. Watson, J. Wilms and A. Wolter (2017b), "An accreting pulsar with extreme properties drives an ultraluminous x-ray source in NGC 5907." *Science*, 355, 817–819.

Israel, G. L., A. Papitto, P. Esposito, L. Stella, L. Zampieri, A. Belfiore, G. A. Rodríguez Castillo, A. De Luca, A. Tiengo, F. Haberl, J. Greiner, R. Salvaterra, S. Sandrelli and G. Lisini (2017c), "Discovery of a 0.42-s pulsar in the ultraluminous X-ray source NGC 7793 P13." *mnras*, 466, L48–L52.

Jiang, Yan-Fei, James M. Stone and Shane W. Davis (2019), "Super-Eddington Accretion Disks around Supermassive Black Holes." *apj*, 880, 67.

Kaaret, P., H. Feng and T. P. Roberts (2017), "Ultraluminous X-Ray Sources." *araa*, 55, 303–341.

Kaaret, P., M. J. Ward and A. Zezas (2004), "High-resolution imaging of the HeII λ4686

emission line nebula associated with the ultraluminous X-ray source in Holmberg II." *mnras*, 351, L83–L88.

Kaaret, Philip and Stéphane Corbel (2009), "A Photoionized Nebula Surrounding and Variable Optical Continuum Emission from the Ultraluminous X-Ray Source in NGC 5408." *apj*, 697, 950–956.

Kaaret, Philip, Hua Feng, Diane S. Wong and Lian Tao (2010), "Direct Detection of an Ultraluminous Ultraviolet Source." *apjl*, 714, L167–L170.

Kajava, Jari J. E. and Juri Poutanen (2009), "Spectral variability of ultraluminous X-ray sources." *mnras*, 398, 1450–1460.

Kalberla, P. M. W., W. B. Burton, D. Hartmann, E. M. Arnal, E. Bajaja, R. Morras and W. G. L. Pöppel (2005), "The Leiden/Argentine/Bonn (LAB) Survey of Galactic HI. Final data release of the combined LDS and IAR surveys with improved stray-radiation corrections." *aap*, 440, 775–782.

Kara, E., C. Pinto, D. J. Walton, W. N. Alston, M. Bachetti, D. Barret, M. Brightman, C. R. Canizares, H. P. Earnshaw, A. C. Fabian, F. Fürst, P. Kosec, M. J. Middleton, T. P. Roberts, R. Soria, L. Tao and N. A. Webb (2020), "Discovery of a soft X-ray lag in the ultraluminous X-ray source NGC 1313 X-1." *mnras*, 491, 5172–5178.

Kaspi, V. M., M. Bailes, R. N. Manchester, B. W. Stappers and J. F. Bell (1996), "Evidence from a precessing pulsar orbit for a neutron-star birth kick." *nature*, 381, 584–586.

Kawashima, Tomohisa, Shin Mineshige, Ken Ohsuga and Takumi Ogawa (2016), "A radiation-hydrodynamics model of accretion columns for ultra-luminous X-ray pulsars." *pasj*, 68, 83.

Kerr, Roy P. (1963), "Gravitational Field of a Spinning Mass as an Example of Algebraically Special Metrics." *prl*, 11, 237–238.

Kimura, Mariko and Chris Done (2019), "Evolution of X-ray irradiation during the 1999-2000 outburst of the black hole binary XTE J1859 + 226." *mnras*, 482, 626–638.

King, A. R. (2008), "Accretion rates and beaming in ultraluminous X-ray sources." *mnras*, 385, L113–L115.

King, A. R. (2009), "Masses, beaming and Eddington ratios in ultraluminous X-ray sources." *mnras*, 393, L41–L44.

King, A. R., M. B. Davies, M. J. Ward, G. Fabbiano and M. Elvis (2001), "Ultraluminous X-Ray Sources in External Galaxies." *apjl*, 552, L109–L112.

King, Andrew, Jean-Pierre Lasota and Włodek Kluźniak (2017), "Pulsing ULXs: tip of the iceberg?" *mnras*, 468, L59–L62.

Kolehmainen, Mari and Chris Done (2010), "Limits on spin determination from disc spectral fitting in GX 339-4." *mnras*, 406, 2206–2212.

Koliopanos, Filippos, Georgios Vasilopoulos, Olivier Godet, Matteo Bachetti, Natalie A. Webb and Didier Barret (2017), "ULX spectra revisited: Accreting, highly magnetized neutron stars as the engines of ultraluminous X-ray sources." *aap*, 608, A47.

Komossa, S. (2015), "Tidal disruption of stars by supermassive black holes: Status of observations." *Journal of High Energy Astrophysics*, 7, 148–157.

Kosec, P., C. Pinto, A. C. Fabian and D. J. Walton (2018a), "Searching for outflows in ultraluminous X-ray sources through high-resolution X-ray spectroscopy." *mnras*, 473, 5680–5697.

Kosec, P., C. Pinto, D. J. Walton, A. C. Fabian, M. Bachetti, M. Brightman, F. Fürst and B. W. Grefenstette (2018b), "Evidence for a variable Ultrafast Outflow in the newly discovered Ultraluminous Pulsar NGC 300 ULX-1." *mnras*, 479, 3978–3986.

Kretschmar, P., E. Nespoli, P. Reig and F. Anders (2012), "The Be X-ray Binary Outburst Zoo." In *Proceedings of "An INTEGRAL view of the high-energy sky (the first 10 years)" - 9th INTEGRAL Workshop and celebration of the 10th anniversary of the launch (INTEGRAL 2012). 15-19 October 2012. Bibliotheque Nationale de France*, 16.

Krist, J. (1995), "Simulation of HST PSFs using Tiny Tim." In *Astronomical Data Analysis Software and Systems IV* (R. A. Shaw, H. E. Payne, and J. J. E. Hayes, eds.), volume 77 of *Astronomical Society of the Pacific Conference Series*, 349.

Kubota, Aya and Chris Done (2004), "The very high state accretion disc structure from the Galactic black hole transient XTE J1550 - 564." *mnras*, 353, 980–990.

Kubota, Aya and Chris Done (2019), "Modelling the spectral energy distribution of super-Eddington quasars." *mnras*, 489, 524–533.

Kubota, Aya, Yasuo Tanaka, Kazuo Makishima, Yoshihiro Ueda, Tadayasu Dotani, Hajime Inoue and Kazutaka Yamaoka (1998), "Evidence for a Black Hole in the X-Ray Transient GRS 1009-45." *pasj*, 50, 667–673.

Lai, Dong (2000), *Physics of neutron star kicks*, volume 254, 127.

Larsson, S. (1996), "Parameter estimation in epoch folding analysis." *aaps*, 117, 197–201.

Lasota, J. P., R. S. S. Vieira, A. Sadowski, R. Narayan and M. A. Abramowicz (2016), "The slimming effect of advection on black-hole accretion flows." *aap*, 587, A13.

Lau, R. M., M. Heida, M. M. Kasliwal and D. J. Walton (2017), "First Detection of Mid-infrared Variability from an Ultraluminous X-Ray Source Holmberg II X-1." *apjl*, 838, L17.

Lau, Ryan M., Marianne Heida, Dominic J. Walton, Mansi M. Kasliwal, Scott M. Adams, Ann Marie Cody, Kishalay De, Robert D. Gehrz, Felix Fürst, Jacob E. Jencson, Jamie A. Kennea and Frank Masci (2019), "Uncovering Red and Dusty Ultraluminous X-Ray Sources with Spitzer." *apj*, 878, 71.

Leahy, D. A., W. Darbro, R. F. Elsner, M. C. Weisskopf, P. G. Sutherland, S. Kahn and J. E. Grindlay (1983), "On searches for pulsed emission with application to four globular cluster X-ray sources : NGC 1851, 6441, 6624 and 6712." *apj*, 266, 160–170.

Lira, P., A. Lawrence and R. A. Johnson (2000), "Multiwavelength study of the nuclei of a volume-limited sample of galaxies - I. X-ray observations." *mnras*, 319, 17–42.

Liu, J., J. N. Bregman and J. E. McClintock (2009), "Hubble Space Telescope Monitoring Reveals a 6.1 Day Period for an Ultraluminous X-Ray Source in NGC 1313." *apjl*, 690, L39–L42.

Liu, Ji-Feng, Joel Bregman, Jon Miller and Philip Kaaret (2007), "Optical Studies of the Ultraluminous X-Ray Source NGC 1313 X-2." *apj*, 661, 165–172.

Liu, Ji-Feng, Joel N. Bregman, Yu Bai, Stephen Justham and Paul Crowther (2013), "Puzzling accretion onto a black hole in the ultraluminous X-ray source M 101 ULX-1." *nature*, 503, 500–503.

López, K. M., M. Heida, P. G. Jonker, M. A. P. Torres, T. P. Roberts, D. J. Walton, D. S. Moon and F. A. Harrison (2017), "A systematic search for near-infrared counterparts of nearby ultraluminous X-ray sources (II)." *mnras*, 469, 671–682.

López, K. M., M. Heida, P. G. Jonker, M. A. P. Torres, T. P. Roberts, D. J. Walton, D. S. Moon and F. A. Harrison (2020), "NIR counterparts to ULXs (III): completing the photometric survey and selected spectroscopic results." *mnras*, 497, 917–932.

López, K. M., P. G. Jonker, M. Heida, M. A. P. Torres, T. P. Roberts, D. J. Walton, D. S. Moon and F. A. Harrison (2019), "Discovery and analysis of a ULX nebula in NGC 3521." *mnras*, 489, 1249–1264.

Luangtip, Wasutep, Timothy P. Roberts and Chris Done (2016), "The X-ray spectral evolution of the ultraluminous X-ray source Holmberg IX X-1." *mnras*, 460, 4417–4432.

Maccarone, Thomas J. and Paolo S. Coppi (2003), "Hysteresis in the light curves of soft X-ray transients." *mnras*, 338, 189–196.

Madau, Piero and Martin J. Rees (2001), "Massive Black Holes as Population III Remnants." *apjl*, 551, L27–L30.

Mahmoud, Ra'ad D., Chris Done and Barbara De Marco (2019), "Reverberation reveals the truncated disc in the hard state of GX 339-4." *mnras*, 486, 2137–2152.

Makishima, K., Y. Maejima, K. Mitsuda, H. V. Bradt, R. A. Remillard, I. R. Tuohy, R. Hoshi and M. Nakagawa (1986), "Simultaneous X-Ray and Optical Observations of GX 339-4 in an X-Ray High State." *apj*, 308, 635.

Manchester, R. N. (2005), "Pulsar Radio and Gamma-Ray Emission." *apss*, 297, 101–108.

Markoff, S., M. Nowak, S. Corbel, R. Fender and H. Falcke (2003), "Exploring the role of jets in the radio/X-ray correlations of GX 339-4." *aap*, 397, 645–658.

Markoff, Sera, Michael A. Nowak and Jörn Wilms (2005), "Going with the Flow: Can the Base of Jets Subsume the Role of Compact Accretion Disk Coronae?" *apj*, 635, 1203–1216.

Martins, F., D. Schaerer and D. J. Hillier (2005), "A new calibration of stellar parameters of Galactic O stars." *aap*, 436, 1049–1065.

McCollough, M. L. and A. H. Rots (2005), "The Impact of the ACIS Readout Streak and Pileup on Chandra Source Detection." In *Astronomical Data Analysis Software and Systems XIV* (P. Shopbell, M. Britton, and R. Ebert, eds.), volume 347 of *Astronomical Society of the Pacific Conference Series*, 478.

Mezcua, Mar (2017), "Observational evidence for intermediate-mass black holes." *International Journal of Modern Physics D*, 26, 1730021.

Middleton, M. J., M. Brightman, F. Pintore, M. Bachetti, A. C. Fabian, F. Fürst and D. J. Walton (2019a), "On the magnetic field in M51 ULX-8." *mnras*, 486, 2–9.

Middleton, M. J., P. C. Fragile, M. Bachetti, M. Brightman, Y. F. Jiang, W. C. G. Ho, T. P. Roberts, A. R. Ingram, T. Dauser, C. Pinto, D. J. Walton, F. Fuerst, A. C. Fabian and N. Gehrels (2018a), "Lense-Thirring precession in ULXs as a possible means to constrain the neutron star equation of state." *mnras*, 475, 154–166.

Middleton, M. J., P. C. Fragile, A. Ingram and T. P. Roberts (2019b), "The Lense-Thirring timing-accretion plane for ULXs." *mnras*, 489, 282–296.

Middleton, M. J., L. Heil, F. Pintore, D. J. Walton and T. P. Roberts (2015a), "A spectral-timing model for ULXs in the supercritical regime." *mnras*, 447, 3243–3263.

Middleton, M. J., T. P. Roberts, C. Done and F. E. Jackson (2011), "Challenging times: a re-analysis of NGC 5408 X-1." *mnras*, 411, 644–652.

Middleton, M. J., D. J. Walton, W. Alston, T. Dauser, S. Eikenberry, Y-F Jiang, A. C. Fabian, F. Fuerst, M. Brightman, H. Marshall, M. Parker, C. Pinto, F. A. Harrison, M. Bachetti, D. Altamirano, A. J. Bird, G. Perez, J. Miller-Jones, P. A. Charles, S. Boggs, F. Christensen, W. Craig, K. Forster, B. Grefenstette, C. Hailey, K. Madsen,

D. Stern and W. Zhang (2018b), "NuSTAR reveals the hidden nature of SS433." *arXiv e-prints*, arXiv:1810.10518.

Middleton, M. J., D. J. Walton, A. Fabian, T. P. Roberts, L. Heil, C. Pinto, G. Anderson and A. Sutton (2015b), "Diagnosing the accretion flow in ultraluminous X-ray sources using soft X-ray atomic features." *mnras*, 454, 3134–3142.

Middleton, M. J., D. J. Walton, T. P. Roberts and L. Heil (2014), "Broad absorption features in wind-dominated ultraluminous X-ray sources?" *mnras*, 438, L51–L55.

Middleton, Matthew J., Lucy Heil, Fabio Pintore, Dominic J. Walton and Timothy P. Roberts (2015c), "A spectral-timing model for ULXs in the supercritical regime." *mnras*, 447, 3243–3263.

Middleton, Matthew J., James C. A. Miller-Jones, Sera Markoff, Rob Fender, Martin Henze, Natasha Hurley-Walker, Anna M. M. Scaife, Timothy P. Roberts, Dominic Walton, John Carpenter, Jean-Pierre Macquart, Geoffrey C. Bower, Mark Gurwell, Wolfgang Pietsch, Frank Haberl, Jonathan Harris, Michael Daniel, Junayd Miah, Chris Done, John S. Morgan, Hugh Dickinson, Phil Charles, Vadim Burwitz, Massimo Della Valle, Michael Freyberg, Jochen Greiner, Margarita Hernanz, Dieter H. Hartmann, Despina Hatzidimitriou, Arno Riffeser, Gloria Sala, Stella Seitz, Pablo Reig, Arne Rau, Marina Orio, David Titterington and Keith Grainge (2013), "Bright radio emission from an ultraluminous stellar-mass microquasar in M 31." *nature*, 493, 187–190.

Miller, B. W. (1995), "The Optical Counterpart to the Extremely Luminous X-Ray Source near Holmberg IX: A Possible Supershell in a Tidal Tail." *apjl*, 446, L75.

Miller, J. M., G. Fabbiano, M. C. Miller and A. C. Fabian (2003), "X-Ray Spectroscopic Evidence for Intermediate-Mass Black Holes: Cool Accretion Disks in Two Ultraluminous X-Ray Sources." *apjl*, 585, L37–L40.

Miller, J. M., J. Homan, D. Steeghs, M. Rupen, R. W. Hunstead, R. Wijnands, P. A. Charles and A. C. Fabian (2006), "A Long, Hard Look at the Low/Hard State in Accreting Black Holes." *apj*, 653, 525–535.

Mineo, S., M. Gilfanov and R. Sunyaev (2012), "X-ray emission from star-forming galaxies - II. Hot interstellarmedium." *mnras*, 426, 1870–1883.

Misner, Charles W., Kip S. Thorne and John A. Wheeler (1973), *Gravitation*.

Mitsuda, K., H. Inoue, K. Koyama, K. Makishima, M. Matsuoka, Y. Ogawara, N. Shibazaki, K. Suzuki, Y. Tanaka and T. Hirano (1984), "Energy spectra of low-mass binary X-ray sources observed from Tenma." *pasj*, 36, 741–759.

Mortlock, Daniel J., Stephen J. Warren, Bram P. Venemans, Mitesh Patel, Paul C. Hewett, Richard G. McMahon, Chris Simpson, Tom Theuns, Eduardo A. Gonzáles-Solares, Andy Adamson, Simon Dye, Nigel C. Hambly, Paul Hirst, Mike J. Irwin, Ernst Kuiper, Andy Lawrence and Huub J. A. Röttgering (2011), "A luminous quasar at a redshift of z = 7.085." *nature*, 474, 616–619.

Motch, C., M. W. Pakull, R. Soria, F. Grisé and G. Pietrzyński (2014), "A mass of less than 15 solar masses for the black hole in an ultraluminous X-ray source." *nature*, 514, 198–201.

Motta, S. E. (2016), "Quasi periodic oscillations in black hole binaries." *Astronomische Nachrichten*, 337, 398.

Mucciarelli, P., L. Zampieri, R. Falomo, R. Turolla and A. Treves (2005), "VLT Observations of the Ultraluminous X-Ray Source NGC 1313 X-2." *apjl*, 633, L101–L104.

Mukai, K. (2017), "X-Ray Emissions from Accreting White Dwarfs: A Review." *pasp*, 129, 062001.

Mushtukov, Alexander A., Adam Ingram, Matthew Middleton, Dmitrij I. Nagirner and Michiel van der Klis (2019), "Timing properties of ULX pulsars: optically thick envelopes and outflows." *mnras*, 484, 687–697.

Mushtukov, Alexander A., Valery F. Suleimanov, Sergey S. Tsygankov and Adam Ingram (2017), "Optically thick envelopes around ULXs powered by accreating neutron stars." *mnras*, 467, 1202–1208.

Mushtukov, Alexander A., Valery F. Suleimanov, Sergey S. Tsygankov and Juri Poutanen (2015), "On the maximum accretion luminosity of magnetized neutron stars: connecting X-ray pulsars and ultraluminous X-ray sources." *mnras*, 454, 2539–2548.

Nandra, K., X. Barcons, Barret D., Fabian A., J. W. den Herder and L. Piro (2016), "The hot and energetic universe." In *A white paper presenting the science theme motivating the Athena+ mission*, 1–19, N/A, N/A.

Narayan, Ramesh and Insu Yi (1995), "Advection-dominated Accretion: Underfed Black Holes and Neutron Stars." *apj*, 452, 710.

Nicastro, F., J. Kaastra, Y. Krongold, S. Borgani, E. Branchini, R. Cen, M. Dadina, C. W. Danforth, M. Elvis, F. Fiore, A. Gupta, S. Mathur, D. Mayya, F. Paerels, L. Piro, D. Rosa-Gonzalez, J. Schaye, J. M. Shull, J. Torres-Zafra, N. Wijers and L. Zappacosta (2018), "Observations of the missing baryons in the warm-hot intergalactic medium." *nature*, 558, 406–409.

Ogilvie, G. I. and G. Dubus (2001), "Precessing warped accretion discs in X-ray binaries." *mnras*, 320, 485–503.

Ohsuga, Ken and Shin Mineshige (2011), "Global Structure of Three Distinct Accretion Flows and Outflows around Black Holes from Two-dimensional Radiation-magnetohydrodynamic Simulations." *apj*, 736, 2.

Ostriker, Jeremiah P. and James E. Gunn (1969), "Magnetic Decay and the Maximum Period of Pulsars." In *Bulletin of the American Astronomical Society*, volume 1, 357–358.

Özel, Feryal and Paulo Freire (2016), "Masses, Radii, and the Equation of State of Neutron Stars." *araa*, 54, 401–440.

Pakull, M. W. and F. Grisé (2008), "Ultraluminous X-ray Sources: Beambags and Optical Counterparts." In *A Population Explosion: The Nature & Evolution of X-ray Binaries in Diverse Environments* (R. M. Bandyopadhyay, S. Wachter, D. Gelino, and C. R. Gelino, eds.), volume 1010 of *American Institute of Physics Conference Series*, 303–307.

Pakull, M. W., F. Grisé and C. Motch (2006), "Ultraluminous X-ray Sources: Bubbles and Optical Counterparts." In *Populations of High Energy Sources in Galaxies* (E. J. A. Meurs and G. Fabbiano, eds.), volume 230 of *IAU Symposium*, 293–297.

Pakull, M. W. and L. Mirioni (2002), "Optical Counterparts of Ultraluminous X-Ray Sources." *ArXiv Astrophysics e-prints*.

Pakull, Manfred W., Roberto Soria and Christian Motch (2010), "A 300-parsec-long jet-inflated bubble around a powerful microquasar in the galaxy NGC 7793." *nature*, 466, 209–212.

Patruno, Alessandro and Luca Zampieri (2008), "Optical emission from massive donors in ultraluminous X-ray source binary systems." *mnras*, 386, 543–552.

Pavlovskii, K., N. Ivanova, K. Belczynski and K. X. Van (2017), "Stability of mass transfer from massive giants: double black hole binary formation and ultraluminous X-ray sources." *mnras*, 465, 2092–2100.

Pfeffermann, E., U. G. Briel, H. Hippmann, G. Kettenring, G. Metzner, P. Predehl, G. Reger, K. H. Stephan, M. Zombeck, J. Chappell and S. S. Murray (1987), "The focal plane instrumentation of the ROSAT Telescope." In *Soft X-ray optics and technology*, volume 733 of *Society of Photo-Optical Instrumentation Engineers (SPIE) Conference Series*, 519.

Pinto, C., W. Alston, R. Soria, M. J. Middleton, D. J. Walton, A. D. Sutton, A. C. Fabian, H. Earnshaw, R. Urquhart, E. Kara and T. P. Roberts (2017), "From ultraluminous X-ray sources to ultraluminous supersoft sources: NGC 55 ULX, the missing link." *mnras*, 468, 2865–2883.

Pinto, Ciro, Matthew J. Middleton and Andrew C. Fabian (2016), "Resolved atomic lines reveal outflows in two ultraluminous X-ray sources." *nature*, 533, 64–67.

Pintore, F. and L. Zampieri (2012), "X-ray spectral states and metallicity in the ultraluminous X-ray sources NGC 1313 X-1 and X-2." *mnras*, 420, 1107–1114.

Pintore, F., L. Zampieri, L. Stella, A. Wolter, S. Mereghetti and G. L. Israel (2017), "Pulsator-like Spectra from Ultraluminous X-Ray Sources and the Search for More Ultraluminous Pulsars." *apj*, 836, 113.

Podsiadlowski, Ph., S. Rappaport and E. Pfahl (2001), *Binary Population Synthesis: Low-*

and Intermediate- Mass X-Ray Binaries, volume 264 of *Astrophysics and Space Science Library*, 355.

Podsiadlowski, Philipp (2014), "The evolution of massive binaries." In *Binary Systems, their Evolution and Environments* (Richard de Grijs, ed.), 13.

Portegies Zwart, Simon F., Holger Baumgardt, Piet Hut, Junichiro Makino and Stephen L. W. McMillan (2004), "Formation of massive black holes through runaway collisions in dense young star clusters." *nature*, 428, 724–726.

Pounds, K. A., A. R. King, K. L. Page and P. T. O'Brien (2003), "Evidence of a high-velocity ionized outflow in a second narrow-line quasar PG 0844+349." *mnras*, 346, 1025–1030.

Poutanen, Juri, Galina Lipunova, Sergei Fabrika, Alexey G. Butkevich and Pavel Abolmasov (2007), "Supercritically accreting stellar mass black holes as ultraluminous X-ray sources." *mnras*, 377, 1187–1194.

Predehl, P., R. A. Sunyaev, W. Becker, H. Brunner, R. Burenin, A. Bykov, A. Cherepashchuk, N. Chugai, E. Churazov, V. Doroshenko, N. Eismont, M. Freyberg, M. Gilfanov, F. Haberl, I. Khabibullin, R. Krivonos, C. Maitra, P. Medvedev, A. Merloni, K. Nandra, V. Nazarov, M. Pavlinsky, G. Ponti, J. S. Sanders, M. Sasaki, S. Sazonov, A. W. Strong and J. Wilms (2020), "Detection of large-scale X-ray bubbles in the Milky Way halo." *nature*, 588, 227–231.

Press, William H., Saul A. Teukolsky, William T. Vetterling and Brian P. Flannery (1992), *Numerical recipes in FORTRAN. The art of scientific computing.*

Ramsey, C. J., R. M. Williams, R. A. Gruendl, C.-H. R. Chen, Y.-H. Chu and Q. D. Wang (2006), "An Optical Study of Stellar and Interstellar Environments of Seven Luminous and Ultraluminous X-Ray Sources." *apj*, 641, 241–251.

Ransom, S. M., S. S. Eikenberry and J. Middleditch (2002), "Fourier Techniques for Very Long Astrophysical Time-Series Analysis." *aj*, 124, 1788–1809.

Rees, Martin J. (1988), "Tidal disruption of stars by black holes of 10^6-10^8 solar masses in nearby galaxies." *nature*, 333, 523–528.

Reig, P., I. Negueruela, J. Fabregat, R. Chato and M. J. Coe (2005), "Long-term optical/IR variability of the Be/X-ray binary <ASTROBJ>LS V +44 17</ASTROBJ>/<ASTROBJ>RX J0440.9+4431</ASTROBJ>." *aap*, 440, 1079–1086.

Reig, Pablo (2011), "Be/X-ray binaries." *apss*, 332, 1–29.

Reis, R. C., A. C. Fabian, R. R. Ross, G. Miniutti, J. M. Miller and C. Reynolds (2008), "A systematic look at the very high and low/hard state of GX339-4: constraining the black hole spin with a new reflection model." *mnras*, 387, 1489–1498.

Remillard, Ronald A. and J. E. McClintock (2006), "Active X-ray States of Black Hole Binaries: Current Overview." In *American Astronomical Society Meeting Abstracts*, volume 209 of *American Astronomical Society Meeting Abstracts*, 07.05.

Risaliti, G., S. Bianchi, G. Matt, A. Baldi, M. Elvis, G. Fabbiano and A. Zezas (2005), "Highly Ionized Iron Absorption Lines from Outflowing Gas in the X-Ray Spectrum of NGC 1365." *apjl*, 630, L129–L132.

Roberts, T., M. Middleton, A. Sutton, M. Mezcua, D. Walton and L. Heil (2015), "ULX behaviour: the ultraluminous state, winds and interesting anomalies." In *The Extremes of Black Hole Accretion*, 57.

Roberts, T. P., J. C. Gladstone, A. D. Goulding, A. M. Swinbank, M. J. Ward, M. R. Goad and A. J. Levan (2011), "(No) dynamical constraints on the mass of the black hole in two ULXs." *Astronomische Nachrichten*, 332, 398.

Roberts, T. P., M. R. Goad, M. J. Ward and R. S. Warwick (2003), "The unusual supernova remnant surrounding the ultraluminous X-ray source IC 342 X-1." *mnras*, 342, 709–714.

Roberts, T. P. and R. S. Warwick (2000), "A ROSAT High Resolution Imager survey of bright nearby galaxies." *mnras*, 315, 98–114.

Rodríguez Castillo, G. A., G. L. Israel, A. Belfiore, F. Bernardini, P. Esposito, F. Pintore, A. De Luca, A. Papitto, L. Stella, A. Tiengo, L. Zampieri, M. Bachetti, M. Brightman, P. Casella, D. D'Agostino, S. Dall'Osso, H. P. Earnshaw, F. Fürst, F. Haberl, F. A. Harrison, M. Mapelli, M. Marelli, M. Middleton, C. Pinto, T. P. Roberts, R. Salvaterra,

R. Turolla, D. J. Walton and A. Wolter (2020), "Discovery of a 2.8 s Pulsar in a 2 Day Orbit High-mass X-Ray Binary Powering the Ultraluminous X-Ray Source ULX-7 in M51." *apj*, 895, 60.

Rybicki, G. B. and A. P. Lightman (1979), "Book-Review - Radiative Processes in Astrophysics." *Astronomy Quarterly*, 3, 199.

Sathyaprakash, R., T. P. Roberts, D. J. Walton, F. Fuerst, M. Bachetti, C. Pinto, W. N. Alston, H. P. Earnshaw, A. C. Fabian, M. J. Middleton and R. Soria (2019), "The discovery of weak coherent pulsations in the ultraluminous X-ray source NGC 1313 X-2." *mnras*, 488, L35–L40.

Servillat, Mathieu, Sean A. Farrell, Dacheng Lin, Olivier Godet, Didier Barret and Natalie A. Webb (2011), "X-Ray Variability and Hardness of ESO 243-49 HLX-1: Clear Evidence for Spectral State Transitions." *apj*, 743, 6.

Seward, Frederick D. and Philip A. Charles (1995), *Exploring the X-Ray Universe*.

Shakura, N. I. and R. A. Sunyaev (1973), "Reprint of 1973A&A....24..337S. Black holes in binary systems. Observational appearance." *aap*, 500, 33–51.

Shapiro, S. L. and S. A. Teukolsky (1983), "Book-Review - Black-Holes White Dwarfs and Neutron Stars." *Journal of the British Astronomical Association*, 93, 276.

Shidatsu, M., C. Done and Y. Ueda (2016), "An Optically Thick Disk Wind in GRO J1655-40?" *apj*, 823, 159.

Siwek, M., A. Sądowski, R. Narayan, T. P. Roberts and R. Soria (2017), "Optical and X-ray luminosities of expanding nebulae around ultraluminous X-ray sources." *mnras*, 470, 361–371.

Sądowski, Aleksander and Ramesh Narayan (2016), "Three-dimensional simulations of supercritical black hole accretion discs - luminosities, photon trapping and variability." *mnras*, 456, 3929–3947.

Smith, R. K., N. S. Brickhouse, D. A. Liedahl and J. C. Raymond (2001), "Collisional Plasma Models with APEC/APED: Emission-Line Diagnostics of Hydrogen-like and Helium-like Ions." *apjl*, 556, L91–L95.

Song, X., D. J. Walton, G. B. Lansbury, P. A. Evans, A. C. Fabian, H. Earnshaw and T. P. Roberts (2020), "The hunt for pulsating ultraluminous X-ray sources." *mnras*, 491, 1260–1277.

Soria, Roberto, K. D. Kuntz, Knox S. Long, William P. Blair, Paul P. Plucinsky and P. Frank Winkler (2015), "The Slim-disk State of the Ultraluminous X-Ray Source in M83." *apj*, 799, 140.

Sowers, J. W., D. R. Gies, W. G. Bagnuolo, A. W. Shafter, R. Wiemker and M. S. Wiggs (1998), "Tomographic Analysis of Hα Profiles in HDE 226868/Cygnus X-1." *apj*, 506, 424–430.

Standish, E. M., Jr. (1990), "The observational basis for JPL's DE 200, the planetary ephemerides of the Astronomical Almanac." *aap*, 233, 252–271.

Stobbart, A. M., T. P. Roberts and J. Wilms (2006), "XMM-Newton observations of the brightest ultraluminous X-ray sources." *mnras*, 368, 397–413.

Straizys, V. and G. Kuriliene (1981), "Fundamental Stellar Parameters Derived from the Evolutionary Tracks." *apss*, 80, 353–368.

Strohmayer, T. E. and R. F. Mushotzky (2009), "Evidence for an Intermediate-mass Black Hole in NGC 5408 X-1." *apj*, 703, 1386–1393.

Strohmayer, Tod and Lars Bildsten (2003), "New Views of Thermonuclear Bursts." *arXiv e-prints*, astro-ph/0301544.

Strohmayer, Tod E. and Richard F. Mushotzky (2003), "Discovery of X-Ray Quasi-periodic Oscillations from an Ultraluminous X-Ray Source in M82: Evidence against Beaming." *apjl*, 586, L61–L64.

Su, Yang, Xin Zhou, Ji Yang, Yang Chen, Xuepeng Chen and Shaobo Zhang (2018), "The Large-scale Interstellar Medium of SS 433/W50 Revisited." *apj*, 863, 103.

Sunyaev, R. A. and L. G. Titarchuk (1980), "Comptonization of X-rays in plasma clouds. Typical radiation spectra." *aap*, 500, 167–184.

Sutton, A. D., T. P. Roberts and M. J. Middleton (2013), "The ultraluminous state revisited: fractional variability and spectral shape as diagnostics of super-Eddington accretion." *mnras*, 435, 1758–1775.

Sutton, A. D., T. P. Roberts and M. J. Middleton (2015), "X-Ray Spectral Residuals in NGC 5408 X-1: Diffuse Emission from Star Formation, or the Signature of a Super-Eddington Wind?" *apj*, 814, 73.

Sutton, Andrew D., Chris Done and Timothy P. Roberts (2014), "Irradiated, colour-temperature-corrected accretion discs in ultraluminous X-ray sources." *mnras*, 444, 2415–2427.

Swartz, Douglas A., Kajal K. Ghosh, Allyn F. Tennant and Kinwah Wu (2004), "The Ultraluminous X-Ray Source Population from the Chandra Archive of Galaxies." *apjs*, 154, 519–539.

Takeuchi, Shun, Ken Ohsuga and Shin Mineshige (2013), "Clumpy Outflows from Supercritical Accretion Flow." *pasj*, 65, 88.

Tananbaum, H., H. Gursky, E. M. Kellogg, R. Levinson, E. Schreier and R. Giacconi (1972), "Discovery of a Periodic Pulsating Binary X-Ray Source in Hercules from UHURU." *apjl*, 174, L143.

Tao, Lian, Hua Feng, Fabien Grisé and Philip Kaaret (2011), "Compact Optical Counterparts of Ultraluminous X-Ray Sources." *apj*, 737, 81.

Tauris, Thomas M., Edward P. J. van den Heuvel and Gerrit J. Savonije (2000), "Formation of Millisecond Pulsars with Heavy White Dwarf Companions:Extreme Mass Transfer on Subthermal Timescales." *apjl*, 530, L93–L96.

Thongpoyai, K., W. Luangtip, U. Sawangwit, T. P. Roberts, S. Komonjinda, V. S. Dhillon and T. R. Marsh (2019), "Thai national telescope studies of ultraluminous X-ray sources." In *Journal of Physics Conference Series*, volume 1380 of *Journal of Physics Conference Series*, 012089.

Titarchuk, Lev (1994), "Generalized Comptonization Models and Application to the Recent High-Energy Observations." *apj*, 434, 570.

Tsygankov, Sergey S., Alexander A. Mushtukov, Valery F. Suleimanov and Juri Poutanen (2016), "Propeller effect in action in the ultraluminous accreting magnetar M82 X-2." *mnras*, 457, 1101–1106.

Urquhart, R., R. Soria, H. M. Johnston, M. W. Pakull, C. Motch, A. Schwope, J. C. A. Miller-Jones and G. E. Anderson (2018), "Multiband counterparts of two eclipsing ultraluminous X-ray sources in M 51." *mnras*, 475, 3561–3576.

van der Klis, M. (1989), "Fourier techniques in X-ray timing." In *NATO Advanced Science Institutes (ASI) Series C* (H. Ögelman and E. P. J. van den Heuvel, eds.), volume 262 of *NATO Advanced Science Institutes (ASI) Series C*, 27.

van Paradijs, J. and J. E. McClintock (1994), "Absolute visual magnitudes of low-mass X-ray binaries." *aap*, 290, 133–136.

VanderPlas, Jacob T. (2018), "Understanding the Lomb-Scargle Periodogram." *apjs*, 236, 16.

Vasilopoulos, G., S. K. Lander, F. Koliopanos and C. D. Bailyn (2020), "M51 ULX-7: superorbital periodicity and constraints on the neutron star magnetic field." *mnras*, 491, 4949–4959.

Vink, J., J. M. Laming, M. F. Gu, A. Rasmussen and J. S. Kaastra (2003), "New X-ray Evidence for Slow Temperature Equilibration behind the Shock Front of SN 1006." In *AAS/High Energy Astrophysics Division #7*, volume 7 of *AAS/High Energy Astrophysics Division*, 26.01.

Voges, W. (1993), "The ROSAT all-sky survey." *Advances in Space Research*, 13, 391–397.

Volonteri, Marta (2010), "Formation of supermassive black holes." *aapr*, 18, 279–315.

Walton, D. J., F. Fürst, M. Bachetti, D. Barret, M. Brightman, A. C. Fabian, N. Gehrels, F. A. Harrison, M. Heida, M. J. Middleton, V. Rana, T. P. Roberts, D. Stern, L. Tao and N. Webb (2016), "A 78 Day X-Ray Period Detected from NGC 5907 ULX1 by Swift." *apjl*, 827, L13.

Walton, D. J., F. Fürst, F. A. Harrison, M. J. Middleton, A. C. Fabian, M. Bachetti, D. Barret, J. M. Miller, A. Ptak, V. Rana, D. Stern and L. Tao (2017), "The Broadband Spectral Variability of Holmberg IX X-1." *apj*, 839, 105.

Walton, D. J., F. Fürst, F. A. Harrison, D. Stern, M. Bachetti, D. Barret, M. Brightman, A. C. Fabian, M. J. Middleton, A. Ptak and L. Tao (2018a), "Super-Eddington accretion on to the neutron star NGC 7793 P13: Broad-band X-ray spectroscopy and ultraluminous X-ray sources." *mnras*, 473, 4360–4376.

Walton, D. J., F. Fürst, M. Heida, F. A. Harrison, D. Barret, D. Stern, M. Bachetti, M. Brightman, A. C. Fabian and M. J. Middleton (2018b), "Evidence for Pulsar-like Emission Components in the Broadband ULX Sample." *apj*, 856, 128.

Walton, D. J., M. J. Middleton, V. Rana, J. M. Miller, F. A. Harrison, A. C. Fabian, M. Bachetti, D. Barret, S. E. Boggs, F. E. Christensen, W. W. Craig, F. Fuerst, B. W. Grefenstette, C. J. Hailey, K. K. Madsen, D. Stern and W. Zhang (2015), "NuSTAR, XMM-Newton, and Suzaku Observations of the Ultraluminous X-Ray Source Holmberg II X-1." *apj*, 806, 65.

Walton, D. J., C. Pinto, M. Nowak, M. Bachetti, R. Sathyaprakash, E. Kara, T. P. Roberts, R. Soria, M. Brightman, C. R. Canizares, H. P. Earnshaw, F. Fürst, M. Heida, M. J. Middleton, D. Stern, L. Tao, N. Webb, W. N. Alston, D. Barret, A. C. Fabian, F. A. Harrison and P. Kosec (2020), "The unusual broad-band X-ray spectral variability of NGC 1313 X-1 seen with XMM-Newton, Chandra, and NuSTAR." *mnras*, 494, 6012–6029.

Walton, D. J., T. P. Roberts, S. Mateos and V. Heard (2011), "2XMM ultraluminous X-ray source candidates in nearby galaxies." *mnras*, 416, 1844–1861.

Watarai, Ken-ya, Jun Fukue, Mitsuru Takeuchi and Shin Mineshige (2000), "Galactic Black-Hole Candidates Shining at the Eddington Luminosity." *pasj*, 52, 133.

Weaver, R., R. McCray, J. Castor, P. Shapiro and R. Moore (1977), "Interstellar bubbles. II - Structure and evolution." *apj*, 218, 377–395.

Weng, S.-S. and H. Feng (2018), "Evidence for Precession due to Supercritical Accretion in Ultraluminous X-Ray Sources." *apj*, 853, 115.

Wijers, Ralph A. M. J. (1997), "Evidence against field decay proportional to accreted mass in neutron stars." *mnras*, 287, 607–614.

Wiktorowicz, G., M. Sobolewska, J.-P. Lasota and K. Belczynski (2017), "The Origin of the Ultraluminous X-Ray Sources." *apj*, 846, 17.

Wilms, J., A. Allen and R. McCray (2000), "On the Absorption of X-Rays in the Interstellar Medium." *apj*, 542, 914–924.

Zampieri, L., D. Impiombato, R. Falomo, F. Grisé and R. Soria (2012), "Searching for the orbital period of the ultraluminous X-ray source NGC 1313 X-2." *mnras*, 419, 1331–1337.

Zampieri, L. and T. P. Roberts (2009), "Low-metallicity natal environments and black hole masses in ultraluminous X-ray sources." *mnras*, 400, 677–686.

Zampieri, Luca, Paola Mucciarelli, Renato Falomo, Philip Kaaret, Rosanne Di Stefano, Roberto Turolla, Matteo Chieregato and Aldo Treves (2004), "The Ultraluminous X-Ray Source NGC 1313 X-2 (MS 0317.7-6647) and Its Environment." *apj*, 603, 523–530.

Zhang, S. N., Wei Cui and Wan Chen (1997), "Black Hole Spin in X-Ray Binaries: Observational Consequences." *apjl*, 482, L155–L158.

Zhou, Ye, Timothy T. Clark, Daniel S. Clark, S. Gail Glendinning, M. Aaron Skinner, Channing M. Huntington, Omar A. Hurricane, Andris M. Dimits and Bruce A. Remington (2019), "Turbulent mixing and transition criteria of flows induced by hydrodynamic instabilities." *Physics of Plasmas*, 26, 080901.